Investigations of close-in exoplanets: starspot transits, and ultra-short period planets

by

Roberto Sanchis Ojeda

Submitted to the Department of Physics
in partial fulfillment of the requirements for the degree of

Doctor of Philosophy

at the

MASSACHUSETTS INSTITUTE OF TECHNOLOGY

June 2014

Signature redacted

Author .....
Department of Physics
May 5, 2014

Signature redacted

Certified by .....
Joshua N. Winn
Associate Professor
Thesis Supervisor

Signature redacted

Accepted by .....
Krishna Rajagopal
Associate Department Head for Education

Investigations of close-in exoplanets: starspot transits, and ultra-short period planets

by

Roberto Sanchis Ojeda

Submitted to the Department of Physics
on May 5, 2014, in partial fulfillment of the
requirements for the degree of
Doctor of Philosophy

Abstract

Over the past 20 years, approximately 1700 planets outside of the solar system have been found. Known as exoplanets, they represent a great opportunity to answer some of the deepest questions about the origin and evolution of our solar system. In this thesis I focus on transiting exoplanets, planets that eclipse their host star from our point of view, reducing momentarily the stellar flux detected by our telescopes.

In the first part of this thesis, I develop a new method to measure obliquities, the angle between the spin axis of the star and orbital plane of each of the planets. In our solar system, the obliquity of all planets is within a few degrees of zero, a natural consequence of the standard theory of planet formation, in which a rotating envelope of gas collapses into a disk-shaped protoplanetary disk from which the planets form. But this is not the case for all exoplanets. Close-in gas giants are frequently found in orbits that are tilted respect to the spin axis, a sign that some process is altering the orbits of these planets.The new technique I develop in this thesis uses the passage of a transiting planet over starspots to obtain information about the obliquity of its host star. In particular, I show how to use this technique for close-in gas giants with low and high obliquities, and I extend it to longer orbital periods and multi-planet systems, where obliquity measurements are scarce and therefore more interesting.

In the second part of this thesis I describe a survey to detect the shortest-period planets discovered with the Kepler space telescope. In this survey I take a different approach to discover ultra-short period transiting exoplanets. A simple Fourier transform is obtained for every Kepler star, and planets are detected by interpreting the amplitudes and frequencies of the different peaks of the Fourier spectrum. This technique has allowed us to detect Kepler-78b, currently the smallest planet with a mass and radius measurement, with an extreme orbital period of 8.5 hours. The last chapter of this thesis is devoted to the survey, from which a list of 106 planet candidates with orbital periods shorter than one day emerged. The properties of these planet candidates are ultimately used to understand the characteristics of ultra-short period planets in general.

Thesis Supervisor: Joshua N. Winn
Title: Associate Professor

Acknowledgments

I want to thank my parents and my sister for raising me to become the man I am, and for understanding that I needed to be 3600 miles away from them to complete my dreams. They have been very supportive through out all different stages of my career, and I am sure they will continue to do so for the years to come. I would also like to thank my entire family, and specially my grandfather and my uncle, both named Juan Jose, for all the life lessons they have taught me since I was a little kid.

I would like to thank the large list of mentors I have benefitted from. Many teachers from the primary school Blasco Ibañez and the high school I.E.S. Vicent Sos Baynat in Castellón de la Plana paid special attention to my education. Special thanks to Isabel Garcia Barceló for being the first person to encourage me to pursue my math interests beyond the class material, and in general to the rest of math and science professors at my high school. I cannot forget Cristobal Sánchez-Rubio, Javier Gil and Fernando Latre, the three high school teachers at I.E.S. Peñgolosa that took the time to train me for the science olympiads that made interested in becoming a scientist. Fernando always had a personal interest in my career, and he introduced me to Luis Ruiz Esteller and Pablo Baigorri, whose moral and economical support was a key factor in me getting a college degree. The support of my high school classmates was also very important for me to move forward. I also want to thank many of my classmates and Physics professors at the University of Valencia, specially my research advisor Pilar Hernández, she supported me and encouraged me to apply to MIT.

I cannot express how grateful I am to my advisor Josh Winn, for all the personal and professional support he has offered me over the past four years. He was patient and brave enough to turn a pencil and paper theoretical physicist into an astronomer, as well as dealing with all the additional complications of having an international advisee. I have learned much from him, and I will be proud if other researches see a bit of him in me, that can only mean that I am doing something right. I have only had the pleasure to work with Saul Rappaport for the last couple of years, but it has been a great experience. I have learned many things from his expertise, but most of all, I

now know that no matter where I go, every Tuesday and Thursday I will be waiting for him to walk into my office and share his latest work or to offer an interesting life experience. I also want to thank Joseph Fromaggio for taking the time to be part of my committee during the first stages, and the same goes to Sara Seager, from which I have also been fortunate enough to obtain some of the best career advice possible.

I would like to thank many of my fellow graduate students at the physics department of MIT, which helped me make the transition to the US and also shared with me countless days and nights working on problem sets or studying for qualifying exams. I want to thank Ian Stewart for allowing me to work with him for the first year, and thank Al Levine for his help when I was preparing for the qualifying exams. I also want to thank Scott Hughes for being my academic advisor and help me get through all the departmental requirements in a timely manner.

Many of the conclusions and ideas developed in this thesis came from discussions with members of the MIT exoplanet community. For that, I would like to thank Simon Albrecht, Josh Carter, Brice Demory, Amaury Triaud, Brice Croll, Kevin Schlaufman, Kat Deck, Bjoern Benneke, Leslie Rogers, Peter Sullivan and Zach Berta-Thomson. I have had the pleasure to collaborate with many great researchers over the past few years, and I would like to mention some of them from which I particularly learned many things: Matt Holman, Dan Fabrycky, Bill Chaplin, Teruyuki Hirano, Dave Latham, John Johnson, Geoff Marcy and Andrew Howard.

This thesis would not have been possible with the support of those friends that shared an apartment and personal experiences with me for a long time: Laura, Eugene, Diego, Ben, Jordi, Nuria and Enrique. I have also been able to enjoy creating an association of students with my Spanish friends, Spain@MIT, that has given me a window to escape from routine and to relieve stress. Thank you Ruben, Maria Jose, Patricia, Maite, Noel, Elisa, Fernando and all the other members of the association. And finally, thanks to Paula Sánchez for loving me during the good and the bad moments, for her care and patience, and for teaching me there is not obstacle big enough when it comes to the things you are truly passionate about. I couldn't have found a better partner to spend the last few years of graduate school with.

Contents

List of Figures

List of Tables

Chapter 1

Introduction

Almost every child becomes familiar with the concept of alien life at an early stage. There are hundreds of movies, videogames and books devoted to the idea of other civilizations, living organisms with different appearances, generally with a more advanced intelligence. It has become increasingly complicated for fiction writers and conspiracy theorists to depict intelligent alien life living somewhere within our solar system. It is now common knowledge that most of the planets in the solar system have been well studied, and it is hard to believe that an advanced solar system civilization would have stayed out of our reach for so long.

People's fantasies are of course shifting towards exoplanets (planets outside our Solar System). Since our own Solar System has at least 8 planets, it always seemed natural to believe that our galaxy would be filled with millions of planets. But it was not shown until relatively recent times that in fact these planets exist ([132] in 1995 and later [38] in 2000). The field has evolved so quickly, that it is currently known that at least 50% of the stars in the sky have a planet [68], and that there could be billions of Earth-like planets with the right temperatures to support life in our galaxy [153]. These discoveries have increased our desire to answer some of the most fundamental questions: are we alone? how did we get here? how did our solar system form? and our planet?

In this thesis I describe my efforts to contribute to finding an answer to some of these questions. In particular, I will describe how measuring certain geometric

properties of exoplanetary systems can get us closer to constraining the mechanisms involved in the formation of these systems. I will also develop a new and simple method to discover ultra-hot exoplanets, and even if they are too hot to sustain the type of intelligent civilization we are looking for, they are helping us to put our own planet into context.

1.1 How exoplanets are discovered

The most successful exoplanet discovery techniques rely on detecting the effects that the presence of a planet has on its host star. Planets are generally much smaller and cooler than their host stars. This means that when observing planetary systems, most of the light received on Earth comes from the star and not from the planets. For a few decades now, astronomers, and specifically planet hunters, have learned how to deal with this inconvenience to successfully detect different types of exoplanets.

The radial velocity technique. When two massive bodies are gravitationally bound, the solution to the equations of motion tells us that both objects orbit around their common center of mass with the same orbital period. This principle can be used to detect exoplanets, by sensing the orbit of the star and inferring the presence of one or several planets. Fortunately, stars emit a continuum of light (black body radiation) which is partially absorbed by cooler surface gases at very particular frequencies. This continuum of light with these absorption lines is referred to as the stellar spectrum. From this spectrum we can learn many things about the star we are observing, such as its temperature, surface gravity and composition. But we can also use stellar spectra to measure the radial velocity of the star, since the absorption line wavelengths are shifted when the star moves due to the Doppler effect. A shift in wavelength can be translated into a radial velocity v with the simple formula $\Delta\lambda/\lambda \approx v/c$, where c is the speed of light. Many instruments reach precisions of $\Delta\lambda/\lambda < 10^{-8}$ allowing the detection of the motion of the star with a precision of a few m/s.

We can quantify what is the expected radial velocity of a star in the presence of a planet with mass m_p, with an orbital period P, inclination i and eccentricity

e, orbiting a star with a mass M_*. The radial velocity of such a star will have a periodicity P and a semi-amplitude K [122] equal to:

$$K = \frac{28.4}{\sqrt{1-e^2}} \frac{m_p \sin i}{M_{\rm Jup}} \left(\frac{M_* + m_p}{M_\odot}\right)^{-2/3} \left(\frac{P}{1\,{\rm yr}}\right)^{-1/3} {\rm m/s}. \quad (1.1)$$

The shape of the signal will be sinusoidal if the eccentricity, e, is zero, but otherwise it will show a characteristic shape that will generally allow us to constrain both K and the eccentricity at the same time. This formula shows that a Jupiter mass planet with an orbital period of 1 year orbiting a Sun-like star can be easily detected if we have precisions of a few m/s. But such precisions were not available from the very beginning, and would certainly not be sufficient to detect an Earth-mass planet with an orbital period of 1 year. The upper panel of Figure 1-1 clearly shows that there has been a steady push by the community to be able to characterize low-mass planets with the RV technique. Only Jupiter mass planets were discovered during the first decade ($M_{\rm Jup} = 317.8\,M_\oplus$), and most of them have short orbital periods (the so-called Hot-Jupiters), which increases the RV semi-amplitude. Year after year, the minimum mass of all planets detected with the RV method has been decreasing exponentially, and we currently have already detected Earth-mass planets [56], although with orbital periods of the order of days rather than years. Uncertainties of the order of tens of cm/s will be required to reach that milestone, since the radial velocity semi-amplitude induced in the Sun by the presence of the Earth is only 9 cm/s.

The RV technique is a very powerful one that has yielded over 440 planet detections to date [233], and it is likely to continue doing so in the next number of years years. One of the virtues of this method is that in principle, all planets should induce an RV signal, unless they are completely face-on with respect to our line of sight. This has been used to quantify how many planets orbit other main sequence stars with a wide range of planet masses and orbital periods [93]. The RV technique has reached a point where given enough observations, and a low level of stellar jitter (which hinders our ability to detect small planets), we can currently detect planets in almost every nearby Sun-like star. However, the main problem with this technique is that in most

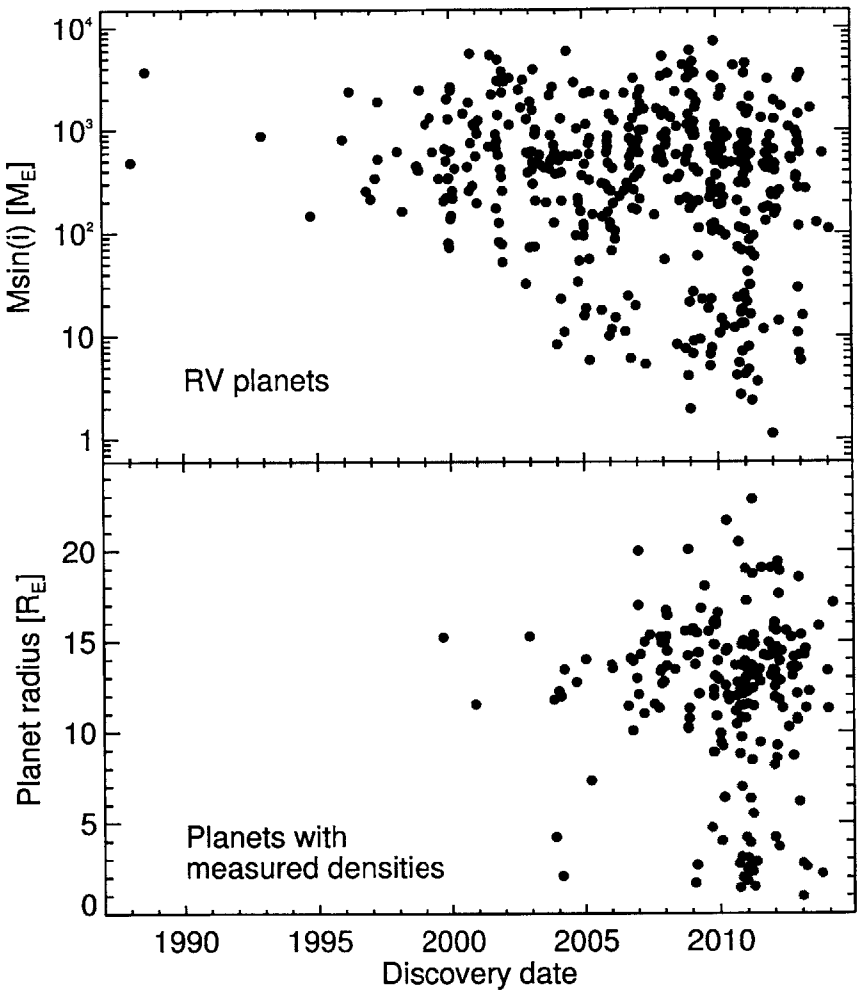

Figure 1-1: A selection of planets discovered to date.
Upper panel: The Radial Velocity method has discovered 440 planets to date [233]. It provides us with the mass of the planet multiplied by the sine of the orbital inclination. Improvements on the different instruments and techniques have led to a steady decline of the minimum mass measured over time. We have reached a point where measuring the mass of Earth-mass planets is not only possible, but will become common in the next few years.
Lower panel: When the planet transits the star, its radius can be measured, and also the orbital inclination. This leads to a measurement of the mass, which in turn can be used to obtain the planet density, a helpful quantity to constrain the composition of an exoplanet. There are 213 planets for which we know the mass and radius with enough precision [233], and we can now start to study the composition of planets smaller than $2R_E$. Planets discovered with the Kepler telescope (a total 53) have been highlighted in red to show that most of the small planet science is now driven by space telescopes.

cases it only provides a lower bound on the planet mass, and no information about the planet radius.

The transit technique. The relative flatness of our Solar System, where most of the planetary orbits are found near the same plane, provides us with the opportunity to observe the inner planets, Mercury and Venus, passing in front of our own Sun. It was expected that something similar will happen with some exoplanets; assuming that planetary systems are randomly oriented in our galaxy, a fraction of them should be oriented such that some planets pass in front of their host stars. One only needs to monitor the photometric flux of those stars that have transiting planets and wait until one of them transits, blocking a small fraction of the received starlight.

Even if the transit technique sounds technically easier than the RV technique, important shortcomings discouraged most planetary scientists from trying to detect the first planets with a transit survey. If we use the solar system as an example (and this was the only example 25 years ago), an Earth-like planet would transit the Sun only once per year for about 6 hours, and it would require a relative photometric precision of 100 parts per million to detect the transit (precision that is rarely achievable from the ground even with the largest telescopes). And this assumes that we know which star has a transiting planet. In reality, only 1 out of 200 stars with an Earth-like planet would be oriented in such a way that we could see the transits of the planet. Without a priori knowledge of the fraction of stars with any type of planets, it looked like the transit technique would have a very limited applicability.

Things changed dramatically with the discovery of the first planets, most of them Hot-Jupiters, with orbital periods of only a few days. Suddenly, there was a group of stars that clearly had a planet, for which the probability of transit was of the order of 10% and for which the transits could be detectable with ground based telescopes (the transit depth is approximately the ratio of projected areas between the planet and the star, 1% for Jupiter-size planets orbiting Sun-like stars). It was in 2000 when transits where detected for first time for HD 209458b ([38], [82]). The orbital inclination was hence known precisely (close to 90° for transiting planets) allowing a determination of the planet mass using the RV semi-amplitude, and also the planet radius was known

from an analysis of the transit light curve. Knowledge of the mass and radius of a planet leads to interesting constraints on its composition, since for example gaseous planets have low densities while rocky planets have densities similar to that of Earth.

The detection of the transits of HD 209458b led to something even more important, the era of transit surveys. With strong indications that close-in Hot-Jupiter could be common (we currently know there is approximately one in every hundred stars), a survey capable of doing 0.5-1% precision photometry on hundreds or thousands of stars could detect many transiting planets, planets for which we would not only know the radius, but we could also use the RV technique a posteriori to measure their masses and densities. The lower panel of Figure 1-1 shows 213 planets for which we currently know the masses and radii, allowing for interesting studies of their composition and diversity (see for example [223]). Until 2009, most of these exoplanets had been found by ground based transit surveys like WASP [157] or HATNet [7], and most of them were Hot-Jupiters.

Things changed dramatically with the launch of two space based missions. First CoRoT starting in 2008 [11] and then Kepler in 2010 [23], inaugurated the era of space-based transit surveys. From space, a telescope can monitor the same star for as long as required, something impossible from most telescope sites on the ground due to the Earth's rotation. Additionally, it is possible to achieve greater photometric precision in the absence of an atmosphere in between the source and the telescope (see Figure 1-2). These two factors have finally allowed the detection of more than 3000 planets, with much longer orbital periods, and much smaller sizes. To emphasize this point, Kepler planets with measured masses and radii are shown on the lower panel of Figure 1-1 as red dots, showing how Kepler has allowed us to characterize a large sample of small planets. But this is not the only new window opened by space transit surveys, and most of this thesis can serve as examples of the new types of analyses that one can do with such a rich dataset.

Other techniques. There are other techniques that can be used to detect exoplanets. In fact, the first exoplanets were discovered thanks to the effect that they have on the timings of the neutron star pulsar that they orbit [232]. This type of

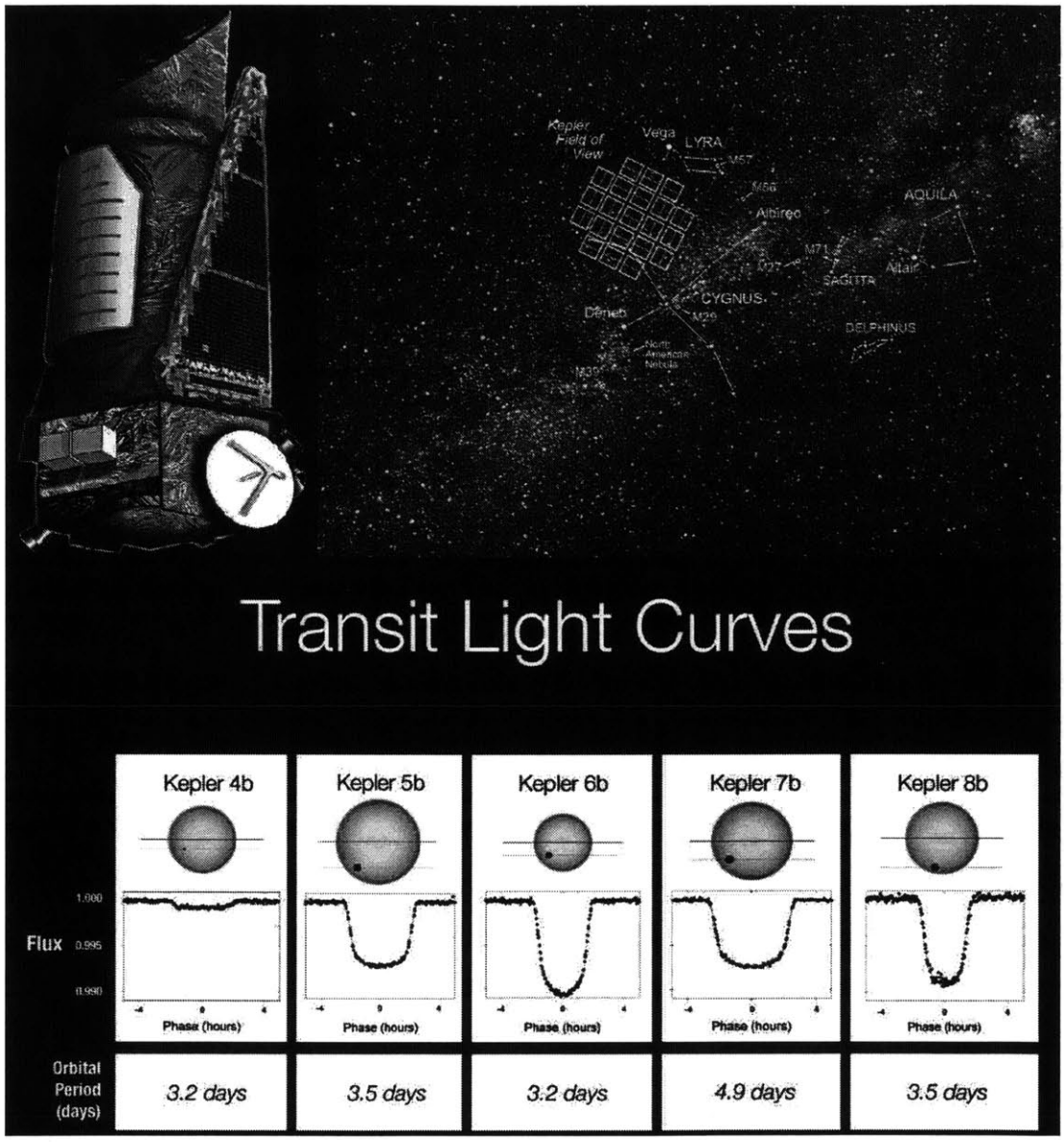

Figure 1-2: The Kepler telescope.
Upper left panel: Representation of the Kepler telescope. (Credit: NASA/Kepler mission)
Upper right panel: Image of the Kepler field, situated in the northern hemisphere between Lyra and Cygnus. (Credit: Carter Roberts)
Lower panel: A reproduction of the light curves of the first five planets discovered by Kepler, showing the great precision obtained with only a few weeks of observations. (Credit: NASA/Kepler mission)

planet has never received as much attention as the other planets discussed in this section since they probably do not have much in common with solar system planets due to their extreme environments.

Another technique is astrometry. For nearby stars, it should be possible to detect the true orbit of the host star on the sky, rather than obtaining the radial velocity through indirect methods, by simply detecting the angular displacement relative to background stars. There have been several claims of planets detected with astrometry alone, but none that has been confirmed to date. This is bound to change with the European astrometric mission GAIA, which will obtain the position of up to a billion stars with great accuracy several times per year. Early estimates show that GAIA could detect hundreds of long period massive exoplanets [199].

One of the most promising techniques is direct imaging, because it is relatively easy to study the atmosphere of a directly imaged planet, by taking images at different wavelengths. A normal image of a planetary system will generally reveal only the presence of the host star, but it is now possible to remove a large fraction of the starlight and detect the presence of high luminosity planets. So far, only very young self-luminous planets have been detected, with the 4 planet system HR8799 as one of the most famous examples [128].

Finally, it is also possible to detect planets via gravitational microlensing. When a foreground star passes in front of another star at a really close sky-projected distance, it can act as a lens, magnifying the amount of light coming from the lensed background star. If the lensing star has a planet, there is a chance that the planet will also act as a lens, modifying the magnification pattern. This technique has been used to detect several planets to date, such as OGLE 2003-BLG-235/MOA 2003-BLG-53, a 2.6 Jupiter mass planet [19], and has the potential to help us understand the frequency of long period, low mass, planets orbiting main sequence stars.

1.2 The formation of exoplanetary systems

It is now clear that exoplanets are very common, which means that the process of forming exoplanets must be quite efficient. For the longest time, astronomers only had information about our own solar system to constrain the different theories of planetary systems formation. The Sun's planets all orbit in the same direction, which is nearly aligned with the spin of the Sun, and have roughly coplanar orbits. These clues suggest that the solar system formed from a disk-shaped structure, and it was hypothesized that such a structure was the result of the collapse of a rotating envelope of gas surrounding the young Sun. Indeed, the collapse of a rotating sphere of gas must flatten out into a disk in order to conserve angular momentum.

The material of the protoplanetary disk quickly grows from tiny dust particles into kilometer size protoplanetesimals. These protoplanetesimals start to collide with each other, giving birth to planetary cores that can grow up to masses of 5-10 $M_{\oplus}$. When that happens, the planet can start accreting gas, and a gas giant is formed. If that critical mass is not reached, or there is not enough gas left on the disk, the planetary core stops accreting mass and remains as a rocky planet. All these planets will have near-circular orbits that will follow the direction of rotation of the original disk, which is the same as the direction of the spin of the star. In principle, the orbits of the planets could remain near the plane of the protoplanetary disk, provided there are no strong planet-planet interactions, which also explains the coplanarity of the solar system planets.

In our solar system, rocky planets are found closer to the Sun than gas giants. The conventional theory for planet formation also has an explanation for this. It is much easier to form gas giants farther away from the stars because temperatures are lower, allowing certain hydrogen compounds such as water or ammonia to condense and form solid ice grains. Sometimes a fiducial line is defined, called the "snow line", as the distance from the Sun at which the temperature is approximately 150K, a temperature that allows the condensation of the mentioned compounds. In the solar system, all gas giants are beyond the snow line (situated at approximately 5 AU),

whereas the rocky planets lie within that line.

Once the solar system was explained with this simple but self-consistent theory of planet formation, many astronomers believed that most planetary systems would be similar to our own. Arguably, this theoretical bias might have delayed the detection of the first exoplanets, since as we argued before, our current technologies have barely started to reach the required precision to detect planets like the ones in the solar system.

The presence of protoplanetary disks similar to the ones predicted in this theory, found in many young stars in the solar neighbor, confirms the collapsing envelope scenario. But this theory cannot explain the existence of Hot-Jupiters. These planets are all found very close to their host stars, well within the snow line. The next section is devoted to explain any evidence for how these planets evolved into their current orbits.

1.3 Obliquities of Hot-Jupiter hosts

The puzzling discovery of Hot-Jupiters was turned into a great opportunity to learn about different process that can alter the structure of a planetary system. In principle, a primordial planet system will have planets with circular orbits oriented in the same direction as the spin of the star. The detection of moderate to high eccentricities for some planets (see for example [32]) was considered a good argument for additional interactions with other bodies or with the protoplanetary disk, interactions that were shaping the orbits of the Hot-Jupiters. However, the strongest argument was the discovery of the first planets for which the orbit of the planet is tilted with respect to the stellar equator ([81], [228]).

The obliquity, or spin-orbit angle, of an exoplanetary system is the angle between the spin axis of the star and orbital axis of the planet. A commonly used technique to measure the obliquity of exoplanet systems is the Rossiter-Mclaughlin (RM) effect [231], which is the spectroscopic equivalent of a planet transit. Since the planet blocks a certain part of the rotating stellar surface, an additional Doppler shift is observed

which depends on the sky-projected obliquity of the system. Thanks to this effect, the obliquity of many Hot-Jupiters systems has been found to be rather large ([226], [214], [6]).

There are two possible ways to explain why the Hot-Jupiters have been found to be misaligned. One is that the spin axis of the star can get tilted with respect to the original position of the protoplanetary disk, either through magnetic interactions [107], chaotic accretion [17] or torques from neighbor stars. In this scenario the Hot-Jupiters migrate inwards on the disk to get to their close-in orbits, and the high obliquities observed are a consequence of the star-disk misalignment. The other possible explanation is that dynamical interactions, such as planet-planet scattering [170] or the interaction with a massive third body via Kozai cycles [58], can tilt the orbits of the planets. The third body is required to have a certain inclination with respect to the plane of the star-planet system. This is what causes the Kozai cycles, in which both the orbital eccentricity of the planet and the obliquity of the host star can reach very large values. Large eccentricities lead to small periastron distances, which increase the interaction between the planet and its host star. Tidal interactions then circularize and shrink the orbit, explaining the close-in orbits of the Hot-Jupiters. In this case, the high obliquities observed are a consequence of the history of dynamical interactions in the system.

The first part of this thesis is devoted to developing a new method to measure the obliquities of exoplanetary systems using photometry alone, with the hope of contributing to our understanding of how Hot-Jupiters reached their current positions and how other types of systems could have formed. The second part of the thesis is dedicated to the study of another family of planets that has likely migrated from their original orbits as well, rocky planets with orbital periods shorter than 1 day. The study of planets that have migrated is the central topic of the complete thesis.

1.4 Thesis overview

Chapters 2 through 6 are devoted to the description and application of a new method of measuring the obliquity of exoplanetary systems. The technique uses the passage of a planet over starspots to obtain information about the obliquity of its host star. The essence of the technique is the following: if a system has a low obliquity, an occulted spot should be occulted in consecutive transits, since the trajectory of the spot will be parallel to the trajectory of the planet.

In Chapter 2, the foundations of this new technique are explained for the first time, and applied to the ground based transit light curves of WASP-4b obtained with the Magellan telescope. Chapter 3 deals with a different type of system, HAT-P-11, in which the planet's orbit is highly tilted with respect to the stellar equator. This gives rise to a particular geometry in which the planet transits from one stellar pole to the other. The exquisite Kepler photometry clearly shows that the spots are concentrated in two active latitudes, a configuration similar to what is observed in the Sun.

Chapter 4 describes the measurement of the obliquity of the first multi-transiting planetary system, the three planet system Kepler-30. The low obliquity of the system is similar to that of the solar system, and it might imply that coplanar multi-planet systems might be less frequently misaligned than Hot-Jupiters. Chapter 5 explains the case of Kepler-63b, a gas giant with an orbital period of 9.4 days orbiting a young solar analog. The high obliquity of the host star is demonstrated both via the RM effect and using the starspot-crossing technique. Finally, Chapter 6 describes an effort to catalog all possible targets for this new technique in the Kepler database. The obliquity of 5 new single transiting systems is shown to be low with a few simple arguments, showing the potential of the technique applied to a large sample.

The thesis takes a turn on Chapters 7 and 8 to discuss close-in rocky planets. Different authors have worked on the idea that Hot-Jupiters might loose their atmospheres due to the high levels of irradiation received from the stars. If that is the case, the cores of these Hot-Jupiters could be discovered transiting Kepler stars. These two chapters describe a survey to detect small objects transiting Kepler stars with orbital

periods shorter than 1 day. Chapter 7 describes in detail the most exciting planet discovered in the survey, Kepler-78b, an Earth-size planet with an orbital period of 8.5 hours. Chapter 8 describes the full survey and draws important conclusions about these new family of planets, mostly arguing against the idea that these planets are former cores of gas giants. The conclusions of the thesis can be read in Chapter 9.

The material of Chapters 2-5 and 7-8 have been already published ([179], [177], [174], [176], [180] and [175]). The material in Chapter 6 has not been published or submitted to a journal yet.

Chapter 2

First obliquity measurement using the starspot-crossing effect

Published as: "Starspots and Spin-orbit Alignment in the WASP-4 Exoplanetary System" Sanchis-Ojeda, R., Winn, J.N., Holman, M.J., Carter, J.A., Osip, D.J., Fuentes, C.I. 2011, ApJ, 733, 127.

We present photometry of four transits of the exoplanet WASP-4b, each with a precision of approximately 500 ppm and a time sampling of 40-60 s. We have used the data to refine the estimates of the system parameters and ephemerides. During two of the transits we observed a short-lived, low-amplitude anomaly that we interpret as the occultation of a starspot by the planet. We also find evidence for a pair of similar anomalies in previously published photometry. The recurrence of these anomalies suggests that the stellar rotation axis is nearly aligned with the orbital axis, or else the star spot would not have remained on the transit chord. By analyzing the timings of the anomalies we find the sky-projected stellar obliquity to be $\lambda = 1^{+12}_{-14}$ degrees. This result is consistent with (and more constraining than) a recent observation of the Rossiter-McLaughlin effect. It suggests that the planet migration mechanism preserved the initially low obliquity, or else that tidal evolution has realigned the system. Future applications of this method using data from the *CoRoT* and *Kepler* satellite will allow spin-orbit alignment to be probed for many other exoplanets.

2.1 Introduction

Spots on the host stars of transiting planets have generally been regarded as a nuisance. They interfere with the determination of the planet's properties, by causing variations in the transit depth, producing chromatic effects that can be mistaken for atmospheric absorption, and causing anomalies in individual light curves when spots are occulted by the planet (see, e.g., [165], [102], [36]).

Silva-Valio pointed out [190] that starspots may be helpful in one respect: observations of spot-occultation anomalies in two closely-spaced transits can be used to estimate the stellar rotation period. In effect, the planet is used to reveal the longitude of the spot during each transit. For the particular case of Corot-2, this method has been used [192] to estimate the rotation period and study the distribution, shape and intensity of the spots. The rotation period of TrES-1 has also been estimated using starspot anomalies [53].

In this paper we show how the recurrence (or not) of starspot anomalies can also be used to test whether the stellar rotation axis is aligned with the planet's orbital axis. Specifically, starspot anomalies are an alternative means of measuring or bounding λ, the angle between the sky projections of the angular momentum vectors corresponding to stellar rotation and orbital motion. Previous spot-modeling efforts ([192], [53]) were restricted to values of λ that were permitted by prior observations of the RM effect, but as we will show, it is possible to obtain tighter constraints on λ using only spot anomalies.

As many authors have pointed out, measurements of stellar obliquities are important clues about the processes of planet formation, migration, and subsequent tidal evolution (see, e.g., [162], [146], [231], [226], [61], [214], [137]).The other main method for measuring λ is the Rossiter-McLaughlin (RM) effect, an anomalous Doppler shift that is observed during transits due to the partial eclipse of the rotating star (see, e.g., [162], [146], [71]).

The particular system studied here is WASP-4b, a giant planet that transits a G7V star with a period of 1.34 days [224]. Refined parameters for this system were

presented by [227], [74], and [198]. Observations of the RM effect by [214] revealed the orbit to be prograde but gave only weak constraints on the projected obliquity: $\lambda = -4^{\circ}\,^{+43^{\circ}}_{-34^{\circ}}$.

This paper is organized as follows. In Section 2.2 we report on observations of four different transits of WASP-4b. In Section 2.3 we identify the anomalies that are interpreted as spot-crossing events, and use the remaining data to compute new system parameters. In Section 2.4 we model the light curves by taking the star spot to be a circular disk with a lower intensity than the surrounding photosphere. In Section 2.5 we determine λ using a simpler geometrical model, which does not make strong assumptions about the size or shape of the spots. Finally, in Section 2.6 we discuss the results and possible future applications of this method.

2.2 Observations and Data Reduction

We observed the transits of UT 2009 August 02, 06 and 10, and also 2009 September 26, with the Baade 6.5m telescope. This is one of the two Magellan telescopes at Las Campanas Observatory in Chile. We used the Raymond and Beverly Sackler Magellan Instant Camera (MagIC) and its SITe 2048×2048 pixel CCD detector, with a scale of $0\farcs069$ pixel^{-1}. At the start of each night, we verified that the time stamps recorded by MagIC were in agreement with GPS-based times to within one second. To reduce the readout time of the CCD from 23 s to 10 s, we used the same technique as was used by [227]: we read out a subarray of 2048×256 pixels aligned in such a manner as to encompass WASP-4 and a nearby bright comparison star of similar color. The telescope was strongly defocused to spread the light over many pixels, allow for longer exposures without saturation, and reduce the impact of natural seeing variations. On each night we obtained repeated z-band exposures of WASP-4 and the comparison star for about 5 hr bracketing the predicted transit time. Autoguiding kept the image registration constant to within 10 pixels over the course of the night.

On the first, second, and fourth nights the skies were nearly cloud-free; the third night was partly cloudy for a short duration, and the data from that time range were

Table 2.1. Observations of WASP-4

Date [UT]	Epoch	Number of data points	Cadence [s]	Airmass	RMS [ppm]	Estimated noise [ppm]
2009 Aug 02	260	369	56	$1.48 \rightarrow 1.02 \rightarrow 1.11$	442	316
2009 Aug 06	263	406	56	$1.48 \rightarrow 1.02 \rightarrow 1.21$	452	315
2009 Aug 10	266	365	55	$1.34 \rightarrow 1.02 \rightarrow 1.30$	487	318
2009 Sep 26	301	355	41	$1.41 \rightarrow 1.02 \rightarrow 1.03$	588	373

excised. In all cases the observations bracketed the meridian crossing of WASP-4 and the maximum airmass was 1.5. We used custom IDL procedures for overscan correction, trimming, flat-field division and photometry. The flat field for each night was calculated from the median of 80-100 z-band exposures of a dome flat screen. We performed aperture photometry of WASP-4 and the comparison star, along with sky regions surrounding each star. Then we divided the flux of WASP-4 by the flux of the comparison star. Trends in the out-of-transit (OOT) data were observed and attributed to color-dependent differential extinction, for which a correction was applied in the form

$$\Delta m_{\rm cor} = \Delta m_{\rm obs} + \Delta m_0 + kz \tag{2.1}$$

where z is the airmass, $\Delta m_{\rm obs}$ is the observed magnitude difference between the target and comparison star, $\Delta m_{\rm cor}$ is the corrected magnitude difference, Δm_0 is a constant used to normalize the OOT flux to one and k is a parameter that quantifies the strenght of the differential extinction. Table 2.1 is a summary of the observations, incuding the standard deviation of the OOT flux, and the theoretical Poisson noise. Figure 2-1 shows the light curves, along with four light curves published previously [198].

2.3 Starspots and System Parameters

The Magellan light curves are well-fitted by a standard transit model, except for two anomalies that are visible in the third dataset ($E = 266$, $t \approx -0.05$ hr since mid-transit) and the fourth dataset ($E = 301$, $t \approx +0.55$ hr since mid-transit). These

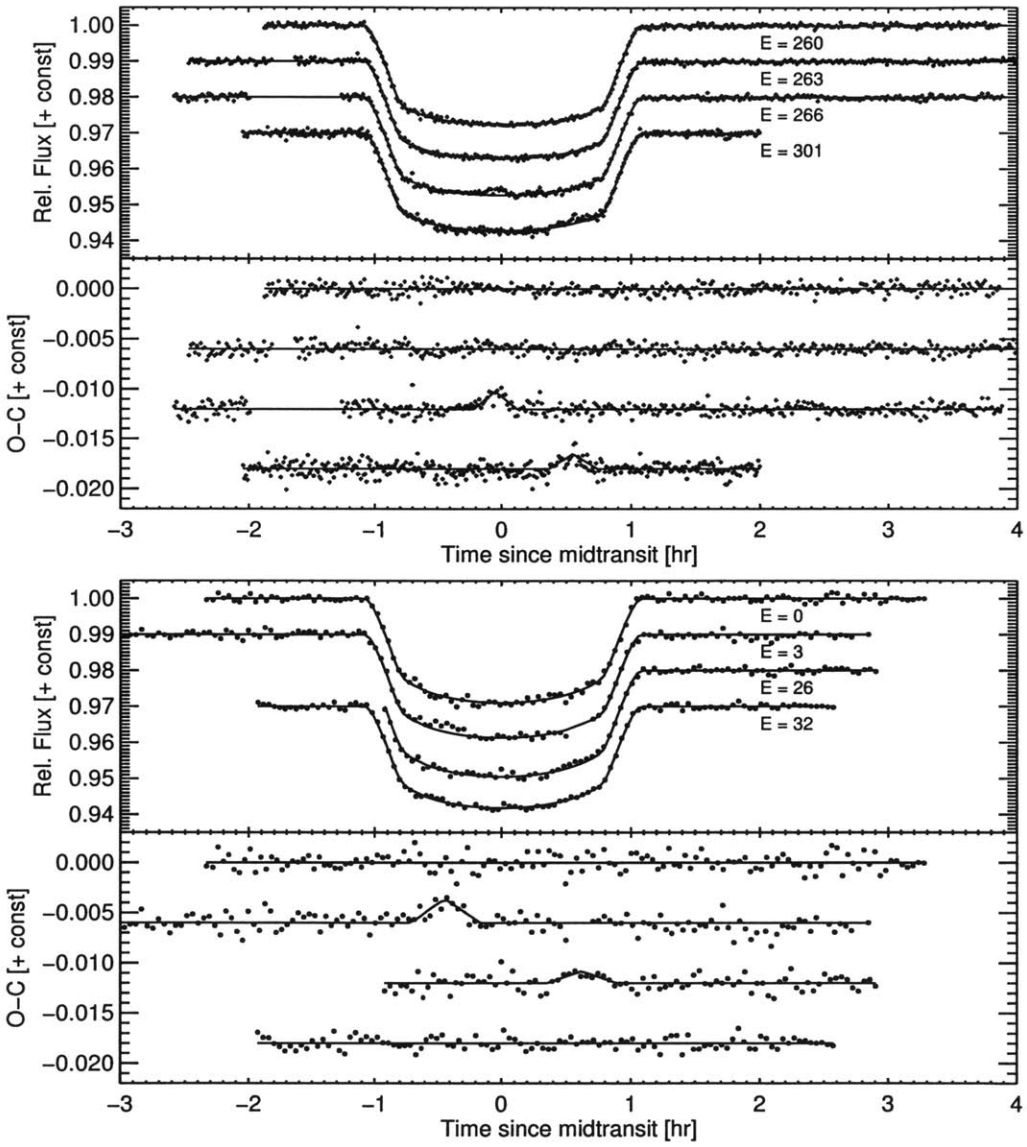

Figure 2-1: WASP-4 transit light curves and starspot anomalies.

Upper panel: Four different transits observed in the z-band with the Magellan/Baade 6.5m telescope. The solid curve shows the best-fitting transit model. The bottom two transits display anomalies in the residuals that we interpret as spot-crossing events. The residuals are shown below, with curves representing a simplified spot model (see Section 2.5). *Lower panel*: A similar presentation of the four R-band transit light curves presented by [198].

anomalies are interpreted as the temporary brightening of the system as the planet moves away from an unspotted portion of the stellar disk and onto a starspot. Because the starspot is relatively cool and dark compared to the surrounding photosphere, the fractional loss of light due to the planet is temporarily reduced and the received flux slightly rises.

The first step in our analysis was to excise the anomalous data and use the rest of the data to update the basic system parameters. For this purpose we fitted the four new data sets simultaneously with the two datasets presented by [227], which were obtained with the same telescope and instrument. We used a standard transit model with a quadratic limb-darkening law [125]. We assumed the orbit to be circular, since no eccentricity has been detected with any of the existing radial-velocity data ([224], [123], [160]). There were 30 adjustable parameters: 6 midtransit times, 6 transit depths (since unocculted starspots may cause variations in transit depth), 2 limb-darkening coefficients, the impact parameter (b), the stellar radius in units of the orbital distance (R_*/a), and 2 parameters per time series for the differential extinction corrections.[1] We refer the reader to the previous paper with the analysis of the first two datasets for a more detailed explanation of the parameter estimation method, which is based on the Monte Carlo Markov Chain technique, and takes correlated noise into account using the "time-averaging" method, in which the ratio β is computed between the standard deviation of time-averaged residuals, and the standard deviation one would expect assuming white noise. This method gave values of $\beta = 1.26$, 1.15, 1.00, and 1.39 for the four new light curves.

The best-fitting light curves are shown in Figure 2-1, and the results for the parameters are in Table 2.2. All parameters agree with the previously published data, and the theoretical limb darkening coefficients are 0.25 and 0.31 [41], which are about two sigma away from our results. The data prefer a smaller center-to-limb variation (smaller $u_1 + u_2$) than the tabulated limb-darkening law. The six individual transit depths (i.e., the individual values of $(R_p/R_*)^2$) had a mean of 0.02386 and

[1]Following [227], we consider the two disjoint segments of the 2008 August 19 observation as two separate time series, for a total of 7 time series.

a standard deviation of 0.00029, as compared to one sigma uncertainties of about 0.00014. This suggests that the transit depth is variable at the level of ≈ 0.00025 or 1%. Such variations could be produced by starspots that are not necessarily on the transit chord. During each transit, a different pattern of starspots may appear on the visible hemisphere of the star, causing variations in the fractional loss of light due to the planet. Since the ligh-curve anomalies implicate individual spots with a fractional loss of light of only $0.1\% - 0.2\%$, the observed transit depth variations of $\approx 1\%$ would have to be caused by larger individual spots, or multiple spots.

The detection of two anomalies in the Magellan data prompted us to search for similar anomalies in previously published data. The only sufficiently precise light curves we found were the single z-band light curve presented by [74], which does not display any obvious anomalies; and the four R-band light curves by [198], two of which do indeed display anomalies similar to those we found in the Magellan data. All four of the [198] light curves are shown in Figure 2-1. Compared to the Magellan data, the R-band data have a scatter that is 40% larger and a sampling rate three times slower, but anomalies can still be seen in the second dataset at $t = -0.4$ hr and (less obviously) in the third dataset at $t = 0.6$ hr. In [198] these anomalies were also noted and the possibility that they were caused by starspot occultations.

To refine the transit ephemeris, and search for any departures from strict periodicity, we fitted the midtransit times with a linear function of epoch. Before doing so we checked on the robustness of the uncertainties by employing an alternative technique, a bootstrap method based upon cyclic permutations of the residuals. The differences between the two methods of estimating uncertainties were no greater than 20%. To be conservative, the ephemeris was computed using the larger of the two uncertainty estimates. The uncertainties quoted in Table 2.2 also represent the larger uncertainties. Figure 2-2 shows the observed minus calculated (O−C) midtransit times. The best fit to the 6 Magellan transit times gives $\chi^2 = 20$ with 4 degrees of freedom. When we also included the other 9 data points reported by [198],[2] we found $\chi^2 = 34.96$ with

[2]To place all the data onto the same time standard, we used the code by [57] to convert $\mathrm{HJD_{UTC}}$ to $\mathrm{BJD_{TDB}}$.

Table 2.2. System Parameters of WASP-4b

Parameter	Value	68.3% Conf. Limits
Transit ephemeris:		
Reference epoch [BJD_{TDB}]	2454697.798226	±0.000048
Orbital period [days]	1.33823187	±0.00000025
Transit parameters:		
Midtransit time on 2008 Aug 19 [BJD_{TDB}]	2454697.798151	±0.000056
Midtransit time on 2008 Oct 09 [BJD_{TDB}]	2454748.651175	±0.000049
Midtransit time on 2009 Aug 02 [BJD_{TDB}]	2455045.738643	±0.000054
Midtransit time on 2009 Aug 06 [BJD_{TDB}]	2455049.753274	±0.000066
Midtransit time on 2009 Aug 10 [BJD_{TDB}]	2455053.767816	±0.000053
Midtransit time on 2009 Sep 26 [BJD_{TDB}]	2455100.605928	±0.000061
Planet-to-star radius ratio, $R_p/R_\star$[a]	0.1544	±0.0009
Orbital inclination, i [deg]	88.80	−0.43, +0.61
Scaled semimajor axis, $a/R_\star$	5.482	−0.022, +0.015
Transit impact parameter, $b = a\cos i/R_\star$	0.115	−0.058, +0.040
Transit duration [hr]	2.1585	−0.0036, +0.0038
Transit ingress or egress duration [hr]	0.2949	−0.0025, +0.0030
Linear limb-darkening coefficient, u_1	0.305	±0.023
Quadratic limb-darkening coefficient, u_2	0.173	±0.089
Mass of the star, $M_\star$ [$M_\odot$][b]	0.92	±0.06
Semimajor axis [AU]	0.02312	±0.00033
Radius of the star, $R_\star$ [$R_\odot$]	0.907	−0.013, +0.014
Radius of the planet, R_p [R_{Jup}]	1.363	±0.020

Note. — The quoted result for each parameter represents the median of the *a posteriori* probability distribution for that parameter, derived from the MCMC method and marginalized over all other parameters. The confidence limits enclose 68.3% of the probability, being based on the 15.85% and 84.15% levels of the cumulative probability distribution.

[a]Represents the weighted average of the 6 different results for the planet-to-star radius ratio. The standard deviation of these 6 results is used as the error of the final value.

[b]The stellar mass of $0.92 \pm 0.06\ M_\odot$ was adopted based on the analysis of [227], and used to derive the following three parameters.

13 degrees of freedom.

The probability of obtaining such a large χ^2 with only random Gaussian noise is only 0.08%. One possibility is that the transiting planet's orbit is being perturbed by the gravity of another planet or satellite. Another possibility is that the light curves are affected by low-level starspot anomalies (not visually recognized and excised) which are biasing the estimates of the midtransit times.

The order-of-magnitude of the apparent timing anomalies caused by occulted spots can be estimated as follows. We write the observed light curve as $1 - \delta(t) + \delta_s(t)$, where $\delta(t)$ is the fractional loss of light due to the planet, and $\delta_s(t)$ is the anomaly due to the occultation of a starspot. Then the shift in the centroid of the light curve due to the spot anomaly is

$$\Delta t_{\rm spot} = \frac{\int [1 - \delta(t) + \delta_s(t)]\,(t - t_c)\,dt}{\int [1 - \delta(t) + \delta_s(t)]\,dt} \approx \frac{\int \delta_s(t)\,(t - t_c)\,dt}{\int [1 - \delta(t)]\,dt}, \tag{2.2}$$

where t_c is the centroid of the idealized light curve. The simplification of the numerator is due to definition of t_c, and the simplification of the denominator assumes the perturbation is small. The spot anomaly $\delta_s(t)$ can be modeled as a triangular function of amplitude A_s, duration T_s and midpoint t_s. For a spot smaller than the planet, the duration T_s is approximately $(R_p/R_\star)T$, where T is the time between the ingress and egress midpoints. In such cases $T_s \ll T$, and Eqn. (2.2) simplifies to

$$\Delta t_{\rm spot} \approx \frac{\frac{1}{2}A_s T_s (t_s - t_c)}{(R_p/R_\star)^2 T}, \tag{2.3}$$

and for a spot anomaly at ingress or egress ($t_s - t_c \approx \pm T/2$),

$$\Delta t_{\rm spot} \approx \pm\frac{A_s T_s}{4(R_p/R_\star)^2} \approx (\pm 23\ {\rm sec}) \left(\frac{A_s}{1500\ {\rm ppm}}\right) \left(\frac{T_s}{0.4\ {\rm hr}}\right), \tag{2.4}$$

where the numerical factors are based on the observed WASP-4 parameters (see the next two sections and Table 2.3, giving the results of photometric spot modeling). The spot anomalies we identified have $A_s \approx 1500$ ppm, but if the very same spot had been crossed on the limb of the star rather than near the center of the disk,

the anomaly would have been reduced by a factor of a 3-5 due to limb darkening and geometrical foreshortening, giving $A_s \approx$ 300-500 ppm. Such a small anomaly would not have been readily detected as a clear "bump" in our data, and according to Eqn. (2.4) it would have produced timing noise of order 5-10 s, which is consistent with the excess scatter observed in the calculated transit midpoints.[3]

We conclude that timing offsets due to starspot anomalies are a plausible explanation for some (and perhaps all) of the excess timing noise that was observed. Confirming the hypothesis of gravitational perturbations would require the detection of a clear pattern in the residuals rather than just excess scatter (see, e.g., [89]), and is not possible with this relatively small number of data points. Table 2.2 gives the results for the reference epoch and orbital period, based on the 15-point fit, and with uncertainties based on the internal errors of the linear fit multiplied by $\sqrt{\chi^2/N_{\rm dof}}$, where $N_{\rm dof}$ is the number of degrees of freedom.

2.4 Spot model: photometric

A central question for our study is whether each pair of starspot anomalies was caused by occultation of the *same* spot. One issue is whether a spot could last long enough to be occulted twice. The two anomalies seen in our data were separated in time by 47 days, and the pair of anomalies in the [198] data were separated by 31 days. On the Sun, individual spots last from hours to months, with a lifetime proportional to size following the so-called GW rule ([76], [220]): $A_0 = WT$, where A_0 is the maximum spot size in MSH (micro-solar hemispheres), T is the lifetime in days, and $W_0 = 10.89 \pm 0.18$ [155]. The photometric amplitude of the WASP-4 anomalies is $\approx$ 0.2%, suggesting that the spot area is of the same order of magnitude, and giving a GW lifetime of 180 days. However, the application of this rule to WASP-4 requires an

[3]We also used the photometric spot model described in § 4 to confirm that the same spots that produced detectable anomalies could also produce timing noise of 5-10 s. Specifically, we computed an idealized transit model $\delta(t)$ and added a spot model $\delta_s(t)$ based on the same spot parameters that were inferred from the actual data, but centered on the ingress rather than near midtransit. We then added Gaussian noise to mimic the actual data and fitted the resulting time series to derive the midtransit time. The offset was 8 s.

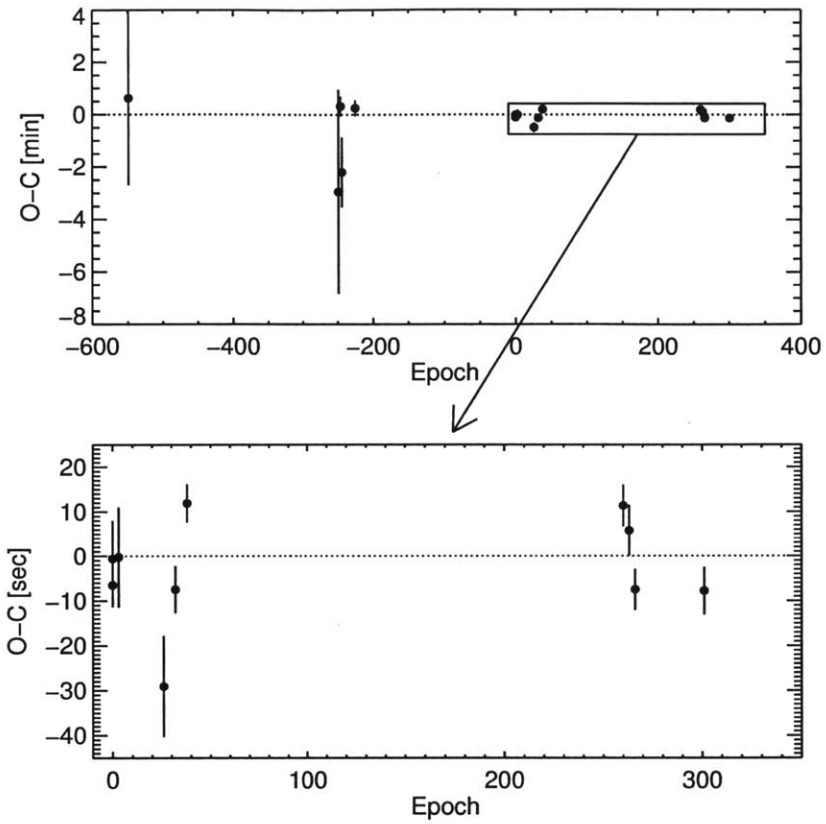

Figure 2-2: Transit timing variations of WASP-4b.

Upper panel: Transit timing residuals for all 15 midtransit times based on this work and others in the literature. *Lower panel*: close-up of the data from the last two years,where the excess of scatter is more noticeable due to the smaller uncertainties.

extrapolation, since the implied spot size is several times larger than most sunspots [196]. A more recent publication [83] studied larger spots, and found them to follow the same rule, but with a relatively small sample size.

From this perspective it is plausible that each pair of anomalies represents two passages of the planet over the same spot. However, the spot that was observed with Magellan is not likely to be the same spot that was observed by [198] because those two groups of observations were conducted one year apart. This conclusion is borne out by the modeling described below.

Another issue is whether the *amplitudes* and *durations* of both events in a pair

are consistent with passage over a single spot. A photometric spot model will make specific predictions regarding the observable anomalies, based on the stellar limb-darkening law, the geometrical foreshortening of the spots and the orbital velocity of the planet. We are reluctant to take such a model too seriously, given the unknown shape of the spot and the potential for time variations in its shape and intensity. In the case of the Sun, spots reach their maximum size within a few days and then shrink with time at a rate of about 30 MSH day^{-1} [196]. Another complication is that spots can migrate to different latitudes, although for the Sun this migration amounts to fewer than 5 degrees [83]. Nevertheless we used a model with static spot properties to perform a consistency check on the hypothesis that the same spot was occulted twice.

The orientation of the star was parameterized by λ, the sky-projected spin-orbit angle, and i_s, the inclination of the stellar rotation axis with respect to the line of sight, using the coordinate system of [146]. The visible hemisphere of the star was pixellated with a 241 $\times$ 241 Cartesian grid (enough to allow for fast computations with tolerable discretization error), and the pixels were assigned intensities using a quadratic limb-darkening law. The planet's trajectory was computed from the known orbital parameters, and zero intensity was assigned to those pixels covered by the planet's silhouette. The spot was taken to be a circle of lower intensity on the stellar photosphere, and its geometrical foreshortening was taken into account in assigning intensities to the affected pixels. The intensity distribution within the spot was taken to be a Gaussian function with a truncation radius equal to three times the standard deviation of the distribution. (We also tried modeling spots with a constant intensity, which gave qualitatively similar results.) The model had seven adjustable parameters: the stellar orientation angles λ and i_s, the rotation period of the spot, the spot intensity and radius, and the initial longitude and latitude of the spot at the time of the first anomaly.

For simplicity we studied the well-aligned case $\lambda = 0°$, $i_s = 90°$. The best-fitting model is displayed in Figure 2-3. The amplitudes and durations of the anomalies are fitted well, and the optimized rotation period is 22.2 days, i.e., the second anomaly

was observed slightly more than two complete rotations after the first anomaly. This is within the broad range of periods, 20-40 days, that is expected for a main-sequence G7 star (see, e.g., [12], [185]). In addition, this value for the rotation period agrees with the value that can be estimated from the sky-projected rotation rate $v \sin i_s$ and the stellar radius $R_\star$ according to

$$P_{\rm rot} \approx \frac{2\pi R_\star}{v \sin i_s} \sin i_s = (21.5 \pm 4.3 \text{ days}) \sin i_s, \tag{2.5}$$

where we have used $v \sin i_s = 2.14 \pm 0.37$ km s^{-1} from the work of [214], and $R_\star = 0.907 \pm 0.014\ R_\odot$ from our analysis.

In the best-fitting model, the spot's intensity profile has a maximum contrast of 32% with respect to the surrounding photosphere. Modeling both the photosphere and the spot as blackbodies, and using $T_{\rm eff} = 5500$ K for the photosphere [224], the corresponding spot temperature is 4900 K. The spot radius is 0.05 $R_\star$, implying that it is significantly smaller than the planet (0.15 $R_\star$). The spot radius and intensity contrast are highly correlated; only their product is well determined.

The fit seems reasonable in all respects and correctly predicts the nondetection of anomalies during the first and second nights of observations. Other local minima in χ^2 can be found involving a larger number of rotations between anomalies, with $P_{\rm rot} = 15.1$ or 11.4 days, but these give $\Delta\chi^2 \approx 10$ relative to the global minimum and rotation periods outside of the expected range. A similar analysis of the [198] data shows that the spot is about the same size, and gives possible rotation periods of 25.5 days and 14.0 days, of which the former is closer to the Magellan result and to the expected value.

We concluded from this exercise that each dataset (ours and that of [198]) is consistent with a single spot and a star that is well-aligned with the orbit. We decided not to pursue the implications of this photometric starspot model further, given that the simplifying assumptions (such as a circular, unchanging spot) lead to more significant uncertainties than the photometric uncertainties. In particular, the results for λ and its uncertainty would depend on the assumed shape of the

spot, because the planet trajectories with $\lambda \neq 0$ could graze the spot at different angles during each encounter. Instead we used a simplified model constrained almost exclusively by the timings of the anomalies, as described in the next section.

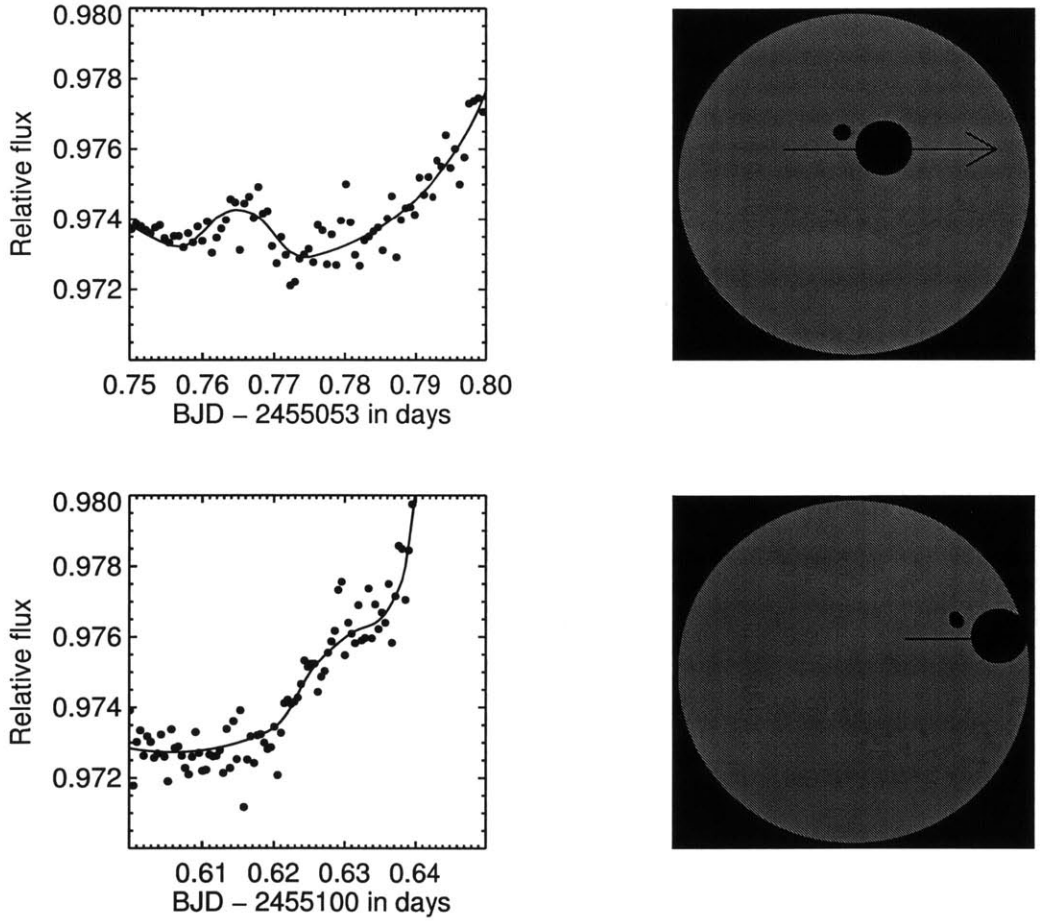

Figure 2-3: Spot-crossing events modeling.
Four panels showing the best fitting light curve of the 2D grid model with circular spots on the left, with the corresponding simulation of the position and size of the spot during that particular transit on the right.

2.5 Spot model: geometric

The recurrence of the anomaly at a later phase of the transit favors the configuration where the orbital angular momentum and the axis of rotation of the star are aligned, because in such a situation the trajectories of the spot on the surface and the planet would be almost parallel. The purpose of the geometric model described in this section is to quantify this statement, based only the observed times of the anomalies, without attempting to model complicated and largely irrelevant aspects of the situation such as the full range of possibilities for the spot size, intensity, and possible nonuniform motions.

To measure the times and gain an appreciation of the statistical significance of each feature, we used a simple triangular model for each anomaly. The triangular model is overplotted upon the residuals in Figure 2-1. Table 2.3 gives the results for the parameter values. As shown in the last few rows of that table, the first three spot anomalies (the two Magellan anomalies, and the first Southworth et al. anomaly) are detected with relatively high confidence. The spot model includes 3 extra free parameters, and improves the fit by $\Delta\chi^2 = 85$, 34 and 25, for each of the first three transits, as compared to the best-fitting model with no spots. The fourth is marginal, with $\Delta\chi^2 = 8$.[4] The weaker amplitude of the fourth event is consistent with the spot model, as the anomaly occurred near the egress where limb darkening and geometrical foreshortening both reduce the amplitude of the photometric effect. However, it remains possible that the "anomaly" is a spurious statistical detection.

Next we defined a likelihood function for λ and i_s, given the observed times of anomalies as well as the observed time ranges of non-detections. The basic idea is to assume that the spot is located within the planet's shadow at the time of the first anomaly, and then compute the position of the spot at the other relevant times for a given choice of the parameters $\{\lambda, i_s, P_{rot}\}$ (a purely geometric calculation). The model is rewarded for producing spot-planet coincidences at the appropriate time, and

[4]All of these comparisons took time-correlated noise into account, in the sense that χ^2 was computed assuming flux uncertainties that have been enlarged by the red-noise factor β. The number of data points and number of degrees of freedom for each case are given in Table 2.3.

Table 2.3. Characterization of the spots

	2009 Aug 10	2009 Sep 26	2008 Aug 23	2008 Sep 23
Amplitude (ppm)	1790	1470	2400	1190
Duration (hours)	0.34	0.38	0.56	0.54
Time of event (BJD_{TDB})	2455053.7658	2455100.6288	2454701.7938	2454732.6172
Epoch E	266	301	3	26
Rms residual (ppm)	523	580	765	722
Number of points	365	355	126	88
χ^2 for straight-line model	435	220	102	69.4
χ^2 for spot model	350	186	77	61.4
Confidence in spot detection	> 99.99	> 99.99	> 99.99	95.4

Note. — Parameters of the best fitting models to the residuals of the four different spot events. Note that χ^2 was computed after enlarging the flux uncertainties by the red-noise factor β described in § 2.3

penalized for producing coincidences at inappropriate times. Each of the two spots—the one observed in 2008, and the one observed in 2009—is given an independent value of $P_{\rm rot}$ to allow for possible differential rotation or peculiar motions of the spots (see Section 2.6 for dicussion). A further constraint is imposed to enforce agreement with the spectroscopic determination of $v \sin i_\star$ by [214]. Mathematically, we used a likelihood $\exp(-\chi^2/2)$ with

$$\chi^2(P_{\rm rot,1} \quad , \quad P_{\rm rot,2}, \lambda, i_s) = \sum_{j=1}^{2} \left(\frac{d_j}{R_p/2}\right)^2 + \left[\frac{(2\pi R_s/P_{{\rm rot},j}) \sin i_s - 2.14}{0.37}\right]^2 + {\rm NDP}, \tag{2.6}$$

where j is the index specifying one of the two anomalies, and d is the distance on the stellar disk between the center of the planet and the center of the spot. Thus, high likelihoods are assigned to spot-planet coincidences within 0.5 R_p at the correct times. This factor is based on the estimation of the size of the spot given by the photometric model, and it would require modification if the spot were bigger than the planet. The factor NDP is the nondetection penalty: models that produce spot-planet coincidences at times when they were not observed are ruled out by incrementing χ^2 by 1000 (an arbitrary number chosen to be large enough to exact a severe penalty). Based on our studies of the amplitude of the spots with the more sophisticated model of

Section 3, the nondetection penalty was only applied for coincidences within 0.9 $R_\star$ of the center of the stellar disk. For the outer 0.1 $R_\star$ (near the limb) the combined effects of limb-darkening and foreshortening would have made such an anomaly undetectable.

We used an MCMC algorithm, with the Gibbs sampler and Metropolis-Hastings criterion, to sample from the posterior probability distribution for the parameters, with uniform priors on λ and $\cos i_s$ (i.e., isotropic in the stellar orientation). We restricted $|\lambda| < 90°$, given the finding of [214] that the orbit is prograde, based on the Rossiter-McLaughlin effect. Given our finding of multiple minima in the photometric model (Section 2.4), we also performed a dense grid search in the two-dimensional space of $P_{\rm rot,1}$ and $P_{\rm rot,2}$. This identified four relevant local minima, with periods >10 days (smaller periods were rejected as unlikely for a star of the observed type). A Markov chain was initiated from each of these 4 minima.

Figure 2-4 shows the 2-d probability distribution for λ and i_s, marginalizing over the periods, for all four possible solutions. The first thing to notice is that small values of λ are favored in all cases, while i_s is poorly constrained. The completely aligned case (upper left corner of the panel) is the global minimum, with $\chi^2 = 0.95$, but none of the other solutions can be firmly ruled out.

These results are easily understood by visualizing the various solutions, as we have done in Figure 2-5. The four different configurations shown in that figure correspond to the four local minima. (One of the minima actually gave a bimodal distribution, as shown in the upper right panel of Figure 2-4; for that case Figure 2-5 shows the small-i_s solution.) The upper right panel shows the completely aligned case. This type of solution is always possible whenever two anomalies from the same spot are observed at different transit phases, unless it is ruled out by the nondetection of anomalies that should be present in other light curves. In our case, the model predicts an anomaly right at the ingress of $E = 0$ and also right at the ingress of $E = 263$. Neither of these anomalies would have been detectable in our data. The other three panels show how an appropriate combination of λ and i_s causes the trajectory of the spot to move outside the transit chord and then back inside in time for the second anomaly.

The well-aligned case is favored not only because of the lower χ^2, but also because

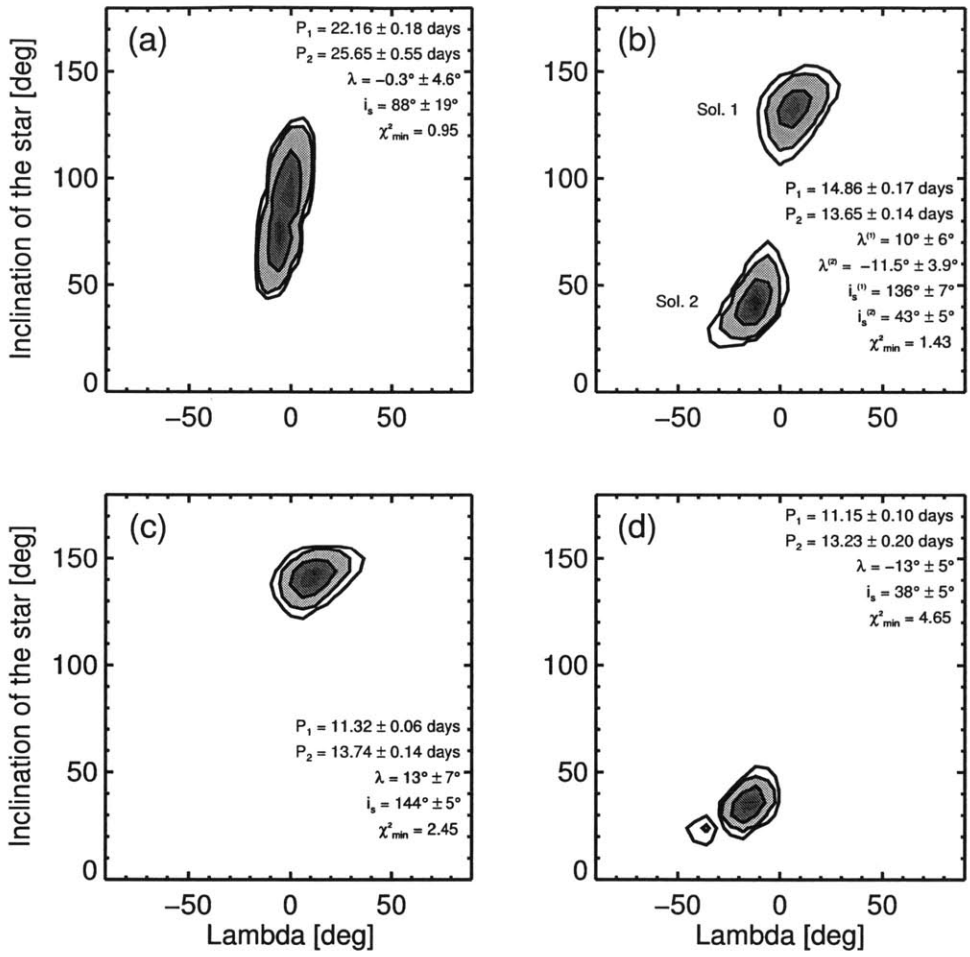

Figure 2-4: Obliquity probability distribution.
Combined probability distribution of λ and i_s four all four different solutions. In each plot the value of the parameters and the associated errors are quoted.

the corresponding rotation periods (22 and 26 days) are within the expected range of 20–40 days, as opposed to the shorter periods associated with the other solutions. One could also argue that for any observational campaign involving only a few transits, the detection of multiple spot anomalies is *a priori* more likely for a well-aligned system than for a misaligned system, because in the former case the spot spends much more time on the transit chord. For simplicity, though, we report a determination of λ based on the simple concatenation of all the Markov Chains corresponding to the four local minima, giving $\lambda = 1^{+12}_{-14}$ degrees.

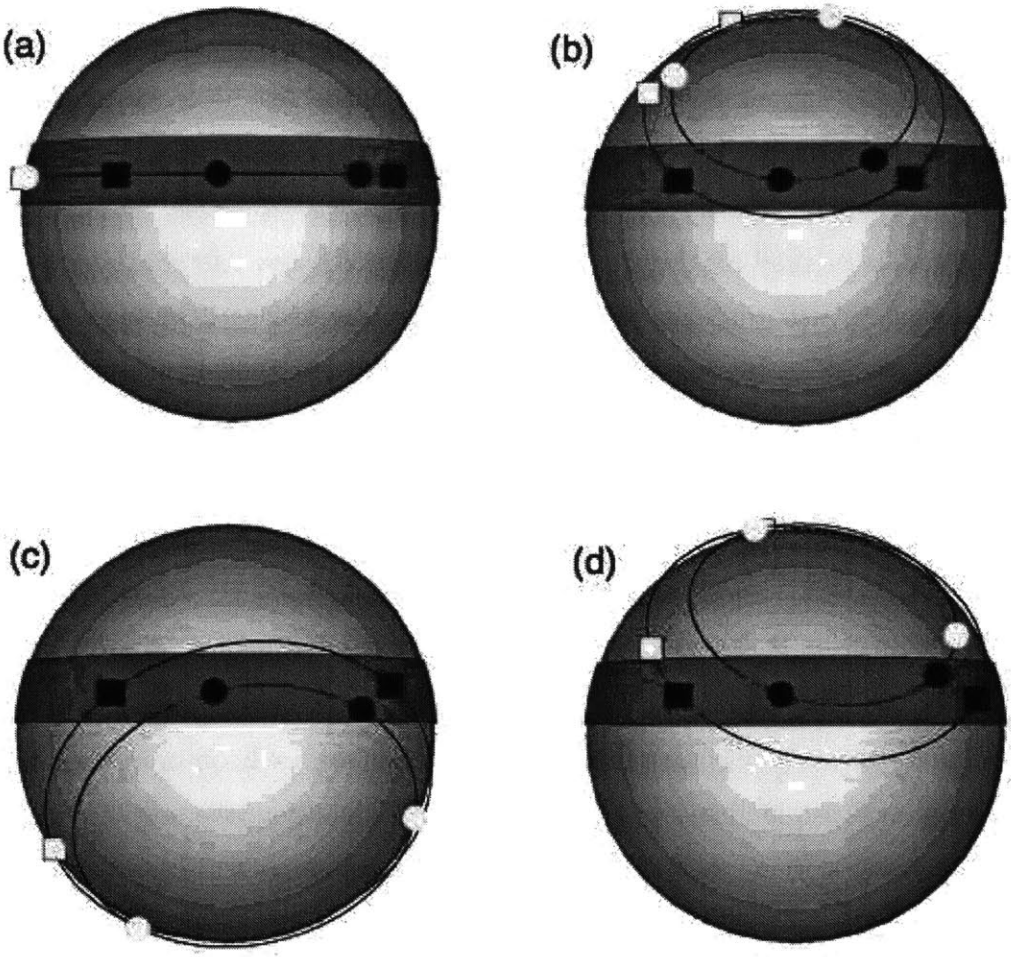

Figure 2-5: 3D models to visualize the four different solutions.
Circles represent the position of our spot during our observed transits, and squares represent the same for Southworth's observations, where the dark ones are detections and the light ones are non-detections. The shaded area of the star represents the transit chord. In the case of the upper right panel, we have plotted only one of the two possible values of i_s that can be extracted from the bimodal distribution, specifically the smallest value.

2.6 Summary and discussion

In this paper, we report the observations of four new transits of the WASP-4b planet, observations that lead to a significant improvement on the errors of the system parameters and the transit ephemerides. Short-lived photometric anomalies, transit timing variations and transit depth variations were all observed, all of which can potentially be explained by the effects of starspots. In particular we have interpreted the photometric anomalies as occultations of starspots by the planet. We have described a simple method for assessing the orientation of a star relative to the orbit of its transiting planet through the analysis of spot occultations. This method has certain advantages and disadvantages compared to observations of the RM effect, the main method for such determinations.

On the positive side, the spot method works well for slowly-rotating stars, for which the RM amplitude is smallest. The spot method also has no particular problem with low impact parameters, unlike the RM effect. These two factors help to explain why the spot method gives tighter constraints on λ than did the RM observations of [214], for the case of WASP-4. The spot method requires that the star be moderately active; this too is complementary to RM observations, which rely on precise Doppler spectroscopy and are hindered by stellar activity. In addition, the spot method is photometric, rather than spectroscopic, and as such it can be pursued with a smaller telescope.

On the negative side, many transits must be observed to have a reasonable chance of detecting multiple anomalies, and to be sure that multiple anomalies are caused by a single spot, rather than distinct spots. In the case of WASP-4, a few more transit observations in the summers of either 2008 or 2009 could have allowed for a more secure validation of the single-spot hypothesis, and removed the four-way degeneracy of the resulting constraints on the stellar orientation. Furthermore, spots are not well-behaved deterministic entities: they have irregular shapes that form and dissolve, governed by poorly understood physical principles.

Regarding that subject, it is interesting to note that all four of the solutions

shown in Figure 2-4 involve slightly but significantly different rotation periods for the spot seen in 2008 as compared to the one seen in 2009. This could be a sign of differential rotation. Assuming WASP-4 has $\lambda = 0°$ and has the same differential rotation profile as the Sun, spots on the top and bottom of the transit chord would have periods differ by 10%, as compared to the 10-15% differences seen in our model results. Thus, differential rotation is a realistic possibility, especially since lower-mass stars such as WASP-4 are expected to have stronger differential rotation than the Sun. Another contributing factor may be peculiar motions of spots, i.e., motions of the spot relative to the surrounding photospheres, which are observed on the Sun at the few percent level respect to the absolute velocity of the spots [173].

For WASP-4, the small value of λ is further evidence that this is a low-obliquity system. Such findings have been interpreted as constraints on the process of planet migration: the mechanism that brought this gas giant planet from its birthplace (presumably a few AU) to its close-in orbit. Low obliquities are suggestive of disk migration, in which the orbit shrinks due to tidal interactions with the protoplanetary gas disk; while large obliquities would favor theories in which close-in orbits results from gravitational interactions with other bodies followed by tidal dissipation. The complicating factor of tidal reorientation was thought to be negligible, but this possibility was recently raised by [226] as a possible explanation for the tendency for high-obliquity stars to be "hot" and low-obliquity stars to be "cool", with a boundary at around 6250 K. Here we will not remark further on the theory underlying this hypothesis, but simply note that WASP-4 conforms to the empirical pattern, as a cool and low-obliquity system.

Looking forward, an opportunity exists to implement this method for other systems using the data from the *CoRoT* and *Kepler* space missions. The CoRoT-2 system in particular has a highly spotted star (see, e.g., [192], [191]) for which our method might be applicable, although the spots are so numerous and influential on the light curve that more complex models may be necessary. *Kepler* employs a 1m space telescope to monitor 150,000 stars with photon-limited precision down to level of $\approx$10 parts per million ([21], [22]). The data released in February 2011 displays a limiting

precision of about 10 ppm in 6 hr combined integrations at *Kepler* magnitude 10 (approximately $r = 10$), and a limiting precision of about 100 ppm for a more typical target star magnitude of 15. Besides high precision, the great advantage of the space missions is nearly-continuous data collection. For a system resembling WASP-4, *Kepler* would observe hundreds of consecutive transits, resulting in much greater power to track individual spots. Furthermore, the brightness variations observed outside of transits will allow for an independent estimate of the stellar rotation period, as well as additional constraints on spot longitudes. A potentially serious problem with the application to *Kepler* is that most stars are observed with a cadence of 30 min, which may be too long to pin down the times of starspot anomalies with the required precision. A subset of targets are observed at the much more favorable cadence of 1 min. Already there is one transit-hosting star in the *Kepler* field, HAT-P-11, that is being observed with 1 min cadence and will assuredly yield interesting results, as λ was found to be approximately 100° by [229] and [85], and the star has long-lived, sizable spots [8].

We gratefully acknowledge support from the NASA Origins program through awards NNX09AD36G and NNX09AB33G, and the MIT Class of 1942. RS has received financial support through the "la Caixa" Fellowship Grant for Post-Graduate Studies, Caixa d'Estalvis i Pensions de Barcelona "la Caixa", Barcelona, Spain. J.A.C acknowledges support for this work by NASA through Hubble Fellowship grant #HF – 51267.01 – A awarded by the Space Telescope Science Institute, which is operated by the Association of Universities for Research in Astronomy, Inc., for NASA under contract NAS 5-26555.

Chapter 3

Active latitudes and spin-orbit misalignment

Published as: "Starspots, spin-orbit misalignment, and active latitudes in the HAT-P-11 exoplanetary system" Sanchis-Ojeda, R., Winn, J.N. 2011, ApJ, 73, 127.

We present the analysis of 4 months of *Kepler* photometry of the K4V star HAT-P-11, including 26 transits of its "super-Neptune" planet. The transit data exhibit numerous anomalies that we interpret as passages of the planet over dark starspots. These spot-crossing anomalies preferentially occur at two specific phases of the transit. These phases can be understood as the intersection points between the transit chord and the active latitudes of the host star, where starspots are most abundant. Based on the measured characteristics of spot-crossing anomalies, and previous observations of the Rossiter-McLaughlin effect, we find two solutions for the stellar obliquity ψ and active latitude l: either $\psi = 106^{+15}_{-11}$ and $l = 19.7^{+1.5}_{-2.2}$, or $\psi = 97^{+8}_{-4}$ and $l = 67^{+2}_{-4}$ (all in degrees). If the active latitude changes with time in analogy with the "butterfly diagram" of the Sun's activity cycle, future observations should reveal changes in the preferred phases of spot-crossing anomalies.

3.1 Introduction

We have been developing a new method to measure the obliquity of a star with respect to the orbital plane of a transiting planet. Obliquities are important because they are fundamental geometric parameters, and because they bear clues about the formation, migration, and tidal evolution of close-in planets (see, e.g., [162], [146], [231], [226], [61], [214], [137]). The traditional method involves observations of the Rossiter-McLaughlin (RM) effect, a spectroscopic anomaly that occurs during transits due to selective blockage of the stellar rotation field (see, e.g., [162], [146], [71]). The new method is purely photometric, and is based on observations of photometric anomalies in transit light curves resulting from the passage of the planet in front of starspots.

When the planet blocks the light coming from a relatively dark portion of the stellar photosphere, the fractional loss of light is temporarily reduced, and a positive "bump" is observed in the light curve (see, e.g., [165]). In Chapter 2 [179] we showed how the recurrence (or not) of these starspot-crossing anomalies can be used to measure or place bounds upon the stellar obliquity. In simplest terms, the recurrence of an anomaly in two closely-spaced transits is evidence for a low obliquity, because otherwise the spot would rotate away from the transit chord. We and our colleagues applied this technique to the particular system WASP-4, showing that the new method gives stronger constraints on the stellar obliquity than the previous observations of the RM effect [214].

Independently, the recurrences of spot-crossing anomalies (as well as the phase of the out-of-transit modulation of the total light) have been used to confirm a low obliquity for CoRoT-2b [144]. More recently, a similar pattern of recurrences was found for Kepler-17b [52], and concluded that the host star has a low obliquity. The pattern in that case was made even more dramatic by the near-integral ratio between the rotational and orbital periods.

Another interesting target for this method would HAT-P-11, a K4V star with a "super-Neptune" planet of mass 26 $M_{\oplus}$ and radius 4.7 $R_{\oplus}$ in a 4.9-day orbit, was

pointed out by [179]. The star was already suspected of having starspots [8], it had been shown to have a high obliquity based on RM observations ([229], [85]), and most importantly, it lies within the field of the view of the *Kepler* photometric satellite [21]. Several months of nearly continuous, highly precise *Kepler* photometry are already available, and several years of data will eventually become available.

In this paper we analyze public data from *Kepler*, which have indeed revealed numerous spot-crossing anomalies, and led to constraints on the stellar obliquity, although not in the manner we anticipated. Section 3.2 presents the data, and Section 3.3 gives our estimates for the basic system parameters as well as the times of spot-crossing anomalies. The anomalies occurred preferentially at two particular phases of the transit. Section 3.4 presents a simple geometric model, in which special phases are the intersection points between the transit chord and the active (starspot-rich) latitudes of the star. Section 3.5 discusses the results.

While preparing this paper we learned that two other analyses of the public *Kepler* data have been undertaken, by [197] and by [48]. We refer the reader to those works for a different perspectives on the data, focusing on refinement of the transit parameters rather than the spin orientation of the star.

3.2 Analysis of out-of-transit data

We used the Multimission Archive at STScI to obtain the *Kepler* data for HAT-P-11 spanning the 140-day interval from 2009 May 02 to September 16, with a time sampling of one minute. In *Kepler* parlance, we used AP_RAW_FLUX short-cadence data from quarters 0, 1, and 2.

The time series is shown in Figure 3-1, after expunging a few glaring outliers and normalizing each quarter of data to have a mean of unity. A total of 26 transits were observed. Two transits were missed due to interruptions in satellite observing. One transit (epoch 17 as identified in Fig. 3-1) exhibited irregular flux jumps that were also observed in light curves of nearby stars, thereby implicating an instrumental problem. Data from this transit were excluded from our analysis.

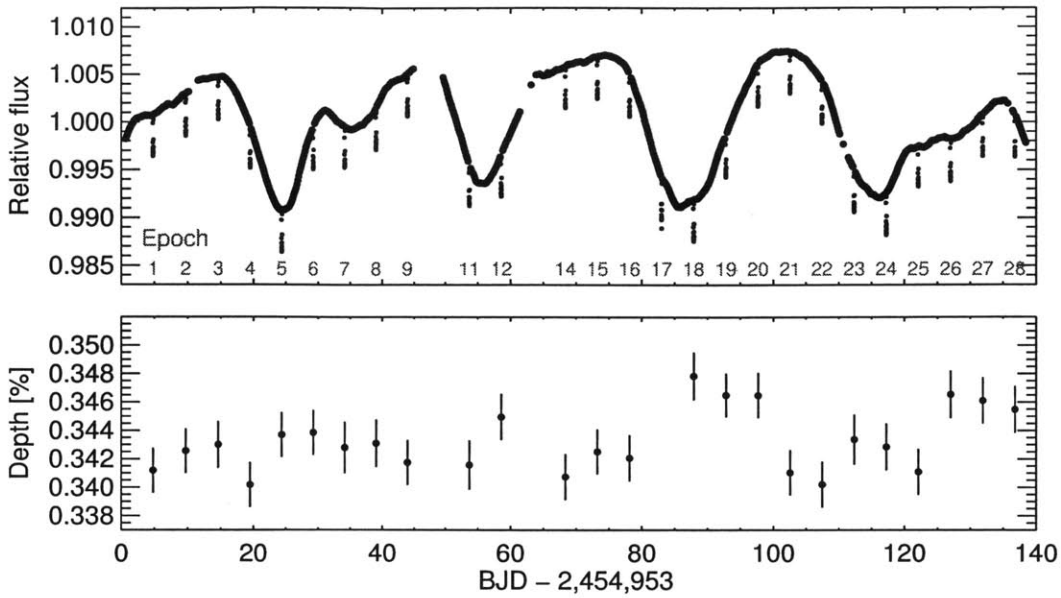

Figure 3-1: *Kepler* photometry of HAT-P-11.

Top.—The time series considered in this paper. The transits are evident as 0.4% dips with a period of 4.9 days, and are labeled with epoch numbers to facilitate cross-referencing with Figures 3 and 4 and the accompanying text. Outside of transits there are 4 prominent minima, probably representing a relatively dark starspot pattern being carried around by stellar rotation. *Bottom.*—The measured depth of each transit, using the procedure described in Section 3. The transit depth is defined as the square of the fitted planet-to-star radius ratio.

The relative flux varied by about 1.5% (peak to peak), with four prominent minima spaced apart by about 30 days. The spacing of the minima probably represents the stellar rotation period. The light curve is not strictly periodic, nor is it expected to be strictly periodic. Among the possible sources of aperiodicity are differential rotation, which causes spots at different latitudes to have differing rotating periods, as well as slow changes in the sizes, shapes, and locations of starspots. The top panel of Figure 3-2 shows a Lomb-Scargle periodogram of the out-of-transit data. We estimate $P_{\rm rot} = 30.5^{+4.1}_{-3.2}$ days, based on the peak and full-width at half-maximum of the periodogram. The bottom panel of Figure 3-2 shows the out-of-transit data folded with a period of 30.5 days. This is consistent with the earlier estimate of 29.2 days by [8] from ground-based photometry.

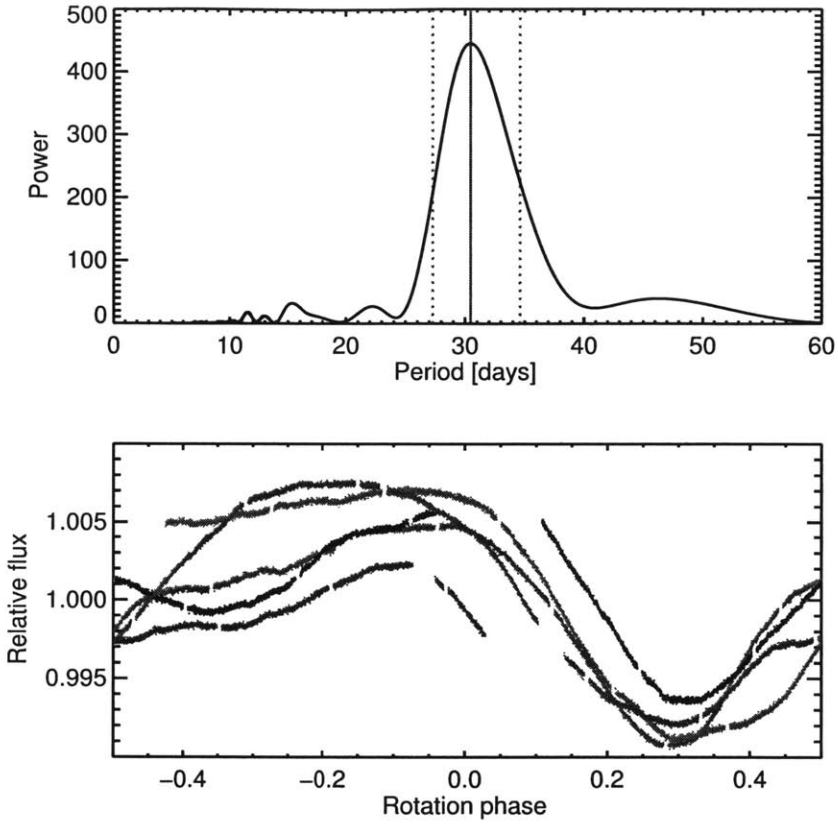

Figure 3-2: Rotation period of HAT-P-11.

Top.—Lomb-Scargle periodogram of the out-of-transit data. The peak (solid vertical line) is at 30.5 days and the full-width at half-maximum (dotted vertical lines) span the range from 27.3 to 34.6 days. *Bottom.*—Relative flux as a function of rotational phase, after folding with a period of 30.5 days. The minima nearly coincide at a phase of 0.3.

3.3 Analysis of transit data

To analyze the transits, we selected all the data within 4.8 hr (twice the transit duration) of any predicted transit midpoint. The data surrounding each transit were fitted with a standard transit model [125], using a quadratic limb-darkening law and allowing for a linear trend in the out-of-transit flux. Nearly every transit showed an anomaly that was not well-fitted by the transit model, which we interpret as the consequence of irregularities on the stellar photosphere. These anomalies were identified "by hand" and assigned zero weight in a subsequent fit to the data. Figure 3-

Table 3.1. System parameters of HAT-P-11

Parameter	Value	Uncertainty
Transit ephemeris:		
Reference epoch [BJD]	2454957.812464	0.000022
Orbital period [days]	4.8878049	0.0000013
Transit parameters:		
Planet-to-star radius ratio, $R_p/R_\star$	0.05862	0.00026
Transit duration [days]	0.09795	0.00006
Transit ingress or egress duration [days]	0.00550	0.00007
Linear limb-darkening coefficient, u_1	0.599	0.015
Quadratic limb-darkening coefficient, u_2	0.073	0.016
Transit impact parameter, b	0.132	0.045
Scaled semimajor axis, $a/R_\star$	15.6	1.5

Note. — Based on a Markov Chain Monte Carlo analysis of the 26 *Kepler* light curves, with uniform priors on $R_p/R_\star$, b, and $a/R_\star$, and Gaussian priors on the eccentricity parameters $e\cos\omega = 0.201 \pm 0.049$ and $e\sin\omega = 0.051 \pm 0.092$. The quoted values and uncertainties are based on the 15.65%, 50% and 84.35% levels of the cumulative distributions of the marginalized posteriors.

3 shows the resulting light curves, along with the best-fitting model and the data points that were excluded from the fit.

In this fit, each transit was allowed to have a unique value of the transit depth. The intention was to allow for the possibility of apparent depth variations due to changes in the flux of the untransited portion of the star. The results for the transit depth were plotted in Figure 3-1. They are essentially consistent with a constant depth, which in retrospect is not surprising since the stellar flux changes by $\pm 0.8\%$ and the individual transit depths are measured with a precision of only $\pm 1\%$. Table 1 gives the results for the system parameters, based on a Monte Carlo Markov Chain algorithm. The quoted value of the planet-to-star radius ratio is based on the mean, and the standard error in the mean, of all 26 measured transit depths.

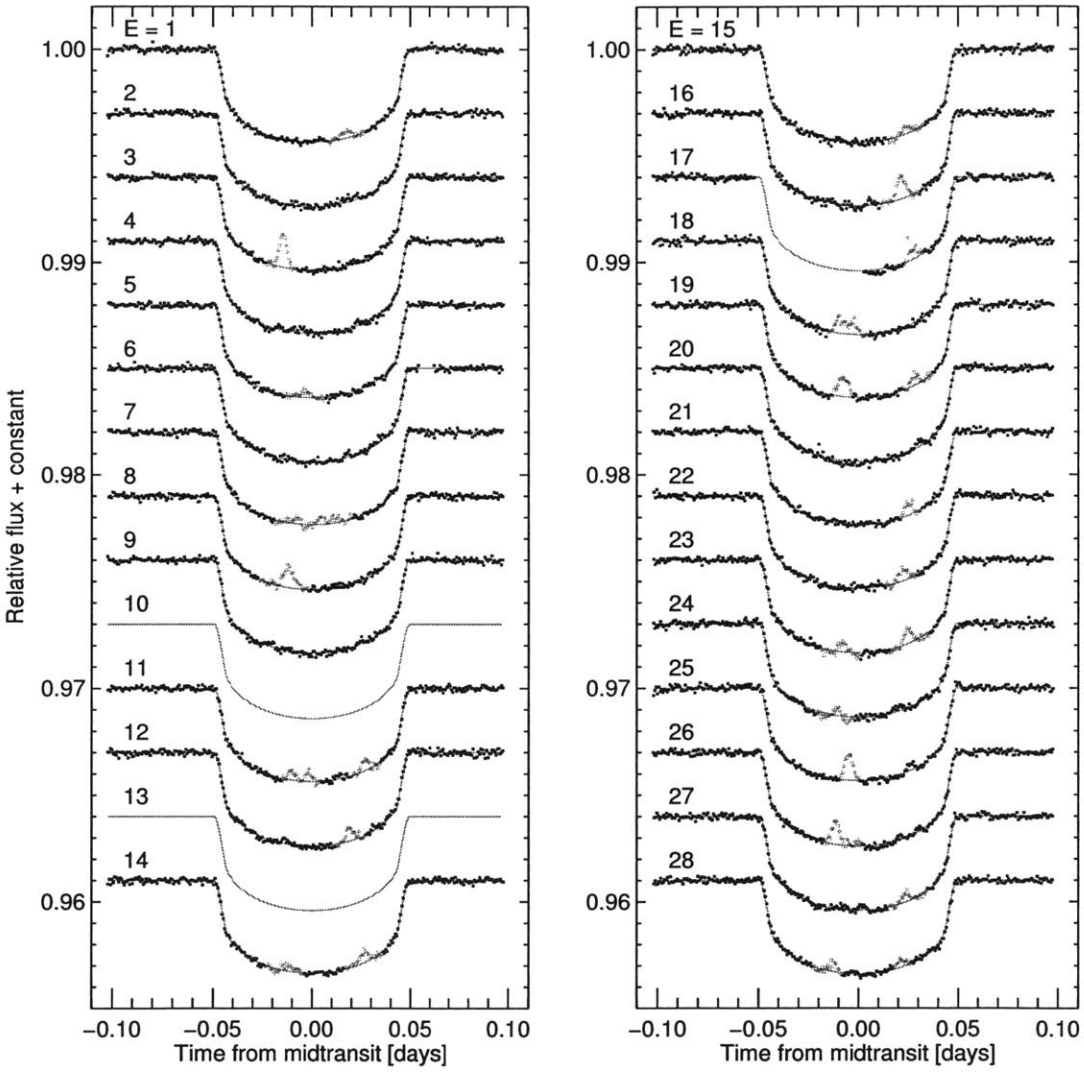

Figure 3-3: *Kepler* observations of transits of HAT-P-11.

Based on data from quarters 0, 1, and 2. The best-fitting model curves are shown as thin gray lines. Red squares are points that are suspected of being strongly affected by spot-crossing events, and were assigned zero weight in the fitting procedure.

3.4 Analysis of spot-crossing anomalies

3.4.1 Simple test for spin-orbit alignment

Because so many spot-crossing anomalies were detected, an immediate test is available for spin-orbit alignment. The logic is as follows. If the stellar obliquity were zero ($\psi = 0$), then the transit chord would correspond to a certain fixed range of latitudes in the reference frame of the star. In that case, after a given spot-crossing anomaly, that same spot would advance along the transit chord due to stellar rotation and future spot-crossing events can be predicted and sought out in the data. For HAT-P-11, a spot-crossing anomaly observed in the first half of the transit would recur at a later phase of the next transit. This is because the orbital period (4.9 days) is shorter than half a rotation, the time it takes for the spot to cross the visible stellar hemisphere. The underlying assumption is that the spot does not move significantly or fade into undetectability within 4.9 days, but that assumption seems justified (for large spots at least) given the observed coherence of the light curve over 4 rotations (see Figure 3-2).

No such recurrence is seen in the *Kepler* data, leading to the conclusion the star's spin axis is misaligned with the planet's orbital axis. Figure 3-4 shows two of the clearest examples of a pair of transits where one spot-crossing anomaly was seen, and the other corresponding anomaly that would be predicted for perfect spin-orbit alignment is missing. Many other examples are evident in Figure 3-3.

3.4.2 Evidence for spin-orbit misalignment

It has been suggested [229] that even for $\psi \neq 0$, the recurrence of spot-crossing anomalies could be observed and used to constrain the stellar obliquity and the stellar rotation period. However, such recurrences require the spots to last for one or more full rotation periods, as opposed to one-sixth of a rotation period, and they also require the rotation period to be a nearly exact multiple of the orbital period. This latter condition may or may not be the case for HAT-P-11, and is *a priori* unlikely.

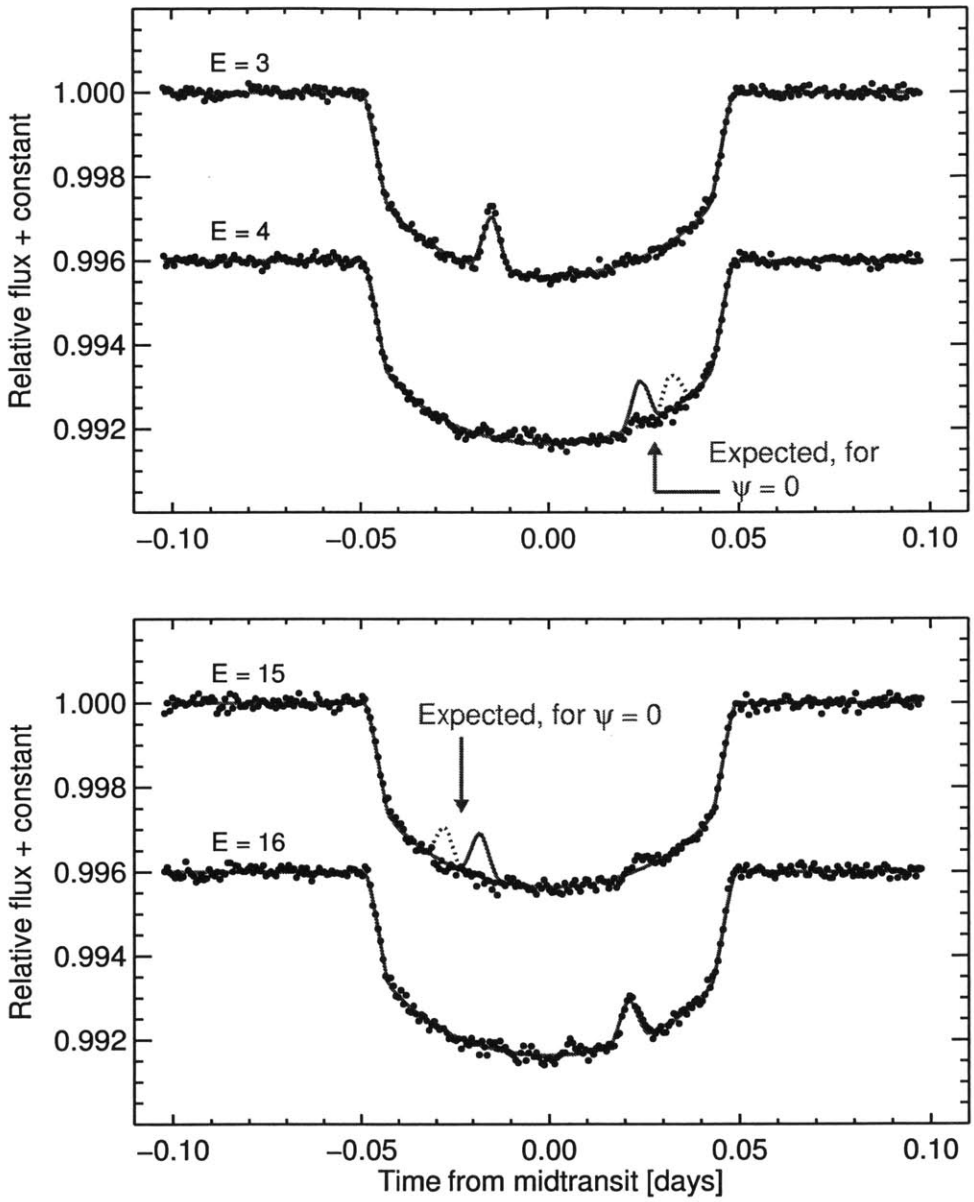

Figure 3-4: Evidence for spin-orbit misalignment.

Shown are two examples of pairs of consecutive transits where one spot-crossing anomaly was observed, and if ψ were zero, there would have been a corresponding spot-crossing anomaly detected in the other transit. No such correspondences were observed in the time series considered in this paper. The black dots are data points, and the red lines are best-fitting models including a circular spot with a lower intensity than the surrounding photosphere. For epochs 4 and 15, two curves for the expected spot signal are plotted (solid and dotted), corresponding to extremes in the range of rotation periods from 27.3 to 34.6 days.

Given the uncertainty in the rotation period, the ratio of rotation to orbital periods is between 5.6 and 7.1. Indeed we could establish no firm correspondences between multiple pairs of spot events.

However, there is a regularity in the pattern of anomalies that we did not anticipate, although perhaps we should have. Figure 3-5 shows the residuals between the data and the best-fitting transit model, as a function of time relative to the nearest midtransit time. The spot-crossing anomalies are manifested as large positive residuals. They do not occur at random phases of the transit, but rather at two specific phases: approximately -0.010 and 0.025 days relative to midtransit. One might initially interpret this as evidence for two long-lived spots on the star, with each bump representing the intersection of one spot's stellar latitude with the transit chord. However, in that situation one would observe at most two anomalies per rotation period, and more likely fewer, unless the orbital and rotational periods were nearly commensurate. In reality we observed at least 25 anomalies over 4 rotation periods. There are evidently many different spots on HAT-P-11 and they are clustered at two particular stellar latitudes.

If spots appeared with equal probability at any latitude, one would expect to see a nearly uniform distribution of outliers in Figure 3-5, except near the ingress and egress where limb darkening and geometrical foreshortening would make some spots undetectable. Likewise, if $\psi = 0$, then a nearly uniform distribution of residuals would be observed even if the spots were clustered in latitude (again, unless there were some near-commensurability between rotational and orbital periods). Therefore, since the data exhibit two particular peaks, we conclude that the system is misaligned *and* that the starspots occur preferentially at certain "active latitudes."

The phenomenon of active latitudes is a familiar one from solar astronomy, which is why we wrote above that we should have anticipated this result. [33] and [200] found that over the course of the Sun's 11-year activity cycle, the mean latitude of sunspots is sharply defined for any few-month interval, and undergoes a gradual shift from high latitudes to the equator. This spatial regularity of the cycle sometimes called the Spörer law. The famous "butterfly diagram" [131], in which sunspot latitude is

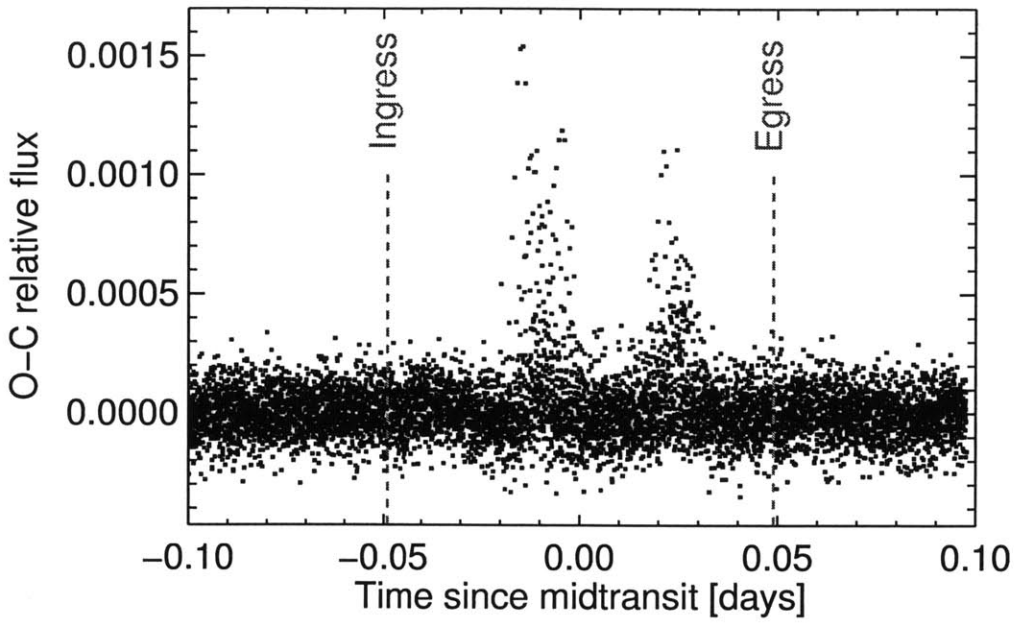

Figure 3-5: Appearence of two prefered spot-crossing phases.

Differences between the data, and the best-fitting transit model, as a function of transit phase. Data from all 26 transits are plotted. Spot-crossing anomalies (the large positive residuals) appear preferentially at two particular phases. These phases are not symmetrically placed with respect to the transit midpoint.

charted against time, can be regarded as a graphical depiction of this law. The regions where sunspots are abundant are well described as relatively narrow bands centered on two particular latitudes placed symmetrically with respect to the solar equator. Early in a cycle, spots appear at latitudes up to 40 degrees. As the cycle progresses, new sunspots appear at increasingly lower latitudes, with the last sunspots of a cycle lying close to the equator [196].

3.4.3 Geometric model

For a quantitative analysis of the spot-crossing anomalies, we fitted each anomaly with a simple triangular model with three parameters, the height (A = the amplitude of the anomaly in relative flux units), the width (τ = total duration) and the midpoint

Table 3.2. Characterization of spot-crossing anomalies

Epoch	Amplitude [ppm]	Duration [min]	BJD− 2,454,953	$\Delta\chi^2$	Phase $[x/R_\star]$
1	386	13.6	4.830	86.7	0.37
3	1711	12.2	14.573	1646.7	−0.31
5	324	16.8	24.360	73.7	−0.08
8	984	16.9	39.015	716.0	−0.25
11	440	10.4	53.680	121.9	−0.22
11	530	7.5	53.689	119.4	−0.04
11	593	10.1	53.717	191.6	0.57
12	660	12.2	58.597	162.0	0.41
14	282	17.3	68.343	61.9	−0.24
14	573	12.7	68.380	186.3	0.57
15	361	13.4	73.266	59.9	0.52
16	1155	14.3	78.151	551.4	0.46
17	618	20.7	83.045	133.4	0.58
18	689	26.9	87.898	310.6	−0.15
19	969	15.1	92.785	578.5	−0.17
19	525	10.8	92.821	146.8	0.60
21	627	12.4	102.594	207.5	0.54
22	519	13.4	107.479	179.7	0.48
23	479	11.4	112.336	97.8	−0.17
23	769	11.4	112.369	248.1	0.53
25	1302	13.9	122.115	656.8	−0.10
26	1127	11.4	126.996	581.4	−0.25
27	444	12.5	131.919	84.8	0.50
28	446	10.7	136.771	101.1	−0.27
28	326	18.8	136.804	84.3	0.45

(t_0 = the time of the event):

$$F(t) = \begin{cases} A - \frac{2A}{\tau}|t - t_0| & |t - t_0| < \tau/2 \\ 0 & |t - t_0| \geq \tau/2 \end{cases} \tag{3.1}$$

Table 3.2 gives the best-fitting values of the model parameters for each anomaly. As a measure of statistical significance, the $\Delta\chi^2$ between a no-spot model and the spot model is also given for each event. All the chosen anomalies have $\Delta\chi^2$ exceeding 50.

Next we used a simple geometric model to constrain the spin orientation of the star as well as the locations and widths of the active zones. The premise of the model is that each of the two features seen in Figure 3-5 represents an intersection between two strips on the stellar disk: the transit chord, which has a width equal to

the planet-to-star radius ratio; and an active zone, a range of latitudes surrounding an active latitude. The intersection points of the two strips determine the centroids of the two features seen in Figure 3-5. The width of the intersection region (which depends on the width of each strip, as well as the angle of intersection) determines the widths of the two features seen in Figure 3-5.

The first step in the model is to characterize the two features by their central phases and widths. We use a coordinate system centered on the stellar disk, with the x-axis aligned with the planet's motion during transits, the y-axis in the perpendicular direction in the sky plane, and the z-axis pointing along the line of sight (see Figure 3-6). All distances are measured in units of the stellar radius. The goal of this step is to determine the central values of x for the two spot-anomaly features, which we denote $\bar{x}_1$ and $\bar{x}_2$, and the Gaussian widths of the features, which we denote $\bar{\sigma}_1$ and $\bar{\sigma}_2$.

To estimate $\bar{x}$, and $\bar{\sigma}$ for each of the two features, we maximized the likelihood

$$\mathcal{L} \propto \prod_{i=1}^{N} \int dx \, \frac{1}{\sqrt{2\pi\sigma_i^2}} \, e^{-\frac{(x-x_i)^2}{2\sigma_i^2}} \, \frac{1}{\sqrt{2\pi\bar{\sigma}^2}} \, e^{-\frac{(x_i-\bar{x})^2}{2\bar{\sigma}^2}}, \tag{3.2}$$

where the index i runs over all spots contributing to the feature, the first exponential within the integral represents the probability distribution for each measurement of a spot location, and the second exponential is the assumed Gaussian model of the spatial distribution of spots surrounding the active latitude. Loosely speaking, this is similar to fitting a Gaussian function to each feature seen in Figure 3-5, after transforming the time coordinate into the x coordinate. The results, based on the same MCMC algorithm used to estimate the system parameters, are $\bar{x}_1 = -0.19 \pm 0.03$, $\bar{x}_2 = 0.51 \pm 0.02$, $\bar{\sigma}_1 = 0.09 \pm 0.02$ and $\bar{\sigma}_2 = 0.07 \pm 0.02$. The quoted values and uncertainties are based on the 15.65%, 50% and 84.35% levels of the cumulative distributions of the marginalized posteriors, distributions that all follow a Gaussian profile.

The next step is to use these results to constrain the spin orientation of the star and the locations of the active zones. The spin orientation of the star is parameterized

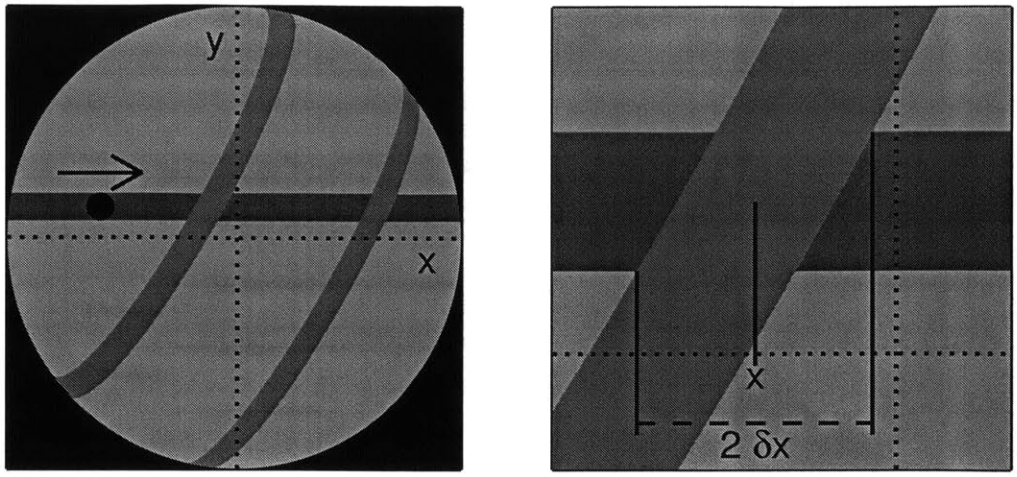

Figure 3-6: Illustration of the coordinate system.

The transit chord is parallel to the x axis. The region of intersection between the transit chord and an active zone is described by x, its center, and δx, its width in the x-direction. All distances are expressed in units of the stellar radius.

by the inclination angle i_s of the north pole with respect to the line of sight, and the sky-plane angle λ between the north pole and the orbit normal (i.e., the same angle probed by observations of the RM effect). In analogy with the Sun, and based on the overall symmetry of the star, we assume the active zones to be symmetrically placed with respect to the stellar equator, centered on latitudes $\pm l$ and with half-widths δl. Therefore our next task is to use spherical trigonometry to relate $\bar{x}_1$, $\bar{x}_2$, $\bar{\sigma}_1$ and $\bar{\sigma}_2$ to i_s, λ, l and δl.

The geometry is illustrated in Figure 3-6. A point $\vec{r} \equiv (x, y, z)$ on the middle of the transit chord has $y = b$ (where b is the impact parameter), $z > 0$ and $x^2 + y^2 + z^2 = 1$. The stellar north pole is at (following the convention of [146])

$$\vec{r}_{\rm NP} = -\sin i_s \sin\lambda\ \hat{x} + \sin i_s \cos\lambda\ \hat{y} + \cos i_s\ \hat{z}. \tag{3.3}$$

The latitude l of a given point on the surface of the star can be calculated given its

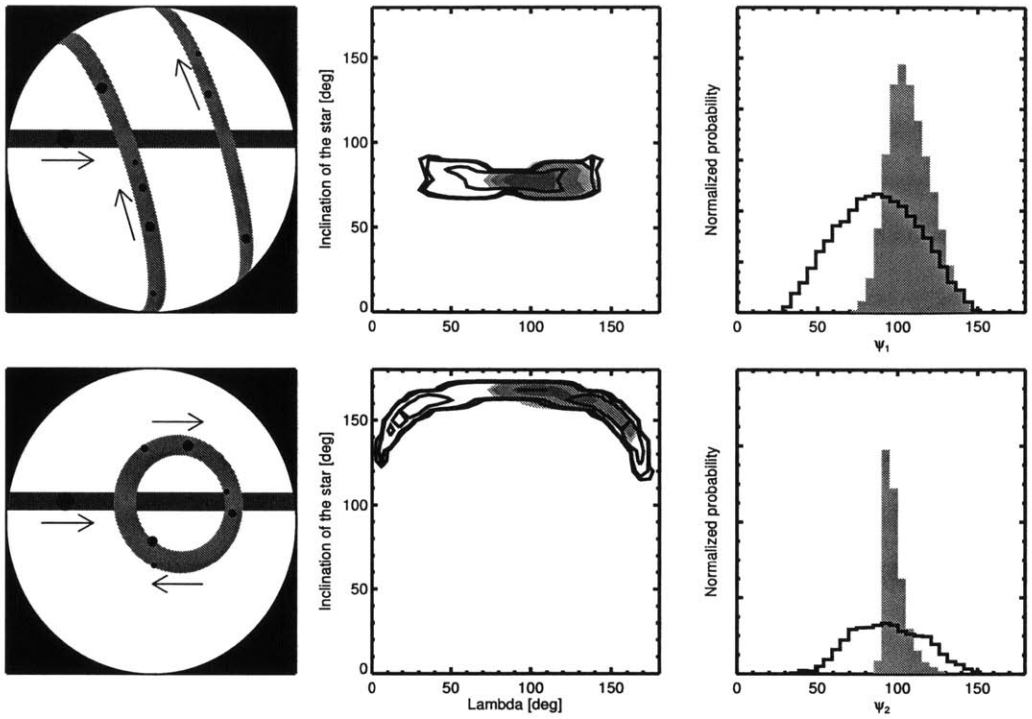

Figure 3-7: Two solutions for the stellar geometry.

The upper panels represent the double-banded, edge-on solution and the lower panels represent the single-band, pole-on solution. The left column of panels are sketches of the system, using the most probable values of the parameters. The central column shows two-dimensional posterior distributions for the stellar orientation parameters λ and i_s, with solid lines representing the results with a uniform prior on λ, and gray scales for the results with a two-sided Gaussian prior $\lambda = 103^{+26}_{-10}$ deg based on the RM results [229]. The confidence levels are 68.3%, 95%, and 99.73%. The right column shows the posterior distribution for the true spin-orbit angle ψ, again with the solid line representing the result from the spot analysis alone, and the shaded distribution representing the joint results of the spot analysis and the RM measurement.

xyz coordinates and the position of the north pole:

$$l = \frac{\pi}{2} - \cos^{-1}\left(1 - d^2/2\right), \qquad d^2 \equiv (\vec{r} - \vec{r}_{\rm NP})^2. \tag{3.4}$$

These relations allow us (after some algebra) to compute the x coordinates of any intersection points of the transit chord and active latitude:

$$x_{1,2}(\lambda, i_s, b, l) = \frac{(b \sin i_s \cos\lambda - \sin l)\sin i_s \sin\lambda \pm \sqrt{f(\lambda, i_s, b, l)}}{1 - \sin^2 i_s \cos^2\lambda}. \tag{3.5}$$

Here, the factor $f(\lambda, i_s, b, l)$, defined as

$$\cos^2 i_s[1 - \sin^2 i_s \cos^2 \lambda - b^2 + 2b \sin l \sin i_s \cos \lambda - \sin^2 l], \tag{3.6}$$

determines whether there are zero, one or two different intersection points for a given set of values of (λ, i_s, b, l). Since we are assuming there are two active latitudes $\pm l$, we can have up to four intersection points. Once all possible solutions have been found, it is necessary to check that they occur on the visible hemisphere of the star ($z > 0$).

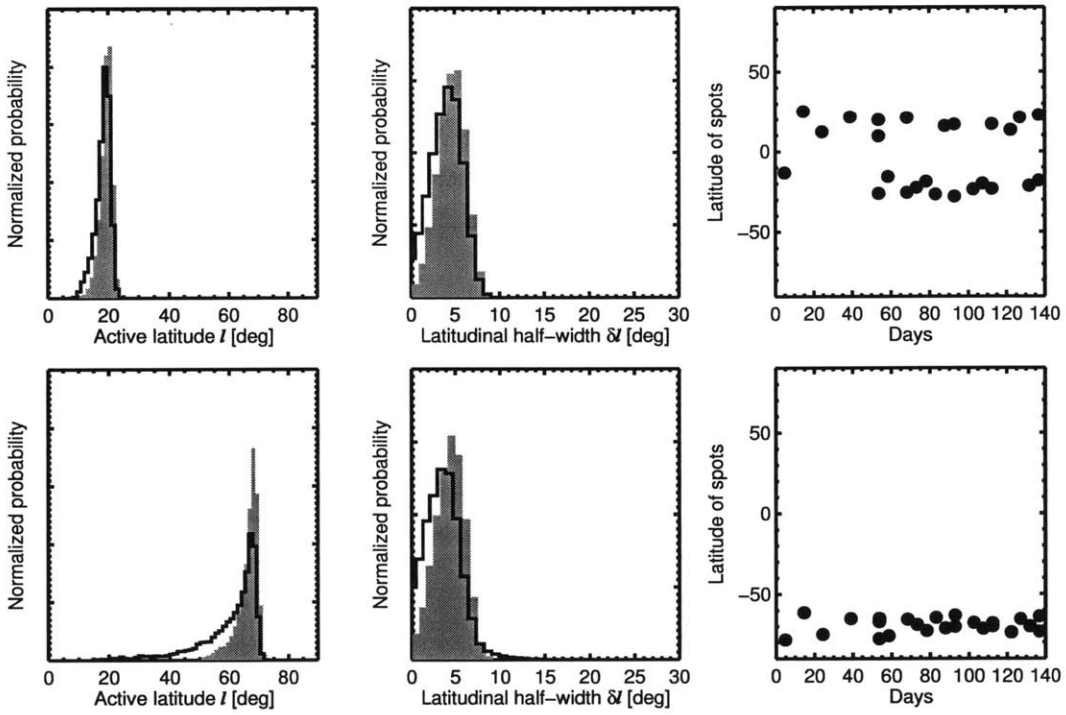

Figure 3-8: Results for the parameters describing the active zones.

Upper panels represent the two-band, edge-on solution and lower panels represent the single-band, pole-on solution. On the left are posteriors for l, the central latitude of the active region. (In the model, the active latitudes are symmetrically placed at $\pm l$.) As in Figure 3-7, the solid line is for the case of a uniform prior in λ, and the shaded histogram is for the case when the RM result for λ was used as a prior. The central column shows the corresponding results for the parameter δl describing the latitudinal half-width of the active regions. The right column shows the butterfly diagram for HAT-P-11, based on the measured phases of the spot anomalies and the best-fitting values of i_s and λ.

The impact parameter b has already been determined from transit photometry.

We can adjust the other parameters λ, i_s and l to achieve a match between the x-values of the intersection points and the previously determined values of $\bar{x}_1$ and $\bar{x}_2$. There are four solutions, two of which are illustrated in the left panels of Figure 3-7. One solution has the active zones at relatively low latitudes, with both the northern and southern active latitudes intersecting the transit chord. The second solution has the star oriented nearly pole-on, so that one active latitude presents an ellipse on the sky that intersects the transit chord twice. The third and fourth solutions are related to the first two by the symmetry $\{\lambda, i_s, l\} \rightarrow \{\pi + \lambda, \pi - i_s, l\}$. These "mirror solutions" give similar results for the three-dimensional obliquity ψ as the other two solutions. However since they give negative values of λ that are ruled out by observations of the RM effect ([229], [85]) for brevity we do not discuss them in the rest of this paper.

Next we make use of the measured widths of the spot-anomaly distributions. Using Eqn. (3.5), we may calculate the four vertices of the intersection region between the transit chord and the band of active latitudes. We then take the difference between the maximum and the minimum values of x and divide by two, a quantity we will call δx. By characterizing the width in this manner, we are effectively assuming that spots are equally likely to form anywhere in the range $l \pm \delta l$. This is computationally very convenient, but it is in mild contradiction with the Gaussian distribution we adopted when estimating $\bar{\sigma}_1$ and $\bar{\sigma}_2$. For this reason, we multiply δx by $\sqrt{2/\pi}$, to give the standard deviation of a Gaussian function that has the same area as a uniform distribution with width δx. This can then be compared with $\bar{\sigma}_1$ and $\bar{\sigma}_2$, using a goodness-of-fit function,

$$\begin{aligned}\chi^2(\lambda, i_s, l, \delta l, b) &= \left(\frac{\bar{x}_{1,\,\mathrm{calc}} - (-0.19)}{0.03}\right)^2 + \left(\frac{\bar{x}_{2,\,\mathrm{calc}} - (0.51)}{0.02}\right)^2 \\ &+ \left(\frac{\sqrt{2/\pi}\;\delta\bar{x}_{1,\,\mathrm{calc}} - 0.09}{0.02}\right)^2 \\ &+ \left(\frac{\sqrt{2/\pi}\;\delta\bar{x}_{2,\,\mathrm{calc}} - 0.07}{0.02}\right)^2, \end{aligned} \tag{3.7}$$

where "calc" indicates the value that is calculated geometrically based on the parameters λ, i_s, l, δl, and b. We thereby enforce agreement between the "observed" and "calculated" properties of the intersection region (their locations and widths), under the assumption that the uncertainties in the 'observed' quantities are Gaussian-distributed.

To explore the parameter space we used an MCMC technique, with the Gibbs sampler and the Metropolis-Hastings algorithm, and a likelihood proportional to $\exp(-\chi^2/2)$. Uniform priors were adopted on all parameters except the impact parameter, for which a Gaussian prior was adopted based on the light curve analysis presented earlier ($b = 0.132 \pm 0.045$), and the stellar inclination angle i_s, for which the prior was uniform in $\cos i_s$ (i.e., isotropic). In addition, we considered two cases: one in which the prior was uniform in λ, and another in which a two-sided Gaussian prior was adopted to enforce agreement with the RM result $\lambda = 103^{+26}_{-10}$ deg [229].

Figure 3-7 shows the results, both as contour plots in the space of the stellar orientation parameters i_s and λ, and as marginalized distributions for the true obliquity ψ that is computed from those two parameters:

$$\cos\psi = \cos i_s \cos i_o + \sin i_s \cos\lambda \sin i_o, \tag{3.8}$$

where i_o is the orbital inclination. As discussed earlier, there are two families of solutions. In one solution, the star's equator is viewed nearly edge-on, while in the second solution, the star is viewed nearly pole-on. Both solutions are compatible with the RM results. When the previous RM results are used as a prior, the results are sharpened. The spot-crossing analysis and the RM analysis are complementary in the sense that the RM analysis is sensitive only to λ, while the spot-crossing analysis is sensitive to a complicated combination of i_s and λ. Although the two families of solutions are quite different in the alignment of the star with respect to Earth, they are similar in that they both represent strongly misaligned systems with $\psi \approx 90°$.

Figure 3-8 shows the results for l and δl, the parameters describing the active zones on the star. The edge-on solution has a lower value of l than the pole-on solution, but

Table 3.3. Results of MCMC analysis

Parameter	Edge-on solution	Edge-on solution (+ RM prior)	Pole-on solution	Pole-on solution (+ RM prior)
Projected obliquity, λ [deg]	90 ± 28	106^{+15}_{-12}	83^{+77}_{-65}	121^{+24}_{-21}
Stellar inclination, i_s [deg]	80^{+5}_{-3}	80^{+4}_{-3}	160^{+9}_{-19}	168^{+2}_{-5}
Obliquity, ψ [deg]	91 ± 27	106^{+15}_{-11}	89^{+27}_{-27}	97^{+8}_{-4}
Latitude of active zone [deg]	$19.3^{+1.7}_{-3.0}$	$19.7^{+1.5}_{-2.2}$	63^{+6}_{-17}	67^{+2}_{-4}
Half-width of active zone [deg]	$4.5^{+1.7}_{-2.1}$	$4.8^{+1.5}_{-1.8}$	$4.0^{+2.3}_{-2.2}$	$4.5^{+1.6}_{-1.9}$

they both give similar results for the latitudinal half-width δl of the active regions. The fitted half-widths are around 5°, which is similar to the observed widths of the active bands on the Sun. The latitude $l \approx 20°$ of the edge-on solution is also a good match to the Sun, while the higher latitude of $l \approx 60°$ for the pole-on solution would be atypically high for the Sun.

For each solution we also plot the analog of the solar butterfly diagram: the latitude of each individual observed spot anomaly as a function of time. We do this in the right column of Figure 3-8, based on the best-fitting model in each of the two families. In the first case, spots cover two symmetric ranges of latitudes, whereas in the second case (the pole-on solution) we see only one band. Eventually, after several more years of *Kepler* data are collected, we might expect this type of diagram to show time variations in the latitudes of spots due to the stellar activity cycle on HAT-P-11. This would be a valuable opportunity to construct a butterfly diagram for a star other than the Sun (see also [18]).

3.5 Discussion

The main results of our study are (1) the finding that the starspots on HAT-P-11 are preferentially found at certain active latitudes; (2) the confirmation that the HAT-P-11 star is misaligned with the orbit of its close-in planet; (3) the placement of quantitative bounds on the three-dimensional stellar obliquity based on the observed pattern of spot anomalies and a simple geometrical model. Two families of geometric solutions were found, one in which the star is viewed nearly pole-on, and the other in

which the star is viewed closer to edge-on. Even though both solutions agree on the stellar obliquity, they differ in the locations of the active latitudes: one solution gives more Sun-like active latitudes of about 20° while the other solution favors a larger latitude of about 60°. Breaking this degeneracy would therefore tell us whether or not the activity cycle on HAT-P-11 resembles that of the Sun in this respect.

One might think that the measurement of $v \sin i_s$ would help to distinguish these two cases, but the two solutions predict values of $v \sin i_s = (2\pi R_\star / P_{\rm rot}) \sin i_s$ equal to 1.3 km s^{-1} and 0.5 km s^{-1}, which are both compatible with the observed value of 1.5 ± 1.5 km s^{-1} [8]. A basic difference between the pole-on and edge-on solutions is that the pole-on solution would produce smaller out-of-transit (OOT) flux variations for a spot of a given size and intensity. Indeed, an exactly pole-on solution would not produce any OOT variations. For nearly pole-on configurations, the OOT variations arise only from small variations in limb darkening and geometrical foreshortening along the nearly-circular trajectory of the spot on the stellar disk. In contrast, for the edge-on solution, the spot disappears from view for half of the rotation period, resulting in larger variations.

Our geometric model did not make use of the information borne by the out-of-transit (OOT) flux variations; could this be used to break the modeling degeneracy and sharpen the constraints? We have made some efforts in this direction, but they have been inconclusive, mainly because the spot sizes and intensties are not known *a priori*. Our simulations show that it is possible that the pole-on solution is correct, and that the 1.5% OOT variations are produced by large and/or dark spots. Another feature of the pole-on model is that each spot crosses the transit chord twice per rotation period, which might lead to a detectable correlation between the observed spot anomalies. We explored this possibility, but could not reach a firm conclusion because a given spot may traverse the transit chord quickly enough that the planet does not always cross it. Nevertheless, future observations with *Kepler* and a more detailed spot-by-spot model might one day be used to break the degeneracy.

Future observations may also reveal the changes in the active latitudes that are analogous to the equatorial drift of the active latitudes on the Sun. As is well known,

over the 11-year solar activity cycle the active latitudes migrate toward the equator, where they disappear and are then recreated at higher latitudes, the phenomenon that underlies the butterfly diagram. Should this also occur for HAT-P-11, we would observe a drift in the phases of the spot-crossing anomalies. Assuming the active latitudes migrate toward the equator, the phases would behave differently for the pole-on and edge-on solutions. In the case of the pole-on solution, the phases will separate apart and move toward the extremes of the transit, while for the edge-on solution, the phases will move closer to one another. Of course, we should not necessarily assume that the active latitudes migrate to lower latitudes, as is seen on the Sun, but the data themselves may be able to confirm this fact, making use of differential rotation. In fact, [135] studied latitude migration on young solar analogues through differential rotation and found that for some stars the active latitudes seem to move poleward rather than migrating toward the equator. A combination of the measurement of the drift of the phases and the change in the period will give us a way of breaking the degeneracy and studying the rate of migration of the active latitudes. (For a review of starspots and the various techniques by which they are observed, see [203])

Independently of the activity cycle of HAT-P-11, the confirmation that the star has a high obliquity is helpful for understanding the origin of the close-in planet HAT-P-11b. There has been a recent resurgence of the theory that close-in planets are emplaced by few-body gravitational interactions followed by tidal capture, rather than by gradual inspiral due to interactions with a protoplanetary disk (see, e.g., [58], [141], [130]). Part of the evidence is the large incidence of high obliquities among stars that host close-in giant planets (see, e.g., [214]). With our corroboration of the RM results by [229] and [85], HAT-P-11 can be firmly added to this roster.

We thank Lucianne Walkowicz, Elisabeth Adams, Drake Deming, Andrew Howard, John Johnson, Mercedes Lopez-Morales, Dan Fabrycky, Philip Nutzman, and Josh Carter for stimulating conversations. We are grateful for financial support from the NASA Origins program (grant no. NNX11AG85G). R.S. was also supported by a Fellowship Grant for Post-Graduate Studies from the "la Caixa" Foundation in Barcelona, Spain. The data presented in this paper were obtained from the Multimis-

sion Archive at the Space Telescope Science Institute (MAST). STScI is operated by the Association of Universities for Research in Astronomy, Inc., under NASA contract NAS5-26555. Support for MAST for non-HST data is provided by the NASA Office of Space Science via grant NAG5-7584 and by other grants and contracts.

Chapter 4

Extending obliquity measurements to multiplanet systems

Published as: "Alignment of the stellar spin with the orbits of a three-planet system" Sanchis-Ojeda, R., Fabrycky, D.C., Winn, J.N., Barclay, T., Clarke, B.D., Ford, E.B., Fortney, J.J., Geary, J.C., Holman, M.J., Howard, A.W., Jenkins, J.M., Koch, D., Lissauer, J.J., Marcy, G.W., Mullally, F., Ragozzine, D., Seader, S.E., Still, M. 2012, Nature, 487, 7408, pp. 449-453.

The Sun's equator and the planest' orbital planes are nearly aligned, which is presumably a consequence of their formation from a single spinning gaseous disk. For exoplanetary systems this well-aligned configuration is not guaranteed: dynamical interactions may tilt planetary orbits, or stars may be misaligned with the proto-planetary disk through chaotic accretion [17], magnetic interactions [107] or torques from neighboring stars. Indeed, isolated 'hot Jupiters' are are often misaligned and even retrograde ([214], [226]). Here we report an analysis of transits of planets over starspots ([179], [144], [52]) on the Sun-like star Kepler-30 [60], and show that the orbits of its three planets are aligned with the stellar equator. Furthermore, the orbits are aligned with one another to within a few degrees. This configuration is similar to the Solar System, and contrasts with isolated hot Jupiters. The orderly alignment seen in the Kepler-30 system suggests that high obliquities are confined to systems

that experienced disruptive dynamical interactions. Should this be corroborated by observations of other coplanar multi-planet systems, then primordial stellar misalignments would be ruled out, and dynamical interactions would be implicated as the origin of hot Jupiters.

4.1 Main Text

Kepler-30 is a star of nearly solar mass and radius, but it is probably younger than the Sun, judging from its faster rotation and more prominent starspots[60].The starspots are crucial to measuring the stellar obliquity (the angle between the rotational and orbital angular momentum vectors). Starspots produce two effects: quasi-periodic variation (QPV) in flux caused by rotation, and shorter-term 'anomalies' in flux caused by the transit of a planet in front of a spot. The obliquity can be measured if one observes a sequence of anomalies ([179], [144], [52]), or a few single anomalies and the accompanying QPV [144], as long as the effects of a single spot or compact group of spots can be isolated. This technique has been previously applied to solitary shortperiod planets, but not longer-period planets or systems of multiple planets. The other widely used technique for measuring stellar obliquities, the Rossiter-McLaughlin effect [231], relies on precise spectroscopy during transits and would be impractical for a star as faint as Kepler-30.

We analysed 2.5 years of nearly continuous photometric time-series data from the Kepler space telescope [21]. The data set includes 27 transits of Kepler-30b ('planet b'; orbital period, $\approx$ 29 days; radius, $\approx$ 4 R_E, where R_E is the Earth's radius), 12 transits of Kepler-30c ('planet c'; 60 days; 13 R_E), and 5 transits of Kepler-30d ('planet d'; 143 days; 10 R_E). After removing instrumental artifacts (see section 4.2), we detected QPV with an amplitude (peak-to-peak) of 1.5%. The stellar rotation period is 16.0 ± 0.4 days, based on a Lomb Scargle periodogram [184] (see section 4.3).

To enable the obliquity analysis, we searched for anomalies during transits that are large enough in amplitude and long enough in duration to be caused by the same starspots that produce the QPV. Many such anomalies were identified during

transits of the largest planet, c. A strong correlation exists between the timing of the anomaly relative to mid-transit, and the phase of the QPV: anomalies observed near mid-transit are found when the QPV is near a local minimum, whereas anomalies occurring before (or after) mid-transit are found before (or after, respectively) a local minimum. This is the signature of a low obliquity star [144].

We used both of the above-mentioned methods to establish quantitative bounds on the obliquity: (1) quantifying the relationship between the anomalies and QPV; and (2) modeling a particular pair of transits for which the anomalies can be attributed to transits over the same spot. To support both of these methods, we determined the basic transit parameters such as the planet-to-star radius ratio (R_{pl}/R_{star}) and impact parameter by fitting the transit data with a standard model for the loss of light during a planetary transit [125]. We excluded the anomalies from the fit, and accounted for transit depth variations due to unocculted spots (see section 4.4 , and Fig. 4-5). Results are given in Table 4.1.

The premise of the first method is that any spot that causes an anomaly must also contribute to the QPV. For a given spatial orientation of the star, geometry dictates a specific relationship between the timing of the anomaly and the phase of the QPV. However, all spots contribute to the QPV, not just the occulted spot. Therefore, to measure the obliquity,we must associate each anomaly with a particular component of the QPV. Out of concern that such associations are ambiguous, we exhaustively tried all plausible associations. We rank ordered the anomalies in order of the loss of light produced by the spot, and focused attention on the five strongest anomalies. We measured the time of each anomaly relative to mid-transit, as well as the time of the transit relative to each local minimum in the QPV within a rotation period (see section 4.5). For one of the anomalies there is only one plausible choice for the associated local minimum, whereas in each of the other four cases there are two candidate local minima, giving a set of 16 possible associations. We find that only one of these 16 is compatible with a single orientation of the host star, and in that case the stellar equator is aligned on the sky with the planet's orbit (see Fig. 4-1), and Fig. 4-2). We explored all allowed orientations with a Monte Carlo Markov Chain

(MCMC) algorithm [65], finding the sky-projected obliquity to be $4° \pm 10°$.

For the second method, we searched for pairs of anomalies produced by the same spot. Between successive transits of planet c, a spot will rotate 3.77 times around the star, thereby advancing in longitude by 0.77 of a full circle or 277°, relative to the meridian defined by the sky projection of the stellar rotation axis. An advance by 277° is equivalent to regression by 83°. Therefore, if a spot persists for at least four rotations, and if the spot's trajectory is parallel to the planet's trajectory (that is, if the obliquity is low), then an anomaly observed in the second half of a transit should be followed by an anomaly in the first half of the next transit. The two anomalies should differ by 83° in the suitably defined 'anomaly phase' (see Fig. 4-1).

Two of the five strongest anomalies have this expected phase relationship (see Fig. 4-3), corroborating the finding of a low obliquity. The QPV produced by this spot is coherent over the interval spanned by the two transits, confirming the persistence of the spot (see Table 4.3). Figure 4-3 shows a spot model fitted to the transit data. For completeness, three spots were included in the model, although only the largest spot (labelled 1) bears information on the stellar obliquity, because it was transited twice by planet c. The model parameters include the spin orientation of the star, the rotation period, and the spot properties (sizes, locations and intensities). Because the rotation period and spot properties are constrained externally from the QPV, the model could be used to constrain the spin orientation, with results given in Table 4.1 (see section 4.6), including a sky-projected obliquity $-1° \pm 10°$. This low sky-projected obliquity is likely to be representative of the true obliquity [61].

Furthermore, all three planetary orbits must be nearly coplanar. The mere existence of multiple transiting planets suggests coplanarity [116], although the possibility remains that the orbits are mutually inclined with nodes (lines of intersection) that happen to lie along the line of sight. However, for Kepler-30, such mutual inclinations would be detectable through variations in transit times and durations caused by nodal precession. To quantify this argument, we performed a four body integration of Newton's equations ([90], [1], [89]). To be compatible with the observed transit times and durations, the mutual inclinations must be smaller than a few degrees.

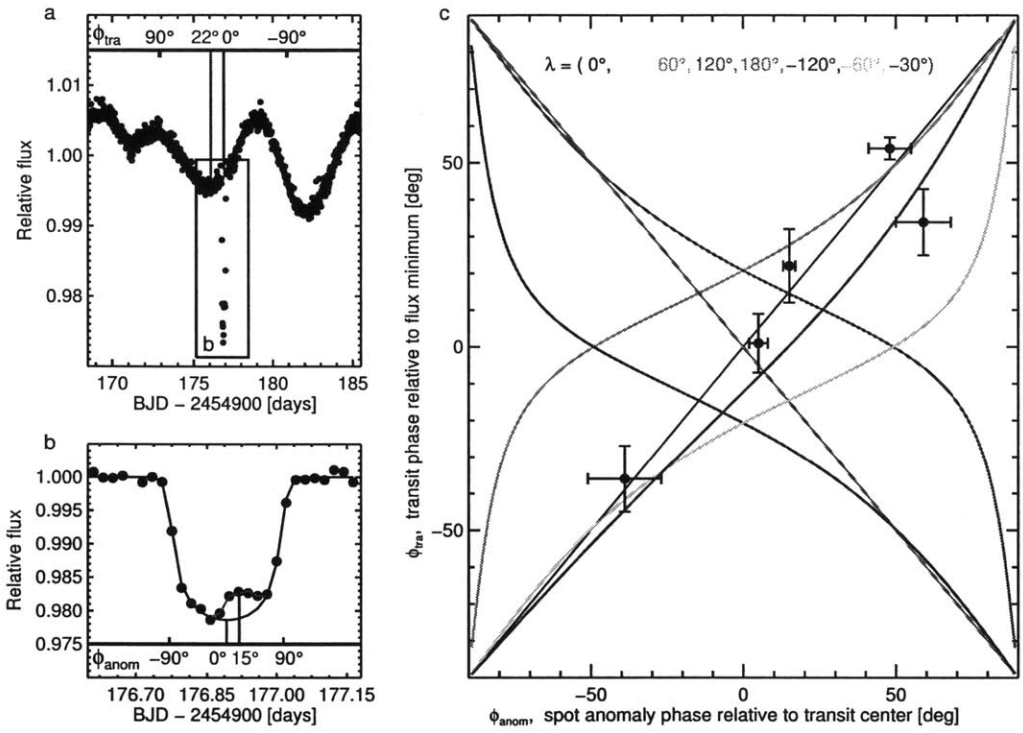

Figure 4-1: Evidence for a low obliquity based on transits over several starspots at differing stellar longitudes.

a, A portion of the Kepler light curve, with a box highlighting the transit of Kepler-30c shown in panel b. The transit occurred just after a local minimum in the QPV. The time of the transit is measured with respect to the selected flux minimum, divided by the rotation period and expressed in degrees, giving the 'transit phase', $\phi_{tra} = 22° \pm 10°$. The transit phase is also computed relative to all other local minima within one rotation period. BJD, barycentric Julian day. **b,** A flux anomaly is observed during the transit. The black line is a model without starspots and the red line is a model with one spot. The 'anomaly phase', which can be directly compared to the transit phase, is defined by $\sin\phi_{anom} = 2x/L$, where x is the distance from the spot to the centre of the transit chord, and L is length of the transit chord. In this case $\phi_{anom} = 15° \pm 2°$, in agreement with ϕ_{tra} and consistent with a low obliquity. **c,** Coloured lines show the expected relation between ϕ_{anom} and ϕ_{tra}, for different sky-projected obliquities (λ) and a fixed stellar inclination of 90°. Because the association between anomalies and minima may be ambiguous, ϕ_{tra} was computed for all plausible associations, for the five largest spot anomalies. Only one such set of associations is consistent with a single choice of the stellar orientation. Shown here for that unique choice of associations (see Table 4.4) is the observed relation between ϕ_{anom} and ϕ_{tra} implying a projected obliquity $\lambda = 4° \pm 10°$. This error, and the errors on all phases, is $\pm$ 1 s.d.

Table 4.1. Parameters of the host star Kepler-30, starspots and planets

Host star parameters[a]			
KIC/KOI number		3832472/806	
Kepler magnitude		15.4	
Mass ($M_\odot$)		0.99 ± 0.08	
Radius ($R_\odot$)		0.95 ± 0.12	
Effective temperature (K)		5498 ± 54	
Gyrochronology age estimate (Gyr)		2.0 ± 0.8	
Quadratic LD coefficient, u_1		0.38 ± 0.09	
Quadratic LD coefficient, u_2		0.40 ± 0.19	
Linear LD coefficient, u		0.54 ± 0.02	
Stellar density (g cm^{-3})		2.00 ± 0.10	
Planetary parameters[b]			
Parameter	Kepler-30b	Kepler-30c	Kepler-30d
Orbital period (days)	29.334 ± 0.008	60.3231 ± 0.0002	143.343 ± 0.009
Mid-transit time (BJD)	2455246.65 ± 0.04	2455357.8870 ± 0.0005	2455273.530 ± 0.010
Eccentricity, e	0.042 ± 0.003	0.0111 ± 0.0010	0.022 ± 0.005
Periapse angle, ω (degrees)	-31 ± 7	-49 ± 6	-163 ± 7
Nodal angle, Ω (degrees)	0.03 ± 0.17	0 (relative to 30c)	1.3 ± 0.5
Planetary mass (M_E)	11.3 ± 1.4	640 ± 50	23.1 ± 2.7
$\lvert I - 90° \rvert$ (degrees)	0.18 ± 0.16	0.32 ± 0.03	0.16 ± 0.02
$(R_{pl}/R_{star})^2$	0.00165 ± 0.00008	0.0162 ± 0.0008	0.0083 ± 0.0004
Planet density (g cm^{-3})	1.02 ± 0.13	1.88 ± 0.17	0.19 ± 0.02
Planet radius (R_E)	3.9 ± 0.2	12.3 ± 0.4	8.8 ± 0.5
Starspot parameters and spin-axis orientation[c]			
Spot rotational period (days)		16.0 ± 0.4	
Spot intensity relative to unspotted photosphere		0.85 ± 0.03	
Inferred spot temperature (K)		5298 ± 65	
Angular radius of spot (degrees)		21^{7}_{3}	
Sky-projected obliquity, recurrence method (degrees)		-1 ± 10	
Sky-projected obliquity, 5-anomaly method (degrees)		4 ± 10	

[a]Most of the host star parameters are obtained from the literature, and are based on the analysis of high-resolution spectra in conjunction with stellar-evolutionary models [60]. The limb darkening (LD) coefficients are obtained from the light curve analysis (see section 4.4). The stellar density is obtained from the dynamical modeling of transit timings and durations.

[b]Most of the planet parameters are obtained from the four-body dynamical model (see Fig. 4-4, Supplementary Table 4), with the exceptions of the impact parameters and $(R_{pl}/R_{star})^2$, which are obtained strictly from the light curve analysis. Periods and epochs are best-fits to constant-period models, with error bars reflecting the 1 s.d. spread in the transit timing measurements. $\lvert I - 90° \rvert$ is the deviation of the orbital inclination I from 90° (edge-on). The results for the planetary masses and radii take into account the uncertainty in the assumed stellar mass. The results for $(R_{pl}/R_{star})^2$ are assigned a relative error of 5% to account for possible contamination of the Kepler photometric aperture by background stars. The mass and radius of planet c agree with theoretical models of gas giant planets [66] (see section 4.7).

[b]The spot parameters are obtained from the spot model (see Fig. 4-3). In all cases the quoted results and statistical uncertainties are based on the 15.85%, 50% and 84.15% levels of the cumulative a posteriori probability distribution (marginalizing over all other parameters), as determined with the MCMC algorithm.

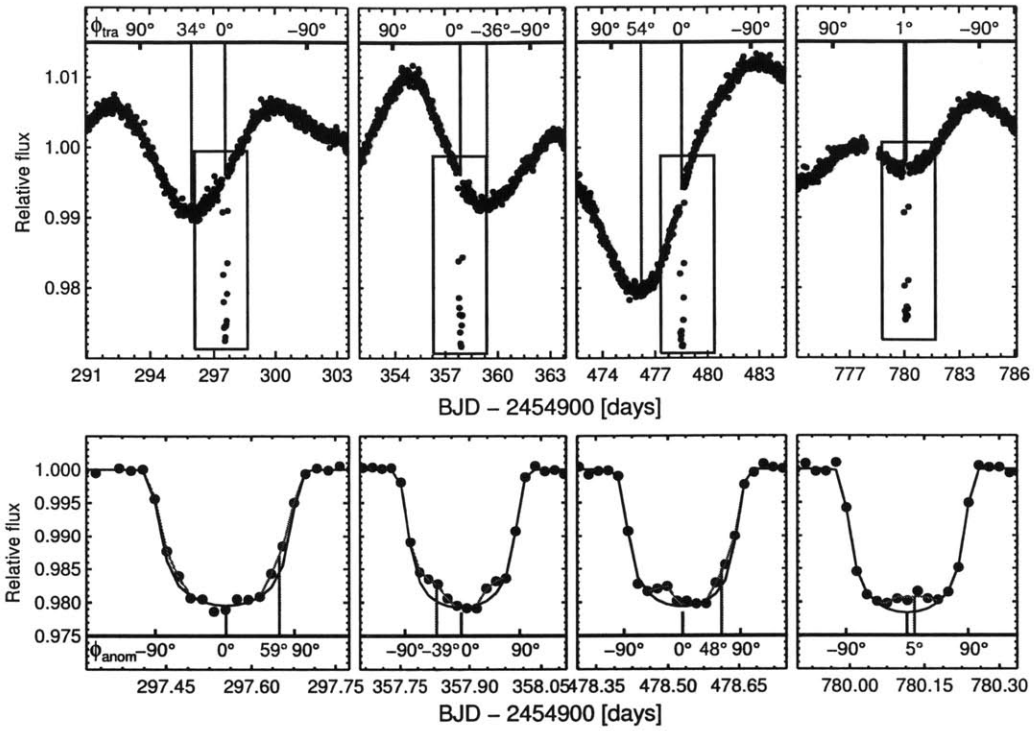

Figure 4-2: Continuation of Fig. 4-1, the transit phases and anomaly phases for the four other spot-crossing events.

The upper panels are the equivalent of panel a of Fig. 4-1, the lower panels the equivalent of panel b, for all four other spot-crossing events. It is important to note that except for the one on the right side, the other three are based in a model with two spots on the transit chord. In those cases, only one out of the two anomalies happens to be caused by a large enough spot, and that is the one connected with the blue vertical line on the lower panels. See table 2S and 3S for more information.

A by-product of our dynamical analysis combined with the transit analysis and the known mass of the star [60] is the determination of the planetary masses and radius (Fig. 4-4, Table 4.1).

Such an orderly arrangement might seem to be a natural consequence of the standard model of planet formation, based on core accretion within a flat disk [111]. Recently, though, the host stars of many 'hot Jupiter' systems have been found with high obliquities, in some cases even spinning backward relative to the planetary orbit ([214], [226]). Indeed, it has been argued that stars with hot Jupiters had initially random obliquities, and the only reason low obliquities are more frequent than ex-

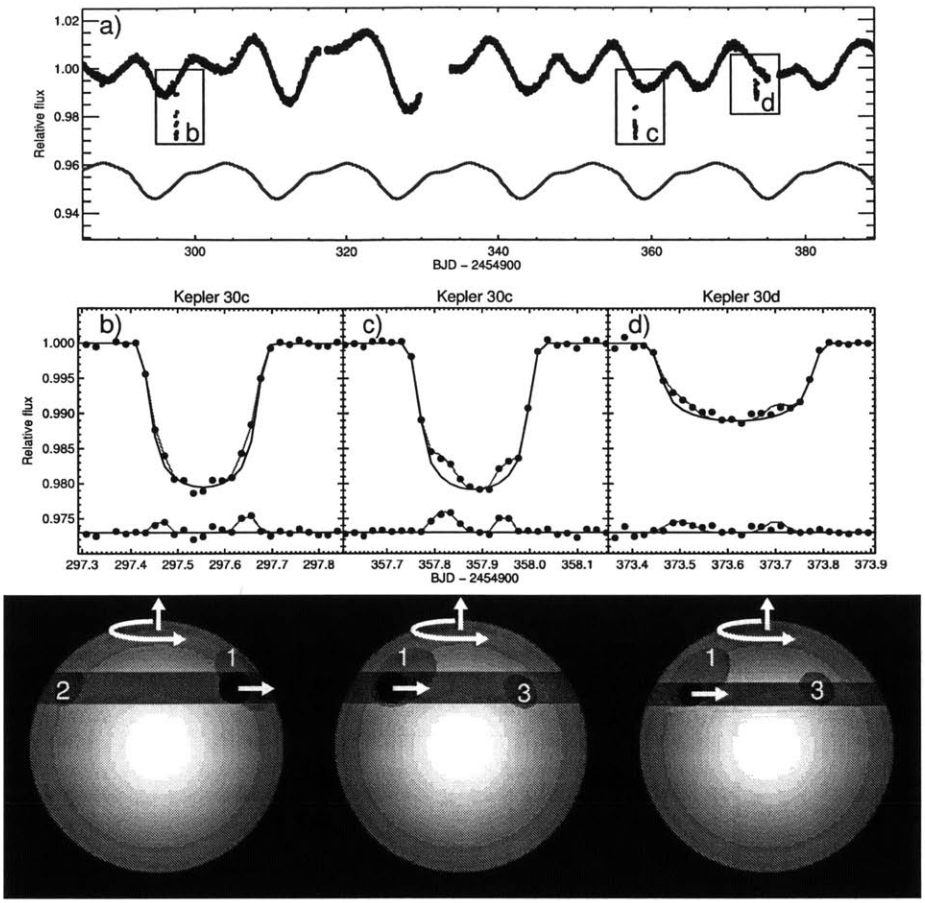

Figure 4-3: Evidence for a low obliquity based on a consecutive pair of transits over a single starspot.

a, Data points (black) are a portion of the Kepler light curve, showing the QPV with an approximate 16-day period. The red curve is a model consisting of three spots (shifted vertically for clarity). The model does not take into account spot evolution or differential rotation and is not expected to fit perfectly. Three particular transits are highlighted with boxes and labelled for subsequent discussion. **b,** Light curve of a transit of planet c. The solid dots are data points, the black curve is a transit model with no spots, and the red curve is the best-fitting model with three spots. Residuals from the best-fitting model are displayed near the bottom of the plot. **c,** Same as the previous panel, but for the next transit of planet c. **d,** Same as the previous panel, but for the next transit of planet d. The key parameter of the model, the projected obliquity, was constrained to be smaller than 10°. **e,** Illustration of the stellar disk, dark spots and transit chord for the time range plotted in panel **b**. The white arrows convey the direction of stellar rotation. The black disk represents the transiting planet. **f, g,** Same as panel **e**, but for the time ranges plotted in panels **c, d** respectively. Panels **e** and **f** show that spot 1 was twice eclipsed by planet c, with nearly four stellar rotation periods between the transits. Then, one stellar rotation later, spot 1 was also eclipsed by planet d (panel **g**). (The smaller spot, 3, may also have been eclipsed by both planets during this time interval, though the eclipse by planet d is not securely detected.)

pected is the obliquity-damping effect of planet-star tidal interactions [226]. The observed high obliquities in hot-Jupiter systems have been interpreted as evidence that hot Jupiters attained their close-in orbits through dynamical interactions (which can strongly perturb a planet's orbital orientation) followed by tidal capture. This view is in opposition to the previous paradigm for the origin of hot Jupiters, in which a gradual transfer of energy and angular momentum to the protoplanetary disk causes their orbits to shrink (and maintain a fixed orientation).

One reason why the scenario involving dynamical and tidal interactions has not gained universal acceptance is that obliquity measurements were previously confined to giant planets with small periastron distances. One would like to make sure that the high obliquities are indeed confined to systems that have experienced dynamical interactions. Otherwise it remains possible that stars and their disks are generally misaligned for reasons unrelated to planets, such as chaotic accretion [17], magnetic interactions [107] or differential torques produced by a neighbouring star.

Kepler-30 is the type of system that needed to be checked: the coplanarity of the planetary orbits suggests a quiescent history without disruptive dynamical interactions, and the planets are too far from the star for strong tidal interactions. The system was selected by virtue of significant spot-crossing anomalies, and not by any criterion that would have biased the result towards low obliquity. Therefore the observed low obliquity is a clue that star-disk misalignments are not the correct explanation for the high obliquities of hot Jupiter hosts, and that hot Jupiters arise from dynamics and tidal capture. There is only a 6% chance of observing such a low obliquity for Kepler-30 if obliquities were drawn from a random initial distribution. To strengthen our interpretation, additional observations of coplanar multiple-planet system are warranted, and are predicted to yield low obliquities.

Kepler was competitively selected as the tenth Discovery mission. Funding for this mission was provided by NASAs Science MissionDirectorate. The data presented in this Letter were obtained from the Mikulski Archive for Space Telescopes (MAST). STScI is operated by the Association ofUniversities for Research in Astronomy, Inc., under NASA contract NAS5-26555. Support for MAST for non-HST data is provided

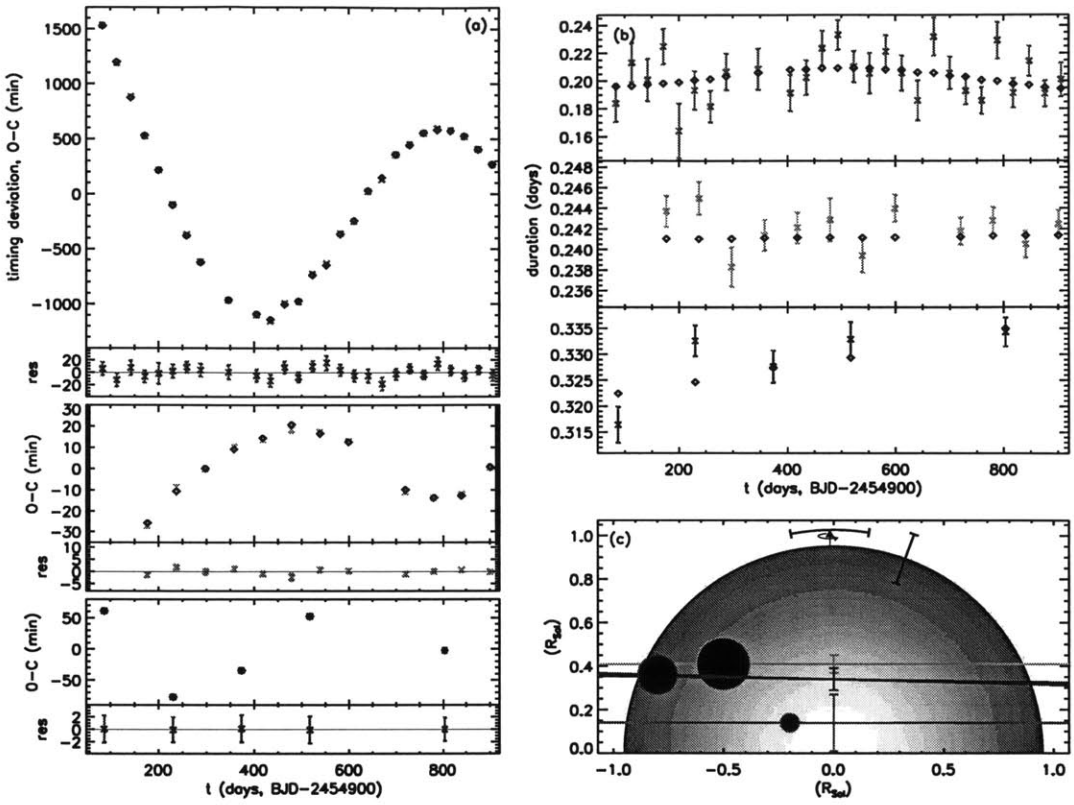

Figure 4-4: Evidence for coplanar planetary orbits based on an analysis of transit times and durations.

Throughout, sub-panels and diagram components using colors red, green and blue refer to planets Kepler-30b, Kepler-30c and Kepler-30d, respectively. **a,** The deviation of individual observed (O) transit times (see Table 4.2 with all errors defined as ± 1 s.d.) from a constant-period calculation (C) versus time. For planets c and d, suspected starspot-crossing anomalies were masked out before the analysis. Calculated transit times based on a model including planetplanet dynamical interactions ([60], [89]) (see section 4.7) are shown as open diamonds. Residuals (Res.) between the data and the model are shown below each O-C plot. **b,** Observed and modeled transit durations. Here the transit duration is defined as the length of time when the centre of the planet is projected in front of the stellar disk. **c,** Diagram of the paths of the planets (black circles with colored rims) across the face of the star. The error bars show the uncertainty in the impact parameters of the orbits, which are constrained from the timescale of ingress and egress. For planets b and d, three lines are shown, delimiting the 1 s.d. region allowed for the rotations around the line of sight, relative to planet c. The lack of secular changes in the durations (b) implies coplanarity to within a few degrees. The error bar on the stellar limb (upper right) is the uncertainty in the stellar radius. The stellar spin axis is denoted (upper middle); its projected orientation is determined from the starspot analysis to be aligned with the planets to within 10° (1 s.d.).

by the NASA Office of Space Science via grant NNX09AF08G and by other grants and contracts. S. Albrecht, E. Agol, J. A. Carter, L. Doyle and A. Shporer provided comments on the manuscript. D.C.F. acknowledges NASA support through Hubble Fellowship grant HF-51272.01-A, awarded by STScI. D.R. acknowledges the Harvard Institute for Theory and Computation. E.B.F., M.J.H. and J.N.W. acknowledge NASA support through the Kepler Participating Scientist programme.

The following material was originally published as the Supplementary Information section of the paper, and it is intended to supplement the Main Text section with a more technical description of the methods used to measure the obliquity of Kepler-30.

4.2 The Kepler photometric time series

Basic characteristics. This work is based on photometric time-series data of KIC 3832472 from the Kepler space telescope [21] obtained between 13 May 2009 and 28 September 2011 (Kepler quarters 1 through 10). Until 29 September 2011 the observing mode resulted in one photometric measurement every 29.4 min, whereupon the observing mode was changed to produce a time series with a finer sampling of 58.8 sec.

Removal of artifacts. We attempted to remove instrumental artifacts as follows. First we separated the transit segments from the rest of the time series. A transit segment was defined as the data obtained during a given transit along with 3 hours of data before the transit, and 3 hours of data after the transit. For the transit segments, instrumental artifacts were well described by a linear function of time. The parameters of this linear model were determined by fitting a straight line to the out-of-transit data. As for the rest of the data, we subtracted the projections between the data vector and the 4 most significant co-trending basis vectors made available by the Kepler project [1]. For some time ranges this correction was not applied, because the data had already been corrected by the Kepler project using the PDC-MAP algorithm ([195], [206]).

4.3 Stellar rotation period

Period determination. To estimate the stellar rotation period, we divided each quarterly time series by its mean, and then computed a Lomb-Scargle periodogram [184] of the entire time series. A clear peak is observed at 16 days. We interpret

[1] http://archive.stsci.edu/kepler/cbv.html

this peak as the stellar rotation period. This conclusion was corroborated by a visual inspection of the time series, in which there are at least ten clear cases of flux minima with a consistent amplitude separated by 16 days, for intervals as long as a year. Evidently, there are large and long-lived starspots. Some of these groups of flux minima are studied in more detail in the next section. We adopt an uncertainty of 0.4 days in the rotation period, based on the range of periods giving a periodogram power at least one-third as large as the peak power. Thus the stellar rotation period was estimated to be 16.0 ± 0.4 days.

Gyrochoronology. The stellar rotation period can be used to estimate the main-sequence age of the star, because Sun-like stars are observed to slow their rotation according to a simple law in which the rotation period is proportional to the inverse of the square root of the age [193]. We used a polynomial relationship [185] between stellar age, rotation, and mass to estimate the age of Kepler-30. The inputs were the rotation period, taken to be a Gaussian random variable with mean 16.0 days and standard deviation 0.4 days, and the stellar mass, taken to be 0.99 solar masses with a standard deviation of 0.08 solar masses. The resulting distribution of stellar ages has a mean of 2 Gyr and standard deviation of 0.8 Gyr, indicating a star younger than the Sun. The uncertainty of 0.8 Gyr reflects only the uncertainties in the rotation period and stellar mass, and not any systematic errors in the polynomial relationship itself.

4.4 Transit light curve analysis

Overview. The analysis of the transit data had several steps, to take advantage of the fact that certain model parameters were assumed to have the same values for all transits, while other parameters were allowed to be specific to each transit. The common parameters were determined by constructing and analyzing a composite transit light curve for each planet, the results of which were then used as constraints in the fit to each individual transit light curve. We performed two iterations of this entire process, the second time enforcing an additional constraint that the orbits

are nearly circular, based on the results of the dynamical integration described in section 4.7 of this supplement.

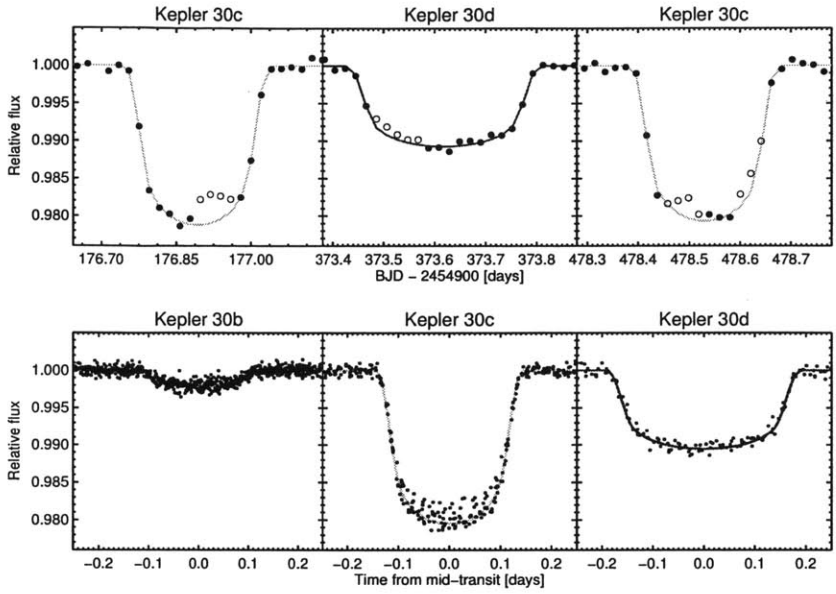

Figure 4-5: Transit curve analysis allowed us to determine the orbital parameters and also the sizes of the planets, properly taking into account the effect spots.

The upper panel shows three different transits in which spot anomalies are observed. The solid dots represent the observed fluxes used to determine the transit parameters. The open dots represent the observed fluxes affected by spot-crossing events, points that were not used in the transit analysis. The line represents the final transit model that fits through the solid dots. The lower panel shows the folded light curve for the three planets in which the solid dots represent all observations and the lines represent the final transit model. The effect of the spots seems to be present for the three planets, but it becomes much more evident for Kepler 30c, the largest planet.

Transit model. In all cases the transit data were fitted with a standard transit model [125] using a quadratic law to describe the stellar limb darkening, with two free parameters for the limb-darkening coefficients. The planet-to-star radius ratio, scaled stellar radius (R/a), and the cosine of the orbital inclination (cos I) were additional free parameters. When data with a cadence of 30 minutes is used, we evaluate the model with a fine time sampling and then time-average the model before comparing it to the data [101].

Spot corrections. For planets c and d, the signal-to-noise ratio of the tran-

sit data was large enough to justify corrections for spot effects. Spot-crossing flux anomalies were visually identified and excluded from the fit (see Figure 4-5). To account for the effect of unocculted starspots we added a new parameter (L_{spot}) specific to each transit representing the light lost due to spots, defined as

$$F_{corr} = \frac{F_{trans} - L_{spot}}{1 - L_{spot}} \tag{4.1}$$

where F_{trans} is the standard transit model with no spots, and F_{corr} is the model that is compared to the data [45]. We allow the Lspot parameters to vary freely except for the case of the shallowest transit, for which this parameter was held fixed at zero. Thus we assumed that the effect of unocculted spots was minimal for that transit, and indeed the shallowest transits of both planets c and d occur near a local maximum in the relative flux, as expected if our assumption were correct.

Parameter estimation. We determined the best-fitting model parameters by minimizing a standard χ^2 function. The weight of each data point was proportional to the square root of the effective exposure time, and the proportionality constants were determined by the condition $\chi^2_{min} = N_{dof}$ (number of degrees of freedom) for the best model. Construction of composite light curves allows for a drastic reduction in data volume and consequent speed-up of the MCMC algorithm. We assumed that the limb-darkening parameters, radius ratios, and R/a parameters were constant across all transits of a given planet, but that cos I (and therefore the transit duration) could vary from one transit to the next. To construct composite light curves, the best-fitting values of the midtransit times were used to calculate the time relative to the nearest mid-transit, and the best-fitting L_{spot} parameters were used to correct the data to zero loss loss-of-light due to unocculted spots. The data were then binned in time with a bin size of 5 minutes. The MCMC algorithm was then used to explore the allowed regions for the global parameters (Table 4.1). The same MCMC algorithm was also used to obtain the individual transit durations and transit midpoints of each event, using constraints on the other parameters based on the analysis of the composite light curves. The results for the transit midpoints and durations were used as inputs to

the dynamical model described in Section 4.7 (see also Table 4.2).

Table 4.2: Transit durations and midpoint times from the transit model

Planet	Transit #	Time [BJD-2454900]	Error	Transit Duration [days]	Error
b	0	83.719	0.007	0.184	0.013
	1	112.858	0.007	0.213	0.014
	2	142.027	0.008	0.201	0.015
	3	171.159	0.007	0.225	0.013
	4	200.326	0.012	0.164	0.020
	5	229.490	0.008	0.193	0.014
	6	258.684	0.006	0.182	0.011
	7	287.895	0.007	0.207	0.013
	9	346.419	0.008	0.209	0.015
	11	405.094	0.007	0.191	0.013
	12	434.432	0.007	0.202	0.012
	13	463.924	0.007	0.224	0.013
	14	493.316	0.006	0.233	0.011
	15	522.874	0.006	0.210	0.011
	16	552.316	0.008	0.205	0.015
	17	581.892	0.006	0.221	0.012
	18	611.352	0.006	0.206	0.013
	19	640.923	0.008	0.186	0.014
	20	670.380	0.007	0.232	0.014
	21	699.923	0.006	0.206	0.012
	22	729.366	0.005	0.193	0.010
	23	758.817	0.005	0.186	0.009
	24	788.230	0.007	0.229	0.013
	25	817.599	0.006	0.191	0.010
	26	846.940	0.006	0.214	0.011
	27	876.243	0.005	0.191	0.009
	28	905.525	0.006	0.201	0.012
c	0	176.8927	0.0007	0.2437	0.0015
	1	237.2268	0.0007	0.2450	0.0016
	2	297.5542	0.0009	0.2383	0.0019
	3	357.8826	0.0007	0.2414	0.0015
	4	418.2062	0.0007	0.2421	0.0015
	5	478.5308	0.0010	0.2429	0.0021
	6	538.8514	0.0007	0.2394	0.0016
	7	599.1696	0.0006	0.2440	0.0013
	9	719.7957	0.0006	0.2418	0.0013
	10	780.1152	0.0006	0.2428	0.0013
	11	840.4375	0.0005	0.2405	0.0013
	12	900.7677	0.0006	0.2425	0.0013
d	0	87.2631	0.0015	0.316	0.003
	1	230.3777	0.0014	0.333	0.003
	2	373.6182	0.0015	0.328	0.003
	3	516.8893	0.0015	0.333	0.003
	5	803.2728	0.0013	0.334	0.003

The errors are estimated using an MCMC algorithm. The transit durations of each planet are constant within the errors, which is used to constrain the mutual inclinations. The transits are not equally spaced, due to gravitational interactions between the planets. We used this information to constrain the masses and orbits of the planets (see Figure 4-4).

Iteration with dynamical modeling. There is a well-known relationship between the orbital parameters, transit parameters, and stellar mean density [225], usually described as a relation between the R/a parameter and the stellar mean density for an assumed circular orbit. Therefore, in a system with multiple transiting planets, an additional constraint is available on the orbital and transit parameters by requiring the individual planet models to agree on the stellar mean density. This only useful when the orbital eccentricities of the planets are known or bounded strongly. In the first iteration of our transit analysis, the planets' orbital eccentricities were unknown and were therefore analyzed individually with no common linkage based on the stellar mean density. Subsequently, the dynamical modeling described in Section 4.2 revealed that the orbital eccentricities must be small. After this finding, we performed a second iteration of the entire process: we repeated our transit analysis with constraints on the orbital eccentricities, thereby gaining additional leverage over the transit parameters, and then refined the dynamical model with the improved parameter set. The output orbital eccentricities were consistent with the results of the first iteration, obviating the need for additional iteration. (We note that iterative procedure could have been avoided by directly coupling the light curve model and dynamical model, a technique that has become known as photodynamics [35], at the cost of increased computation time.)

Limb darkening results. The fitted limb darkening coefficients $u_1 = 0.38 \pm 0.09$ and $u_2 = 0.40 \pm 0.19$ can be compared with tabulated values based on theoretical models of the atmosphere of the host star [42]. According to those models, a Sun-like star with log g = 4.5, Teff = 5500 and Z = 0.2 (parameters similar to those of Kepler-30) is expected to have limb-darkening coefficients $u_1 = 0.47$ and $u_2 = 0.22$, in agreement with our results.

4.5 Obliquity determination from transits over starspots at differing longitudes

Identifying significant anomalies: first method. When a planet transits a spot, the observed flux is higher than when the planet is transiting the brighter unspotted surface of the star. This is what causes the flux anomalies in the transit light curves. To simplify the analysis we wanted to identify those particular anomalies caused by the largest spots, which are expected to produce the most significant modulation of the out-of-transit flux. One can estimate the total flux deficit caused by the spot or at least of the portion of the spot transited by the planet by computing the difference between observed and modeled flux during an anomaly, and then multiplying by an appropriate scale factor [48]. However, this will underestimate the effect of spots that are transited near the limb, due to the effect of geometrical foreshortening. For this reason we employ a modified spot metric,

$$\Delta F = \frac{\sum(f_{obs} - f_{theo})\Delta t}{\tau\sqrt{1-r^2}} \tag{4.2}$$

where τ is the ingress time of the transiting planet, r is the projected distance from the center of the spot to the center of the star (in units of the stellar radius), Δt is the time spacing between observations, and f_{obs} and f_{theo} are the observed flux and the (spot-free) modeled flux respectively. The sum is evaluated for all data points during the spot anomaly. We ranked all spot anomalies according to this metric, and identified the six most significant spots, for which $\Delta F > 0.4\%$.

Identifying significant anomalies: second method. As an alternative means of classifying the spot anomalies, we also fitted a parameterized model to the anomaly data. Our spot model is based on the premise of a limb-darkened star with circular starspots [179]. In addition to the usual transit parameters, which were held fixed in this analysis, there were four parameters for each spot (size, relative intensity, and two-dimensional location in the rotating frame of the star). We specify the spot size by the angular radius, defined as the opening angle of the cone that connects

the boundary of the circular spot with the stellar center. Since the rotation period is slow enough that the spot does not move appreciably over the duration of a planetary transit, the model coordinates of the spot are assumed to be constant throughout the transit, coinciding with the projected center of the planet at the midpoint of the anomaly. The size and the relative intensity of the spot are free parameters, as are the transit midpoint and out-of-transit flux level, since those latter two parameters are correlated with the spot parameters. The model flux is calculated as the surface integral of the intensity of the visible hemisphere of the star, excluding the area blocked by the planet. The parameters of the best-fitting model are used to estimate the loss of light due to the entire spot, assuming a circular shape. This is in distinction with the first method, which is less model-dependent but gives only the loss of light due to the portion of the spot that was transited by the planet.

Both methods of ranking the spots give agreement on the top six spots. These spots should produce the largest quasi-periodic flux variations outside of transits. The six largest anomalies should each correspond to a flux variation exceeding 1%, which is readily detectable in the Kepler data.

Associating flux anomalies with nearby local minima in the out-of-transit flux. Spots cause a modulation in the disk-integrated flux, as they are carried across the disk by stellar rotation. Due to limb darkening, the loss of light due to a particular spot is largest when that spot is closest to the center of the stellar disk. The quasi-periodic variation thereby encodes some information about the location of the spot, which we use in the obliquity determination. For each of the six transits with the most significant anomalies, we search all of the data within one stellar rotation period to identify local flux minima deeper than 0.4%, i.e., deep enough to be caused by the same spot that is the origin of the transit anomaly. This search becomes more complicated if the transits are located close to a large data gap, like safe mode events, since the shape of the flux minima might be compromised. For this reason we discarded one of the transits with one large anomaly that happened close to the beginning of quarter 10. We checked that dropping this anomaly did not affect the conclusions of this paper.

For one of the remaining 5 transits, only one minimum is identified, and we conclude that the spot that caused the flux anomaly is the same that caused the flux minimum. The alternative interpretations are unlikely. For example there could be bright spots (faculae) situated in such a way as to cancel out the loss of light from the dark spot, but such large faculae have never been observed in active stars [67], and no evidence is found for transits over faculae. Another possibility is that two large spots can combine to cause the same effect as one larger spot. This is possible, but in these cases the two spots would necessarily have a similar rotational phase, and thus the computation of transit phases described below would be largely unaffected. In the other 4 large flux anomalies, there were two local minima in the vicinity of the transit. For these we tried all possible associations between flux anomalies and local minima, as described below.

Computing ϕ_{tra}, the phase of each transit within a stellar rotation cycle. For each transit we computed the phase of the transit (ϕ_{tra}) relative to each of the candidate minima. The phase is defined as the time of the transit, relative to the time of the flux minimum, divided by the rotation period and expressed in degrees. To measure this transit phase we first needed to measure the times of minimum light. This was done by fitting a parabolic function to the data near the minimum. These timings, along with formal statistical uncertainties, can be found in Table 4.3.

In the cases where PDC-MAP data were available, we repeated this procedure with both the flux series obtained with our detrending algorithm (fitting the co-trending vectors) and the PDC-MAP flux series. We found differences up to 0.1 days, several times larger than the formal statistical uncertainties. This demonstrates that the times of minimum light are dependent on the details of the detrending algorithm. Therefore, to obtain more robust results, we analyzed not only the local minimum closest in time to the transit, but the entire periodic sequence of local minima that occur within 4 stellar rotation periods of the transit in question. The large spots evidently lasted for several rotation periods, enabling this analysis. The timings of all those minima are also given in Table 4.3. We then fitted the times of minimum light for each spot with a linear function of cycle number.

Table 4.3: Measured timings for relevant flux minima used to estimate the rotational phases of the spots occulted during transit.

Spot group	Epoch	Timing	MCMC error	Final error	Period	Period error
I	0	150.242	0.007	0.40	16.11	0.08
I	2	182.153	0.010	0.40	16.11	0.08
	3	198.270	0.013			
	4	213.745	0.016			
	5	230.999	0.046			
	6	246.851	0.034			
II	0	144.264	0.016	0.44	16.01	0.08
	1	160.129	0.011			
	2	175.927	0.014			
	4	209.054	0.063			
	5	224.423	0.016			
	6	239.824	0.025			
III	0	264.863	0.021	0.40	15.94	0.06
Spot 1	1	280.107	0.010			
See figure 4-3	2	296.037	0.012			
	3	312.369	0.008			
	4	328.385	0.010			
	5	344.021	0.012			
	6	359.480	0.015			
	7	376.611	0.037			
IV	0	259.306	0.044	0.42	14.78	0.18
	1	273.199	0.012			
	2	288.296	0.020			
	3	303.549	0.027			
V	0	350.727	0.010	0.13	15.67	0.02
	1	366.291	0.011			
	2	382.016	0.011			
	3	397.571	0.012			
	4	413.266	0.010			
	5	428.724	0.009			
	6	444.762	0.008			
	7	460.272	0.006			
	8	476.165	0.008			
VI	0	681.771	0.014	0.57	15.16	0.12
	2	712.747	0.014			
	3	726.574	0.069			
	5	758.225	0.154			
	6	772.537	0.033			
VII	0	639.490	0.022	0.37	15.61	0.04
	3	686.184	0.023			
	4	702.226	0.014			
	5	718.260	0.019			
	6	733.743	0.027			
	7	748.411	0.026			
	8	764.116	0.038			
	9	780.078	0.019			
	10	795.897	0.011			

The flux minima are grouped according to periodicity, and each group represents one large active region or spot. MCMC errors are based in a parabola fit to each flux minima, whereas the final errors used are based on the standard deviation of the residuals of the linear fit to all the timings of a given group. The rotation period and its error are based on that same linear fit. The nine timings that occur close to one of the five transits that show large spot-crossing events are underlined. Written in bold and enclosed inboxes are the five flux minima uniquely determined (see Section 4.5).

The standard deviation of the residuals which was up to 20 times larger than the formal statistical uncertainty in each time of minimum light was adopted as a more realistic estimate of the uncertainty of each of the timings. The slope of the line is interpreted as the period of rotation of the given spot, in all cases close to the value 16.0 ± 0.4 days established in Section 4.2.

The transit phase is then defined

$$\phi^j_{tra} = \frac{360°(t_0 - t^j)}{P} \tag{4.3}$$

where P is the rotation period of the spot, t^j represents the time of minimum light, and t_0 is the mid-transit time. The uncertainty in this phase ($\delta\phi^j_{tra}$) is obtained by propagating the uncertainties of all the input parameters.

Computing ϕ_{anom}, the phase of each anomaly within the transit. The timing of the spot-crossing anomaly relative to the mid-transit time also bears information about the location of the spot, in this case with respect to the transit chord. Each spot-crossing anomaly was assigned an anomaly phase (ϕ_{anom}), defined as

$$\phi_{anom} = \sin^{-1}\left(\frac{x}{\sqrt{1-b^2}}\right) \tag{4.4}$$

where x is the location of the spot measured along the transit chord, in units of the stellar radius, and b is the impact parameter of the transit. To determine this phase and its uncertainty ($\delta\phi_{anom}$), we use the spot transit model previously mentioned, in which x is a free parameter. We used an MCMC algorithm to determine the allowed range of this parameter, and then propagate the uncertainty appropriately to obtain ϕ_{anom} (see Table 4.4).

Using the relation between ϕ_{tra} and ϕ_{anom} to determine the obliquity. Given a certain spin-orbit orientation and a particular impact parameter, there is a one-to-one geometrical relationship between these two phases. Symbolically we write this relationship as

$$\phi_{tra,theo} = f(\lambda, i_s, \phi_{anom}, b) \tag{4.5}$$

Table 4.4. Final transit and anomaly phases for each of the largest spots occulted by planet Kepler 30c.

Kepler Transit #	ϕ_{anom}[deg]	Error	ϕ_{tra}[deg]	Error
0	15	2	22	10
2	59	9	34	9
3	-39	12	-36	9
5	48	7	54	3
10	5	3	1	8

and, for each of the 16 possible associations between flux anomalies and local minima, we define the goodness-of-fit as

$$\chi^2(\lambda, i_s, b, \phi_{anom}, j) = \sum \left[\frac{\phi_{tra,theo} - \phi^j_{tra}}{\delta\phi^j_{tra}} \right]^2 + \sum \left[\frac{\phi_{anom,param} - \phi_{anom}}{\delta\phi_{anom}} \right]^2 + \left[\frac{b - b_c}{\delta b_c} \right]^2 \quad (4.6)$$

where λ is the sky-projected stellar obliquity, is is the inclination of the stellar rotation axis with respect to the line of sight, the index j ranges over the 16 possible associations, and b_c and δb_c are the measured impact parameter of planet c and its associated uncertainty (Table 4.1). For each of the 16 possible associations, we evaluate the minimum of the χ^2 function in a 2D uniform grid in λ and i_s, with λ ranging from 180° to 180° and i_s ranging from 0° to 180°, with a spacing of less than half degree. With eight parameters and eleven measurements, we have three degrees of freedom. We only find one association that gives an acceptable fit, with a minimum $\chi^2 \approx 5.2$ and a p-value of 0.16. The next best association gives a minimum $\chi^2 \approx 26.5$, with a p-value of 0.000008. This test thereby uniquely determines the associations between flux anomalies within a transit, and nearby minima in the out-of-transit flux (see Table 4.4 for final value of the phases). Once this is decided, we used an MCMC algorithm to obtain the final value of λ and its uncertainty, using the correct association. (As expected is is unconstrained by this analysis.)

4.6 Obliquity determination from two transits over a single starspot

A second, independent determination of the obliquity was undertaken, based on the observed recurrence of flux anomalies by the same spot in two different transits. For this task the spot model was changed appropriately. To give an acceptable fit to the light curves it was necessary to include three spots in the model, even though only one of those spots (the one that was transited twice) is of interest. The largest spot, labeled 1 in Figure 4-3, is the crucial spot that was transited twice by planet b. The smaller spots 2 and 3 were included for completeness but do not have any bearing on the stellar obliquity. These two spots are fixed to the transit chord as previously explained. For simplicity, all the spots were assigned the same intensity, since for spots 2 and 3 this parameter is degenerate with the spot angular radius. More information is available for spot 1 because Kepler- 30c transited this spot twice. The model is also modified (relative to the model described in Section 4.5) to account for the changing position of the spot on the disk of the star. We model the trajectory of the spot with the two angles specifying the stellar orientation, the rotation period of the star, and a particular time when the spot is closest to the center of the star.

The transit data alone would not allow the spot parameters to be determined uniquely, especially because the transits are well separated in time and the spots are large. However, we can apply some crucial constraints on the model based on the analysis of the out-of-transit quasiperiodic flux variations. Specifically, Gaussian priors were imposed on the stellar rotation period, and on the amplitudes and phases of the out-oftransit flux variations implied by the spot locations (Table 4.3). To compute the amplitude of the quasi-periodic flux variations for a given set of spot parameters, we used the Dorren model [55], an analytic expression that gives the loss of light from a circular spot of a certain size, brightness contrast and location. This model uses a linear law for the limb darkening profile. We assumed that the limb-darkening law was the same for spots as for the surrounding photosphere. The spots were required to have a lower intensity than the surrounding photosphere, and a

maximum angular size of 60° to protect against outlandish solutions. The individual transit times and out-of-transit flux levels were allowed to vary freely. The allowed regions for the parameters were determined with an MCMC algorithm [65], and are given in Table 4.1. We used the best-fitting (zero obliquity) solution to plot the quasi-periodic flux variations using the same Dorren model, and in Figure 4-3, panel a, the result is plotted in red. The spot model captures the general amplitude of the modulations and the phase of the largest spot, but does not fit perfectly. This was expected, since we are not modeling all the smaller spots that may exist on the surface or trying to fit the quasi periodic flux variations point by point, nor are we taking into account spot evolution or differential rotation.

4.7 Dynamical modeling

Overview. A dynamical model was fitted to the observed transit times and durations, in order to determine the planet masses and especially the mutual inclinations between the planetary orbital planes. The model consisted of four spherical bodies (the star and three planets) dynamically interacting according to Newton's equation of motion. This model was advanced, using a root-finding technique [59], to each moment of closest sky-projected separation between each of the planets and the star. This moment is the model midtransit time. This distance of closest sky-projected separation, in units of stellar radii, is the model impact parameter b (averaged over the transits which are observed). The model transit duration is the width of the star along that transit chord, $2R_*\sqrt{1-b^2}$, divided by the sky-projected relative velocity of the planet and the star (v). These three types of quantities are compared to the measurements (Table 4.2), and the χ^2 function (the sum of the squares of the differences between model and data, normalized by the observational errors) is minimized using the Levenberg-Marquardt algorithm [127].

Model parameters. The parameter set used in the model are osculating orbital elements in Jacobian coordinates: each planet's orbit is referenced to the center of mass of all bodies on interior orbits, with instantaneous Keplerian orbits defined using

Table 4.5. Dynamical fit to Transit Times and Durations (Table 4.2) and Impact Parameters (Table 4.1).

Planet	P (days)	T_0 (BJD-2454900)	$e\sin\omega$	$e\cos\omega$	i (deg)	Ω (deg)	M_p/M_* (x 10^{-6})
b	29.33434	346.6476	0.03616	-0.02204	90.179	0.035	34.29
+/-	0.00815	0.0401	0.00185	0.00638	0.167	0.167	3.03
c	60.323105	357.887042	0.00728	-0.008332	90.3227	0.00	1935
+/-	0.000244	0.000520	0.00133	0.000767	0.0302	(def)	167
d	143.34394	373.53020	-0.02060	-0.00635	89.8406	1.319	70.09
+/-	0.00858	0.00969	0.00510	0.00239	0.0202	0.475	5.76

the total mass of all interior bodies and that planet. The numerical integrations use Cartesian, astrocentric coordinates (at a common dynamical epoch BJD 2455550), coordinates into which the parameter set is converted prior to the integration. The parameters are orbital period, P; mid-time of a transit near the dynamical epoch, T_0; the parameters (e $\sin\omega$) and (e $\cos\omega$), where e is the eccentricity and ω is the angle between the periastron and the node, the latter being the location the planet passes through the sky plane moving towards the observer; the inclination of the orbital plane with respect to the plane of the sky, i; the rotation angle of the node about the line of sight, Ω. Finally, we fit the mass of each planet with respect to the star, M_p/M_*. We have used this method previously to fit transit midtimes ([60], [89], [43]), and in Table 4.5, we give the resulting orbital parameters.

Obtaining the density of the host star. An additional step of this analysis was to find the density of the star, ρ_*. In practice, we fix the stellar mass at 0.99 $M_\odot$ and use stellar radius R_* as an additional fit parameter, which we convert to ρ_* using the adopted stellar mass. The rationale of this approach is that under the transformation of masses $M_* \to \alpha M_*$, Newton's equations have the scaling property of time $t \to \sqrt{\alpha}t$ and of distances/radii $R_* \to \alpha^{1/3}R_*$ and thus $M_*/R_*^3 \to M_*/R_*^3$, meaning that photometric data uniquely constrain only densities. While fitting a certain timing dataset, the fit can still be rescaled to various masses and radii. Another way to demonstrate this is to note the dependencies of parameters which together determine the stellar radius: $R_* = D/(2v\sqrt{1-b^2})$. The shape of transits determines the parameter b and duration D; they are independent of M_*. The sky-projected

orbital velocity v comes from the numerical integration. The orbital period is fixed by the observations, so v scales the same way as semi-major axis with stellar mass, i.e. $v \propto M_*^{1/3}$. Thus the inferred R_* scales as $M_*^{1/3}$, so with the integrations assuming a certain M_*, what is really being constrainced is the stellar density.

The best fitting model For this analysis, the average impact parameters we used were given in Table 4.1. The resulting goodness-of-fit statistic and number of data points for were $\chi^2/\#$:

Times of planet b :	18.3/27
Times of planet c :	12.9/12
Times of planet d :	0.02/5
Durations of planet b:	39.9/27
Durations of planet c:	16.1/12
Durations of planet d:	10.5/5
Impact parameter of planet b:	1.4/1
Impact parameter of planet c:	0.1/1
Impact parameter of planet d:	0.03/1

The total χ^2 of 99.4 for 70 degrees of freedom is marginally acceptable: according to the chi-squared test, it has a p-value of 0.012. The durations and impact parameter of planet b have high deviations from their measured errors (Table 4.1, 4.2). Kepler 30b is a special case because its ingress and egress have very low signal-to-noise per transit, so the determination of errors of durations and impact parameter is especially difficult.

Mutual events. Note that planets c and d have nearly the same impact parameter, and there is evidence that they cross the same spot. This suggests that if they transited the star at the same time, their disks might intersect, in projection. Such a geometry would lead to a momentary brightening, relative to the two-planet eclipse model, called a mutual event [166]. In the current dataset, no such anomalies exist, and the best-fitting model has no such events spanning $\approx$ 8 years of data possible from Kepler. However, ground-based telescopes may survey this system thereafter

[209], presuming the planets have not nodally precessed onto differing transit chords by then.

Planet parameters. Although the main motivation for our dynamical analysis was the determination of mutual inclinations, a by-product is the determination of the planetary masses and densities, which were heretofore poorly known. From table 4.5, we obtain the planet to star mass ratio that combined with the stellar mass obtained from the spectra (Table 4.1) gives us the mass of the planets. This same mass ratio, together with the new precise density of the star, and the planet to star radius ratio, allows us to get the densities. Then it is straightforward to obtain the planetary radius from these. We confirm that b is akin to Neptune, and c is a gas giant similar to Jupiter. Planet d has the lowest mean density of any exoplanet smaller than Jupiter [233], although we caution that the mass of planet d is less robustly constrained than the other two planet masses. The constraint on d's mass relies on the analysis of its gravitational pull on c, which is itself engaged in a resonance with b, making the effects difficult to isolate.

To test the robustness of these measurements, we adopt a theoretical stance and assume that the mass and radius of Kepler 30c should conform to theoretical models of giant planets, which are thought to be reliable for cool (not strongly irradiated) giant planets [66]. Thus, the massive giant planet can be used as a reference object, instead of the usual practice of using the star as the only reference object. With an orbital period of 60 days around a Sun-like star, and being so massive, in theory the size of this planet depends chiefly on its age and the composition of the solid core at its center. With the estimate of the age from the rotational period and the mass fixed to 2 Jupiter masses, we estimate the largest size possible as the cool Jupiter with no core and age of 1 Gyr, which is 1.14 times the radius of Jupiter. On the other end, to provide a lower bound on the planet radius, we choose a cool Jupiter with a very large core, 100 times the mass of Earth, and as old as 4.5 Gyrs, giving a size of 0.97 Jupiter radii. Putting these results together, we set a value for the radius of 1.05 ± 0.09 Jupiter radii for Kepler 30c, or what is the same, 11.8 ± 1.0 Earth radii. With this estimate, and the knowledge of the relative sizes of the planets, one can determine the sizes

of the smaller planets, whose radii depend strongly on composition and thus are not well constrained by theory. For Kepler 30b we obtain a radius of 3.8 ± 0.3 Earth radii, and for Kepler 30d we obtain a radius of 8.4 ± 0.8 Earth radii. All these values agree with the observed values, showing the robustness of our analysis. Even using this slightly smaller radius for the Kepler 30d, we obtain a density of 0.21 ± 0.07 g cm^{-3} that is still the lowest among all exoplanets smaller than Jupiter. We emphasize that in this analysis, theoretical models for giant planets influence the planet properties, whereas the original values reported in Table 4.1, which have smaller uncertainties, are also independent of such models.

Chapter 5

Polar spots and high obliquities: The case of Kepler-63b

Published as: "Kepler-63b: A Giant Planet in a Polar Orbit around a Young Sun-like Star" Sanchis-Ojeda, R., Winn, J.N., Marcy, G.W., Howard, A.W., Isaacson, H., Johnson, J.A., Torres, G., Albrecht, S., Campante, T.L., Chaplin, W.J., Davies, G.R., Lund, M.N., Carter, J.A., Dawson, R.I., Buchhave, L.A., Everett, M.E., Fischer, D.A., Geary, J.C., Gilliland, R.L., Horch, E.P., Howell, S.B., Latham, D.W. 2013, ApJ, 775, 54.

We present the discovery and characterization of a giant planet orbiting the young Sun-like star Kepler-63 (KOI-63, $m_{\rm Kp} = 11.6$, $T_{\rm eff} = 5576$ K, $M_\star = 0.98\,M_\odot$). The planet transits every 9.43 days, with apparent depth variations and brightening anomalies caused by large starspots. The planet's radius is $6.1 \pm 0.2\ R_\oplus$, based on the transit light curve and the estimated stellar parameters. The planet's mass could not be measured with the existing radial-velocity data, due to the high level of stellar activity, but if we assume a circular orbit we can place a rough upper bound of $120\ M_\oplus$ (3σ). The host star has a high obliquity ($\psi = 104°$), based on the Rossiter-McLaughlin effect and an analysis of starspot-crossing events. This result is valuable because almost all previous obliquity measurements are for stars with more massive planets and shorter-period orbits. In addition, the polar orbit of the planet combined

with an analysis of spot-crossing events reveals a large and persistent polar starspot. Such spots have previously been inferred using Doppler tomography, and predicted in simulations of magnetic activity of young Sun-like stars.

5.1 Introduction

There are good reasons why planet hunters try to avoid chromospherically active stars. For those who use the radial-velocity technique, starspots and plages distort the absorption lines, inducing radial-velocity signals that can be similar to those of planets (see, for example, [121]). A good example of these complications is CoRoT-7 [110], for which different authors have measured different planet masses based on the same radial-velocity data, due to the strong activity of the host star ([161], [158], [63], [79]).

Starspots can also be a source of noise in the transit technique. Starspots are carried around the star by rotation, inducing flux variations that could be hard to detect from ground-based telescopes. When they go unnoticed, they can bias the determination of the transit parameters ([45], [36]). In addition, when the planet crosses over a dark starspot, it temporarily blocks less light than expected, causing a brightening anomaly [189]. These can be an additional source of error, or be confused with transits of other bodies in the system ([159], [165]).

Space-based transit surveys have the potential to overcome these problems, thanks to their high photometric precision and nearly continuous time coverage. The data from these surveys provide the opportunity to study the general activity levels of thousands of stars [13] as well as spot evolution and magnetic cycles of individual systems [20]. With hundreds or even thousands of transiting objects detected to date, spot-crossing events are more readily observed. They bear information about the sizes, temperatures, and positions of the spots [189], as well as the stellar rotation period ([190], [53]).

Spot-crossing events can also provide information about the architecture of exoplanetary systems. Measurements of the angle between the spin axis of the star and

the orbital plane of the planet (known as the obliquity) can help test theories of formation and evolution of these systems ([162], [231]). Most of the obliquity measurements to date have been based on the Rossiter-McLaughlin (RM) effect, a spectroscopic effect observed during transits (see, e.g., the recent compilation by Albrecht et al. 2012). One can also test whether a transit-hosting star has a high obliquity using asteroseismology ([75], [37]), the combination of $v \sin i_\star$, stellar radius, and stellar rotation period ([185], [86]), or starspot-crossing events ([179], [144], [52], [212]).

The basic idea behind using starspot-crossing events to measure the obliquity is that when the obliquity is low, any such events are expected to recur in consecutive transits. This is because in such cases the trajectory of the spot is parallel to the trajectory of the planet across the stellar disk; when the planet transits again, the spot is likely to have remained on the transit chord and a spot-crossing event will occur at a later phase of the transit. In contrast, the rotation of a highly oblique star would carry the spot away from the transit chord, and the anomalies would not recur in consecutive transits. For a more detailed explanation and recent elaborations of this technique, we refer the reader to [178]. One interesting feature of the starspot-crossing technique is that in the case of highly misaligned system, the planet may transit across a wide range of stellar latitudes ([48], [177]). In these systems we have the rare opportunity to measure the latitudes of starspots and their evolution in time.

In this paper we present Kepler-63b, a new transiting planet discovered with the *Kepler* space telescope. The paper is organized as follows. Section 5.2 describes the *Kepler* observations and other follow-up observations necessary to confirm the planetary nature of Kepler-63b. Section 5.3 describes the effort to characterize the age, radius and mass of the Kepler-63 host star. Section 5.4 explains how we characterized the planet in the presence of large and dark starspots. Section 5.5 demonstrates that Kepler-63 has a large obliquity, using the RM effect. Section 5.6 confirms the high obliquity of the system using spot-crossing events. Section 5.7 summarizes what we have learned about the starspots on Kepler-63, including their latitudes. The paper finishes with a discussion of the results in the context of current theories for stellar activity and planetary systems.

5.2 Observations

5.2.1 *Kepler* observations

For more than 4 years, the *Kepler* space telescope monitored approximately 150,000 stars in the constellations of Cygnus and Lyra ([103], [21]). The observations consisted of a series of 6 s exposures that were combined into final images with an effective exposure time of 1 min (short-cadence mode, [72]) or 29.4 min (long-cadence mode). The target star Kepler-63 was identified in the *Kepler* Input Catalog [26] as KIC 11554435 (also 2MASS J19165428+4932535) with *Kepler* magnitude 11.58 and $V = 12.02$. Because of the relative brightness of the star, and the high signal-to-noise ratio (S/N) of the flux dips, it was identified as a transiting-planet candidate early in the mission and designated Kepler Object of Interest (KOI) number 63. For this study we used long-cadence observations from quarter 1 through 12, spanning nearly three years (2009 May 13 through 2012 March 28). Short-cadence observations were also used whenever available (quarters 3-12, as well as one month in quarter 2).

The *Kepler* pipeline provides data with time stamps expressed in barycentric Julian days in the TDB (Barycentric Dynamical Time) system. Two sets of fluxes are provided: simple aperture photometry, which is known to be affected by several instrumental artifacts [100]; and fluxes that have been corrected with an algorithm called PDC-MAP that attempts to remove the artifacts while preserving astrophysical sources of variability ([206], [195]). For this study we used the PDC-MAP time series. Because of the large pixel scale (4 arcseconds) of *Kepler*'s detectors it is always important to consider the possibility that the reported fluxes include contributions from neighboring stars ("blends"). The time series of the measured coordinates of the source of light are useful diagnostics. For Kepler-63, we used the coordinates of the center-of-light based on PSF-fitting (PSF_CENTR) which were provided by the *Kepler* pipeline (see 5.4.1).

5.2.2 Spectroscopic observations

We used the spectroscopic observations gathered by the *Kepler* Follow-up Program (KFOP). One spectrum was obtained with fiber-fed Tillinghast Reflector Échelle Spectrograph (TRES) on the 1.5m Tillinghast Reflector at the Fred Lawrence Whipple Observatory on Mt. Hopkins, Arizona, with a resolution of 44,000. The observation took place on 2009 June 13 with a exposure time of 24 min, giving a S/N of 64 in the Mg I b order. Another spectrum was taken with the HIRES spectrograph [219] on the 10m Keck I telescope at Mauna Kea, Hawaii, with a resolution of 48,000. The observation took place on 2009 August 1 with an exposure time of 20 min, giving a S/N of 250. Three more spectra were taken with the FIber-fed Échelle Spectrograph (FIES) on the 2.5m Nordic Optical Telescope (NOT) on La Palma, Spain [54], with a resolution of 46,000. The observations took place on 2010 June 2, 5 and 6, with a typical exposure time of 20 min, giving a S/N of about 80.

We conducted additional observations to try to measure the radial-velocity signal induced by the planet on the star, and also to detect the RM effect. We used HIRES on the Keck I 10m telescope to obtain 7 spectra during the two weeks before the transit of 2011 August 20/21. Then, during the night of the transit, we obtained 30 spectra with a typical exposure time of 10 minutes, starting 3 hours before the transit and finishing 3 hours afterward. We determined relative radial velocities in the usual way for HIRES, by analyzing the stellar spectra filtered through an iodine cell (wavelength range 500–600 nm). For the analysis, we used a modified version of the original code by [31]. Table 5.1 gives the radial velocities.

5.2.3 Speckle imaging

High-resolution images are useful to establish which stars are contributing to the *Kepler* photometric signal. Speckle imaging was conducted on the night of 2010 September 17, using the two-color DSSI speckle camera at the WIYN 3.5m telescope on Kitt Peak, Arizona. The speckle camera simultaneously obtained images in two filters: V (5460/400Å) and R (6920/400Å). These data were processed to produce a final re-

Table 5.1. Relative Radial Velocity Measurements of Kepler-63

BJD_{TDB}	Radial velocity [m s^{-1}]	Uncertainty [m s^{-1}]
2455782.054444	−19.6	3.3
2455782.937924	31.3	3.0
2455787.771381	−26.7	3.0
2455788.809546	−5.6	3.2
2455789.858820	−7.5	3.1
2455790.807157	−23.2	2.8
2455792.775137	−37.4	2.7
2455793.743264	4.2	2.2
2455793.750173	−4.9	2.1
2455793.757280	0.6	2.1
2455793.791469	−2.5	2.2
2455793.798830	1.3	2.2
2455793.806157	−2.7	2.2
2455793.813541	−2.3	2.0
2455793.821018	−1.4	2.3
2455793.828321	7.8	2.2
2455793.835717	2.2	2.1
2455793.843124	2.7	2.2
2455793.850578	13.2	2.1
2455793.857834	16.6	2.6
2455793.865369	11.6	2.4
2455793.872800	18.8	2.4
2455793.880404	20.8	2.4
2455793.887626	9.9	2.3
2455793.895195	7.3	2.2
2455793.902278	15.1	2.8
2455793.912105	0.3	3.0
2455793.919987	12.5	3.3
2455793.927382	5.9	2.6
2455793.934894	−7.0	2.7
2455793.942232	3.8	2.8
2455793.949546	−7.3	2.9
2455793.957266	−3.3	3.3
2455793.964546	−19.0	3.1
2455793.972081	0.7	3.1
2455793.979569	−6.7	3.1
2455794.010807	−10.1	2.9

Note. — RVs were measured relative to an arbitrary template spectrum; only the differences are significant. Column 3 gives the internally estimated measurement uncertainty which does not account for any "stellar jitter."

constructed speckle image for each filter. Details of the processing were presented by [95]. The speckle observations are sensitive to companions between 0.05–1.5 arcseconds from Kepler-63. We found no companion star within this range of separations, and can place an upper limit on the brightness of such stars corresponding to ΔR = 4-5 mag and ΔV = 3-5 mag below the brightness of Kepler-63.

5.3 Stellar characterization

5.3.1 Rotation period and age estimate

We identified Kepler-63 as an interesting target based on its high level of chromospheric activity, and the high S/N with which individual transits are detected. The high level of activity is evident from the quasi-periodic stellar flux variations. To study these variations we used the published transit ephemeris [15] to remove the transit signals. To reject outliers we clipped those data points more than 3σ away from the median flux over the surrounding 10 hr interval. Since the star's light fell on a different CCD during each of the four *Kepler* observing seasons, we had to make a choice for the normalization of each quarterly time series. We chose to divide each quarterly time series by the mean flux in that quarter, since it seemed to be the easiest way to avoid large flux discontinuities between quarters.

The upper panel of Figure 5-1 shows the relative flux time series. The short-term variability on the scale of a few days is presumably caused by spots being carried around by the rotation of the star. There is also long-term variability, probably reflecting spot evolution. The peak-to-peak variability reaches a maximum value near 4%. There are also intervals with much lower variability. A Lomb-Scargle periodogram [184] shows a strong peak at 5.4 days, with a full width at half-maximum of 0.014 days. Sometimes the highest peak in a periodogram actually represents a harmonic of the true period, but in this case there is no significant signal at twice the candidate period and there is a (weaker) signal at half the candidate period, supporting our identification. Therefore we interpret the strongest peak as the rotation

period, and adopt $P_{\rm rot} = 5.401 \pm 0.014$ days.

This is nearly commensurate with the orbital period of Kepler-63b, with $P_{\rm rot}/P_{\rm orb} = (4.01 \pm 0.01)/7$. Whether this relationship is caused by a physical process or is merely a coincidence, it has an important consequence for the interpretation of spot-crossing anomalies, as pointed out by [229] in the context of the HAT-P-11 system. The near-commensurability causes a "stroboscopic" effect in the pattern of anomalies, and may lead to the detection of recurrences even in the case of misaligned systems. For example, [52] used the stroboscopic effect to boost the S/N of the spot signals in the Kepler-17b system.

Other lower-power peaks are present in the periodogram, which could be a sign of differential rotation or spot evolution. We checked for any variability of the position of the highest-power peak by computing a running periodogram: for each time t we calculated the Lomb-Scargle periodogram of a 50-day time interval centered on t. We performed these periodograms for a sequence of t values spaced apart by 5 days. Since there are occasional gaps in the data collection, we only computed periodograms for those intervals for which the gaps constitute less than 20% of the interval. (Removing the transits only eliminates 2% of the data.) The results are shown in the lower part of Figure 5-1, with red colors indicating higher periodogram power. The black line is where $P_{\rm rot}/P_{\rm orb} = 4/7$. It seems that the highest peak was quite stable over the three years of observations.

Our spectroscopic analysis (see section 5.2.2), shows that Kepler-63 is a Sun-like star. With such a short rotation period of 5.4 days, and assuming the star has not been spun up due to tidal or other interactions, Kepler-63 is likely to be relatively young. The Sun had a rotation period of 6 days at an age of approximately 300 Myr, based on the [193] law in which the rotation period grows as the square root of time. None of the Sun-like stars in the Hyades or Praesepe have rotation periods as short as 5.4 days [98]. Thus Kepler-63 is likely younger than 650 Myr, the approximate age of these clusters. [185] presented a convenient polynomial relationship between stellar mass, age, and rotation period; using this relationship we find for Kepler-63 an age of 210 ± 35 Myr. We also used the polynomial relationship given by [12] and

updated by [134]; applying this relationship with $B - V = 0.7$ for Kepler-63 gives an age of 210 ± 45 Myr.

Independent evidence for youth comes from a high observed level of chromospheric emission. The Mt. Wilson $S_{\rm HK}$ index, obtained from the Keck spectra, has an average value of 0.37, from which we estimate a chromospheric flux ratio $\log R'_{\rm HK} = -4.39$. Using the correlation between chromospheric emission and rotation period presented by [143], and an estimated $B - V = 0.7$ for this star, one would expect the star's rotation period to be 6.8 days, in good agreement with our photometrically-derived period. The relationship presented by [124] between $\log R'_{\rm HK}$ and stellar age gives in this case an age of 280 Myr.

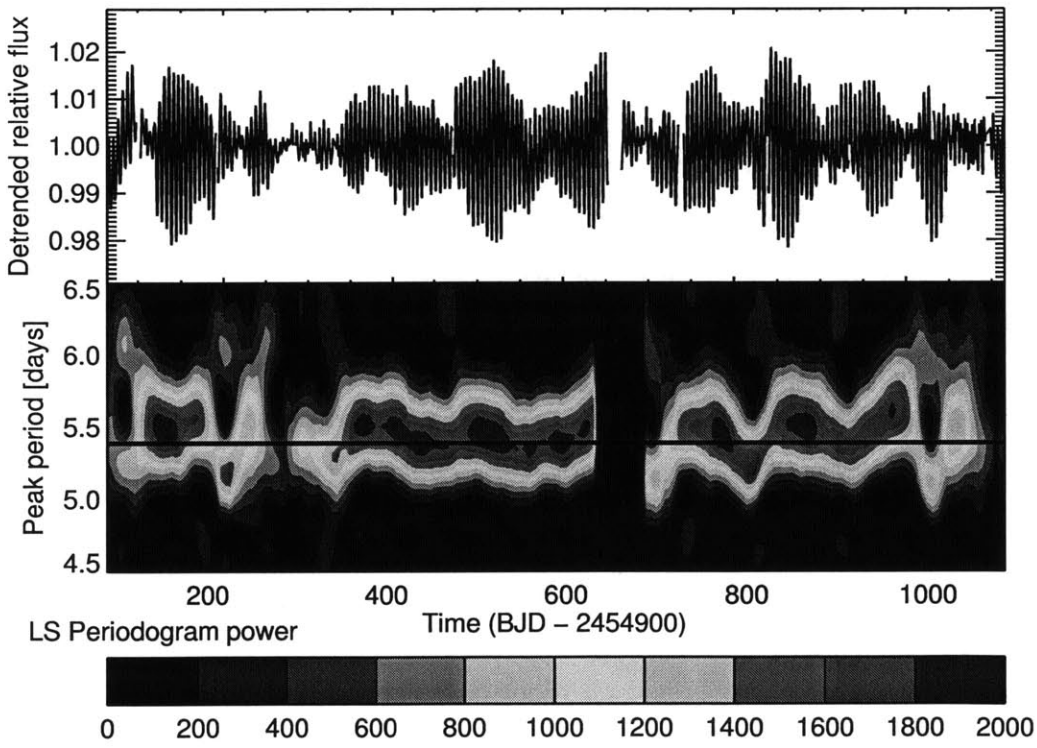

Figure 5-1: Determination of the stellar rotation period from *Kepler* photometry. *Top.*—The time series used to estimate the rotation period, after removing the transit signals. The short-term variability is presumably from spots being carried by the stellar rotation. The longer-term variations may be caused by spot evolution. *Bottom.*—Running periodogram. Red colors represent high power, and the black line is where $P_{\rm rot}/P_{\rm orb} = 4/7$.

5.3.2 Stellar dimensions

At first we determined the star's spectroscopic parameters by applying the spectral synthesis code Spectroscopy Made Easy (SME; [217]) to the Keck spectrum. The results were $T_{\rm eff} = 5698 \pm 44$ K, [Fe/H] $= +0.26 \pm 0.04$, $v \sin i_\star = 5.8 \pm 0.5$ km s^{-1}, and $\log g = 4.64 \pm 0.06$. We then recognized that this value of $\log g$ is anomalously high for a young Sun-like star, which was otherwise suggested by the star's effective temperature and relatively short rotation period. One would instead expect $\log g$ to be closer to the Solar value of 4.44. In fact, by consulting the Yonsei-Yale (Y^2) stellar evolution models [234] we found that the SME-based value of $\log g$ would place the star in a very unusual location on the theoretical H-R diagram, at a higher gravity than any of the isochrones for the nominal metallicity. This mismatch probably reflects the well-known biases in spectroscopic determinations of $\log g$ (see, e.g., [211]).

To address this issue we used an updated version of the Stellar Parameter Classification code [30] which determines the spectroscopic parameters subject to a prior constraint on the surface gravity. In this implementation, SPC is used to provide an initial guess at the effective temperature and metallicity for the star and select the Y^2 evolutionary models which are compatible with this initial guess within fairly wide intervals ($\pm$250 K in $T_{\rm eff}$, $\pm$0.3 dex in [m/H][1]). The selected evolutionary models then provide an interval of allowed surface gravities, which are used to construct a prior on the surface gravity for a second iteration of SPC. The final results, based on weighted averages of the results for all of the spectra (3 FIES, 2 TRES, and one HIRES), are: $T_{\rm eff} = 5576 \pm 50$ K, [m/H] $= 0.05 \pm 0.08$, $\log g = 4.52 \pm 0.10$, and $v \sin i_\star = 5.4 \pm 0.5$ km s^{-1}.

Finally, we used the Y^2 models to determine the stellar dimensions, based not only on the spectroscopic parameters but also the rotation-based constraint on the stellar age (see section 5.3.1). A comparison of our spectroscopic parameters with the Y^2 models for ages between 100 and 600 Myr suggests a surface gravity of $\log g =$

[1]Throughout this paper the generic metallicity index [m/H] computed with SPC in the Mg I b region will be considered as equivalent to the more commonly used [Fe/H] index, as is usually the case for stars with near-solar composition.

4.52 ± 0.02. Using the initial spectroscopic parameters, but with the smaller 0.02 dex uncertainty on $\log g$, we then used the Y^2 models to determine the stellar mass ($M_\star$), radius ($R_\star$), and mean density ($\rho_\star$). We proceeded in a Monte Carlo fashion, randomly drawing 100,000 sets of temperature, metallicity, and surface gravity values from assumed Gaussian distributions of those quantities based on the above results, and inferring the stellar properties for each set. Our final results were obtained from the mode of the corresponding posterior distributions, and the ("1-σ") uncertainties from the 15.85% and 84.15% percentiles of the cumulative distributions. These values are reported in Table 5.2. Based on the absolute and apparent magnitudes, the distance to the system is 200 ± 15 pc.

5.4 Planet characterization

5.4.1 Constraints on blend scenarios

The speckle image of Kepler-63 (see section 5.2.3) puts tight constraints on any background star that could be responsible for the transit signal. We also used the PSF-fitted image centroids provided with the *Kepler* data to further restrict the possibilities for background blend scenarios ([16], [28]). Using a similar approach as [37], we selected the long-cadence column and row centroids within a 2 hr interval centered on each transit, and used the surrounding three hours of data before and after the transits to correct for linear trends caused by pointing drifts and other instrumental effects. We phase-folded the centroid data and computed the mean differences between the row and column values inside and outside of the transits. The centroid shifts were 12 ± 11 μpix in the column direction and 28 ± 14 μpix in the row direction.

If the source of the transits were a background star situated at a distance Δx from Kepler-63, the expected centroid shift would be approximately $dx = (\Delta x)\,\delta$, where δ is the transit depth. Adding both the row and column shift in quadrature, we obtain $dx = 30 \pm 18$ μpix, or $dx < 84$ μpix (3σ). The radius of confusion r, defined as the maximum angular separation of any hypothetical background source that could

be responsible for the transit signal, can be obtained dividing by the transit depth and multiplying by 4 arcsec pix^{-1}, giving $r = 0.084$ arcsec. The more sophisticated techniques described by [28] indicate that the source of photometric variability is offset from the bright target star by 0.02 ± 0.02 arcsec (based on the Data Validation Reports provided by the *Kepler* team). These results are compatible with Kepler-63 as the origin of the flux variations, and require any hypothetical background source of the variations to be aligned with Kepler-63 to within a small fraction of an arcsecond, an unlikely coincidence.

This type of analysis cannot exclude the possibility that the transit signal is caused by a planet orbiting a companion star that is gravitationally bound to the intended target star. However, the starspot anomalies that are detected in many transits show that the planet is orbiting a heavily spotted star. This star must be the main source of light in the aperture, because the 4% flux variations observed would be unphysically large if they actually represented the diluted variations of a fainter star. This possibility is also excluded by the good agreement between the temperature of the occulted spots and the size of the flux variations observed (see section 5.7). We conclude that the transit-like signals do indeed arise from transits of a planet around the star Kepler-63.

5.4.2 Transit analysis

To obtain accurate transit parameters we needed to correct for the effects induced by starspots (see, e.g., [45], [36], [174]). We chose to work only with the short-cadence data, since the 30-minute time sampling of long-cadence data is too coarse to allow a clear identification of the spot-crossing events. We defined the transit window as an interval of 4 hr centered on the expected transit time. The out-of-transit (OOT) portion was defined as the 2 hr preceding the transit window plus the 2 hr following the transit window, giving a total of 4 hr of data. First, the data from each transit window were normalized such that the OOT data had a median flux of unity. Figure 5-2 shows an illustrative example. We visually inspected the 96 transit light curves and identified 145 spot-crossing events. All of them were temporary

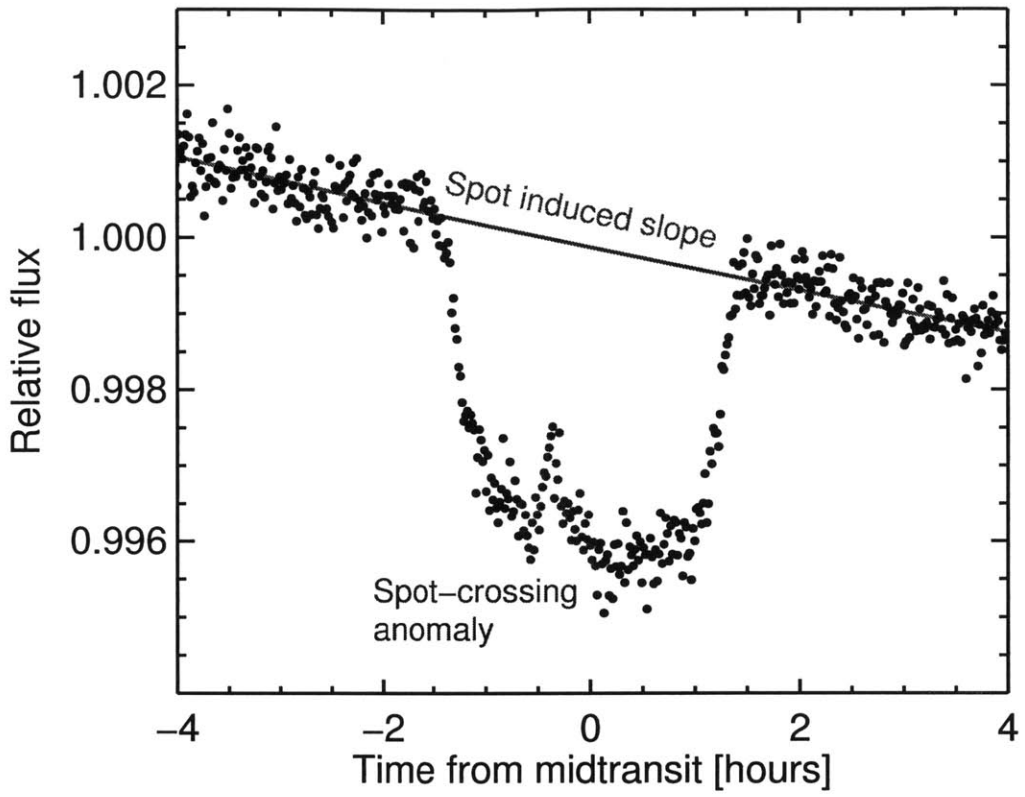

Figure 5-2: Example of the effects of starspots on transit signals.

The black dots are *Kepler* data points for a particular transit. Spot-crossing anomalies (blue dots) are identified visually and masked out. Variability on the longer timescale is modeled as a second-order polynomial (red line).

brightenings (rather than fadings), implying that the detectable spots on the surface of Kepler-63 have a temperature lower than the photosphere. This is in accordance with a general trend observed for very active stars [67]. In order to properly estimate the transit parameters, the data points within these anomalies were assigned zero weight in the fits. More than 25% of the in-transit data points were assigned zero weight, which speaks to the high level of activity on the particular region that the planet is transiting.

Figure 5-2 also shows the effect of the longer-term variations in stellar flux. Large starspots combined with the short rotation period introduce strong gradients in the out-of-transit flux, and occasionally significant curvature, especially if the transit

happens near a flux minimum or maximum. As long as we have removed the spot-anomalies correctly, the observed flux can be described as [36]

$$F(t) = F_0 \left[1 - \epsilon(t)\right] - \Delta F(t) \tag{5.1}$$

where F_0 is the stellar flux in the absence of transits or spots, $\epsilon(t)$ is the fractional loss of light due to starspots, and $\Delta F(t)$ is the flux blocked by the planet. The function $\epsilon(t)$ is responsible for the overall gradient in time throughout the transit (see the red line in Figure 5-2). To obtain the normalized flux we divide Eqn. (5.1) by $F_0[1-\epsilon(t)]$. We then model the OOT variation by a second-order polynomial in time, giving

$$f(t) \approx 1 + c_0 + c_1(t - t_c) + c_2(t - t_c)^2 - \frac{1}{1 - \epsilon(t_c)} \frac{\Delta F(t)}{F_0}, \tag{5.2}$$

where the out-of-transit variation is described by a second-order polynomial in time, and $\epsilon(t_c)$ represents the relative flux lost due to spots at the time of transit t_c. To determine the coefficients c_i, we fitted a second-order polynomial to the OOT portion of the data. We then subtracted the best-fitting polynomial from the data in the entire transit window, to "rectify" the data. The loss of light due to the planet, $\Delta F(t)/F_0$, was assumed to be the same for all transits, but each transit was assigned an independent value of $\epsilon(t_c)$. To avoid having to fit all the data with hundreds of parameters, we performed the transit modeling in four stages, described below.

Step 1. Initial folded light curve analysis.

First we needed good initial guesses for the transit parameters. We created a phase-folded light curve based on the normalized transits, using the orbital period from [15]. We averaged the phase-folded light curve into 4 min bins, chosen to improve computation speed without a significant loss of accuracy. At this stage we ignored the transit-to-transit variations and simply modeled the folded light curve with an idealized [125] model, the free parameters being $(R_p/R_s)^2$, R_s/a, the impact parameter b, and two linear combinations of the quadratic limb-darkening coefficients (chosen to

minimize correlations as recommended by [150].

Step 2. Individual transit analysis.

Next we wanted to obtain individual transit times and depths. The 5 parameters of the best-fitting model from step 1 were held fixed, and the data from each transit window were fitted with three additional parameters: the time of transit t_c, the linear coefficient c_1 from Eqn. (5.2), and the spot-coverage factor $\epsilon(t_c)$ (which for brevity we hereafter denote simply ϵ). The linear coefficient c_1 was allowed to vary because it is covariant with the transit time. We assigned an uncertainty of 279 ppm to each individual SC data point, as this is the standard deviation of the OOT portion of the unbinned folded light curve. We found the best-fitting model for each individual transit light curve and used a Markov Chain Monte Carlo (MCMC) algorithm to explore the allowed parameter space.

We fitted a linear function of epoch to the transit times and used it to estimate the orbital period and a particular transit time (chosen to be the first transit observed with short cadence). Figure 5-3 shows the residuals between the observed and calculated transit times. There is no clear structure, but the fit has $\chi^2 = 202$ with 94 degrees of freedom, suggesting that the uncertainties on the transit times have been underestimated. We attribute this excess scatter to uncorrected effects of stellar spots (see, e.g., [179], [148]), although transit-timing variations could also be present due to another planet orbiting the same star ([1], [90], [142]). To account for the excess scatter we enlarged the uncertainties in the orbital period and the transit epoch by 46% (such that $\chi^2 = N_{\rm dof}$).

In our procedure each transit is associated with a particular value of ϵ, but it is a more common practice to report an effective depth for each transit. The transit depth obtained in this way would be equivalent to the transit depth fixed in step 1, shared by all transits, divided by $1 - \epsilon$. In the lower panel of Figure 5-3, we plot this effective depth for each transit. The variability of the apparent transit depths is as high as 10%. There is no clear correlation of the apparent depths with the *Kepler* quarter, implying that contamination from background stars, if present, must be very

small or common to all the photometric apertures used in the different quarters. The observed variability is most likely induced by starspots.

Step 3. Choice of the baseline transit depth.

In order to obtain the final transit parameters, we readjusted the scale by which ϵ is measured, thereby renormalizing the transits. The distribution of spot coverage factors (ϵ) had a mean near zero and standard deviation close to 3%. This choice would make sense if the effects of dark starspots and bright plages were comparable on average. However, we did not detect any plage-crossing events whereas we did detect many spot-crossing events. Assuming that dark starspots dominate the stellar flux variations, the true loss of light should always be positive, and the shallowest effective transit depth should occur when the star has the smallest spot coverage. For that particular transit the true $\epsilon \approx 0$ and the rest of spot coverage factors are positive ([36], [174]).

A simple approach would be to identify the transit with the smallest value of ϵ, and subtract that value from the entire distribution of ϵ values. We chose instead a more robust method that does not depend entirely on a single ϵ value. First we removed outliers from the distribution of ϵ factors using a 3σ clipping algorithm. Then we assumed that the distribution is Gaussian and computed the standard deviation of the remaining ϵ factors. Finally we shifted the distribution of ϵ values to force the median of the distribution to be two standard deviations above zero. This procedure ensures that most of the ϵ factors are positive.

Step 4. Final transit parameters.

To obtain the final transit parameters, we used the ϵ values determined in step 3 to renormalize each transit light curve. The intention was to correct all of the transit signals to have a uniform shape, similar to what one would observe if the planet were transiting a spot-free star. The transit data were then folded using the newly calculated linear ephemeris, binned to have a time sampling of one minute, and modeled with the same five-parameter transit model used in step 1. Table 5.2 gives

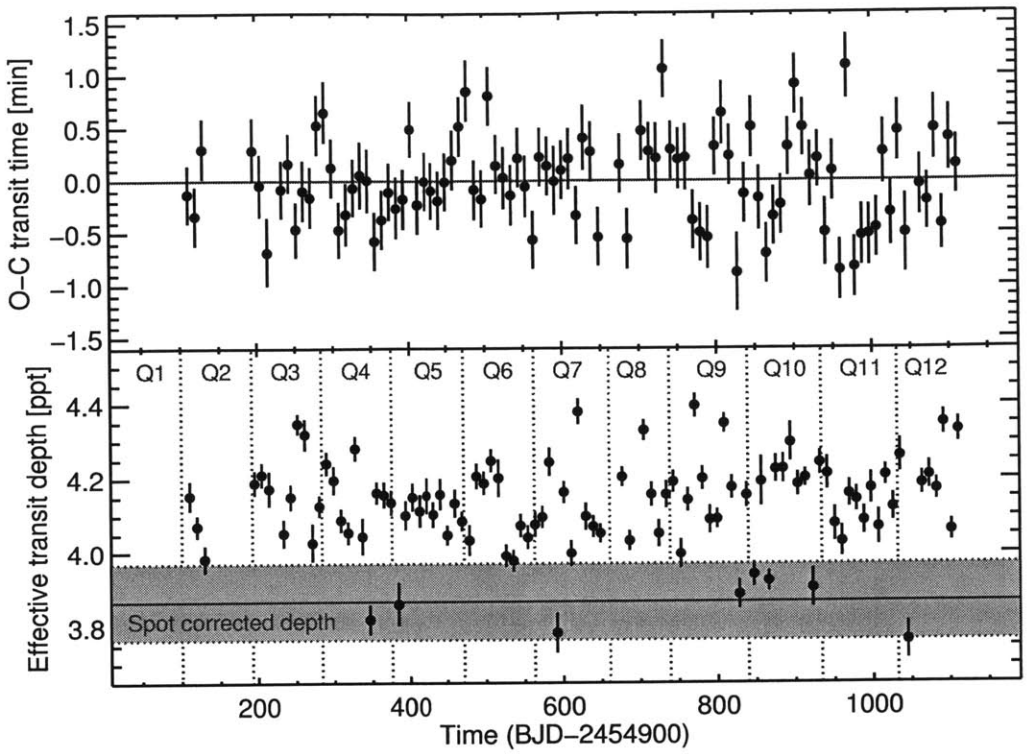

Figure 5-3: Variations in transit times and apparent depths.

Top.—Residuals of a linear fit to the transit times of Kepler-63b. The excess of scatter is significant ($\chi^2 = 202$ with 94 degrees of freedom) and is likely due to uncorrected spot-crossing events. *Bottom.*—The black dots represent the effective depth of individual transits in parts per thousand (ppt). No strong correlation with the quarter is observed, suggesting that the variability is mostly due to starspots as opposed to variable amounts of blended flux. The final adopted value for the transit depth (red line) and its 1σ confidence interval (shaded region) were obtained by assuming that the star is nearly spot-free during the transits with the smallest effective depth (see section 5.4.2).

the final parameter values, with uncertainties estimated using an MCMC algorithm. The uncertainty in the transit depth was enlarged beyond the statistical uncertainty, to take into account the procedure we have described in step 3. We used the width of the distribution of measured depths as the measure of systematic uncertainty in the transit depth. The final value of the depth with the enlarged uncertainty is depicted in Figure 5-3.

5.4.3 Orbital eccentricity

The orbital period of Kepler-63b is long enough that it is not safe to assume the orbital eccentricity has been damped by tides to a negligible level. We attempted to learn the orbital eccentricity in two different ways: by searching for occultations (secondary eclipses); and by using the mathematical relationship between the transit parameters, the mean stellar density, and the orbital eccentricity and argument of pericenter.

If the orbit were circular, occultations would occur halfway in between transits, with a duration equal to that of the transits. For an eccentric orbit, the timing and duration of the secondary eclipse depend on the eccentricity e and the argument of periastron ω (see, e.g., [225]). A grid search was performed to detect the occultation, but the result was negative. This is not surprising, since the occultation depth would be of order $(R_p/a)^2 = 10$ ppm, below our level of detectability.

One can also obtain information about the eccentricity of the orbit by combining the orbital period, scaled semimajor axis, and mean stellar density $\rho_\star$ (see, e.g., [47]). We compute

$$\frac{1 + e\sin\omega}{\sqrt{1-e^2}} \approx \frac{2\sqrt{R_p/R_\star}}{\sqrt{T_{14}^2 - T_{23}^2}} \left(\frac{3P}{G\pi^2\rho_\star}\right)^{1/3} = 0.92 \pm 0.02, \tag{5.3}$$

where T_{14} is the duration between first and fourth contact, and T_{23} is the duration between second and third contact. This expression is close to unity when the eccentricity is low. Based on the measured values of T_{14}, T_{23}, P, and $R_p/R_\star$, and the estimated value of $\rho_\star$ from section 5.3.2 we find $e < 0.45$ (3σ). The formal 68.3% confidence interval is 0.08–0.27. Thus the eccentricity is not likely to be very high, but moderate values cannot be excluded.

5.4.4 Radial velocity analysis

For the radial-velocity analysis, we used the 7 Keck radial velocities obtained before the transit night. We also took the mean of all the pre-transit radial velocities from

Table 5.2. System Parameters of Kepler-63

Parameter	Value	68.3% Conf. Limits	Note
KIC number / KOI number	11554435 / 63		
Kepler apparent magnitude	11.582		
Right ascension (J2000)	$19^h16^m54^s.28$		
Declination (J2000)	$+49°32'53''.52$		
Stellar surface gravity, $\log(g$ [cm s^{-2}])	4.52	±0.02	a
Stellar effective temperature, $T_{\rm eff}$ [K]	5576	±50	b
Stellar metallicity [Fe/H]	0.05	±0.08	b
Stellar mass, $M_\star$ [$M_\odot$]	0.984	-0.04, $+0.035$	b
Stellar radius, $R_\star$ [$R_\odot$]	0.901	-0.022, $+0.027$	b
Stellar mean density, $\rho_\star$ [$\rho_\odot$]	1.345	-0.083, $+0.089$	b
Stellar luminosity, $L_\star$ [$L_\odot$]	0.696	-0.059, $+0.076$	b
Stellar rotation period [days]	5.401	±0.014	c
Mt. Wilson chromospheric index $S_{\rm HK}$	0.37		d
Chromospheric flux ratio $\log R'_{\rm HK}$	-4.39		d
Distance from Earth [pc]	200	±15	b
Reference epoch [$\rm BJD_{TDB}$]	2455010.84307	±0.00005	e
Orbital period [days]	9.4341505	±0.0000010	e
Planet-to-star radius ratio, $R_{\rm p}/R_\star$	0.0622	±0.0010	e
Transit impact parameter, b	0.732	±0.003	e
Scaled semimajor axis, $a/R_\star$	19.12	±0.08	e
Transit duration (1st to 4th contact) [hr]	2.903	±0.003	e
Transit duration (1.5 to 3.5) [hr]	2.557	±0.004	e
Transit ingress or egress duration [hr]	0.346	±0.004	e
Linear limb-darkening coefficient, u_1	0.31	±0.04	e
Quadratic limb-darkening coefficient, u_2	0.354	-0.05, $+0.07$	e
Orbital inclination, i [deg]	87.806	-0.019, $+0.018$	e
Orbital eccentricity, e	<0.45 (3σ)		f
Orbital semimajor axis [AU]	0.080	±0.002	b,e
Planet radius, R_p [$R_\oplus$]	6.11	±0.20	b,e
Planet mass, M_p [$M_\oplus$]	<120 (3σ)		b,g
Planet mean density, ρ_p [g cm^{-3}]	<3.0 (3σ)		b,e,g
Sky-projected stellar obliquity, λ [deg]	-110	-14, $+22$	h
Sky-projected stellar rotation velocity, $v \sin i_\star$ [km s^{-1}]	5.6	±0.8	h
Inclination of stellar rotation axis [deg]	138	±7	i
Stellar obliquity, ψ [deg]	145	-14, $+9$	j

Note. — Each quoted result represents the median of the *a posteriori* probability distribution derived from the MCMC, marginalized over all other parameters. The confidence limits enclose 68.3% of the probability, and are based on the 15.85% and 84.15% levels of the cumulative probability distribution.

[a]Based on the SPC analysis of the spectra and the Y^2 models, using the gyrochronology age as a constraint (see section 5.3).

[b]Based on the SPC analysis of the spectra and the Y^2 models (see section 5.3). The stellar density is given in units of $\rho_\odot = 1.408$ g cm^{-3}.

[c]Based on the periodogram of the *Kepler* photometric time series (see section 5.3.1).

[d]Based on the Keck/HIRES spectrum (see section 5.3.1).

[e]Based on the analysis of the transit light curves (see section 5.4.2).

[f]Based on the combination of transit parameters, orbital period, and mean stellar density (see section 5.4.3).

[g]Based on the analysis of the Keck radial velocities, assuming zero eccentricity (see section 5.4.4).

[h]Based on the analysis on the RM effect (see section 5.5).

[i]Based on the combination of $P_{\rm rot}$, $R_\star$, and $v \sin i_\star$ (see section 5.6.1).

[j]Based on the analysis of the RM effect and starspot-crossing events (see section 5.6.2).

the night of 2011 August 20/21, and treated this mean velocity as a single additional data point. A planet somewhat smaller than Jupiter in a 10-day orbit should induce a radial velocity signal with a semiamplitude of order tens of m s^{-1}. For a chromospherically quiet star, eight radial velocities with a precision of a few m s^{-1} would have been enough to determine the mass of the planet. However, in the case of Kepler-63, we expect spurious radial velocities of order tens of m s^{-1}, the product of $v \sin i_\star$ and the fractional photometric variability. This greatly complicates the mass determination.

The top panel of Figure 5-4 shows that the stellar flux variations during the radial velocity observations were approximately sinusoidal. The simplest explanation is that a single large dark spot was always on the visible side of the star. In such configurations, it is possible to estimate the spurious radial velocity $V_{\rm spot}$ due to starspots using the so-called FF' method of [2]. Those authors showed that the spurious radial velocity can be approximated by a function of the normalized stellar flux $f(t)$ and its derivative,

$$V_{\rm spot}(\epsilon, \kappa\delta V_c) = \dot{f}(t)\,[1 - f(t)]\,\frac{R_\star}{\epsilon} + [1 - f(t)]^2\,\frac{\kappa\delta V_c}{\epsilon}, \tag{5.4}$$

where the normalization is such that the $f(t) = 1$ level is one standard deviation above the maximum observed flux. There are two free parameters: ϵ is the relative loss of light due to the spot if it were situated at the center of the stellar disk; and $\kappa\delta V_c$ specifies the alteration of the convective blueshift due the spot. With this ingredient, our model for the radial velocity signal was

$$V_{\rm calc} = -K \sin\left[n(t - t_c)\right] - V_{\rm spot}(\epsilon, \kappa\delta V_c) + \gamma. \tag{5.5}$$

In this formula we have assumed a circular orbit for the planet, with K being the planet-induced radial velocity semiamplitude, and t_c the time of transit. The parameter γ represents a constant offset. The mean motion n is defined as $2\pi/P_{\rm orb}$. Both $P_{\rm orb}$ and t_c are known precisely from the transit analysis.

We optimized the model parameters through a standard least-squares fit. Figure

5-4 displays the data and the optimized model. Given the typical measurement uncertainty of 2.5 m s^{-1}, the minimum χ^2 was 78.6 with 4 degrees of freedom. This poor fit is at least partly due to the simplicity of the spot model (which assumes that there is only one small spot on the surface). By adding a "jitter" term of 12.5 m s^{-1} in quadrature to the measurement uncertainties we obtain $\chi^2 = N_{\rm dof}$. We use this jitter term and an MCMC algorithm to determine credible intervals for the model parameters, from which we derive a planet mass of $M_p = 45 \pm 26\ M_\oplus$. The 3σ upper bound is 120 $M_\oplus$.

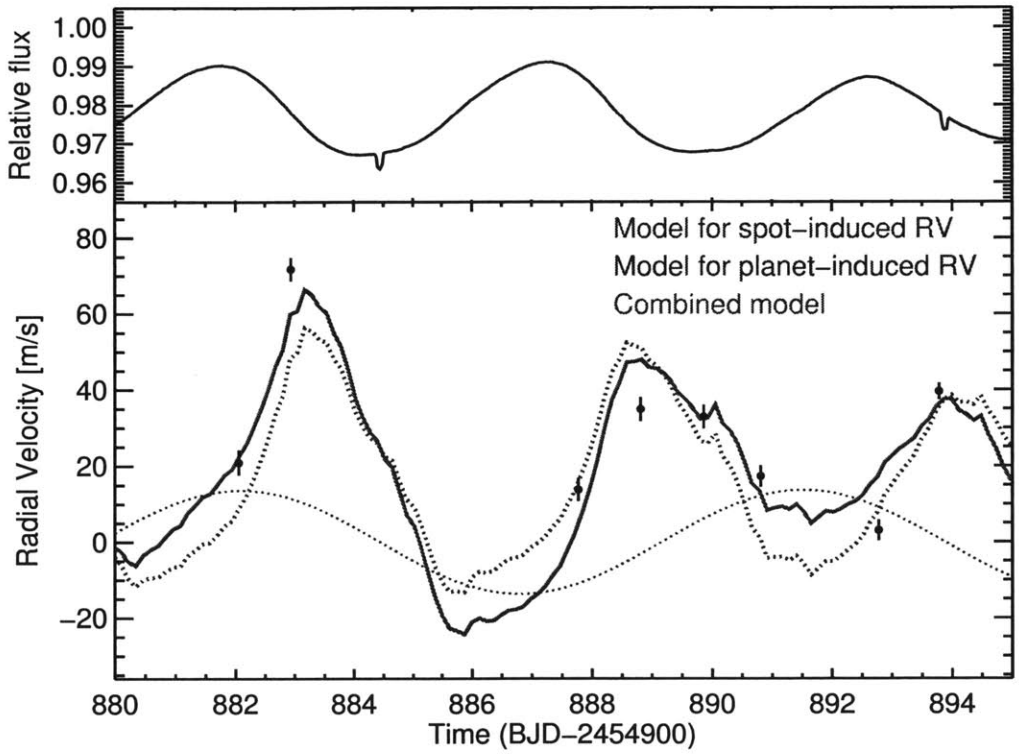

Figure 5-4: Radial-velocity analysis.

Top.—Relative stellar flux of Kepler-63 during the radial velocity observations. *Bottom.*—The black dots represent the radial velocity observations, with vertical bars indicating the internally estimated measurement uncertainties (with no "jitter" term added). The red line represents the optimized model, which is the sum of a sinusoidal function representing the planetary signal (blue line) and the FF' model representing the spurious radial velocity due to rotating starspots (brown line).

Given the severe limitations of this analysis—the weak detection, the imperfect fit of the FF' model, and the assumption of zero eccentricity—we do not claim to have

detected the radial-velocity signal due to the planet. Rather, we interpret the results as a coarse upper bound on the mass of the transiting object, placing it within the planetary regime.

5.5 Sky-projected obliquity from the RM effect

The RM effect is more easily detected than the orbital motion, mainly because the timescale of the RM effect is much shorter than the rotation period of the star, allowing a clean separation between the RM effect and the spurious starspot-induced radial velocities (see, e.g., [71]). Prior to the Keck observations we had performed enough spot modeling to be able to predict that the anomalous Doppler shift would be a pure redshift throughout the transit. The results of the RM observations, displayed in Figure 5-5, confirmed this prediction. However, the *Kepler* photometry of the same transit (shown in the bottom panel of Figure 5-5) revealed at least three spot-crossing events, complicating the modeling.

To model the RM effect, one needs the usual parameters describing the loss of light as well as 4 additional parameters: $v \sin i_\star$ and λ to describe the amplitude and shape of the signal, and a slope $\dot{\gamma}$ and offset γ to account for the orbital motion of the star. Usually the loss of light is computed based on the transit parameters b, R_s/a, $R_p/R_\star$ and the time of transit. Here, given the presence of spot-crossing anomalies, we chose to take the loss of light directly from the *Kepler* photometric time series, since this naturally takes the anomalies into account, and the cadence and precision are more than sufficient for our purpose. To obtain the loss of light corresponding to each point in the RV time series, we averaged the corresponding *Kepler* photometric data points. The final averaged light curve is shown in the lower panel of Figure 5-5 as the sequence of red dots.

The anomalous RV was then computed with the formulas of [88], using the planet position and loss of light as inputs. This code takes into account the effects of macro-turbulence, pressure broadening, and instrumental broadening. Model fitting and parameter estimation were performed using the protocols of [5]. In particular we

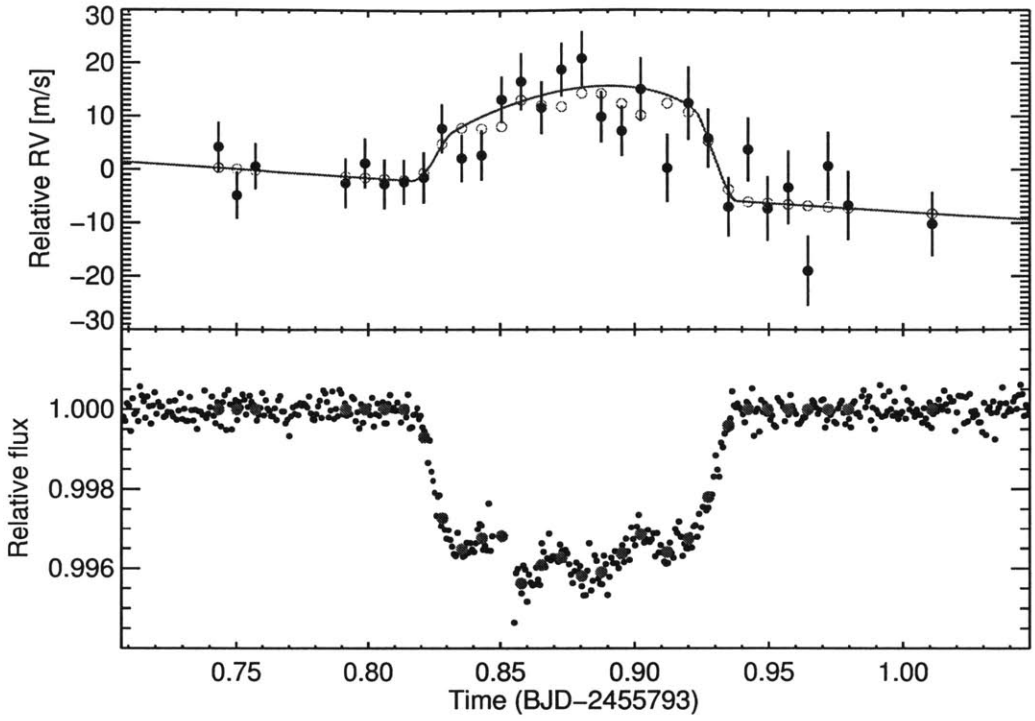

Figure 5-5: Evidence for a high obliquity based on the RM effect.

Top.—The solid dots are the measured radial velocities. The signal is a redshift throughout the transit, applying a high obliquity, as opposed to the red-then-blue signal of a low-obliquity system. The open dots represent the best-fitting model. The red curve shows a model with the same geometric parameters but with the loss of light appropriate for a spotless star, to illustrate what one might have observed in the absence of starspots. *Bottom.*—Transit observations in SC mode obtained with *Kepler*. Black dots represent the data and red dots represent the binned light curve used to model the RM effect.

imposed Gaussian priors on T_{14} and T_{12}, based on the parameters reported in Table 5.2. We also used the parameter combinations $\sqrt{v \sin i_\star} \sin \lambda$ and $\sqrt{v \sin i_\star} \cos \lambda$ rather than $v \sin i_\star$ and λ, to minimize correlations. The uncertainty in each RV data point was taken to be the quadrature sum of the internally estimated uncertainty and 4.8 m s^{-1}, the value for which $\chi^2 = N_{\rm dof}$. The result for the sky-projected obliquity is $\lambda = -110^{+22}_{-14}$ deg.

There are some other interesting results of this analysis. We find the projected rotation speed to be $v \sin i_\star = 5.6 \pm 0.8$ km s^{-1}, in agreement with the value obtained from the basic spectroscopic analysis (see section 5.3.2). The result for the out-of-

transit velocity slope $\dot{\gamma} = -30 \pm 15$ m s^{-1} day^{-1} can be translated into an estimate of the velocity semiamplitude due to the planet, using the orbital period and assuming a circular orbit. The result is $K_{\rm RM} = -\dot{\gamma} P_{\rm orb}/2\pi = 40 \pm 20$ m s^{-1}. This slope is compatible within the uncertainties with the measured K from the RV analysis (approximately 15 m s^{-1}), although the uncertainties are large, and the effects of spots were not taken into account in this determination of $K_{\rm RM}$. In this case, by chance, the transit happened about a quarter of a rotation cycle before a flux minimum, which is when the spot-induced spurious acceleration is expected to be small.

5.6 Obliquity measurement from starspots

5.6.1 Stellar inclination from $v \sin i_\star$

We combined the values of the rotation period $P_{\rm rot}$, stellar radius $R_\star$, and sky-projected stellar rotation velocity $v \sin i_\star$, to obtain $\sin i$, the inclination of the stellar rotation axis with respect to the line of sight. Based on the values given in Table 5.2, the stellar rotation velocity is $v = 2\pi R_\star / P_{\rm rot} = 8.4 \pm 0.2$ km s^{-1}. This is significantly larger than $v \sin i_\star = 5.6 \pm 0.8$ km s^{-1} obtained from the analysis of the RM effect, implying $\sin i_\star < 1$. The implied stellar inclination angle is either 42 ± 7 deg or 138 ± 7 deg. As we will see in the next section, the latter value of the stellar inclination is favored. Since Kepler-63b is transiting with an orbital inclination of 87.81 ± 0.02 deg, this simple analysis demonstrates the star has a high obliquity, independently of the RM effect.

We used the marginalized posterior for λ obtained in the last section, as well as those for the stellar and orbital inclinations (Table 5.2), to obtain the true obliquity ψ. Using the formula from [61], the result is $\psi = 104^{+9}_{-14}$ deg.

5.6.2 Sky-projected obliquity from spot-crossing anomalies

In principle the obliquity of the system is also encoded in the pattern of photometric variability and spot-crossing anomalies, but in this case the anomalies are so numer-

ous that the pattern has proven difficult to interpret unambiguously. Rather than attempt a rigorous independent determination of the obliquity, we discuss here a starspot model that at least demonstrates the compatibility between the photometric variability, the starspot-crossing events, and the preceding results for λ and $i_\star$.

We focused attention on a time interval when the overall photometric variability seemed relatively simple: a nearly sinusoidal pattern with peak-to-peak amplitude of about 1.5%. This interval spans four consecutive transits, specifically epochs 71-74 (see Figure 5-6). A large and long-duration spot-crossing anomaly is seen in the first half of the first transit. We proceeded by assuming this is the same spot that is producing the quasi-periodic stellar flux variation, and attempted to model all of the data under this premise.

The orientation of the star was parameterized by the sky-projected obliquity λ and the inclination angle $i_\star$. The rotation period was a free parameter, which was tightly constrained by the quasi-periodic variability. A Gaussian prior constraint was imposed on $v \sin i_\star$ based on the results of section 5.6.1.

We modeled the out-of-transit variability using the [55] equations for the loss of light due to a starspot. We fixed the limb-darkening coefficient to a value of 0.56, which provides the best fit to the light curve constructed in section 5.4.2. The spot's brightness contrast relative to the photosphere was taken to be a constant over the interval of the observations. The observed phase of the out-of-transit variability specifies the spot longitude, and the stellar rotation period is also well constrained. Therefore, given particular choices for the orientation of the star and the spot latitude, we could calculate the location of the spot at any time, including the times of the four transits.

The transits were modeled using the geometric transit parameters from section 5.4.2, and a pixelated stellar disk. At any particular time we computed the sum of the intensities of all the pixels, some of which were darkened by the spot or hidden by the planet [179].

The best-fitting value for λ was $-115°$, in agreement with the result based on the RM effect. The model also prefers $i_\star = 135°$, selecting one of the two values for the

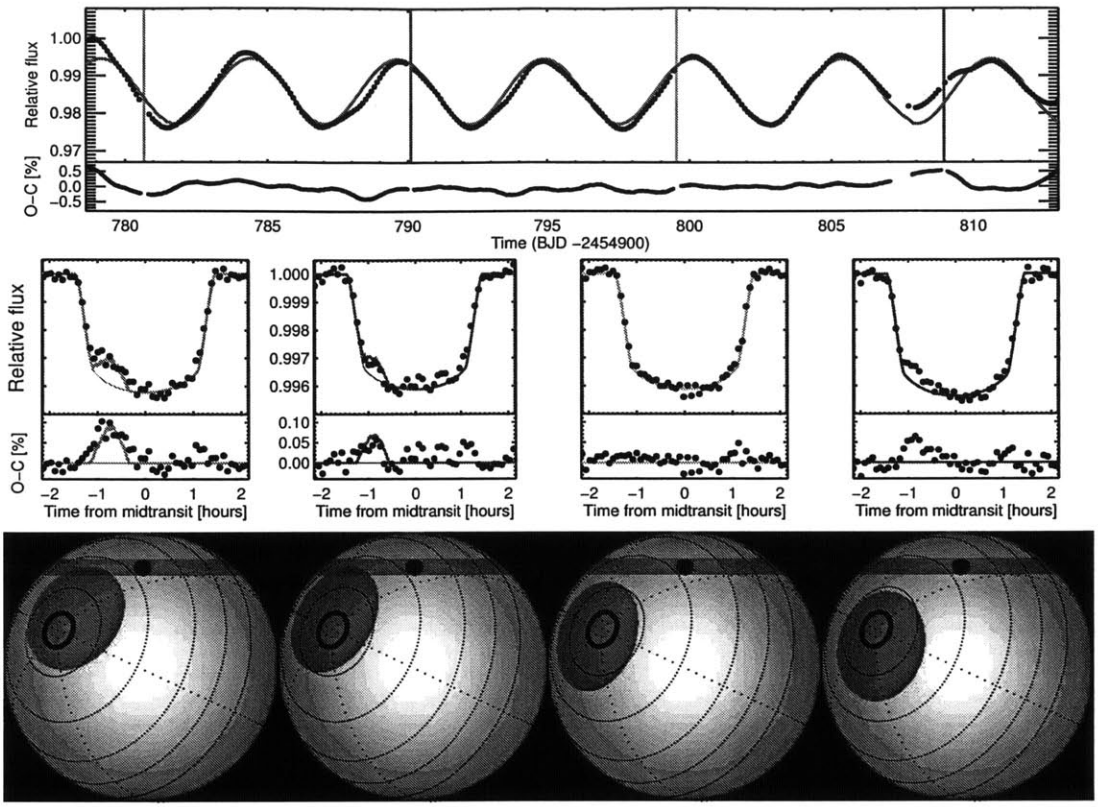

Figure 5-6: Evidence for a large obliquity from a single-spot model.

Top.—Relative flux of Kepler-63 (black dots) over a time range spanning four transits. The transit times are marked with vertical lines. The red line represents the best-fitting model with a single starspot. *Center.*—Transit light curves, with 5 min sampling. The thick curves represent the best-fitting model with a single starspot; the thin curves show the model with the spot darkening set equal to zero. The model accounts for the two largest spot-crossing anomalies but the residuals indicate that more spots are present. *Bottom.*—Locations of the spot, transit chord, and planet at midtransit, according to the best-fitting model.

inclination that were allowed by the analysis in section 5.6.1. This constraint arises from the requirement that the spot must cross the transit chord before its closest approach to the center of the stellar disk. In the optimized model, the spot is large and resides near one of the rotation poles.

The simple one-spot model is therefore compatible with the overall photometric variability and the largest spot anomaly. The smaller spot anomaly during the second transit can also be attributed to this spot, as illustrated in Figure 5-6. Certainly, though, this model does not capture all of the sources of photometric variability:

there are at least six other smaller anomalies that are not well-fitted, and which it does not seem worthwhile to try and model. The large anomaly in the fourth transit agrees in phase with the two other explained anomalies. It is possible that the same spot is responsible for this anomaly, if the spot has an irregular shape.

5.7 Starspot characteristics and magnetic cycles

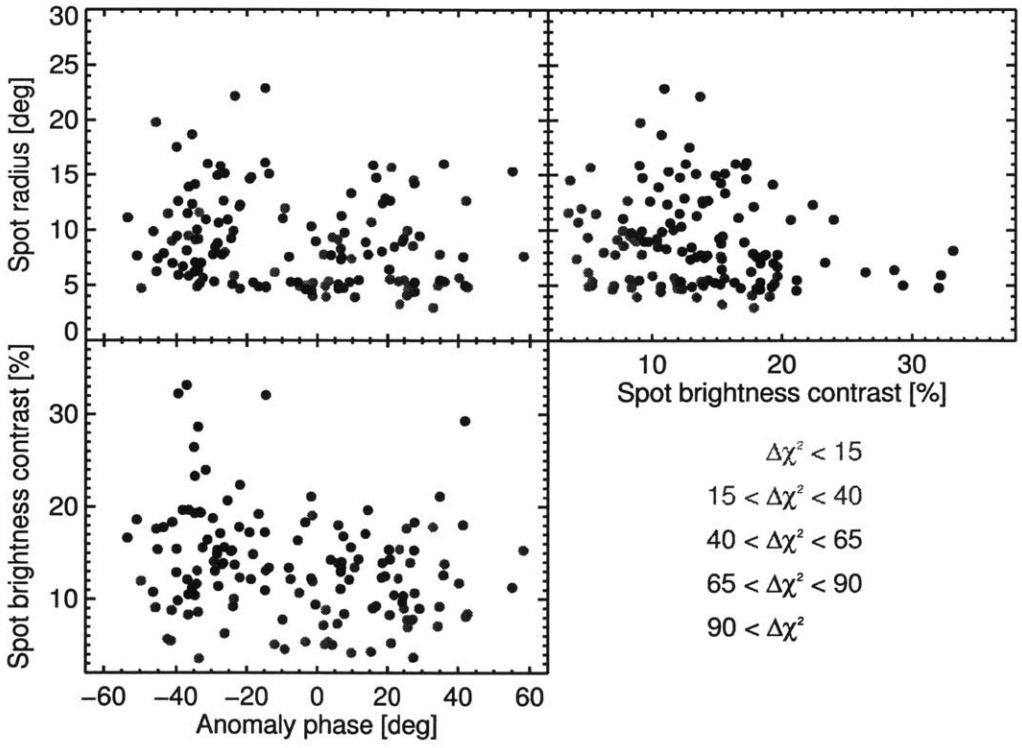

Figure 5-7: Characteristics of the spot-crossing anomalies in Kepler-63b.

The figure shows the best-fitting values of the angular radius, brightness contrast, and phase of the 145 spot-crossing anomalies that were identified. Darker dots represent more significant detections.

As discussed in section 5.4.2, we visually identified 145 spot-crossing anomalies. To study the position, sizes, and temperatures of the spots, we modeled the individual spot-crossing anomalies with the same pixelated spot model discussed in section 5.6.2. The parameters describing each spot-crossing event were the spot's angular radius and brightness contrast, as well as the timing of the event, which we express as an

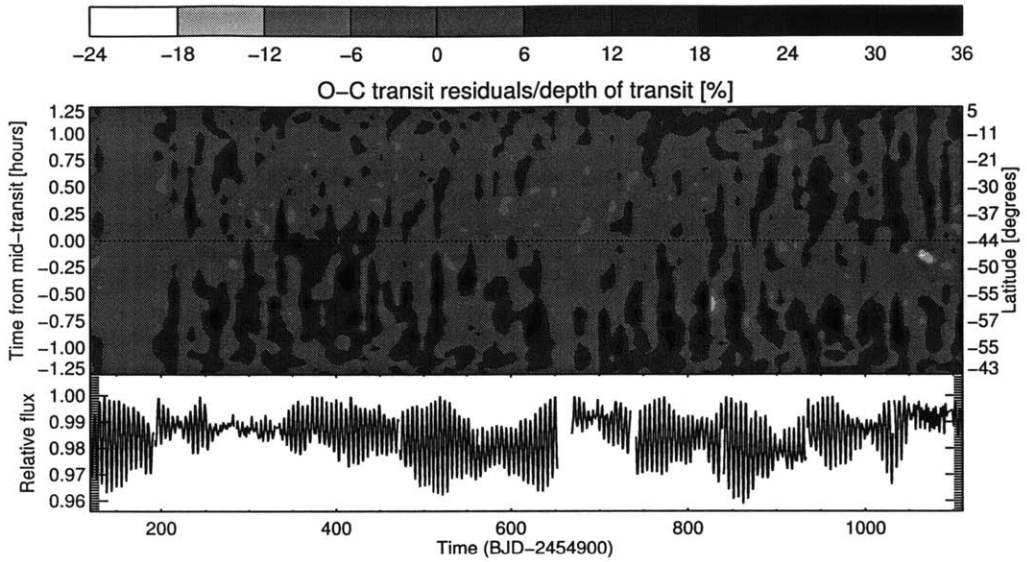

Figure 5-8: Spot latitude evolution.

Top.—Residuals between the SC transit data and the best-fitting model, after dividing by the transit depth. The dark regions represent spot-crossing anomalies. The vertical axes indicate the time relative to the midtransit time (left) and the corresponding latitude of the position of the planet (right). The high-latitude spot is crossed every fourth transit. Some activity is also seen at lower latitudes. *Bottom.*—Relative flux variation over the same time interval. For this plot the data from each *Kepler* quarter were normalized by the maximum quarterly flux.

"anomaly phase" ranging from $-90°$ (ingress) to $90°$ (egress). The other transit parameters, including the spot coverage factor ϵ, were taken from the analysis of section 5.4.2. To evaluate the significance of detection of the anomalies, we used $\Delta\chi^2$ between the best-fitting spot model and the best-fitting spot-free model.

There is a degeneracy between the modeled position and radius of a spot, because we lack the precision to measure the impact parameter between the planet and spot (and there is anyways no reason to think the spot is perfectly circular). To avoid this degeneracy, we assumed that the planet passes through the center of the spot. It should be understood, then, that the "spot radius" in our model is really a measure of the length of the intersection between the spot and the transit chord.

Figure 5-7 shows the results. Unsurprisingly, the significance of detection increases with the size and the brightness contrast of the spots. The anomalies that appear in

the first half of the transit (negative anomaly phase) are generally more significant and more abundant. The typical spot radius is 10°, and the largest spots have a radius of 15–20°. The typical brightness contrast is 15-20%. To produce a 20% brightness contrast in the *Kepler* bandpass (450–850 nm) would require an effective temperature approximately 300 K lower than the photosphere, assuming blackbody spectra.

Figure 5-8 shows the time evolution of the spot-crossing events. To create this figure we subtracted a model for the loss of light due only to the planet, and then divided the residuals by the transit depth. The normalized residuals were then plotted as a function of both time (horizontal axis) and phase within the transit (vertical axis). Given the known orientation of the star, we can also translate the phase within the transit into a stellar latitude (second vertical axis). The transit chord spans latitudes from $-60°$ to 5°, that is, a large portion of the southern hemisphere. Note also that the relation between the transit phase and the stellar latitude is nonlinear; indeed some latitudes cross the transit chord in more than one location.

Spot-crossing events are visible as dark regions in this plot. Most of the activity is seen in the early portions of the transits. This indicates a long-lived polar active region. After the first few years of observations (starting at around day 875) spot-crossing anomalies began to appear in the second half of the transit, corresponding to lower stellar latitudes. Anomalies at mid-transit were comparatively rare, especially once the second half of the transit chord became active. Perhaps this is a sign that active regions tend to be segregated in latitude, with some activity at high polar latitudes and some at more equatorial latitudes.

These initial explorations of the spatial distribution of activity on Kepler-63 could be continued in the future by developing a multi-spot model, fitted to both the stellar flux variations and the spot-crossing anomalies (see, e.g., [20], [147]). Here we have focused mainly on the anomalies, which provide snapshots of the transit chord every 9.4 days; there are undoubtedly some spots that are missed with this approach [117].

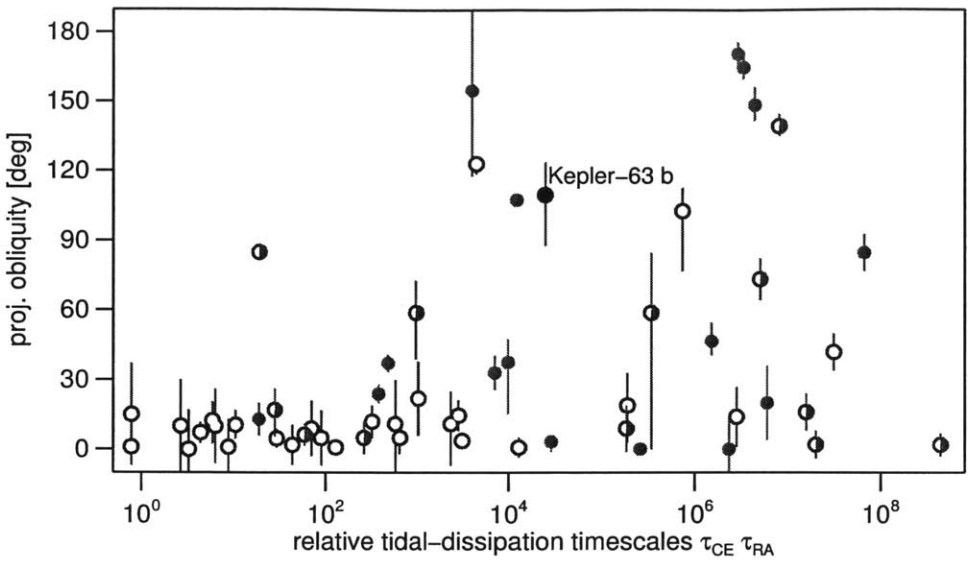

Figure 5-9: Sky-projected obliquities as a function of relative timescale for tidal dissipation.

See [5] for the original figure on which this is based, and for details on its construction. In short, the relative tidal dissipation timescale is assumed to be proportional to $q^2(a/R_\star)^6$ for stars with $T_{\rm eff} < 6250$ K (blue dots) and proportional to $q^2(1+q)^{5/6}(a/R_\star)^{8.5}$ for hotter stars (red dots), where q is the planet-to-star mass ratio. The hot and cool stars are placed on the same scale using an empirical calibration based on observations of binary-star circularization periods. Dots with both colors represent stars for which the measured $T_{\rm eff}$ straddles the boundary. Lower obliquities are seen in systems with relatively rapid tidal dissipation, suggesting that tides are responsible for damping stellar obliquities. Even though Kepler-63 is a cool star which is relatively dissipative, the orbital distance is large enough that tides are relatively weak, and the high stellar obliquity fits well with this observed trend. In addition to Kepler-63 this plot features new and updated values of λ for CoRoT-11b [70], WASP-19b [212], WASP-32b and WASP-38b [25] and HAT-P-17b [69].

5.8 Discussion

In this paper we have presented Kepler-63b, a giant planet transiting a star on an orbit that is highly inclined with respect to the stellar equator. On the one hand the star's high levels of chromospheric activity interfered with our ability to characterize the system through transit light curve analysis and radial-velocity monitoring. On the other hand the *Kepler* data allowed us to partly correct for the effects of activity; and also to take advantage of the activity to determine the stellar rotation period, explore the spatial distribution of starspots, and perform a consistency check on the

stellar obliquity that was determined via the Rossiter-McLaughlin effect.

The measurement of the planet's mass through radial-velocity measurements was unsuccessful because the spurious radial velocities caused by starspots were larger than the planet-induced signal. To measure the mass, a large body of additional radial velocities will be required, in a campaign that is carefully designed to try and separate the effects of rotating starspots and orbital motion. The information about the general spot characteristics presented in this paper may help in designing such a campaign.

The star's high obliquity corroborates the scenario proposed by [226] and [5] in which hot Jupiters have orbital inclinations that are initially nearly random with respect to the stellar equator, and are eventually damped to low inclinations if the tidal interactions between the star and planet are sufficiently strong. In this scenario a high obliquity is expected for Kepler-63, because even though the star is relatively cool and has a thick convective envelope (a factor leading to relatively rapid tidal dissipation), the orbital distance is relatively large. To be quantitative we used the metric developed by [5], in which binary-star data are used to calibrate tidal dissipation timescales. Figure 5-9 shows that the expected timescale for tidal dissipation for this system is in the regime where random alignment is observed among the other close-in giant planets. The fact that the star is young also helps to understand why it has not yet been realigned [213]. This measurement is interesting because among planet-hosting stars with measured obliquities, only HAT-P-11b is comparable to Kepler-63b in size and orbital period, being smaller (4.7 $R_{\oplus}$) than Kepler-63b but also having a shorter orbital period (4.9 days).

A proposed interpretation for these findings is that hot Jupiters begin far away from the star, beyond the snow line, where it is easier to understand their formation. The initial obliquity of the system is low, as a consequence of the formation of the entire system from a single disk of gas and dust. Then, dynamical interactions such as planet-planet scattering [170] or Kozai cycles induced by the influence of a distant companion [58], move the planet into a highly eccentric orbit with a more random orientation. In this highly eccentric orbit, the planet passes very close to the star,

where tidal interactions are significant. This tidal interactions will circularize and shrink the orbit and, if they are strong enough, will realign the spin axis of the star with the orbital angular momentum. In the context of this theory, pursuing obliquity measurements for systems with smaller planets and longer orbital periods is interesting because at a certain point those planets might have been able to form *in situ*, leading to an expectation of a population of well-aligned systems.

[171] have proposed that at least some of the high obliquities might have nothing to do with planet formation *per se* but are instead the consequence of reorientation of stellar photospheres due to the redistribution of angular momentum by internal gravity waves. Their theory is applicable to stars with radiative envelopes, and is therefore not applicable to Kepler-63, nor to the other three cool stars with high obliquities that are seen in Figure 5-9.

In addition to measuring the obliquity of Kepler-63 we have confirmed that the planet is passing in front of a large, dark, persistent spot (or group of spots) located near one of the star's rotation poles. Such spots are not seen on the present-day Sun, where the spot latitudes follow an 11-year cycle in which they start appearing at medium latitudes (30–40°) and end up appearing near the equator (for a review, see [196]). However, there was previous evidence that polar spots are common around young Solar analogs. This was based on simulations of magnetic activity ([24], [188]) as well as empirical evidence from Doppler imaging of young and rapidly rotating stars such as EK Dra [204]. Even though such polar spots were detected in different occasions and with different techniques [205], and multiple tests were performed to validate the technique ([215], [27]), an independent confirmation using a different method was previously lacking. Our study provides further evidence for these types of spots, through a direct method based on periodic occultations of the spots by a planet with a well-understood geometry. The current information gathered about stellar spots on Kepler-63, and future studies that could analyze the information from stellar flux variations, may provide useful information about the activity of young Sun-like stars. It would also be interesting to find additional active stars with transiting planets in the *Kepler* database, as a probe not only of stellar obliquities

but also starspot characteristics and evolution.

We thank the anonymous referee for numerous insightful suggestions that led to major improvements in this paper. We also thank Andrew Collier Cameron, Bryce Croll, and Benjamin Brown for helpful discussions, and the entire Kepler team for the success of the mission. R.S.O. and J.N.W. acknowledge NASA support through the Kepler Participating Scientist program. Kepler was competitively selected as the tenth Discovery mission. Funding for this mission was provided by NASA's Science Mission Directorate. The data presented in this article were obtained from the Mikulski Archive for Space Telescopes (MAST). STScI is operated by the Association of Universities for Research in Astronomy, Inc., under NASA contract NAS5-26555. Support for MAST for non-HST data is provided by the NASA Office of Space Science via grant NNX09AF08G and by other grants and contracts. J.A.C. acknowledges support by NASA through a Hubble Fellowship (grant HF-51267.01-A). RID is supported by the NSF-GRFP (DGE-1144152). J.A.J. is supported by generous grants from the Alfred P. Sloan Foundation and the David and Lucile Packard Foundation. T.L.C., W.J.C., and G.R.D. acknowledge the support of the UK Science and Technology Facilities Council (STFC). Funding for the Stellar Astrophysics Centre is provided by The Danish National Research Foundation (Grant agreement DNRF106). This research was partly supported by the ASTERISK project (ASTERoseismic Investigations with SONG and Kepler) funded by the European Research Council (Grant agreement no. 267864). G.T. acknowledges partial support for this work from NSF grant AST-1007992.

Chapter 6

SCEC: The starspot-crossing events catalog

The last four chapters have shown the potential of using spot-crossing events to measure the obliquity of transiting planet hosts. In this chapter I introduce the starspot-crossing events catalog (SCEC), a list of Kepler systems in which there are good indications that one object (whether is a planet or a star) is occulting the starspots of a chromospherically active host star. I use two different criteria to include objects in the SCEC; 1) the detection of an excess of scatter on the flux observations during transits, likely caused by the spot-crossing events, 2) the detection of spot-crossing events on individual transit light curves. Although it will not be possible to measure the obliquity of all of the objects in the SCEC, I have selected a large number of single transiting planet candidates (43), multi-transiting systems (26) and eclipsing binaries (52) which probably includes all systems for which it might be possible to measure the obliquity, pending future analysis. In this chapter I describe the pipeline used to select systems and describe the characteristics of a few selected objects. In particular, the recurrence of spot-crossing events is used to show that 5 single transiting candidate planets (with orbital periods from 3.8 to 23.7 days) have low obliquities.

The purpose of this catalog is to serve as starting point for any future study of spot-crossing events using Kepler data. It is a much simpler task to start with a

reduced set of interesting objects rather than having to select the best objects from a list of about 4000 planet candidates and 3000 eclipsing binaries. I expect that this catalog will be used by our group at MIT and other researchers to study the effects of stellar activity on the light curves of transiting planets and eclipsing binaries. It is beyond the scope of this chapter to attempt to measure the obliquity of these 121 systems, an enormous task that would likely serve as the basis for several scientific papers.

6.1 Spot-crossing events on the transits of Kepler planet candidates

In the past three chapters we have explored the potential to apply the spot-crossing technique to measure obliquities using Kepler data. The cases of HAT-P-11, Kepler-30 and Kepler-63 have taught us that this technique requires two key ingredients; 1) an active star, for which moderate to large quasiperiodic flux variations due to rotating spots have been detected, and 2) the detection of individual transits with a high enough signal-to-noise ratio to be able to distinguish the small spot-crossing events in the presence of photometric noise.

6.1.1 Selecting objects with well detected individual transits

The Kepler telescope has become a very successful tool for finding planet candidates, with a total of 3,845 planet candidates discovered to date [3], 965 of them confirmed as bona fide planets (a large fraction of those using multiplicity arguments, see [114]). Most of these planet candidates could not have been detected based only on observations of one or two transits, but that it is generally not an important issue, since the success of the Kepler mission always relied on the ability to combine several transits of each object to increase the signal-to-noise ratio and allow the detection of small rocky planets. The detection of these shallow transits is crucial to determine the distribution of orbital periods and planet radii, which provides information about

planet formation and evolution [92]. However, they do not represent a great opportunity for obliquity measurements using spot-crossing events, a technique which generally requires the detection of individual transits with high signal-to-noise ratio.

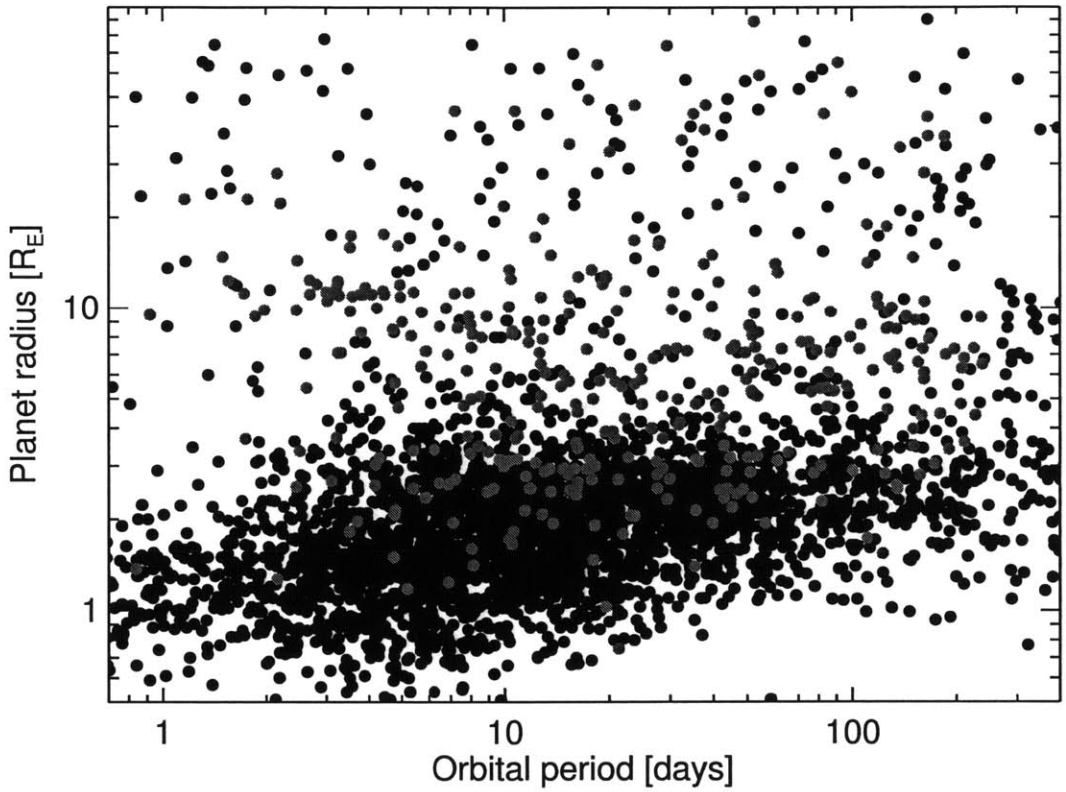

Figure 6-1: Preliminary selection of targets for SCEC based on signal-to-noise ratio. Planet radius vs orbital period for all planet candidates on the active KOI list [3]. Red dots represent planet candidates with at least 5 well detected individual transits (see text) and available transit times [133]. Black dots represent the rest of the candidates. As expected, the selected targets tend to be larger than a typical Kepler candidate.

In order to select those planet candidates where there is potential for a detection of spot-crossing events, we estimate the signal-to-noise ratio (SNR) of individual transits using the combined differential photometric precision (CDPP). The CDPP is a statistic determined by the *Kepler* team's data analysis pipeline that is intended to represent the effective photometric noise level for detecting a transit of duration 6

hours [40]. The SNR can then be estimated as

$$SNR_{\mathrm{CDPP}} \equiv \frac{\delta_{\mathrm{tran}}}{\sigma_{\mathrm{CDPP,6\ hr}}}\sqrt{\frac{T}{6\,\mathrm{hr}}} \tag{6.1}$$

where δ_{tran} is the transit depth and T is the transit duration. This $\mathrm{SNR_{CDPP}}$ is calculated for those KOIs that are currently active planet candidates [3] with a KOI number smaller than 3000, since the rest of KOIs have lower signal-to-noise ratio and have not been vetted as much as the earlier KOIs. For this selection I use only observations up to Q10 because the catalog of individual transit times only covers this range of observations [133], even though there are now 6 more quarters of data. I required at least 5 transits detected within the 2.7 years of data obtained during Q1 through Q10. A total of 361 planet candidates with $\mathrm{SNR_{CDPP}} > 20$ were selected for further study. In Figure 6-1, all planet candidates are represented as black dots, where the y-axis represents the planet radius and the x-axis represents the orbital period. Our 361 selected planet candidates are represented with red dots, and as expected, they tend to be larger than the typical Kepler planet candidate.

6.1.2 Selection based on the excess of scatter during transits

With the list of 361 planet candidates with high SNR transits, it is now time to assess whether spot-crossing events are present or not. The most detectable signature of spot-crossing events is the excess of scatter during transits. A simple transit model that does not take into account spot-crossing events will fail to fit for the positive bumps that appear when dark starspots are occulted. The residuals of the fit will show structure, and the standard deviation of the residuals of the transit portion will be higher than the one measured with points right outside of transit. This becomes more evident when several transits are phase folded, giving enough points during transit to robustly estimate the excess of scatter.

We used the transit times reported in [133] to identify individual transits in the Long Cadence (LC) Kepler light curves. For each transit we defined the transit window as all observations taken in the interval $[-0.75T, 0.75T]$ centered on the transit

time, where T is the transit duration reported by the Kepler team [15]. This conservative window was chosen to avoid issues with underestimated transit durations, transit timing variations and the 30 minute integration time. We defined the out of transit portion (OOT) as the union of the intervals $[-1.1T, -0.75T]$ and $[0.75T, 1.1T]$. In those cases for which $0.35T < 0.2$ days, we set the limits at $\pm(0.75T + 0.2)$. Following the procedure described in the last chapter, a second order polynomial is fitted to the OOT portion of the transit and used to correct for systematic trends caused by stellar activity or instrumental effects. A phase folded light curve is then constructed using the individual transit times, and the number of points is reduced by adding consecutive observations, so that the effective final cadence is 10 minutes. A standard transit model [125] that takes into account the 30 minute integration time is used to fit the folded light curve, a model that has 6 free parameters: time of transit, impact parameter, transit depth $(R_p/R_*)^2$, scaled semi-major axis and the two limb darkening coefficients.

A new folded light curve is now constructed with no binning at all. The transit parameters are used to evaluate the theoretical flux for each data point and to obtain the flux residuals. Points within the interval $[-0.4T, 0.4T]$ centered on the mid-transit are used to evaluate the standard deviation inside of transit, where T is the transit duration obtained from the best fit transit model described in the last paragraph. Points in the intervals $\pm[0.5T+0.01,\ 1.1T\ ]$ are used to evaluate the standard deviation outside of transit. The relative uncertainty on each standard deviation is defined as the inverse square root of the number of points in the corresponding interval. And the uncertainty on the ratio of the two different standard deviations is obtained using standard propagation of uncertainties.

The distribution of values for the standard deviation ratio can be seen in Figure 6-2. The distribution peaks near 1.25 instead of 1, a sign that several factors might be affecting the data during transit (stellar activity being one of them). HAT-P-11b has a ratio of 2.64, whereas Kepler-63b has a ratio of 3.03, which can be used to put these numbers into perspective. Taking into account the shape of the distribution of ratios, I selected for further study 55 systems with a ratio larger than 1.7.

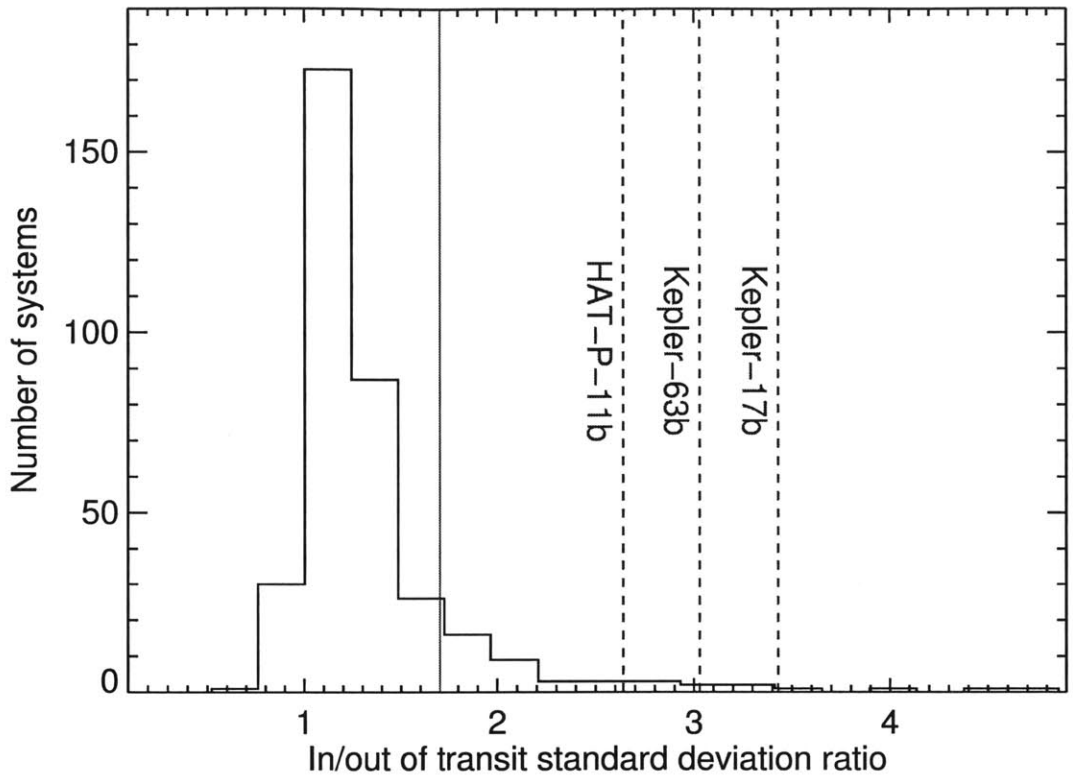

Figure 6-2: Selection of targets according to the excess of scatter during transit.

Histogram showing the distribution of the standard deviation of the residuals during transit normalized to the standard deviation right outside of transit. The distribution peaks around a standard deviation ratio of 1.25, a sign that our filtering procedure might be causing an additional 25% of noise during transit. A large fraction of targets in the final SCEC catalog are found by inspecting those objects that have a standard deviation ratio of 1.7 or larger (to the right of the red line). For comparison, the standard deviation ratio for three of the planets for which spot-crossing events have been already analyzed shown in blue.

6.1.3 Selection based on the detection of spot-crossing events

In the last section we presented a very simple process to select good candidates for SCEC, but this procedure does not give a complete catalog of sources. It could be possible that some systems have detectable spot-crossing events but have a scatter ratio smaller than 1.7. I created a pipeline that tries to address this problem by fitting individual transits with models designed to detect spot-crossing events.

Based on our expertise obtained during the analysis of Kepler-63b, I decided to fit each individual transit with a three parameters model; the transit time, the spot

coverage factor ϵ and a general flux slope. The spot coverage factor (see Chapter Kepler-63b) allows us to fit transits with changing depths, something particularly appropriate when dealing with chromospherically active stars. The rest of parameters required to fit the transit, transit depth, impact parameter, scaled semi-major axis and limb darkening coefficients, are held fixed. This is what I define as a no-spot model, in which spot-crossing events are not modeled. Defining the uncertainty of individual flux measurements as the OOT standard deviation (see previous section), the best fit model is obtained and the χ^2 value is stored.

The next step is to attempt to fit a model with one spot-crossing event, and look for those cases where the spot-crossing model represents a substantial improvement over the no-spot model. The new spot model has the same three free parameters that the no-spot model has, but it has three additional parameters to define a triangular model of the spot-crossing event (see Kepler-63b chapter). The three parameters are the amplitude of the triangle, the duration, and the transit phase, defined to be the longitude of the occulted spot measured along the transit chord (see Kepler-30 chapter). The best fit model is found for each individual transit, and the difference in χ^2 between the spot model and the no-spot model is calculated.

A transit for which the spot-model represents an improvement in χ^2 larger than 10, is considered as a detection in this selection process, where the number 10 has been chosen after visual inspection of several transits with different $\Delta\chi^2$. We selected for further study those systems for which we detected at least 4 spot-crossing events, on average one spot-crossing event for every 10 transits and where at least one of those spot-crossing event was detected with a $\Delta\chi^2 > 20$. This new selection criterion found many objects of the list created in the last section, and added 37 new objects to study in detail. The only important downside of this selection criterion is that computation time is larger by 1 or 2 orders of magnitude.

6.1.4 Visual inspection of the light curves

After reducing the original list of approximately 2500 candidates down to 92, it is now possible to inspect the light curves one by one to detect the most interesting systems.

We found three different sources of systematic effects that cause irregularities during transit that have led to the selection of objects that do not have spot-crossing events.

One of them is an effect introduced by the Kepler team's pipeline, and it particularly affects those systems for which the transits are V-shaped rather than box-shaped. The pipeline sometimes interprets that the lowest point of certain individual transits is caused by a cosmic ray rather than an object transiting a star[1]. The pipeline then corrects this point and brings it closer to the pre and post transit flux levels. Once the transits are phase folded, the corrected fluxes appear higher than expected, which can lead both to an increased level of scatter inside transit and the detection of individual spot-crossing events.

Another effect is transit depth variations caused either by a physical phenomena or by quarterly dependent crowding effects due to neighboring stars. Strong dynamical interactions can cause planets to change their orbital inclinations with time, on timescales short enough to be detectable with a few years of Kepler data. In those cases, the planet will be transiting a slightly different area of the star during each transit. Combining this with a strong limb darkening profile leads to a changing transit depth. When observed, this effect can also mean that the planet candidate in question is a star, since triple stars cause this effect quite frequently. In same cases transit depth changes are mainly seen from one quarter to the other. The Kepler space telescope rotates 90° every 3 months, and the photometric aperture used to create the light curves changes accordingly. Each aperture can capture different fractions of light from other stars in the field, which leads to transit depth variations. In both cases transit depth variations provide an additional source of noise during transit, than can be high enough to be detected by the section of the pipeline that selects objects due to a higher standard deviation inside of transit.

Finally, in some cases the host star might be a pulsator or might show solar-like oscillations. In some special cases, the pulsations can be mistaken for spot-crossing events, inducing the false detection.

The three effects combined lead to the removal of 35 systems from the preliminary

[1]See Kepler Data release notes 21 at http://archive.stsci.edu/kepler/

SCEC. These false detections are shown in Figure 6-3 in green, where the inside vs outside of transit scatter ratio is plotted in the y-axis. The x-axis represents the level of stellar activity of the star, and it is simply defined as the standard deviation of the stellar flux time series once the transits have been removed. The other 57 systems are divided in two main groups. There are 21 planet candidates that are found in multi-transiting systems (see Table 6.1). These deserve special attention because in most cases, several planets transit the star at the same time, which has the potential to give a false positive detection. The second order polynomial used to remove trends on the stellar flux is likely to fail due to the additional transit signals, increasing the scatter of the folded transit light curve. In fact, it seems that an obliquity measurement using starspots might only be possible for one or two additional multi-transiting Kepler systems, with KOI 2672 giving the best opportunity after Kepler-30. A more detailed analysis of the multi-transiting systems is beyond the scope of this chapter, and might require the creation of more sophisticated tools, an analysis worth doing due to the high scientific interest of these systems, as it was described in Chapter 4.

The other 36 planet candidates are found in single transiting systems (see Table 6.2). These systems are much easier to interpret, and most of them are likely affected by spot-crossing events in some way. However, these also suffer from a much larger false positive rate, since they are not part of multi-transiting systems [114] and are pretty large, making them more likely to be false positives due to low-mass binary companions [181]. In particular, KOI 340.01 and KOI 1786.01, two of the most promising objects for spot-crossing analysis, have already been found to be binary stars [181].

6.1.5 More targets and eclipsing binaries

Over the past couple of years, I have created different versions of the same pipeline, which have been used to detect spot-crossing events from different lists of Kepler Objects of Interest. A few objects previously detected in these different runs were not selected in the last run. Most of these objects do not represent the best targets in this catalog, but it is worth mentioning them for future reference. In the case

Table 6.1. Multi transiting systems in the SCEC

KOI	KIC	N_{pl}	N_{SC}	KOI	KIC	N_{pl}	N_{SC}
70	6850504	5	42	401	3217264	3	3
72	11904151	2	31	464	8890783	2	27
82	10187017	5	43	564	6786037	3	6
94	6462863	4	21	620	11773022	3	15
111	6678383	3	38	676	7447200	2	29
137	8644288	3	42	676	7447200	2	29
157	6541920	6	42	806	3832474	3	30
245	8478994	3	36	872	7109675	2	27
271	9451706	3	24	884	7434875	3	30
279	12314973	3	34	1353	7303287	2	14
316	8008067	3	24	1781	11551692	3	12
377	3323887	3	30	1858	8160953	2	9
398	9946525	3	24	2672	11253827	2	15

Note. — N_{pl} is the number of planets in the system. N_{SC} is the number of months of Short Cadence observations

Table 6.2. Single transiting systems in the SCEC

KOI	KIC	Period [days]	N_{SC}	KOI	KIC	Period [days]	N_{SC}
3	10748390	4.89	34	652	5796675	16.08	4
10	6922244	3.52	31	680	7529266	8.60	9
12	5812701	17.86	45	767	11414511	2.82	15
63	11554435	9.43	43	774	11656840	7.44	3
97	5780885	4.89	18	802	3453214	19.62	12
131	7778437	5.01	7	805	3734868	10.33	9
183	9651668	2.68	18	846	6061119	27.81	0
186	12019440	3.24	13	868	6867155	235.97	11
190	5771719	12.26	27	883	7380537	2.69	15
191	5972334	38.65	24	889	757450	8.88	18
203	10619192	1.49	30	895	7767559	4.41	12
212	6300348	5.70	6	902	8018547	83.91	17
217	9595827	3.91	16	913	8544996	4.08	0
219	6305192	8.03	0	918	8672910	39.64	16
254	5794240	2.46	30	974	9414417	53.51	31
261	5383248	16.24	28	984	1161345	4.29	24
318	8156120	38.58	33	1066	8260218	5.71	0
318	8156120	38.58	33	1074	10272640	3.77	12
372	6471021	125.63	10	1255	8494263	78.93	0
421	9115800	4.45	0	1391	8958035	7.98	15
425	9967884	5.43	12	1456	7832356	7.89	12
652	6716021	110.76	0				

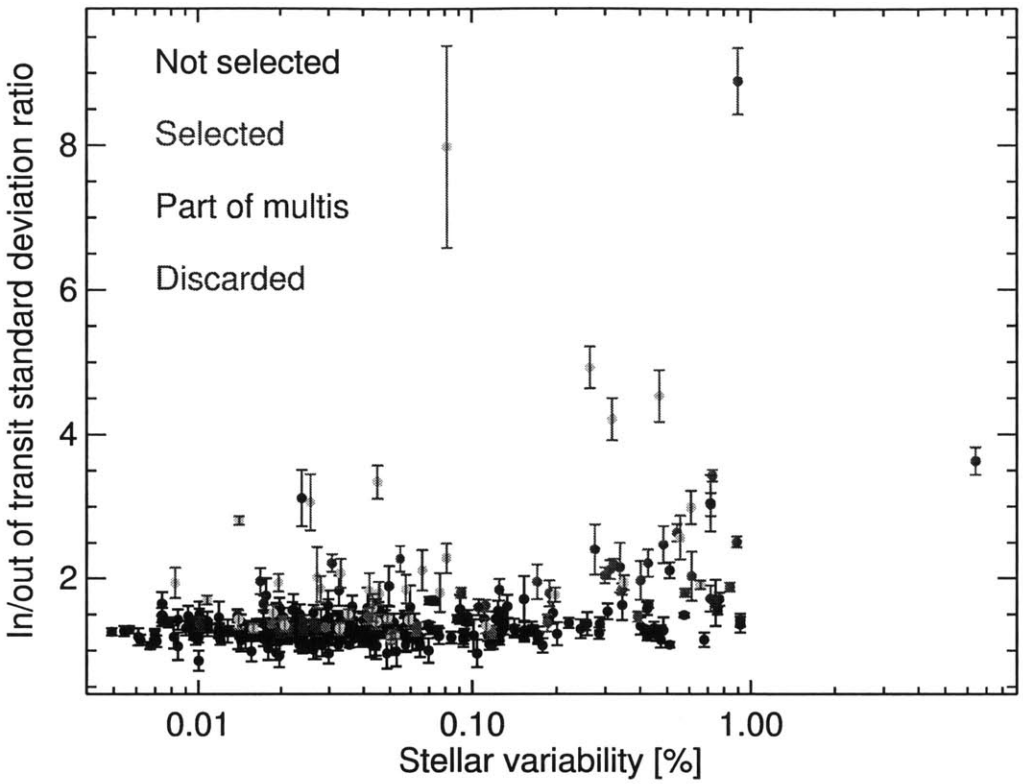

Figure 6-3: Stellar activity of our selected stars.

The scatter of the residuals inside of transit relative to the scatter right outside of transit is compared to the level of variability of the host star due to stellar activity. The stellar variability is defined as the standard deviation of the fluxes after removing the transits. Black points represent objects that were selected in the first step (high transit signal-to-noise ratio) but that were not selected for further inspection. Green dots represent the 35 objects removed after visual inspection. Our targets (in red) tend to be orbiting active stars as expected.

of single transiting systems, 10 more objects have been added to Table 6.2, those transiting the stars with KOI numbers 131, 183, 186, 254, 318, 652, 767, 902, 974 and 984. In the case of the multi-transiting systems, 8 more systems have been added to Table 6.1, those transiting the stars with KOI numbers 70, 82, 245, 377, 398, 464, 676 and 1858.

Previous attempts to create SCEC detected KOIs that were considered good planet candidates at the time, but are currently considered false positives. The Kepler team revisits all KOIs with every new catalog, and the additional data can some-

Table 6.3. Eclipsing binaries in the SCEC

KIC	Period [days]	N_{SC}	KIC	Period [days]	N_{SC}
2438502	8.36	6	8460600	6.35	3
3955867	33.70	0	8580438	6.49	0
4737267	9.50	2	8702921	19.40	0
5014753	3.17	3	8953059	5.50	3
5098444	26.95	7	9291629	20.69	0
5193386	21.40	0	9446824	4.20	18
5270698	3.96	12	9576197	7.96	3
5282049	5.90	3	9649222	5.92	3
5306862	2.02	4	9655129	2.75	6
5310435	4.93	0	9705459	2.49	12
5370302	7.80	3	9774400	10.82	0
5376836	3.48	10	10014830	3.03	0
5700330	53.22	0	10015516	67.75	3
6205460	3.72	5	10068383	7.30	12
6307537	29.75	4	10287248	4.72	13
6548447	10.80	3	10330495	18.10	3
6603756	5.20	12	10485250	16.47	9
6613006	7.40	0	10616571	23.67	15
6694186	5.60	1	10747445	4.60	3
7885570	1.73	8	10936427	14.35	0
7940533	3.90	4	11235323	19.67	0
7943602	14.70	0	11404644	5.90	3
8016214	3.17	4	11408935	16.00	3
8081482	2.82	9	11449844	38.50	16
8180020	5.80	9	11517719	2.50	9
8230809	4.08	3	11673686	4.60	4

Note. — N_{SC} is the number of months of Short Cadence observations

times help detect the secondary eclipse of the KOI, which in most cases points toward self-luminous objects (except for the shortest-period Hot-Jupiters). Sometimes RV follow-up shows a large signal in phase with the transits of the KOI, another sign that the object might be a binary star. This exactly what has happened in the search described in this chapter with KOI 340.01 and KOI 1786.01. Together with these two eclipsing binary stars, 23 more KOIs currently cataloged as false positives have been added to SCEC (see Table 6.3).

An official Kepler Binary catalog exists [194] containing over 2600 eclipsing binaries, which has the potential to reveal many more interesting objects to be added

to SCEC. In principle, eclipsing stars that are large enough to cause a deep eclipse but small enough to provide flat-bottomed eclipses will be great targets for the spot-crossing method. A significant fraction of the 2600 eclipsing binary stars are contact binaries, in which individual transits cannot be distinguished. The lack of an eclipse time catalog also provides an additional complication. Fortunately, the catalog does provide a parameter that measures how detached a binary is [129]. A set of approximately 1000 detached eclipsing binaries was selected for visual inspection, in which several dozens of eclipses of each system were inspected looking for spot-crossing events. This process yielded 27 more objects that we have added to SCEC (see Table 6.3), for a total of 52 eclipsing binaries in the catalog. A visual inspection process can sometimes lead to questions about the completeness of the final list, and once an eclipse timing catalog is available, it will be worth using the more sophisticated techniques described in this chapter to detect as many good candidates for the spot-crossing technique as possible. It is worth noting that in the case of the planet candidates, a preliminary visual inspection was able to detect the best candidates, and I am confident that the list of eclipsing binaries in the SCEC also contains the best of them already.

6.2 Measuring the obliquities of a few selected objects

The main scope of this chapter is to document the effort to create an SCEC, a catalog that should serve as a good guide to anybody interested in stellar activity and its effects on planet transits. It should also serve as a guide on how to search for targets for spot-crossing events analysis for future exoplanet missions. But we also have the opportunity to measure the obliquity of several systems just with a simple visual inspection. In this section I focus on 5 new systems for which we can conclude that the obliquity of the system is low, based on the recurrence of spot-crossing events at different transit phases (see Chapter 2).

Out of the 121 objects on SCEC, I focused on those KOI single-transiting systems with no transit time variations, with several quarters of Short Cadence (SC) observations and with many detections of spot-crossing events. The importance of the SC observations resides on the increased frequency of observations (1 minute cadence) that allows for a better detection and characterization of the spot-crossing events. 8 systems satisfied these criteria, with HAT-P-11b, Kepler-17b and Kepler-63b representing the best cases, and 5 new systems with enough spot-crossing events to measure their obliquities.

A very simple argument will be used to show that a system has a low obliquity. A detection of a clear spot-crossing event, and knowledge of the rotation period of that particular spot, leads to a prediction for when the spot will be occulted again by the transiting object and what will be the transit phase measured along the transit chord in that case. Indeed, if a spot-crossing event is detected at a phase equal to ϕ_0, n transits later the phase at which the spot will be occulted should be

$$\phi_n = \phi_0 + \frac{d\phi}{dn} n \qquad \frac{d\phi}{dn} \equiv \frac{2\pi P_{orb}}{P_{rot}} \tag{6.2}$$

where the derivative of the phase only depends on the orbital period, which is well known, and the rotation period of the spot. We can in principle approximate the rotation period of the spot by the rotation period of the star, obtained from a Lomb-Scargle periodogram [184] of the transit-removed stellar fluxes, as long as the differential rotation is not very strong and the number of transits n is small. This formula only works when the predicted phase is within $-\pi/2$ and $\pi/2$ ($\mathrm{mod}\, 2\pi$), since outside that range the spot will be on the non-visible side of the star where it cannot be occulted by the transiting object.

In order to apply this formula, the SC observations up to Q16 for our 5 objects were analyzed in the same way the LC observations were analyzed to create the SCEC. A folded light curve was generated from which we obtained new and more accurate transit parameters. Individual transits were fitted first with a no-spot model and then with a triangular spot model. When a spot-crossing event was the detected, the

transit was inspected by eye. In all five cases (see Figures 6-4, 6-5, 6-6, 6-7 and 6-8), equation 6.2 applies very well to the observed spot-crossing events, which represents very strong evidence that these systems have low obliquities. If the same spot can be occulted by the planet candidate at different phases, a portion of the spot must always be contained on the transit chord, which means that the obliquity of these systems cannot be much larger than $\Psi_{lim} = \pm \arctan(R_p/R_*)$ [52]. In all our cases, this translates into a bound to the obliquity of approximately $\pm 10°$.

All five objects are transiting cool stars, which is expected since cool stars have stronger levels of magnetic activity. The low obliquities of KOI 217.01, KOI 895.01 and KOI 1074.01 could be attributed to tidal interactions, since they should be strong enough to have realigned them by now due to the proximity of the planets to their host stars [226]. To be quantitative we used again the metric developed by [5], in which binary-star data are used to calibrate tidal dissipation timescales, as described in Chapter 5. Assuming that all three planets the same mass as Jupiter, we can estimate a relative timescale between 200 and 1500 for this three objects, which would situate these three objects in the region of Figure 5-9 where all systems are aligned. Note that this is an upper bound to this timescale, because the planets are likely to be more massive (they could be even be brown dwarfs or M-dwarfs), which would increase the strength of the tidal interactions, reducing the timescale for realignment substantially.

More interesting is the case of KOI 889.01 with an orbital period of 8.9 days. Assuming the same mass as Jupiter I obtain a relative timescale near 10^6, much larger than the timescale for Kepler-63b. If this system had a primordial large obliquity, tidal interactions would not have been strong enough to realign it. Here the absence of a good mass estimate becomes more relevant. It would only take a mass of 20 $M_{\rm Jup}$ to decrease the relative timescale to 2000, where tidal interactions would have been strong enough to realign the system. The case of KOI 340.01 is special since it is an eclipsing binary, so its formation scenario could be completely different from that of Hot-Jupiters. Even with an orbital period of 23.7, tidal interactions could have played an important role on the current low obliquity of the system. The detection

of secondary eclipses that are not half-way between transits, indicates that the orbit has a significant eccentricity, adding another interesting constraint on the geometry of this system. As [181] point out, the long transit duration and the large RV semi-amplitude, which gives a preliminary mass of $0.7M_{\odot}$ for KOI 340.01, indicate that the primary star is likely an evolved star, given that the eclipse depth is only 2%. It would required to go beyond the simple description of the relative timescale to understand the role of tidal interactions on this system, but this is beyond the scope of this chapter.

It is important to note that several different decisions in the selection process of these 5 objects might have led to the final result of obtaining five low obliquities. One of them stands above all; once the recurrence of spots is not observed it becomes quite hard to interpret a system, since it is often the case that spots might vanish before the transiting object had the time to occult them again. However, these five cases truly show the potential of this technique to provide a large sample of obliquity measurements without any follow-up observations.

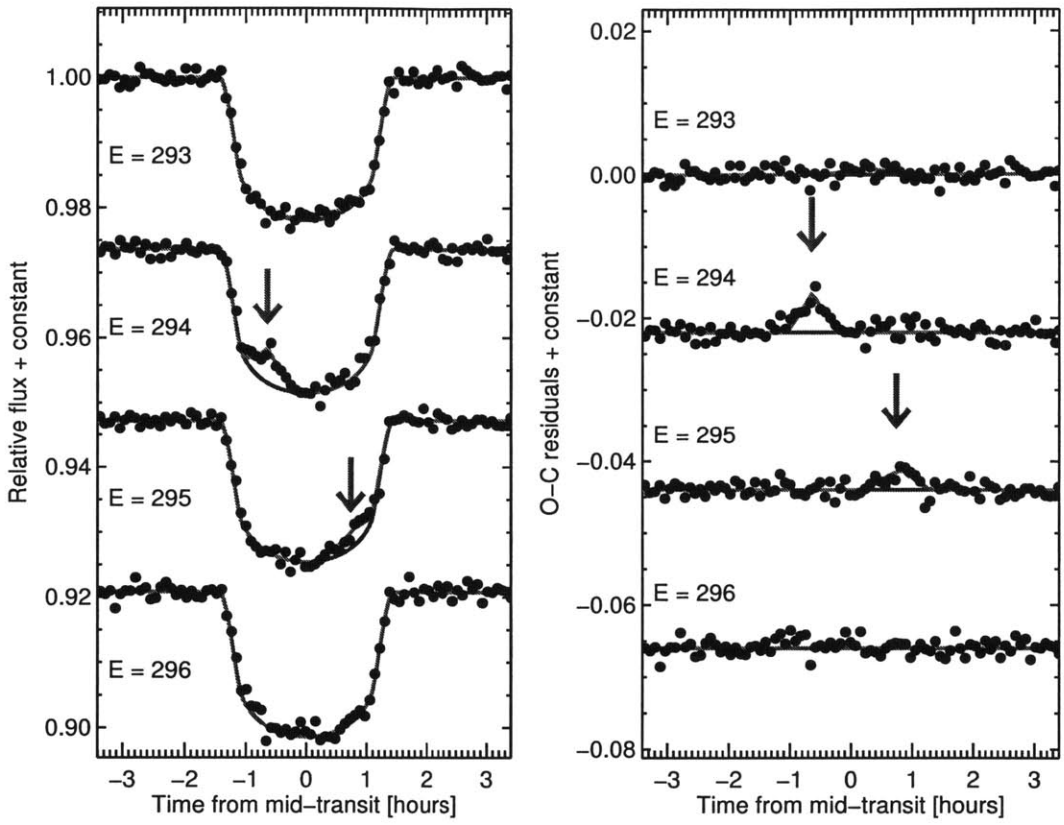

Figure 6-4: A low obliquity for KOI 217.01.

In all the following figures, black dots represent Short Cadence observations binned to an effective cadence of 5 minutes, except for the case of KOI 340.01, where the effective cadence is 30 minutes. On the left panel blue lines represent the no-spot transit model while the red line is the spot model, in which each individual transit has the same transit parameters but a different a triangular model for one spot-crossing even. The phases of the spot crossing events are free parameters in each transit. On the right panel the O-C residuals are shown, where the no-spot model is subtracted from the data points and both the no-spot and the spot model. In the case of KOI 217.01, 4 consecutive transits are shown. With an orbital period of 3.9 days and a rotation period of 21 days, spots are expected to move along the transit chord with $d\phi/dn = 67°/\text{transit}$. A first spot-crossing event is observed in transit 294 with a transit phase that is equal to $-30°$ (green arrow). The model predicts another spot-crossing event on the next transit at a phase that is equal to 37° (brown arrow), and the spot model gives a best-fit phase of 40°.

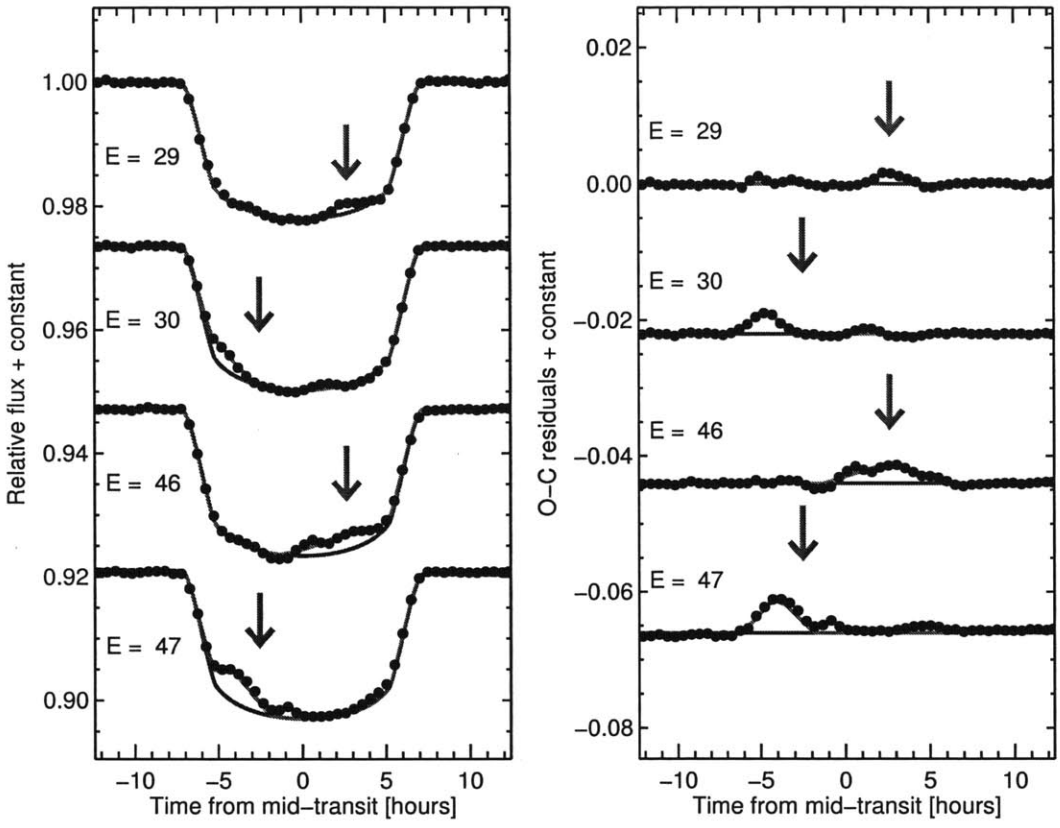

Figure 6-5: A low obliquity for KOI 340.01.

The case of KOI 340.01 is a bit more complex. With an orbital period of 23.7 days and a rotation period of 12.7 days, spots are expected to recede from one transit to the next at a rate of $d\phi/dn = -50°/\text{transit}$. Transits 29 and 46 show a spot-crossing event with a phase of 25° (green arrows). The low-obliquity model predicts another spot-crossing event at a phase of $-25°$ (brown arrows). The recurrence of the spot is observed in both cases, but the spot-crossing events happen $15° - 25°$ earlier than expected. This is still compatible with a low-obliquity system with a non-zero differential rotation profile. In this case, spots on the transit chord seem to have a rotation period of 13.0-13.2 days, a bit slower than the latitude integrated rotation period of 12.7 days that can be obtained from the Lomb-Scargle periodogram.

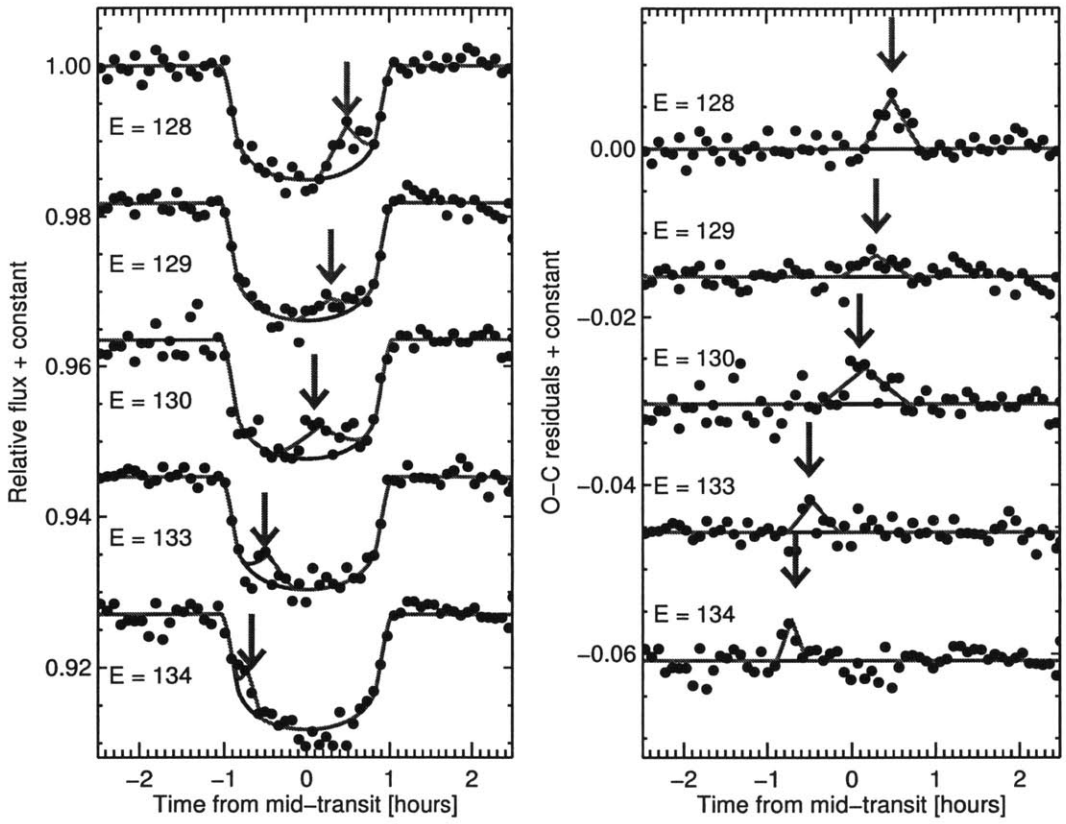

Figure 6-6: A low obliquity for KOI 889.01.

In the case of KOI 889.01, 5 close transits are shown. With an orbital period of 8.9 days and a rotation period of 19.2 days, spots are expected to move along the transit chord with $d\phi/dn = 167°/\text{transit}$. This situation is equivalent as seeing the same spot recede 26° every two transits, with a transit in the middle where the spot should not be observed. In the figure, a large spot is occulted during transit number 128 at a transit phase equal to 32°. This same spot is observed at transit 130 with a phase of 10° and at transit 134 with a phase of −51° as predicted. A different spot is observed at transit 129 with phase of 19° which recurs at transit 133 with a phase of −30°.

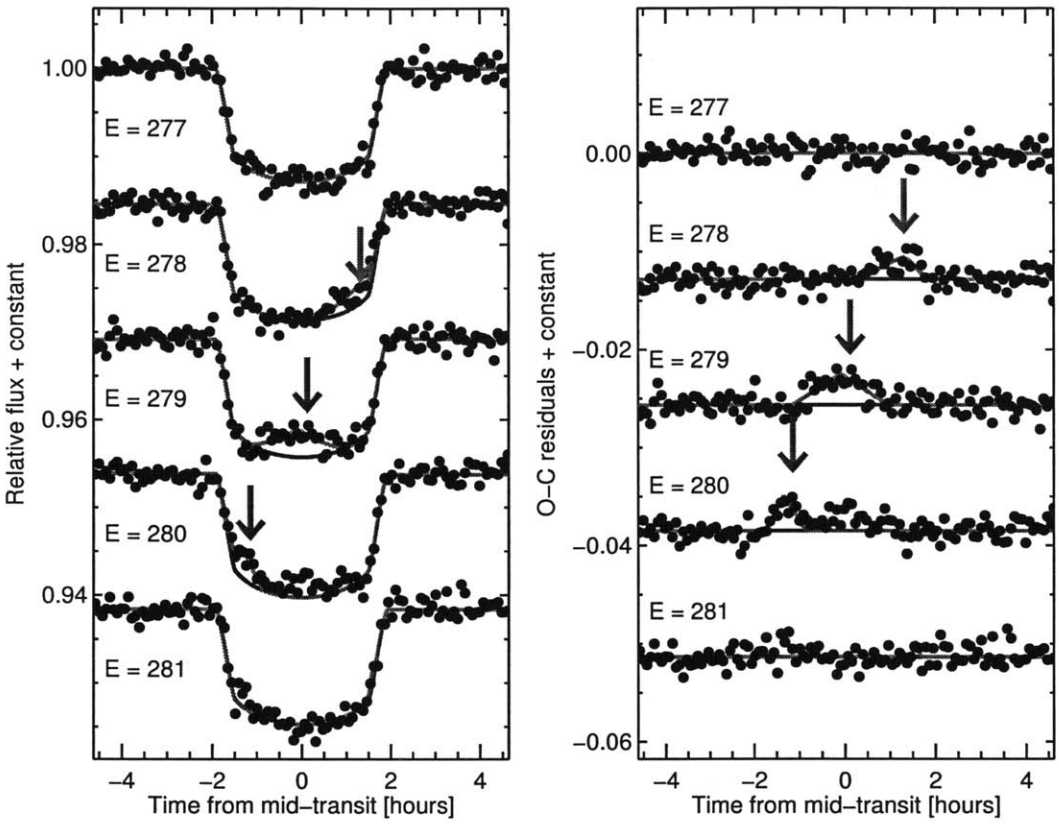

Figure 6-7: A low obliquity for KOI 895.01.

The case of KOI 895.01 is simpler. With an orbital period of 4.4 days and a rotation period of 5.1 days, spots are expected to recede from one transit to the next at a rate of $d\phi/dn = -46°$/transit. Transits 278 shows a spot-crossing event at a phase equal to 50° (green arrow). The zero-obliquity model predicts spot-crossing events for the next two transits at phases equal to 4° and −42° (brown arrows). The two events are detected at phases 0° and −50° as predicted.

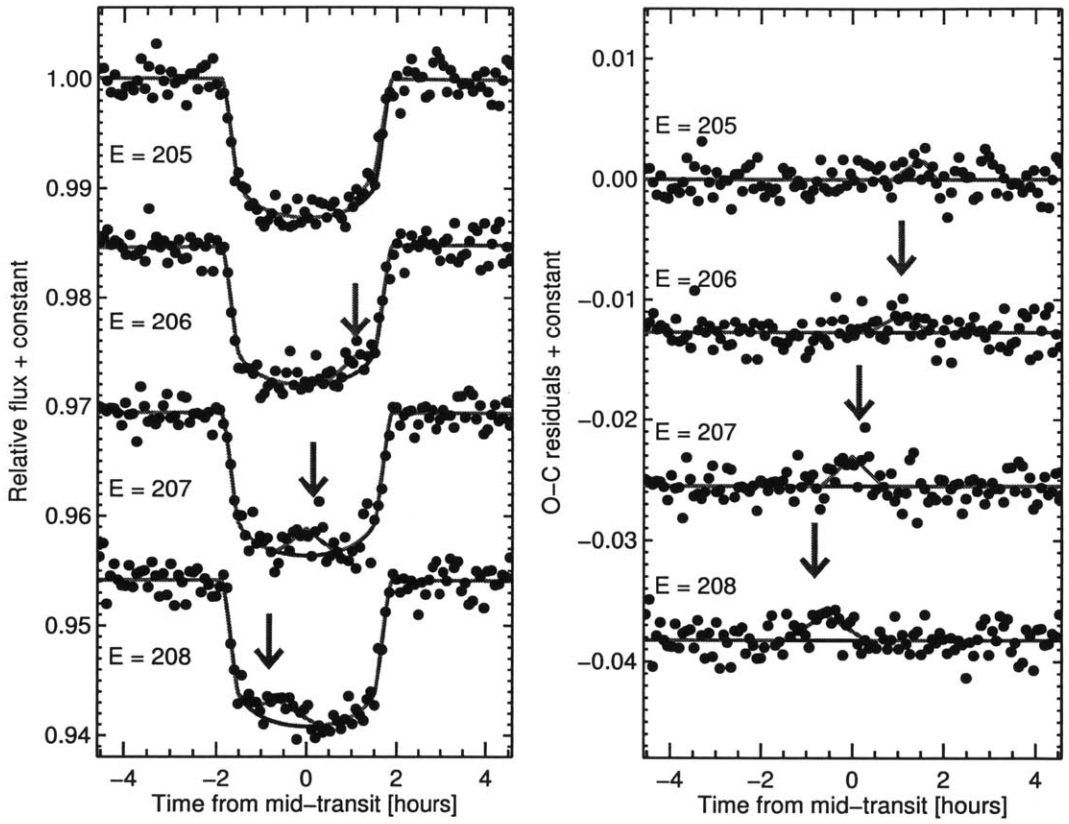

Figure 6-8: A low obliquity for KOI 1074.01

The case of KOI 1074.01 is similar to the case of KOI 895. With an orbital period of 3.8 days and a rotation period of 4.2 days, spots are expected to recede from one transit to the next at a rate of $d\phi/dn = -34°$/transit. Transits 206 shows a spot-crossing event at a phase equal to 39° (green arrow). The zero-obliquity model predicts spot-crossing events for the next two transits at phases equal to 5° and $-29°$ (brown arrows). The two events are detected at phases 0° and $-21°$ as predicted. A small spot-crossing event is observed on transit 205 at a phase equals to 70°, as the model would also predict.

Chapter 7

The shortest-period planets: discovery of Kepler-78b

Published as: "Transits and Occultations of an Earth-Sized Planet in an 8.5-Hour Orbit" Sanchis-Ojeda, R., Rappaport, S., Winn, J.N., Levine, A., Kotson, M.C., Latham, D.W., Buchhave, L.A. 2013, ApJ, 774, 54.

We report the discovery of an Earth-sized planet ($1.16 \pm 0.19\ R_\oplus$) in an 8.5-hour orbit around a late G-type star (KIC 8435766, Kepler-78). The object was identified in a search for short-period planets in the *Kepler* database and confirmed to be a transiting planet (as opposed to an eclipsing stellar system) through the absence of ellipsoidal light variations or substantial radial-velocity variations. The unusually short orbital period and the relative brightness of the host star ($m_{\rm Kep} = 11.5$) enable robust detections of the changing illumination of the visible hemisphere of the planet, as well as the occultations of the planet by the star. We interpret these signals as representing a combination of reflected and reprocessed light, with the highest planet dayside temperature in the range of 2300 K to 3100 K. Follow-up spectroscopy combined with finer sampling photometric observations will further pin down the system parameters and may even yield the mass of the planet.

7.1 Introduction

The work described here was motivated by our curiosity about planets with the shortest possible orbital periods. Although many exoplanets have been discovered with orbital periods of a few days—most famously the "hot Jupiters"—relatively few are known with periods shorter than *one* day. [92] found that such planets are less common than planets with periods of 2–3 days, based on data from the *Kepler* spacecraft. The shortest-period transit candidate is the 4.5-hour signal in the KOI 1843 system found by [145], although this candidate has not yet been thoroughly vetted. Among the well-documented planets the record holder is Kepler-42c, with a period of 10.9 hr [139]. The planet 55 Cnc e is the shortest-period planet (17.8 hr) for which the radius and mass have both been measured ([230], [49]). In all of these cases the planet is smaller than about 2 $R_\oplus$. Among giant planets, the shortest period belongs to WASP-19b ($P = 18.9$ hr [80]).

The rarity of giant planets with $P < 1$ day could reflect the vulnerability of such planets to tidally-induced decay of their orbits (see, e.g., [187] for specific predictions), a possible tidal-inflation instability [78], Roche-lobe overflow [77], or evaporation (see, e.g., [140]. If so, then because smaller rocky planets are less vulnerable to these effects, one would expect smaller planets to be more common than large planets at the shortest periods. A suggestion that this is indeed the case comes from perusing the list of the active *Kepler* Objects of Interest (KOI)[1]. In this list we find only 17 active planet candidates with $P < 16$ hr, all of which have inferred planet sizes smaller than that of Neptune. However, this result is difficult to interpret because of the possibility of false positives due to eclipsing binary stars. There are already 55 known false positives in that period range, and the vetting is incomplete for most of the 17 candidates that remain.

There is also the possibility that the KOI catalog is missing some objects with short periods or short transit durations, as noted by [68]. Other authors have performed independent searches of the *Kepler* database using the Box Least Squares (BLS)

[1]http://exoplanetarchive.ipac.caltech.edu/

algorithm [105] and found new candidates ([145], [96]). The BLS algorithm is designed for finding transit signals of short duration compared to the orbital period. For the shortest-period planets, though, the transit duration is a sizable fraction of the orbital period, and a Fourier Transform (FT) analysis should be sufficient for detection. The FT has the advantages of simplicity and speed. This was the technique used to detect the apparently disintegrating planet KIC 12557548b, with an orbital period of 15.6 hr [168].

Here we describe an Earth-sized planet with an orbital period of 8.5 hr, which was not among the *Kepler* Objects of Interest, and was identified in our FT-based survey of the *Kepler* data. Because so many transits have been observed and the star is unusually bright (with *Kepler* magnitude 11.5), the process of validation is simplified, the planetary occultations and illumination variations are easily detected, and further observations should be rewarding.

Section 7.2 of this paper describes the initial detection of the signal, our follow-up ground-based spectroscopic observations, and the properties of the parent star. Section 7.3 presents the analysis of the *Kepler* light curve and the determination of the system parameters. Section 7.4 demonstrates that the signal almost certainly arises from a transiting planet, as opposed to an eclipsing binary star, based on the lack of detectable ellipsoidal light variations or radial-velocity variations. Section 7.5 discusses the possibilities for the surface temperature and reflectivity of the planet, based on the observed properties of the illumination curve and occultations. We end with a brief discussion of the future prospects for studying the shortest-period planets.

7.2 Observations

7.2.1 Initial detection

To carry out an independent search for the shortest-period planets, we subjected all the *Kepler* long-cadence light curves to a FT analysis using data from Quarters 1-

14. The light curves used for this study had all been processed with the PDC-MAP algorithm ([206], [195]), which removes many of the instrumental artifacts from the time series while retaining the bulk of the astrophysical variability. The time series from each quarter was divided by its median value. Then, the normalized data from all quarters were stitched together into a single file. The FT was then calculated. We searched for the presence of at least one peak more than 4.6 standard deviations above the local noise level in the Fourier spectrum. To be considered further, we also required that the FT exhibit at least one harmonic or subharmonic that stands out at the 3.3 σ level. The candidates were then examined by eye. Only those that showed several harmonics with a slow falloff in amplitude with increasing frequency, and no sign of stellar pulsations, were selected for further study.

The surviving candidates underwent a period-folding analysis. To remove the slow flux variations caused by starspots and stellar rotation, we applied a moving-mean filter to the flux series, with a width in time equal to the candidate orbital period. Then we folded the time series with that period and inspected the resulting light curve, looking for the characteristic shape of a transit. We applied the same filtering algorithm to the time series of the row and column positions of the image photocenter (MOM_CENTR) provided by the *Kepler* pipeline. Systems with large photocenter shifts were discarded; such large shifts indicate that the flux variations belong to a neighboring star and not the intended *Kepler* target. We also checked for any significant differences in the depths of the odd- and even-numbered transits, which would reveal the candidate to be an eclipsing binary with twice the nominal period. A list of 20 potentially new short-period planet candidates passed all these tests, with orbital periods between 4 and 16 hours. As expected, this list is comprised entirely of objects smaller than Neptune. We will report on the entire collection in a separate paper. For this initial report we chose to focus on KIC 8435766 (from now on designated Kepler-78b), because it has the brightest host star, one of the shortest orbital periods, and the most significant detection of the illumination curve and occultations.

Figure 7-1 shows the time series, FT, and folded light curve for Kepler-78. The

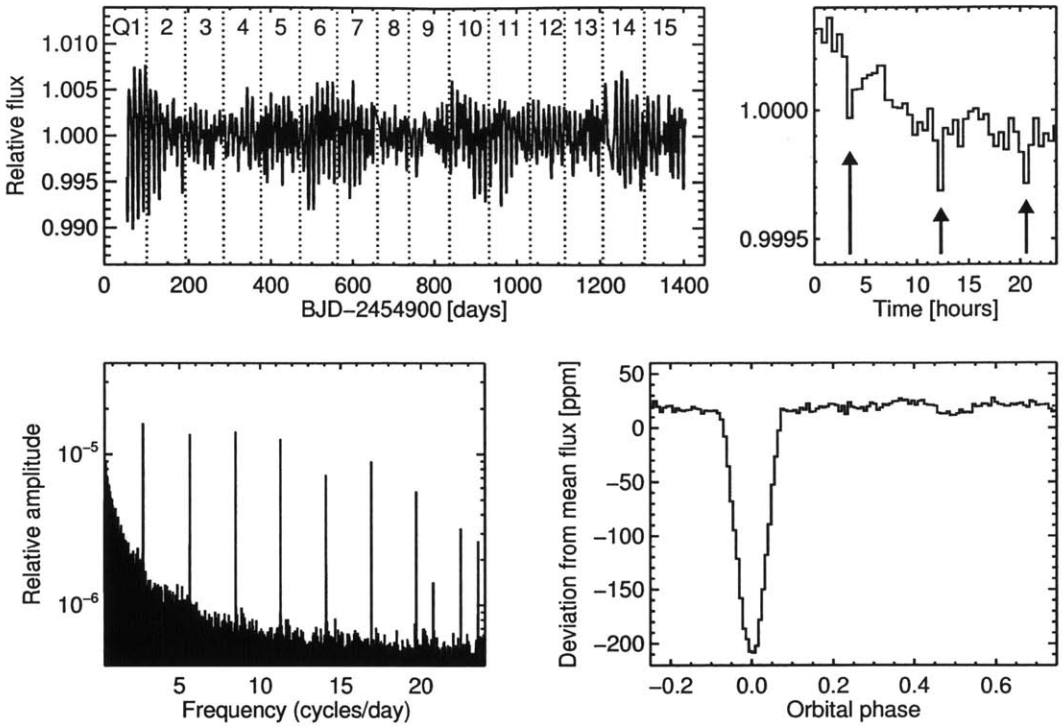

Figure 7-1: *Kepler* data for Kepler-78 (KIC 8435766).

Top.—Time series, based on quarterly-normalized PDC-MAP data. The quasiperiodic flux variations are characteristic of starspots and rotation. The right panel focuses on one arbitrarily chosen day of data, to allow several transits to be seen by eye (single 30 minute bins). *Lower left panel.*—Fourier transform, before any filtering of the starspot-induced signal. *Lower right panel.*—Light curve, after filtering and then folding the time series with a period of 8.5201795 hr.

time series exhibits quasiperiodic flux variations with an amplitude of a few percent and a period of 12.5 days, likely the result of spots on a rotating star. The FT also shows a base frequency at $\nu = 3$ cycles day^{-1}, and at least 9 higher harmonics, two of which are aliases resulting from reflection about the Nyquist limit of 25 cycles day^{-1}. No subharmonics of these frequencies are seen; a positive detection would have been indicative of a binary with primary and secondary eclipses of nearly equal depth. The folded light curve shows a transit with a depth of 220 ppm and an occultation with a depth of 10 ppm. The illumination curve—the rise in flux between transit and occultation—is less obvious; see Figure 7-3 for a better view.

7.2.2 Spectroscopy

Spectroscopic observations were undertaken to characterize the host star and to search for radial-velocity variations. We obtained five spectra with the fiber-fed Tillinghast Reflector Échelle Spectrograph on the 1.5m Tillinghast Reflector at the Fred Lawrence Whipple Observatory on Mt. Hopkins, Arizona. The observations took place in 2013 on March 23, 25, and 29, and on April 2 and 4. Individual exposure times of about 15 minutes yielded a signal-to-noise ratio (S/N) per resolution element in the Mg I b order ranging from 26 to 44, depending mostly on the seeing and sky transparency.

Spectroscopic parameters for the host star were determined with the Stellar Parameter Classification code (SPC [30]). We derived the parameters from each spectrum, and then computed weighted averages. The results were $T_{\rm eff} = 5089 \pm 50$ K, [m/H] $= -0.14 \pm 0.08$, $\log g = 4.60 \pm 0.1$, and $v \sin i = 2.4 \pm 0.5$ km s^{-1}. We also estimated the radial velocity of the star at $\gamma = -3.44 \pm 0.08$ km s^{-1}.

To estimate the stellar mass and radius, we used the calibrated relationships provided by [210] between the spectroscopic parameters and stellar dimensions. These relationships give a stellar mass $0.81 \pm 0.05\, M_\odot$, radius $0.74^{+0.10}_{-0.08}\, R_\odot$, and mean density $\langle \rho \rangle = 2.8^{+1.1}_{-0.8}$ g cm^{-3}. Error propagation was performed assuming independent Gaussian errors in the stellar parameters, along with a 6% systematic error in the stellar mass due to the uncertainty in the calibration formulas. The final values are summarized in Table 7.2. Following [211] we checked the derived mass and the radius by comparing the spectroscopic parameters to the outputs of stellar evolutionary models [234]; the resulting values were similar.

We can also estimate the age of the star based on the rotation period. [185] gave a calibrated polynomial formula relating stellar age, mass, and rotation period. Given the preceding estimates for the mass and rotation period, the [185] formula gives an age of 750 ± 150 Myr. As a consistency check we note that the stellar radius of $0.74\ R_\odot$ and the rotation period of 12.5 days imply a rotation velocity of 3 km s^{-1}, which is compatible with the spectroscopic estimate of $v \sin i$ (assuming $\sin i \approx 1$).

Radial velocities were determined via cross-correlation against synthetic tem-

Table 7.1. Relative Radial Velocities for Kepler-78

BJD-2456300	RV (m s^{-1})	RV_e[a](m s^{-1})
74.9484	23.66	22.62
76.9663	-36.37	19.13
81.0154	19.65	20.21
84.9219	26.03	19.13
86.9066	-32.99	25.51

[a]Estimated 1-σ uncertainty in the relative radial velocity.

plates, as described by [29] and [163]. The results are presented in Table 7.1, where the mean radial velocity has been subtracted. The five data points have a standard deviation of 32 m s^{-1}, and internally-estimated measurement uncertainties of 20-25 m s^{-1}. By fitting a sinusoid with the same period and phase as the transit signal, we obtain a velocity semiamplitude $K = 36 \pm 12$ m s^{-1}. However, the true uncertainty is undoubtedly larger because of the spurious radial velocities produced by rotating starspots, which are expected to be of order 30 m s^{-1} (the product of $v \sin i$ and the 1% photometric modulation). Hence we consider the data to be consistent with no radial-velocity variation. Any variation with the same period and phase as the transit signal is smaller than about 100 m s^{-1} (3σ), corresponding to a companion mass of about 0.3 $M_{\rm Jup}$ (100 $M_\oplus$) orbiting Kepler-78.

7.2.3 UKIRT image

The *Kepler* time series is based on summing the flux within an aperture surrounding the target star Kepler-78 specific to each "season" (the quarterly 90° rotations of the field of view). The aperture dimensions change with the season; they are as large as 5 pixels (20″) in the column direction and 6 pixels (24″) in the row direction, with a total of 12-20 pixels used in a given season. To check whether the summed flux includes significant contributions from known neighboring stars, we examined the J

band image from the UKIRT survey of the *Kepler* field[2].

Two neighboring stars were detected (see Figure 7-4). Relative to Kepler-78, the first neighbor is 4.5 mag fainter and 4.8″ away, contributing 1.5% of the J-band flux to the *Kepler* photometric aperture. The second neighbor is 3.1 mag fainter and 10.3″ away. If this star were wholly within the aperture it would have contributed 5.5% of the total J-band flux; however, since it falls near the edge of the aperture, the contribution is likely smaller and is expected to vary with the *Kepler* seasons. In section 7.4 we will show that neither of these fainter stars can be the source of the transit signal.

7.3 Light curve analysis

7.3.1 Transit times and orbital period

In the first step of the light-curve analysis we determined the orbital period P, and checked for any transit-timing variations (TTV). Using the initial FT-based estimate of P, we selected a 6-hour interval (12 data points) surrounding each predicted transit time. We corrected each transit interval for the starspot-induced flux modulation by masking out the transit data (the central 2 hours), fitting a linear function of time to the out-of-transit data, and then dividing the data from the entire interval by the best-fitting linear function. A total of 3378 individual transits were detected and filtered in this way; a few others were detected but not analyzed further because fewer than 2 hours of out-of-transit data are available.

In order to obtain precise transit times, we first need to obtain an empirical transit template. For that, the time series was folded with the trial period. As seen in Figure 7-1, the transit shape can be approximated by a triangular dip, due to the 30-minute averaging time of the *Kepler* observations. For transit timing purposes we used a triangular model, with three parameters describing the depth, duration, and time of the transit. We found the best-fitting model to the phase-folded light curve,

[2]http://keplergo.arc.nasa.gov/ToolsUKIRT.shtml

Table 7.2. System Parameters of Kepler-78b

Parameter	Value	68.3% Conf. Limits
KIC number	8435766	...
R.A. (J2000)	19h 34m 58.00s	...
Decl. (J2000)	44°26'53.''99s	...
Effective temperature, $T_{\rm eff}$ [K][a]	5089	±50
Surface gravity, $\log g$ [g in cm s^{-2}][a]	4.60	±0.1
Metallicity, [m/H][a]	−0.14	±0.08
Projected rotational velocity, $v \sin i$ [km s^{-1}][a]	2.4	±0.5
Radial velocity of the star, γ [km s^{-1}]	−3.44	±0.08
Mass of the star, $M_\star$ [$M_\odot$][b]	0.81	±0.05
Radius of the star, $R_\star$ [$R_\odot$][b]	0.74	+0.10 −0.08
"Spectroscopic" mean stellar density, $\langle \rho_\star \rangle$ [g cm^{-3}][b]	2.8	+1.1 −0.8
Rotation period [days]	12.5	±1.0
Reference epoch [BJD$_{\rm TDB}$]	2454953.95995	±0.00015
Orbital period [days]	0.35500744	±0.00000006
Square of planet-to-star radius ratio, $(R_{\rm p}/R_\star)^2$ [ppm]	201	+57, −18
Planet-to-star radius ratio, $R_{\rm p}/R_\star$	0.0142	+0.0019, −0.0007
Scaled semimajor axis, $a/R_\star$	3.0	+0.5, −1.0
Orbital inclination, i [deg]	79	+9, −14
Transit duration (first to fourth contact) [hr]	0.814	+0.021, −0.015
"Photometric" mean stellar density[c], $\langle \rho_\star \rangle$ [g cm^{-3}]	3.8	+2.2, −2.7
Seasonal dilution parameters [%][d]	3.5, 0, 0.9, 5.5	± 1.2, 0, 1.2, 1.2
Occultation depth, $\delta_{\rm occ}$ [ppm]	10.5	±1.2
Amplitude of illumination curve, $A_{\rm ill}$ [ppm]	4.4	±0.5
Amplitude of ellipsoidal light variations, $A_{\rm ELV}$ [ppm]	<1.2	(3σ)
Planet radius, $R_{\rm p}$ [R$_\oplus$]	1.16	+0.19, −0.14
Planet mass, $M_{\rm p}$ [$M_\oplus$][e]	<8	(3σ)

Note. — The *Kepler* input catalog gives magnitudes $m_{\rm Kep} = 11.55$, $g = 12.18$, $r = 11.46$, $J = 10.18$, and $T_{\rm eff} = 4957 \pm 200$ K.

[a]Obtained from an SPC analysis of the spectra.

[b]Based on the relationships from [210].

[c]Defined as $\langle \rho_\star \rangle = (3\pi/GP^2)(a/R_\star)^3$

[d]In order, these refer to season 0, 1, 2 and 3.

[e]Based on absence of ellipsoidal light variations, assuming zero dilution.

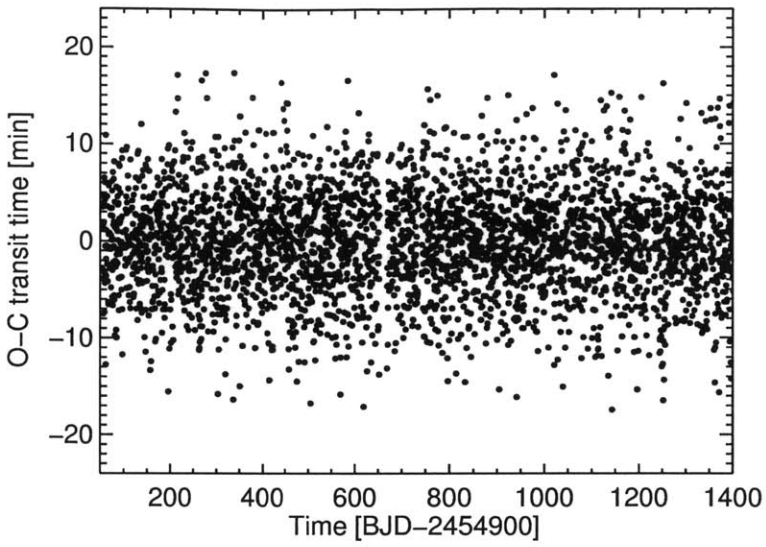

Figure 7-2: Deviations of individual transit times from strict periodicity.

and then fitted each individual transit with the same model, allowing only the time of transit to be a free parameter. As an estimate of the uncertainty in each data point, we used the standard deviation of the residuals of the phase-folded light curve.

The mean orbital period P and a fiducial transit time T_c were determined from a linear fit to the individual transit times, after performing 5 σ clipping to remove outliers. Table 7.2 gives the results, and Figure 7-2 shows the $O - C$ residuals. We searched the residuals for periodicities in the range 10-1000 days using a Lomb-Scargle periodogram [184], but found none with false alarm probability lower than 1%.

To search for any secular variation in the period, such as a period decrease due to tidal decay, we tried modeling the transit times with a quadratic function. The fit did not improve significantly. Based on this fit, the period derivative must be $|dP/dt| < 3.5 \times 10^{-10}$ (2σ). Using Kepler's third law, this can be transformed into a lower bound on the tidal decay timescale $a/\dot{a}$ of 4 Myr. This is not a particularly interesting bound, given that the stellar age is estimated to be 750 Myr.

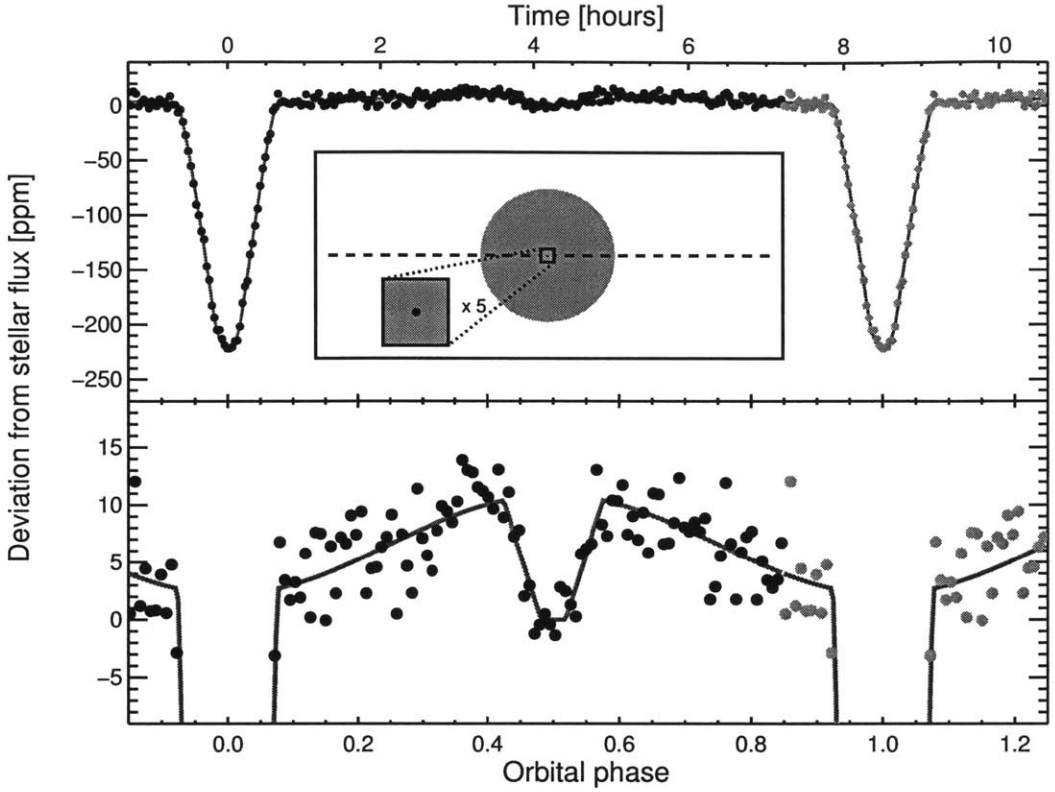

Figure 7-3: Transit and phase light curve of Kepler-78b.

Upper panel.—The final light curve (dots) and best-fitting model (red curve). The inset panel is a scale illustration of the system, where the length of the dashed line represents one possible orbital distance (both the impact parameter and the orbital distance are highly uncertain). The transits look V-shaped because of the 30 minute sampling, but shorter-cadence observations should reveal a much longer flat bottom in the middle of the transit. *Lower panel.*—Close-up of the illumination curve and occultation. The data have been binned to 4 min for clearer visual inspection.

7.3.2 Transit and illumination curve analysis

We then returned to the original time series and repeated the process of filtering out the starspot-induced variations, this time with the refined orbital period P and a slightly different procedure. The basic idea was to filter out any variability on timescales longer than the orbital period. First, we divide the flux series by its global flux maximum. Then, for each data point $f(t)$, a linear function of time was fit to all the out-of-transit data points at times t_j satisfying $|t - t_j| < P/2$. Then $f(t)$ was replaced by $f(t) - f_{\rm fit}(t) + 1$, where $f_{\rm fit}$ is the best-fitting linear function. Figure 3

shows the resulting light curve, after further correcting for seasonal-specific dilution as described below.

Subsequent analysis was restricted to data from quarters 2-15, since quarters 0 and 1 had shorter durations and the data seem to have suffered more from systematic effects. For each season, we phase-folded the data with period P and then reduced the data volume by averaging into 2 min samples. We then fitted a model including a transit, an occultation, and orbital phase modulations.

The transit model $f_{\rm tran}(t)$ was based on the [125] equations for the case of quadratic limb darkening. The parameters were the midtransit time t_0, the zero-limb-darkening transit depth $\delta_{\rm tran} = (R_p/R_\star)^2$, the impact parameter b, the scaled orbital separation $a/R_\star$, and the limb darkening coefficients u_1 and u_2. The orbital period was held fixed, and a circular orbit was assumed. The limb-darkening coefficients were allowed to vary, but the difference $u_1 - u_2$ was held fixed at 0.4, and the sum $u_1 + u_2$ was subjected to a Gaussian prior of mean 0.7 and standard deviation 0.1. These numerical values are based on the theoretical coefficients given by [42].

The occultation model $f_{\rm occ}(t)$ was a simple trapezoidal dip, centered at an orbital phase of 0.5, and with a total duration and ingress/egress durations set equal to those of the transit model. The only free parameter was the depth $\delta_{\rm occ}$.

The out-of-transit modulations were modeled as sinusoids with phases and periods appropriate for ellipsoidal light variations (ELV), Doppler boosting (DB), and illumination effects (representing both reflected and reprocessed stellar radiation). Expressed in terms of orbital phase $\phi = (t - t_c)/P$, these components are

$$A_{\rm DB} \sin(2\pi\phi) - A_{\rm ELV} \cos(4\pi\phi) - A_{\rm ill} \cos(2\pi\phi) \tag{7.1}$$

A constant was added to the model flux, specific to each of the 4 seasons, representing light from neighboring stars or differences in the fraction of starlight captured by the season-specific photometric apertures. Since a degeneracy prevents all 4 constants from being free parameters, we set this "dilution flux" equal to zero for season 1, for which initial fits showed that the dilution was smallest. The other constants

should be regarded as season-specific differences in dilution. The final parameter in the model is an overall flux multiplier, since only the relative flux values are significant. In the plots to follow, the normalization of the model and the data was chosen such that the flux is unity during the occultations, when only the star is seen.

For comparison with the data, the model was evaluated once per minute, and the resulting values were averaged in 29.4-min bins to match the time averaging of the *Kepler* data. Initial fits showed that the ELV and DB terms were consistent with zero. The non-detection of the DB term can, in principle, also be used to place upper bounds on several other effects, like inhomogeneities of the planetary albedo or a displacement of the hottest atmospheric spot on the surface of the planet with respect to the substellar point [62]. In the absence of these phenomena, the DB signal is expected to be negligible for this system (~ 0.02 ppm), so we set $A_{\rm DB} = 0$ in subsequent fits. We optimized the model parameters by minimizing the standard χ^2 function, and then used the best-fitting dilution parameters to correct all of the data to zero dilution.

Finally, we combined all of the dilution-corrected data to make a single light curve with 2-min sampling, and determined the allowed ranges for the model parameters using a Monte Carlo Markov Chain algorithm. The uncertainties in the flux data points were assumed to be identical and Gaussian, with magnitude set by the condition $\chi^2 = N_{\rm dof}$. Figure 7-3 shows the final light curve, with 4-min sampling, and the best-fitting model. Table 7.2 gives the results for the model parameters.

Some of these transit parameters might be affected by our choice for the filter. Using a filtering interval length of $2P$ or $3P$ rather than P gives similar-looking light curves but with increased scatter, as expected, since the accuracy of the linear approximation for the stellar flux modulation degrades for longer time intervals. We fit these two noisier light curves with the same model and found that most of the transit parameters are not changed significantly. The secondary eclipse depth obtained were 9.8 and 10.0 ppm, slightly smaller than the value quoted on Table 7.2. In the case of $A_{\rm ill}$, we obtained 4.30 and 4.65 ppm. We set the systematic error induced by the filtering to be equal to the standard deviation of the three values obtained with the three

different filtering periods, and add those in quadrature to the uncertainties obtained from the MCMC routine. In both cases this procedure increased the uncertainties by only 10%.

One notable result is that the transit impact parameter is nearly unconstrained, i.e., $0 \leq b \leq 0.9$. This is because the ingress and egress duration are poorly constrained, due to the 30 min averaging of the *Kepler* long-cadence data. For the same reason, $a/R_\star$ is poorly determined.

We were able to place an upper limit on the ELV amplitude of <1.2 ppm (3σ). This can be translated into an upper bound on the mass of the transiting companion using the formula ([136], [10]):

$$\begin{aligned} A_{\rm ELV} &= \left[\frac{0.15(15+u)(1+g)}{3-u}\right] \frac{M_{\rm p}}{M_\star} \left(\frac{R_\star}{a}\right)^3 \sin^2 i \\ &\approx 1.5 \, \frac{M_{\rm p}}{M_\star} \left(\frac{R_\star}{a}\right)^3 \end{aligned} \tag{7.2}$$

where u is the linear limb-darkening coefficient and g is the gravity-darkening coefficient. In this case we expect $u \approx 0.65$ and $g \approx 0.5$ [42]. The upper limit on the ELV amplitude thereby corresponds to a mass limit $M_p < 8\ M_\oplus$ (3σ). (This assumes the photometric signal is entirely from the transited star, with no dilution from neighboring stars; see the following section for a discussion of possible dilution.)

The preceding analysis assumed the orbit to be circular, which is reasonable given the short orbital period and consequently rapid rate expected for tidal circularization. We can also obtain empirical constraints on the orbital eccentricity e based on the timing and duration of the occultation relative to the transit. For this purpose we refitted the data adding two additional parameters, for the duration and phase of the occultation. As expected the data are compatible with a circular orbit, and give upper limits $|e\cos\omega| < 0.016$, $|e\sin\omega| < 0.15$ and $e < 0.24$ (3σ).

7.4 Validation as a planet

What appears to be the shallow transit of a planet may actually be the eclipse of a binary star system superposed on the non-varying light from the brighter intended target star. The binary could be an unrelated background object, or it could be gravitationally bound to the target star and thereby be part of a triple star system. In this section we examine these possibilities, and find it more likely that the signal actually arises from the transits of a planet.

7.4.1 Image photocenter motion

We start with an analysis of the image photocenter location, to try to extract information about the spatial location of the varying light source (see for example [100]). For each of the four *Kepler* seasons, we filtered the time series of the photocenter row and column pixel coordinates in the same manner that was described in Section 7.3.2 for the flux time series. For each of these time series, we calculated the mean of the in-transit coordinate, the mean of the out-of-transit coordinate, and the differences between those means, which we denote dx and dy. Using the filtered flux time series for each season, we also calculated the mean of the in-transit fluxes and the mean of the out-of-transit fluxes, both normalized to the overall mean flux. We denote the difference between these two means as df.

We then examined the ratios dx/df and dy/df. When either of these is multiplied by the pixel size (4"), one obtains the angular offset between the varying source of light and the out-of-transit image photocenter. One can then compare these offsets to the locations of the stars revealed in the UKIRT images. Since the celestial coordinates of the signals in the *Kepler* aperture are difficult to obtain with high accuracy, we used the center-of-light of the three detected stars in the J-band UKIRT image as our estimate for the celestial coordinates of the out-of-transit photocenter of the *Kepler* signal. The resulting determinations of the spatial location of the varying light source are shown in Figure 7-4. These results indicate that the source of the transit signal cannot be either of the two known neighboring stars. The variable source must be

located within 1" of Kepler-78, close enough to severely restrict the possibility of a blend with a background binary [138].

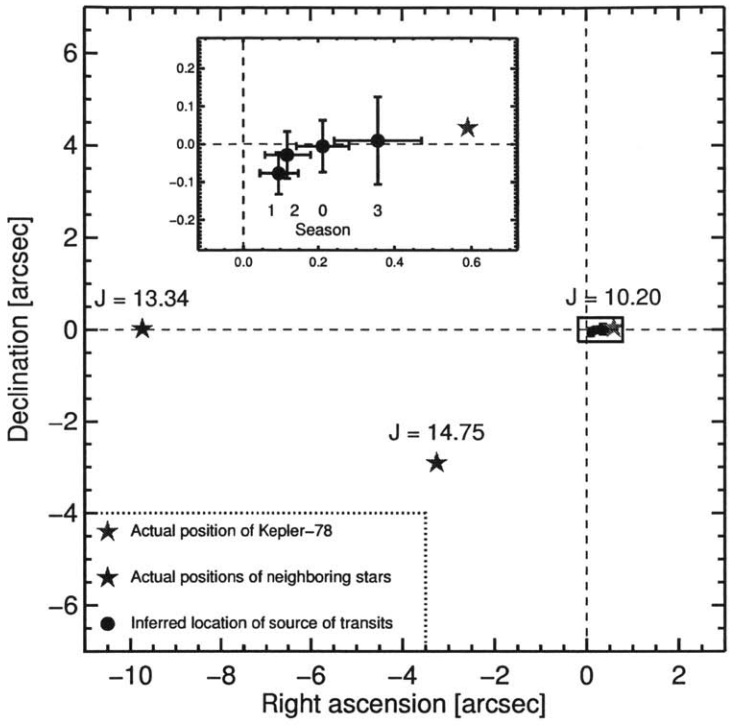

Figure 7-4: Centroid analysis and stellar companions.

Position of the three brightest stars (star symbols) in the vicinity of Kepler-78 relative to the center of light in J band (intersection of dashed lines). The positions of the source of the transits obtained from the centroid shifts (see text), represented by solid small circles with error bars, are close to the position of Kepler-78. The inset shows an expanded view of the vicinity of Kepler-78.

The inferred coordinates of the time-variable source are correlated with the *Kepler* seasonal dilution parameters (see Table 7.2), in a manner that is consistent with variable contamination by the brighter of the two neighboring stars. In season 1, when the diluting flux was found to be smallest, the centroid shift was also smallest (0.10 ± 0.06 arcsec). A zero centroid shift during transit implies that other sources of light have a negligible contribution to the total light within the aperture. Based on this, the brighter neighboring star can contribute no more than 1-2% of the total flux within the aperture during season 1. This supports our choice of a dilution parameter

equal to zero for season 1.

This analysis of the photocenter motion is sufficient for our purposes. However, as pointed out by [28], for a more detailed analysis it would be advisable to fit the pixel data using the *Kepler* Pixel Response Function, rather than using moment-based centroids as we have done.

7.4.2 Ellipsoidal light variations

The photocenter analysis cannot rule out the possibility that the observed phenomena are due to a background eclipsing binary gravitationally bound to the target star in a triple system or coincidentally within 1" of the target star. In such cases, though, the ELVs would generally be larger than the observed upper bound, as we show presently. This technique was recently used by [164] to validate a hot Jupiter.

In Section 7.3.2 we found that the upper limit on $A_{\rm ELV}$ leads to an upper limit on the companion mass of 8 $M_\oplus$. This analysis was based on the assumption that the dilution was small. If the signal arises from a faint unresolved eclipsing binary, the ELV signal could have been diluted by a large factor, weakening the constraint on the companion mass. However, an upper bound on the dilution factor can be obtained from further analysis of the folded light curve. This can be understood qualitatively as follows. If the dilution is severe, then the true transit/eclipse is much deeper than 200 ppm and the ratio of the radii of the secondary and primary star must be larger than the ratio inferred assuming no dilution. A large radius ratio implies relatively long ingress and egress durations, which at some point become incompatible with the observed light curve shape. The sensitivity of this test is hindered by the 29.4 min cadence of the *Kepler* data, but in this case it still provides a useful constraint.

For a quantitative analysis we reanalyzed the phase-folded light curve in a manner similar to that presented in Section 7.3.2. We suppose that the observed flux is $f(t) = f_0(t) + C$, where f_0 is the undiluted transit/occultation signal and C is the diluting flux. Since our model is always normalized to have unit flux during the occultation, we use units in which $f_0(t) = 1$ during the occultation, and we also

defined a normalized version of $f(t)$,

$$f_n(t) = \frac{f_0 + C}{1 + C}. \tag{7.3}$$

With this definition $A_{\rm trans} \approx (1 + C)A_{\rm trans,0}$, where $A_{\rm trans,0}$ is the observed depth of the transit and $A_{\rm trans}$ is the actual depth before dilution. We stepped through a range of values for C, finding the best-fitting model in each case and recording the goodness-of-fit χ^2. We found $C < 370$ with 3σ confidence.

In the presence of dilution, Eqn. (7.2) can be used to solve for the mass ratio,

$$\frac{m}{M} \approx \frac{2}{3}\,(1 + C)\,A_{\rm ELV}\left(\frac{a}{R}\right)^3, \tag{7.4}$$

using notation that does not presume the secondary is a planet (m and M are the secondary and primary masses, and R is the primary radius). An upper limit on the mass ratio follows from the constraints $C < 370$, $A_{\rm ELV} < 1.2$ ppm, and $a/R \lesssim 1.25P/(\pi T)$. The latter constraint follows from the requirement that the maximum eclipse duration of $\approx 1.25RP/\pi a$ exceed the observed eclipse duration T; the factor of 1.25 arises from the fact that at the maximum possible dilution the secondary star is approximately 1/4 the size of the primary star. The result is

$$\frac{m}{M} \lesssim \frac{2}{3}\,C\,A_{\rm ELV}\left(\frac{1.25P}{\pi T}\right)^3 \approx 0.023 \quad . \tag{7.5}$$

Having established that $m \ll M$ regardless of dilution, we may obtain a second condition on the mass ratio by using Kepler's third law, $GM/a^3 = (2\pi/P)^2$, to eliminate a from Eqn. (7.4). This gives

$$\frac{m}{M} \approx \frac{2}{3}C\,A_{\rm ELV}\left(\frac{GM}{R^3}\right)\left(\frac{P}{2\pi}\right)^2, \tag{7.6}$$

which leads to another inequality,

$$m < 3\,M_{\rm Jup}\left(\frac{M}{M_\odot}\right)^2\left(\frac{R}{R_\odot}\right)^{-3}. \tag{7.7}$$

The scaling with R^{-3} makes clear that the most massive secondaries are allowed for small primary stars, i.e., main-sequence stars and not giants. On the lower main sequence, $R \propto M$, allowing this inequality to be expressed purely as a function of primary mass,

$$m < 3\ M_{\rm Jup} \left(\frac{M}{M_\odot} \right)^{-1}. \tag{7.8}$$

The maximum value of m that satisfies both Eqn. (7.8) and Eqn. (7.5) is 8 $M_{\rm Jup}$, for $M = 0.36\ M_\odot$. On the upper main sequence, $R \propto M^{0.6}$ and there is little variation in M^2/R^3. Hence regardless of the primary mass, the secondary mass is in the planetary regime.

These ELV-based constraints allow for the possibility that the secondary is a giant planet or "super-Jupiter." However, we find scenarios involving a giant planet to be implausible. This is because no giant planet with a period <10 hr has ever been detected by any transit or Doppler survey, despite those surveys' strong sensitivity to such objects; it would be peculiar indeed for the first such system to be discovered as a blend with a *Kepler* target star. This is in addition to the theoretical problems of tidal decay, tidal inflation instability, Roche-lobe overflow, and evaporation that were mentioned in Section 1. Finally the absence of detectable image photocenter motion significantly reduces the probability of blend scenarios. We henceforth assume that the dilution is small and that the system is what it appears to be at face value: an Earth-sized planet in an extremely tight orbit around the target star.

7.5 Simple Physical Models

It is unusual to have access to the occultation and illumination signals of such a small planet. The only other terrestrial-sized planet for which these signals have been clearly detected is Kepler-10b [14], for which the planet is larger and the signal-to-noise ratio is lower than for Kepler-78b.

Extremely hot rocky planets are expected to be tidally-locked and have low-pressure atmospheres, free of volatiles which are removed from their surfaces by high intensity stellar winds and extreme-UV fluxes. Their atmospheres should mostly be

composed of heavier-element vapors with low pressure, which will not be efficient at bringing heat from the dayside to the nightside of the planet. [109] have modeled many of these effects, and proposed to call such objects "lava-ocean planets." If the nightside of the planet is much darker than the dayside we expect $\delta_{\rm occ} \approx 2A_{\rm ill}$, i.e., the system flux should be about the same during occultations as it is when only the nightside of the planet is in view. This has also been observed for some hot Jupiters, especially those with the highest temperatures, a sign that it is difficult to circulate heat to the night side [44]. Our light-curve analysis gives $\delta_{\rm occ}/2A_{\rm ill} = 1.20 \pm 0.15$, compatible with unity within 1.3σ. This is a good consistency check on the interpretation as a planet. If we repeat the light-curve analysis after imposing the constraint $\delta_{\rm occ} = 2A_{\rm ill}$, we find $\delta_{\rm occ} = 9.2 \pm 0.8$ ppm vs. the value of 10.5 ± 1.2 ppm without this constraint.

In this section we use simple physical models to interpret the occultation and illumination signals. These models assume that there is no mechanism for redistributing the energy across the planetary surface. Reflection, absorption and reradiation occur locally. Each element of the planet surface reflects a portion of the incident starlight and absorbs the remainder. The spectrum of the reflected starlight is taken to be identical to that of the incident starlight. The absorbed starlight heats the surface, which then radiates with a blackbody spectrum characterized by the local temperature. The directionality of both the reflected and thermally-emitted radiation are assumed to follow Lambert's law. Under these assumptions, the geometric albedo is 2/3 of the Bond albedo [44].

The equilibrium temperature $T_{\rm eq}$ of each element of the planet's surface is found through the expression

$$\sigma_{\rm SB} T_{\rm eq}^4 = (1 - A) F_{\rm inc}, \tag{7.9}$$

where A is the Bond albedo, $F_{\rm inc}$ is the power per unit surface area of the incident starlight, and $\sigma_{\rm SB}$ is the Stefan-Boltzmann constant. The finite size of the star and its finite distance from the planet are taken into account in computing $F_{\rm inc}$ via the evaluation of a numerical integral. The equilibrium temperature varies from a maxi-

mum value at the substellar point to zero in those regions where no part of the star is visible.

The *Kepler* telescope and detectors respond differently to radiation sources with different spectra. The differences are incorporated into our simple models via ratios of bolometric correction factors. These bolometric corrections were calculated with an accuracy adequate for the present purposes by numerically integrating blackbody spectra over the bandpass of the *Kepler* observations.[3] The stellar spectrum was taken to be that of a 5089 K blackbody.

Models were made for each of three sets of system parameters. The crucial parameters $\{a/R_\star, R_\mathrm{p}/R_\star\}$ took on the values $\{2.5, 0.0160\}$, $\{2.9, 0.0145\}$ and $\{3.3, 0.0130\}$ in the three models, spanning the reasonable range for these two parameters. The orbital inclination was set to give the observed transit duration. For each of the three models, the calculations were carried out for values of the Bond albedo A ranging from 0 to 1 in steps of 0.02.

The results of the calculations are shown in Figure 7-5. All three models yielded occultation depths consistent with the measured occultation depth (within 1σ). The thick black line represents the best-fitting models, which favor $A = 0.4$–0.6. However the uncertainty in the transit parameters remains large enough that any value of the albedo is allowed. In all of these models, the occultation depth is very nearly equal to the peak-to-peak amplitude of the illumination curve, as observed. Figure 7-5 also shows the model-derived maximum planet surface temperatures, which occur at the substellar point. The possibilities range from $T_\mathrm{eq} \approx 3000$ K for $A = 0$, to $T_\mathrm{eq} \lesssim 1500$ K for $A = 0.95$. The "lava-ocean model" would predict a relatively high albedo, in which a combination of low absorption and efficient backscatter of incident light by the melted materials could explain the high reflectivity [172]. A high albedo has also been inferred for Kepler-10b [14].

These considerations show that the occultation and illumination signals are compatible with the planetary interpretation. Both energy considerations and the observed illumination curve amplitude suggest that the nightside is darker than the

[3] http://keplergo.arc.nasa.gov/CalibrationResponse.shtml

dayside, but this conclusion depends on the unknown fraction of the occultation depth that is contributed by reflection as opposed to thermal emission. The thermal emission coming from the nightside, relative the stellar flux, is approximately $\delta_{\rm occ} - 2A_{\rm ill} = 1.7 \pm 1.6$ ppm. We can translate this into a constraint on the temperature of the nightside, by assuming a uniform temperature and taking into account the appropriate bolometric corrections. The result is $T_{\rm n} < 2700$ K (3σ). The dayside could have a similar temperature if the albedo is high enough, leaving open the possibility that the surface of the planet has a nearly uniform temperature—which, in turn, would imply efficient heat redistribution from the dayside to the nightside. Observations of the secondary eclipse in one or several different wavelengths will help distinguish between different models, allowing for a better measurement of the albedo and the day-night heat redistribution efficiency. Further modeling of the planet would also benefit from better knowledge of $a/R_\star$ and $R_p/R_\star$, which might be obtained from more finely-sampled photometric observations.

7.6 Discussion

We have interpreted the results as the discovery of the planet Kepler-78b orbiting a late G-type star with an orbital period of 8.5 hours, the shortest period among all of the well-documented planets transiting a main-sequence star. Our spectroscopic observations and light-curve analysis of Kepler-78 are all consistent with this scenario. The lack of radial velocity variations tells us that if the planet orbits Kepler-78, then its mass cannot be higher than $100\,M_\oplus$. The lack of ellipsoidal light variations confirms this with an even more stringent limit of only $8\,M_\oplus$. The ELV limit also eliminates the alternative scenario in which the signal is due to a blended eclipsing binary, since the transiting object must then have a mass lower than $8\,M_{\rm Jup}$. Those blend scenarios involving massive planets are also disfavored by the lack of anomalous image photocenter motion.

With a *Kepler* magnitude of 11.5, large ground-based telescopes could be used to detect the transit with several repeated observations. It may also be possible

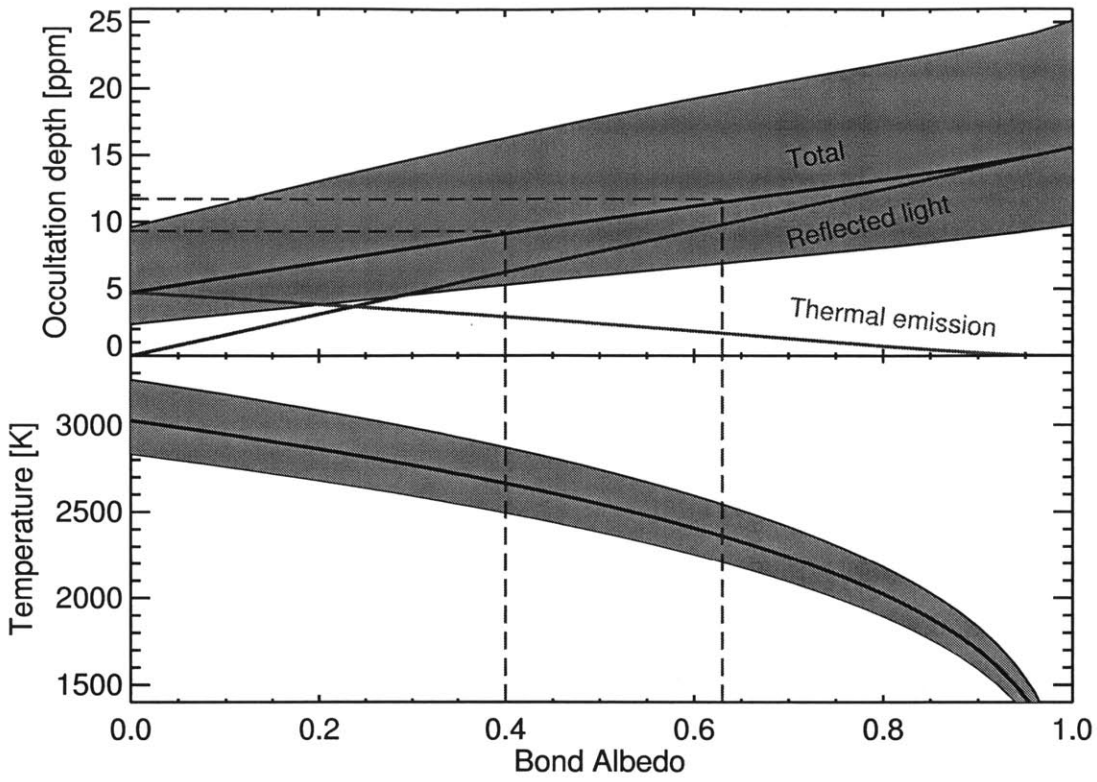

Figure 7-5: Interpreting the secondary eclipse depth

Upper panel.—Calculated occultation depth $\delta_{\rm occ}$ in parts per million as a function of the planet albedo. For the best fit solution the red curve shows the contribution from the thermal emission, while the blue curve represents the reflected light component. The brown dashed horizontal lines show the ± 1 σ region of the measured depth, and the vertical lines represent the allowed albedo values. *Lower panel.*— Maximum planet surface temperature as a function of albedo. In both panels, the shaded regions represent the $\pm$ 1 sigma interval of possible values.

to measure the mass of the planet through radial-velocity monitoring of the host star. An Earth-mass planet would induce a 1 m s^{-1} signal over a single night. The observations would require careful treatment of the starspot-induced spurious radial velocities, which should occur with amplitude $\approx$30 m s^{-1} over the 12.5-day stellar rotation period. If achieved, this would be the smallest planet with a measured mass [4]. Currently the only planets with radius smaller than 1.8 $R_\oplus$ for which the mass

[4]As discussed in the introduction of the next chapter, the mass measurement was achived by two different groups using two different instruments ([94], [151]). With a mass of $1.7M_\oplus$, it is currently the smallest planet with a mass and radius measurement.

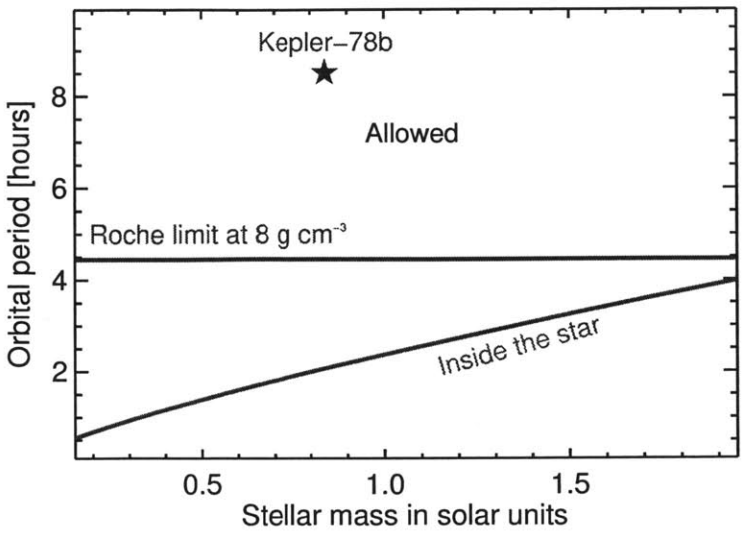

Figure 7-6: Shortest allowed periods of rocky planets as a function of the mass of a main-sequence host star.

The red curve is the limiting period at which the planet would be grazing the stellar photosphere. The green curve represents the limit on the orbital period at which the planet would be located at its Roche limit with a fiducial density of 8 g cm^{-3}. We also note that for really low mass planets, even rocky material could quickly evaporate at the equilibrium temperatures implied by these close distances, making those planets inviable at distances larger than their Roche limit. This is not the case for super-Earths which may be able to survive evaporation for very long intervals at orbital periods of only a few of hours (see, e.g., [152]).

has been measured are CoRoT-7b ([110], [161]), Kepler-10b [14], Kepler-11b ([112], [113]) and Kepler-36b [34], and none of these are smaller than 1.4 $R_{\oplus}$.

The robust detections of the occultations of the planet by the star, and of the time-variable illuminated fraction of the planet as it orbits around the star, make the system important for future observational and theoretical work. Observations with finer time sampling could better pin down the transit parameters. This in turn would clarify the equilibrium temperature of the planet's dayside, as explained in the previous section. It is unclear at this point if the occultations would be large enough in any band to be detected with any telescope besides *Kepler*, but the prospect of studying the surface or atmosphere of an Earth-sized exoplanet may be attractive enough to justify a large investment of telescope time.

In addition to the questions surrounding the existence and evolution of very hot terrestrial bodies, the relative ease with which this planet was detected and vetted shows the practical importance of searches for the shortest-period planets. We plan to document our list of short-period planet candidates found via Fourier transform analysis in the near future, which should provide other good targets for follow-up and shed some light on their occurrence rate and general characteristics. As a final note we point out that rocky planets could well exist with even shorter periods than we have found for Kepler-78b. We show in Fig. 7-6 that it is at least sensible to search for planet periods down to ~4 hours (see [169]).

We are indebted to Allyson Bieryla and Gilbert Esquerdo for their assistance with the spectroscopic follow-up observations. We also thank the referee, Nick Cowan, for a thorough critique of the manuscript. We thank Bryce Croll, Brice Demory, Amaury Triaud and Kevin Schlaufman for helpful discussions about this object, and of course we are grateful to the entire Kepler team for providing a wonderful tool for discovery. R.S.O. and J.N.W. acknowledge NASA support through the Kepler Participating Scientist Program. D.W.L. acknowledges partial support for the spectroscopic work from the Kepler mission under NASA Cooperative Agreement NNX13AB58A with the Smithsonian Astrophysical Observatory. This research has made use of the NASA Exoplanet Archive, which is operated by the California Institute of Technology, under contract with the National Aeronautics and Space Administration under the Exoplanet Exploration Program. The data presented in this article were obtained from the Mikulski Archive for Space Telescopes (MAST). STScI is operated by the Association of Universities for Research in Astronomy, Inc., under NASA contract NAS5-26555. Support for MAST for non-HST data is provided by the NASA Office of Space Science via grant NNX09AF08G and by other grants and contracts.

Chapter 8

Characteristics of the shortest-period planets

Published as: "A Study of the Shortest-Period planets Found With Kepler" Sanchis-Ojeda, R., Rappaport, S., Winn, J.N., Kotson, M.C., Levine, A., El Mellah, I., 2014, ApJ, 787, 47.

We present the results of a survey aimed at discovering and studying transiting planets with orbital periods shorter than one day (ultra–short-period, or USP, planets), using data from the *Kepler* spacecraft. We computed Fourier transforms of the photometric time series for all 200,000 target stars, and detected transit signals based on the presence of regularly spaced sharp peaks in the Fourier spectrum. We present a list of 106 USP candidates, of which 18 have not previously been described in the literature. This list of candidates increases from 2 to 7 the number of planet candidates with orbital periods shorter than about 6 hours. In addition, among the objects we studied, there are 26 USP candidates that had been previously reported in the literature which do *not* pass our various tests. All 106 of our candidates have passed several standard tests to rule out false positives due to eclipsing stellar systems. A low false positive rate is also implied by the relatively high fraction of candidates for which more than one transiting planet signal was detected. By assuming these multi-transit candidates represent coplanar multi-planet systems, we are able to infer

that the USP planets are typically accompanied by other planets with periods in the range 1-50 days, in contrast with hot Jupiters which very rarely have companions in that same period range. Another clear pattern is that almost all USP planets are smaller than 2 $R_{\oplus}$, possibly because gas giants in very tight orbits would lose their atmospheres by photoevaporation when subject to extremely strong stellar irradiation. Based on our survey statistics, USP planets exist around approximately $(0.51 \pm 0.07)\%$ of G-dwarf stars, and $(0.83 \pm 0.18)\%$ of K-dwarf stars.

8.1 Introduction

The field of exoplanetary science rapidly accelerated after the discovery of hot Jupiters with orbital periods of a few days ([132], [126]). More recently, another stimulus was provided by the discovery of terrestrial-sized planets with periods shorter than one day. These objects, which we will refer to as ultra-short period or USP planets, have many interesting properties. They are so close to their host stars that the geometric probability for transits can be as large as 40%. The expected surface temperatures can reach thousands of kelvins, allowing the detection of thermal emission from the planets' surfaces ([172], [50], [176]). The induced stellar orbital velocities can be as high as a few m s^{-1}, allowing the planet masses to be measured with current technology even for stars as faint as $V = 12$ ([94], [151]). Among the best known USP planets are 55 Cnc e ([46], [230], [49], CoRoT-7b ([110], [161]), and Kepler-10b [14].

The NASA *Kepler* space telescope [21] monitored the brightness of about 200,000 stars for 4 years, long enough to observe thousands of transits of a typical USP planet. Along with Kepler-10b, some of the more prominent USP discoveries have been the innermost planets of Kepler-42 [139] and Kepler-32 ([60], [207]) and the system Kepler-70, where two very short period planets were inferred by means of the light reflected by their surfaces [39]. However, since it was not clear that the official lists of *Kepler* USP planet candidates were complete, we and several other groups have performed independent searches. One object that emerged from our search was

the Earth-sized planet Kepler-78b [176], which has an orbital period of 8.5 hours and is currently the smallest exoplanet for which measurements of the mass and radius are both available ([94], [151]). [99] performed an independent search for planets with periods $P < 0.5$ day, finding several new candidates. More general surveys for *Kepler* planets have also found USP planets ([96], [145]). Particularly interesting is the discovery of KOI 1843.03 [145], a planet with an orbital period of only 0.18 days or 4.25 hr. [169] demonstrated that in order to survive tidal disruption, the composition of this Mars-sized planet must be dominated by iron as opposed to rock.

In this paper we describe a survey to detect USP planets using the entire *Kepler* dataset. Section 8.2 describes the data that we utilized in our study. Our Fourier-based transit search technique is explained in Section 8.3, along with the steps that were used to winnow down thousands of candidates into a final list of 106 likely USP planets. Section 8.4 presents the properties of the candidates. The issue of false positives within the USP list is examined in Section 8.5, with the conclusion that the false-positive probability is likely to be low. As a corollary we infer that most USP planets are accompanied by somewhat more distant planets. Section 8.6 gives estimates for the occurrence rate of USP planets, and its dependence upon period, radius, and the type of host star. Finally, Section 8.7 provides a summary of our findings and some remarks about the relevance of USP planets within the field of exoplanets.

8.2 Observations

8.2.1 Kepler data

To carry out an independent search for the shortest-period planets, we used the *Kepler* long-cadence time-series photometric data (30 min samples) obtained between quarters 0 and 16. A list was prepared of all ≈200,000 target stars for which photometry is available for at least one quarter, and the version 5.0 FITS files, which were available for all quarters, were downloaded from the STScI MAST website. We

used the data that had been processed with the PDC-MAP algorithm (Stumpe et al. 2012; Smith et al. 2012), which is designed to remove many instrumental artifacts from the time series while preserving any astrophysical variability. We also made use of the time series of the measured X and Y coordinates of the stellar images (the "centroids") in order to test for false positives (see section 8.3.2). Finally, we used the information in the file headers to obtain estimates of the combined differential photometric precision (CDPP). The CDPP is a statistic determined by the *Kepler* team's data analysis pipeline that is intended to represent the effective photometric noise level for detecting a transit of duration 6 hours [40]. We used this quantity in our analysis of survey completeness (see Section 8.5.1).

8.2.2 Stellar properties

For estimates of basic stellar properties including not only radii, but also masses and effective temperatures, we relied upon the catalog of [97]. This catalog is based on a compilation of photospheric properties derived from many different sources. Although it is not a homogeneous catalog, it likely provides the most accurate stellar parameters that are currently available. Stars for which only broadband photometry is available have radii that could be uncertain by up to ~40%, while stars for which spectroscopic or even astroseismic constraints are available have radius uncertainties as small as 10%.

8.3 The search

8.3.1 The Fourier Transform Technique

In our study of short-period planets, we elected to use a Fourier transform ("FT") search. Since this is different from the standard algorithm for transit searching—the Box Least Squares ("BLS") algorithm [105]—it seems appropriate to provide some justification for our choice. The BLS is designed to have the greatest efficiency for transits with a duration that is short in comparison to the orbital period. The Fourier

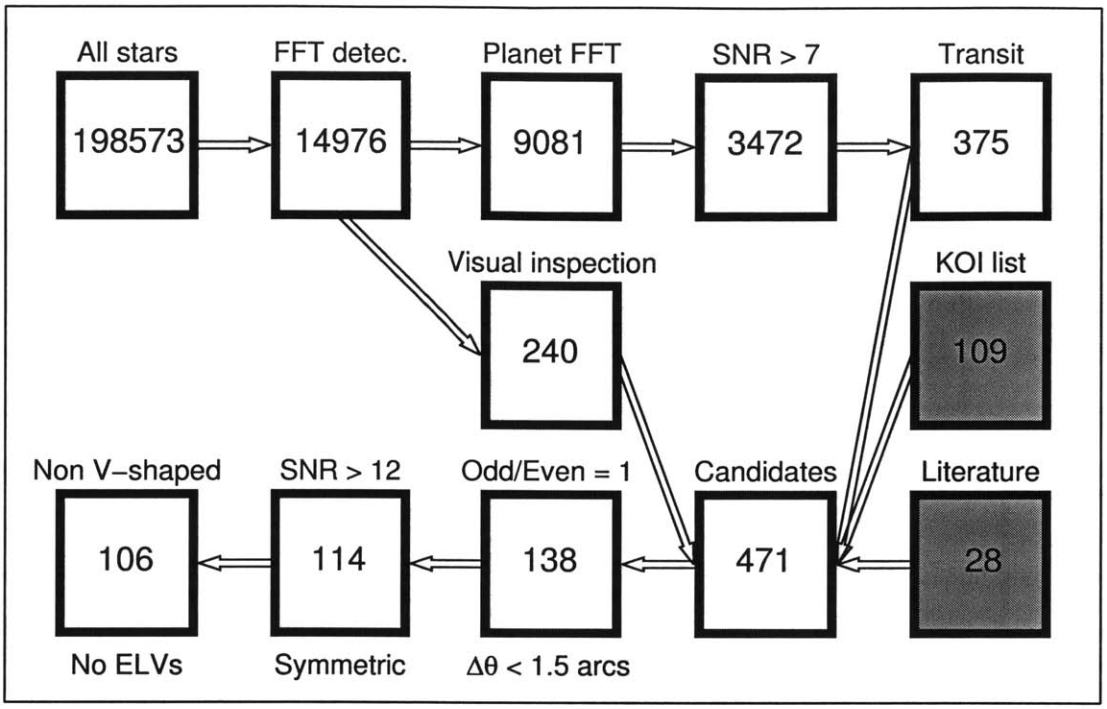

Figure 8-1: Flow diagram for our USP planet search.

The value in each box is the number of objects that remained at each successive stage of the search, beginning in the upper left corner with the 198,573 stars observed by *Kepler*. The upper row represents the automated portion of the search, which, together with visual inspection of the folded light curves (fifth box) yielded 375 candidates. This set of objects was combined with the objects that were identified by visual inspection, and some that had already been designated *Kepler* Objects of Interest (KOIs) or identified by other teams (gray boxes), to yield a total of 471 distinct candidates that were studied in greater detail. After applying several tests for false positives caused by foreground and background binary stars (see Figure 8-4), and imposing a limiting signal-to-noise ratio of 12 in the folded light curve, we arrived at a final list of 106 USP candidates.

spectrum of an idealized transit light curve has a peak at the orbital period and a series of strong harmonics. By using a matched filter, the BLS algorithm effectively sums all of the higher harmonics into a single detection statistic, which seems like a superior approach.

However, the standard BLS has a few drawbacks. One is that the BLS spectrum includes peaks at multiples of the orbital period *and* at multiples of the orbital frequency, thereby complicating attempts to ascertain the correct period. In addition, we have found that the standard BLS algorithm produces spurious signals at periods that are integer multiples of the *Kepler* sampling period of $\approx$0.02 day. These spurious

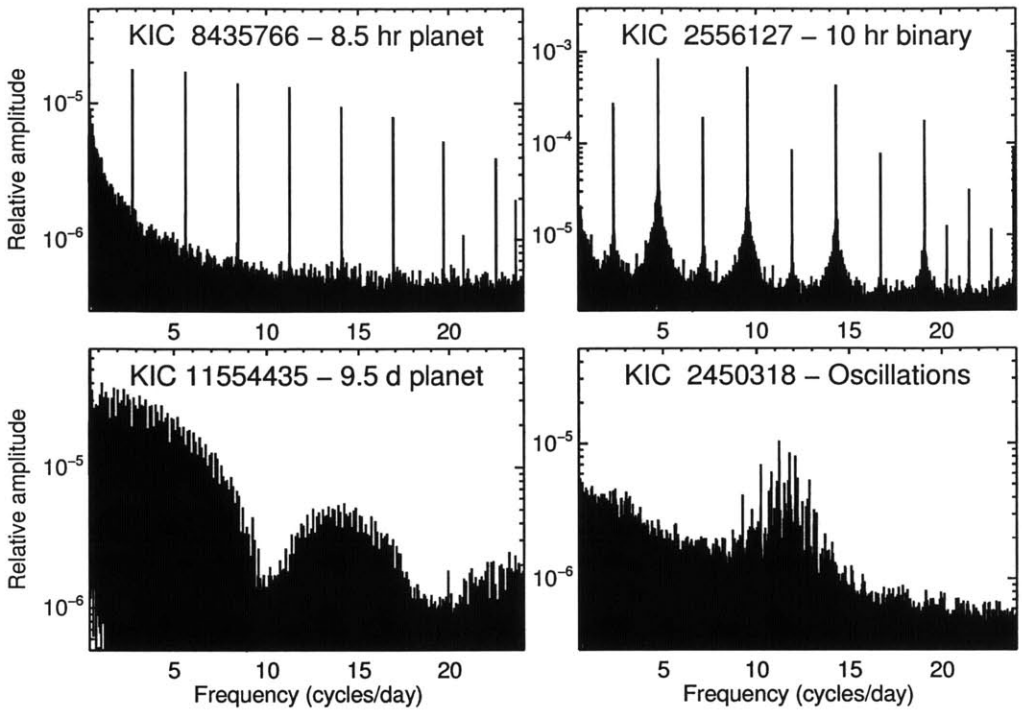

Figure 8-2: Illustrative FT amplitude spectra for different types of systems.

Upper left.—A short-period planet (Kepler-78b; see Chapter 7), showing a series of harmonics with amplitudes that decrease monotonically and gradually with frequency. *Upper right.*—An eclipsing pair of stars, showing peaks that alternate in amplitude. *Lower left.*—A long-period planet (Kepler-63b; see Chapter 5), showing very closely-spaced harmonics; the presence of long-period planets complicates the Fourier-based detection of any short period planets. *Lower right.*—Oscillations of a subgiant star.

peaks constitute a highly significant noise background in searches for planets with periods $\lesssim$0.5 day. These spurious peaks can be partially suppressed by pre-whitening the data, i.e., attempting to remove the non-transit astrophysical variability prior to computing the BLS spectrum, but the introduction of such a step complicates the search.

A key advantage of the FT method is that FTs can be computed so quickly that it was practical to repeat the search of the entire database several times while the code was being developed (see for example the simulations by [104]). Although the FT of a transit signal has power that is divided among several harmonics, the number of significant harmonics below the Nyquist limit declines as the orbital period is

decreased, and the FT is therefore quite sensitive to the shortest-period planets. The ratio of transit duration to period, or duty cycle, varies as $P^{-2/3}$ and is as large as 20% for USP planets, in which case the efficacy of the FT search is nearly equivalent to that of the BLS. Furthermore, it is straightforward to detect a peak in the FT and its equally-spaced harmonics, either by means of an automated algorithm or by eye. The absence of any subharmonics is a useful and important property of true planet transits as opposed to background blended binaries (which often produce subharmonics due to the difference in depth between the primary and secondary eclipses).

Regardless of the justification, it is often worthwhile to carry out searches with different techniques. Thus far, the independent searches of the *Kepler* database have utilized the BLS technique ([145], [96], [154], [99]), and for this reason alone it seemed worthwhile to take a different approach. In the end, though, the proof of the effectiveness of an FT search lies in what is found, and in this work we demonstrate empirically that the FT is a powerful tool for finding short-period planets.

8.3.2 Preliminary analysis of the candidates

Figure 8-1 is a flow chart illustrating the numbers of the $\sim 200,000$ *Kepler* stars that survived each stage of our search program. The PDC-MAP long-cadence time series data from each quarter was divided by the median flux of that quarter. We removed outliers with flux levels 50% above the mean (likely due to cosmic rays), and all of the quarterly time series were stitched together into a single file. We further cleaned the data using a moving-mean filter with a length of 3 days. Using a filter to clean the data does not affect our ability to detect high frequency signals as long as the length of the window captures a few cycles of the target signal, and, at the same time, it increases the sensitivity to signals at intermediate frequencies, since it removes long-term trends that have the potential to increase the FT power at these frequencies. To prepare the data for the application of the Fast Fourier Transform (FFT), gaps in the time series were filled by repeating the flux of the data point immediately prior to the gap. The mean flux was then subtracted, giving a zero-mean, evenly-spaced time series. The FFT was then evaluated in the conventional manner all the way up

to the Nyquist limit, i.e., the number of frequencies (n_f) in the transform is equal to half the number of data points.

We searched for the presence of at least one peak that is more than 4 times the local mean level in the Fourier amplitude spectrum (square root of the power spectrum), with a frequency higher than 1 cycle day^{-1}. The local mean level was estimated using the closest $n_f/250$ frequencies, a number close to 120 for stars with 16 quarters of data. (This number is large enough to ensure that the interval used to estimate the local mean level is much wider than the FFT peaks, and that any possible contribution to the mean local level due to the peak is much smaller than the true local mean level.) In order for the target to be considered further, we also required that the FT exhibit at least one additional harmonic that stands out at least 3 times the local mean. For the selected objects, we increased the accuracy of the peak frequencies by calculating the FFT of a new flux series that was built from the original series by adding as many zeroes as needed to multiply the length of the array by a factor of 20 (a process known as "frequency oversampling").

Approximately 15,000 objects were selected by virtue of having at least one significant high-frequency peak and a harmonic. These objects underwent both visual and automated inspection.

First, all the Fourier spectra were examined by eye. Those that showed peaks at several harmonics with slowly monotonically decreasing amplitudes, all of which were higher than 1 cycle day^{-1}, were selected for further study (see Figure 8-2 for some examples of the FT spectra). This process resulted in 240 objects worthy of attention, and was effective in quickly identifying the targets with the highest signal-to-noise ratios (SNRs) and periods shorter than 12-16 hours, such as Kepler-78b [176].

Second, our automatic vetting codes were used to try to identify and reject unwanted sources such as long-period planets, eclipsing binaries, and pulsators. The initial step in this process was to find all significant FT peaks with an amplitude 4 or more times the local noise level. Next, all objects with more than 10 significant frequencies between 1 and 10 cycles day^{-1}, a clear sign that the system is a pulsator or long-period planet and not a short-period transiting planet, were rejected. In other

cases where frequencies lower than 1 cycle day^{-1} were detected and successfully identified as the true periodicity of the signal, the sources were also rejected. Application of these filters reduced the number of candidates from 15,000 to $\sim 9,000$.

The surviving candidates then underwent a time-domain analysis. To remove the slow flux variations caused by starspots and stellar rotation, a moving-mean filter was applied to the flux series, with a width in time equal to the candidate orbital period. The data were then folded with that period, and the light curve was fitted with three models: a simple transit model, a sinusoid with the candidate period, and a sinusoid with twice the candidate period. For a candidate to survive this step, the transit signal needed to be detected with SNR ≥ 7, and the transit model needed to provide a fit better than the fits of either of the sinusoidal models. This automated analysis reduced the number of objects from 9,000 to $\sim 3,500$.

The folded light curves were then inspected by eye. We found that in many cases the automated pipeline was still passing through some longer-period planets and pulsators. However, with only 3,500 objects, it was straightforward to reduce the list further through visual inspection of the folded light curves. We selected only those light curves with plausible transit-like features, including transit depths shallower than 5 to 10%, to reduce the list of surviving candidates along this pathway to 375.

We then combined the following lists: the 240 candidates from visual inspection of the FTs; the 375 candidates from the automated pipeline followed by visual inspection of the folded light curves; the 109 candidates with $P < 1$ day in the KOI list (as of January 2014; [3]); and the 28 candidates with $P < 1$ day that emerged from the independent searches of [145], [96] and [99]. There was substantial overlap among these various lists (see Figure 8-3). The result was a list of 471 individual candidates. The next step was to subject these candidates to selected standard *Kepler* tests for false positives [16].

The first in this series of tests was the image centroid test which was used to reject those systems wherein the apparent motion of the stellar image during transits was large enough to rule out the *Kepler* target as the main source of the photometric variations. To carry out this test, the time series comprising the row (X) image

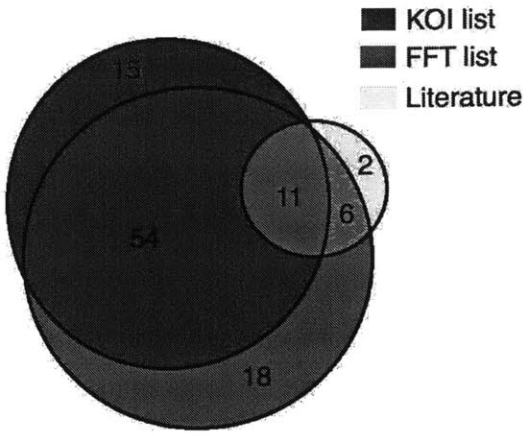

Figure 8-3: A Venn diagram describing the origin of the 106 USP candidates in our final list.

Our pipeline has been able to independently detect 89 out of these 106 candidates, with all missed planets having orbital periods longer than 12 hours. The literature contribution only counts those planets that were first detected by other groups ([145], [96] and [99]) for a total of 19 USP planet candidates, since currently we have no knowledge about how many of the other 87 USP planet candidates they could have detected independently.

centroid estimates and that comprising the column (Y) estimates were each processed with the moving-mean filter that was used for the flux time series. Each filtered time series was folded with the candidate period. The degree of correlation between the flux deviations and the centroid deviations was then calculated by computing the values of dY/df and dX/df, where dX and dY represent, respectively, the in versus out of transit change in row or column pixel position, and df represents the in versus out of transit change in relative flux. These gradients were multiplied by the *Kepler* plate scale of 4 arcsec pixel^{-1} in order to estimate the location of the flux-variable source with respect to the center-of-light of the sources within the photometric aperture ([100], [28]).

A significant centroid shift implies the presence of more than one star in the *Kepler* aperture, but does not necessarily imply that the object should be classified as a false positive; even if the intended *Kepler* target is indeed the source of the photometric variations, the steady light of other nearby stars would cause the centroid to move during transits. Ideally, one would use the measured centroid shift and the known

positions and mean fluxes of all the stars within the *Kepler* aperture to pinpoint the variable star. In the present case, though, the best available images (from the UKIRT *Kepler* field survey[1]) only allow us to differentiate fainter companion stars outside of a limiting separation that is target-dependent. For example, a star 2 magnitudes fainter than the target star may be difficult to distinguish from the target star at separations less than an angle as small as 1" or as large as 3" [221].

Our procedure was to rely on the fact that very large centroid shifts almost always indicate a false positive, since the *Kepler* target is, by construction, intended to be the dominant source of light in the photometric aperture. The distribution of positions relative to the center of light among the objects under study may be reasonably modelled by the superposition of a uniform distribution out to distances beyond 40" and a Gaussian distribution centered at the center of light and having a width in each orthogonal coordinate characterized by a standard deviation close to 0.5". Based on this, we discarded those sources where the best-fit distance from the flux-variable source to the center-of-light exceeded 1.5" and a 3σ lower bound exceeded 1". This test assures that the "radius of confusion" (the maximum distance from the target star where a relevant background binary could be hiding) for almost all of the candidates is smaller than 2". This is illustrated in the upper left panel of Figure 8-4. It was shown by [137] that by shrinking the radius of confusion to this level, the probability of false positives due to background binaries is reduced to of order 5%. This centroid test eliminated half of the remaining candidates, confirming that short-period eclipsing binaries in the background are an important source of false positives.

The second in this series of tests was a check for any statistically significant ($>3\sigma$) differences between the depths of the odd- and even-numbered transits. Such a difference would reveal the candidate to be an eclipsing binary with twice the nominal period (see lower left panel of Figure 8-4). Approximately 40% of the objects were removed on this basis.

Third, there were five cases in which primary eclipses with a depth in the range 0.5-2% were accompanied by secondary eclipses 5 to 10 times shallower, similar to

[1]http://keplerscience.arc.nasa.gov/ToolsUKIRT.shtml

what is expected for a high-albedo hot Jupiter in such a short period orbit. However, the orbits of all 5 objects were found to be synchronized with the rotation of their host stars, and a close inspection revealed that in all cases the secondary's brightness temperature (inferred from the secondary eclipses) was higher than what would be expected from a planet (assuming zero albedo and inefficient transfer of heat to the nightside), both of which are signs that these objects are probably low-mass stars rather than planets (see [51]).

Finally, we eliminated every candidate with a transit signal-to-noise ratio less than 12, after judging that such detections are too weak to put meaningful constraints on false positive scenarios, and also out of concern that the pipeline might not be complete at low signal-to-noise ratios (as confirmed in Section 8.5.1). This eliminated 22 more candidates. Within the remaining systems were two special cases, KIC 12557548 and KOI-2700 ([168], [167]), which have asymmetric transit profiles that have been interpreted as signs that these planets are emitting dusty comet-like tails. Since the relationship between transit depth and planet radius is questionable for these objects, they were removed from our sample at this stage.

8.4 Light curve analysis

Once the number of USP candidates was reduced to 114, we performed a more sophisticated light curve analysis. In particular, we wanted to make sure that systems with non-planetary transits or out-of-eclipse variations were completely removed. These tests, described below, also led to more reliable determinations of the transit parameters.

8.4.1 Transit times and orbital period

Using a trial period obtained from the FT, we folded each light curve, binned it in phase, and fitted a simple trapezoidal model representing the convolution of the transit profile and the 30 min sampling function. The free parameters were the duration, depth, the ingress (or egress) time, and the time of the midpoint.

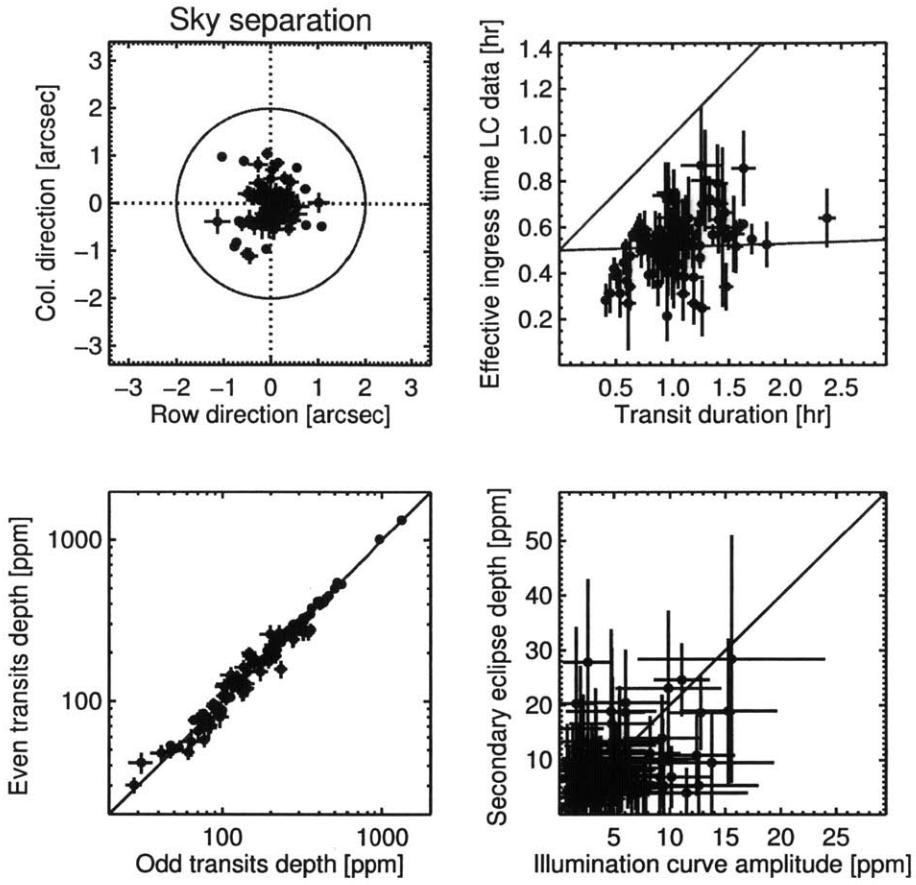

Figure 8-4: The four main tests for false positives

. Shown here are those 106 USP candidates in our final list, which have passed all our tests designed to rule out false positives. *Upper left.*—Centroid test. The measured change in position of the stellar images during transits was converted into a sky separation between the variable star and the center of light within the *Kepler* aperture. The blue circle at 2 arcsec represents the approximate radius of confusion (see text) for all our objects. *Upper right.*—Ingress/egress test. A comparison between the apparent ingress/egress time and total transit duration. A small planet would produce a data point on the blue line, where the ingress time is approximately equal to 29.4 min (the sampling time of the observations), whereas a background eclipsing binary with comparably sized stars and a characteristically V-shaped light curve would produce a data point on the red line. *Lower left.*—Odd/even test. The even and odd transit depths are statistically indistinguishable for all our candidates, constraining the possible background binaries to be close to identical stars. *Lower right.*—For a true USP planet, any detected illumination curve should be accompanied by a secondary eclipse with a depth equal to twice the illumination amplitude (blue line). Otherwise, the out of eclipse variations could be attributed to ELVs from a background binary with twice the orbital period.

With the best-fitting model in hand, the orbital period was recalculated according to the following procedure. For most of the candidates, individual transit events could not be detected with a sufficiently high SNR to obtain individual transit times. Instead, we selected a sequence of time intervals each spanning many transits, and the data from each interval were used to construct a folded light curve with a decent SNR. To decide how long the time intervals should be, we considered $\mathrm{SNR}_q = \mathrm{SNR}/\sqrt{q}$, where SNR is the signal-to-noise ratio of the transit in the full-mission folded light curve and q is the total number of quarters of data available. For the cases with $\mathrm{SNR}_q < 10$, the intervals were chosen to span two quarters. For $10 < \mathrm{SNR}_q < 20$, the intervals spanned one quarter. For $20 < \mathrm{SNR}_q < 30$, the intervals spanned one-third of a quarter (approximately one month), and finally for $\mathrm{SNR}_q > 30$ the intervals spanned one-sixth of a quarter (approximately half a month). The trapezoidal model was fitted to each light curve to determine a mean epoch. For these fits, all parameters except the mean epoch were held fixed at the values determined for the full-mission folded light curve. Then, the collection of mean transit epochs was used to recalculate the orbital period. The formal uncertainty of each mean epoch was calculated using $\Delta\chi^2 = 1$, where χ^2 was normalized to be equal to the number of degrees of freedom. We then fitted a linear function to the mean epochs. In this manner the final transit ephemeris was determined. We examined the residuals, and did not find any cases of significant transit-timing variations. This finding is consistent with the prior work by [201] who noted that such short-period planets tend to avoid near mean-motion resonances with other planets.

8.4.2 Transit and illumination curve analysis

We then returned to the original time series and repeated the process of filtering out variability on timescales longer than the orbital period, including starspot-induced variations. In this instance, the refined orbital period P and a slightly different procedure were used. For each data point f_0 taken at time t, a linear function of time was fitted to the out-of-transit data points at times t_j within $P/2$ of t_0. Then $f_0(t)$ was replaced by $f_0(t) - f_{\mathrm{fit}}(t) + 1$, where f_{fit} was the best-fitting linear function.

Illustrative filtered and folded light curves are shown in Figure 8-5.

Further analysis was restricted to data from quarters 2-16, since quarters 0 and 1 were of shorter duration than the other quarters, and the data seem to have suffered more from instrumental artifacts. For each system, the data were folded with period P and then binned to reduce the data volume and to enhance the statistics. The bin duration was 2 min unless this resulted in fewer than 240 bins, in which case the bin duration was set to $P/240$ (as short as 1 minute for orbital periods of 4 hours). The trapezoidal model was fitted to this binned light curve. Due to the long cadence 30 min time averaging, the effective ingress duration of the transit of a typical short-period small planet (with a transit duration of one to two hours) will then be slightly longer than 30 min. However, in the case of a background binary, the ingress time can be much longer, up to half the duration of the entire event (see the upper right panel of Figure 8-4). Once the best-fitting parameters were found, the allowed region in parameter space was defined with a Markov Chain Monte Carlo (MCMC) routine , which used the Gibbs sampler and the Metropolis-Hastings algorithm, and a likelihood proportional to $\exp(-\chi^2/2)$ (see, e.g., Appendix A of [208], or [91]). We found that five of the USP candidates had ingress times significantly longer than 45 minutes (with $>3\sigma$ confidence). These were removed from the candidate list.

With the list now reduced to 109 candidates, final transit parameters were determined. Our final model included a transit, an occultation, and an orbital phase modulation. For the transit model we used an inverse boxcar (zero ingress time, and zero limb darkening) for computational efficiency. More realistic transit models are not justified given the relatively low SNR and the effects of convolution with the 30 min sampling function. The parameters were the midtransit time t_0, the transit depth $\delta_{\rm tran} \equiv (R_p/R_*)^2$, and the transit duration. The orbital period was held fixed, and a circular orbit was assumed.

The occultation (i.e., secondary eclipse) model $f_{\rm occ}(t)$ was also a boxcar dip, centered at an orbital phase of 0.5, and with a total duration set equal to that of the transit model. The only free parameter was the occultation depth $\delta_{\rm occ}$. The orbital phase modulations were modeled as sinusoids with phases and periods appropriate

for ellipsoidal light variations (ELV), illumination effects (representing both reflected and reprocessed stellar radiation) and Doppler boosting (DB). Expressed in terms of orbital phase $\phi = (t - t_c)/P$, these components are

$$-A_{\rm ELV}\cos(4\pi\phi) - A_{\rm ill}\cos(2\pi\phi) + A_{\rm DB}\sin(2\pi\phi) \quad , \tag{8.1}$$

respectively, where t_c is the time of the transit center. The final parameter in the model is an overall flux multiplier, since only the relative flux values are significant and there is always an uncertainty associated with the normalization of the data. In the plots to follow, the normalizations of the model and the data were chosen to set the flux to unity during the occultations when only the star is visible. For comparison with the data, the model was evaluated every 30 seconds, and the resulting values were averaged in 29.4 min bins to match the time averaging of the *Kepler* data.

Finally we determined the allowed ranges for the model parameters using a Monte Carlo Markov Chain algorithm. The errors in the flux data points in a given folded and binned light curve were set to be equal and defined by the condition $\chi^2 = N_{\rm dof}$. No ELVs were found with amplitudes at or exceeding the $>3\sigma$ confidence level; hence, all of the candidates passed this test. Secondary eclipses were detected in seven cases with amplitudes consistent with those of USP planets. In three cases, an illumination component was detected while the corresponding secondary eclipses were not detected: $\delta_{\rm occ}/A_{\rm ill} < 2$ with 3σ confidence. For one of them the DB component was also detected (the only system that did not past that test). Those three candidates were eliminated from the list because only a background binary with twice the nominal period could plausibly be responsible for the out-of-eclipse variability without producing a secondary eclipse (see the lower right panel of Figure 8-4). We can also compare our results with some literature values. We obtained a secondary eclipse of 7.5 ± 1.4 ppm for Kepler-10b, a bit smaller than the value found by [64] of 9.9 ± 1.0 ppm, using only the SC data, but slightly larger than the original value reported by [14] of 5.8 ± 2.5.

Based on the measured transit depth, and the stellar radius from [97], we calcu-

lated the implied planet radius. Based on our results for Kepler-78b [176], we added a 20% systematic uncertainty to the marginalized distribution of transit depths to account for the lack of limb darkening in our transit model. In almost all cases the uncertainty in the planet radius was still dominated by the uncertainty in the stellar radius.

One of the limitations of our transit analysis is that we could not readily obtain a value for the scaled semi-major axis (a/R_*), which can ordinarily be obtained when fitting high-SNR transit light curves, and is needed for computing planet occurrence rates due to its role as the inverse geometric transit probability. We can obtain a good estimate using the approximate relation:

$$\frac{a}{R_\star} \approx \frac{P}{\pi T}\sqrt{1-b^2} \tag{8.2}$$

where P is the known orbital period, T is the total duration of the transit, and b is the impact parameter. For each of the values of T obtained in the MCMC analysis, we evaluate the expression on the right-hand side using a value of b drawn from a uniform distribution over the interval 0.0 to 0.9. The latter limit was not set to 1.0 because the transits in very high impact parameter cases are very short in duration and therefore very difficult to detect. Since the uncertainty in a/R_*, estimated as the standard deviation of the final distribution, is large and dominated by the wide range of allowed b values, the *systematic* error induced by using equation (8.2) can be neglected.

Within our final list of 106 USP planet candidates, 8 candidates emerged uniquely from our search, including Kepler-78b (see Fig. 8-3 for a diagram describing the origin of all 106 candidates). Another 10 objects were flagged by the *Kepler* pipeline but were marked as false positives in the updated KOI list [3], because, in at least some of the cases, the pipeline gave the wrong orbital period (the pipeline is not intended to work with periods below 12 hours). The transit light curves of these 18 candidates are shown in Figure 8-5, and the transit parameters are given in Table 8.3.

An examination of the KOI list shows that 27 KOI planet candidates with orbital

periods shorter than 1 day were excluded in our analysis, either because of a low SNR (8 KOIs), or because those candidates did not pass our tests intended to exclude false positives (19 KOIs). Similarly, 7 planet candidates proposed by [145], [96], or [99] did not appear in the KOI list, and also did not pass our tests. This information is summarized in Table 8.1.

Table 8.1: USP planet candidates that appear in the literature but do not appear in our final list.

SNR ¡ 12	Odd-even difference	Phase curve analysis
KIC2986833 / KOI4875.01	KIC4844004 / KOI1662.01	KIC6690836 / KOI2699.01
KIC3550372 / KOI4357.01	KIC5387843 / KOI1762.01	KIC8564672 / HUANG13
KIC5033823 / KOI4546.01	KIC5801571 / KOI225.01	KIC10453521 / JACKSON13
KIC5208962 / KOI4912.01	KIC6028860 / KOI2950.01	KIC11456279 / KOI3204.01
KIC5371777 / KOI4327.01	KIC6129694 / KOI4131.01	KIC12692087 / HUANG13
KIC7668416 / KOI3089.01	KIC7681230 / KOI4294.01	
KIC10140122 / KOI4545.01	KIC9044228 / KOI1988.01	
KIC11973517 / KOI4862.01	KIC9535585 / HUANG13	
	KIC11774303 / KOI2269.01	
	KIC12109845 / KOI3765.01	

Centroid shift	Other[b]
KIC2558370 / KOI3855.01	KIC5475431 / KOI1546.01 (BD)
KIC5436161 / KOI4351.01	KIC6526710 / OFIR13 (NF)
KIC6185496 / HUANG13	KIC8639908 / KOI2700.01 (ATP)
KIC6209798 / HUANG13	KIC12557548 / KOI3794.01 (ATP)
KIC6279974 / KOI1812.01	
KIC9752982 / KOI3871.01	
KIC12069414 / KOI4512.01	

Planets with no assigned KOI number have a name tag built from the first
name of the first author of the discovery paper followed by the two digit year of publication ([145], [96], and [99]).
b)BD stands for likely Brown Dwarf. ATP stands for asymmetric transit profile, likely due to a dust
tail emerging from the planet ([168], [167]). NF stands for not found in the data.

8.4.3 Planetary radius distribution

Figure 8-6 shows the radii and orbital periods of the 106 USP candidates. In this figure we have identified the planets orbiting G and K dwarf stars (4100 K $< T_{\rm eff} <$ 6100 K, 4.0 $<$ log $g <$ 4.9), which represent the subset of stars where most of the planets are detected. One striking feature of this group is the relative scarcity of planets larger

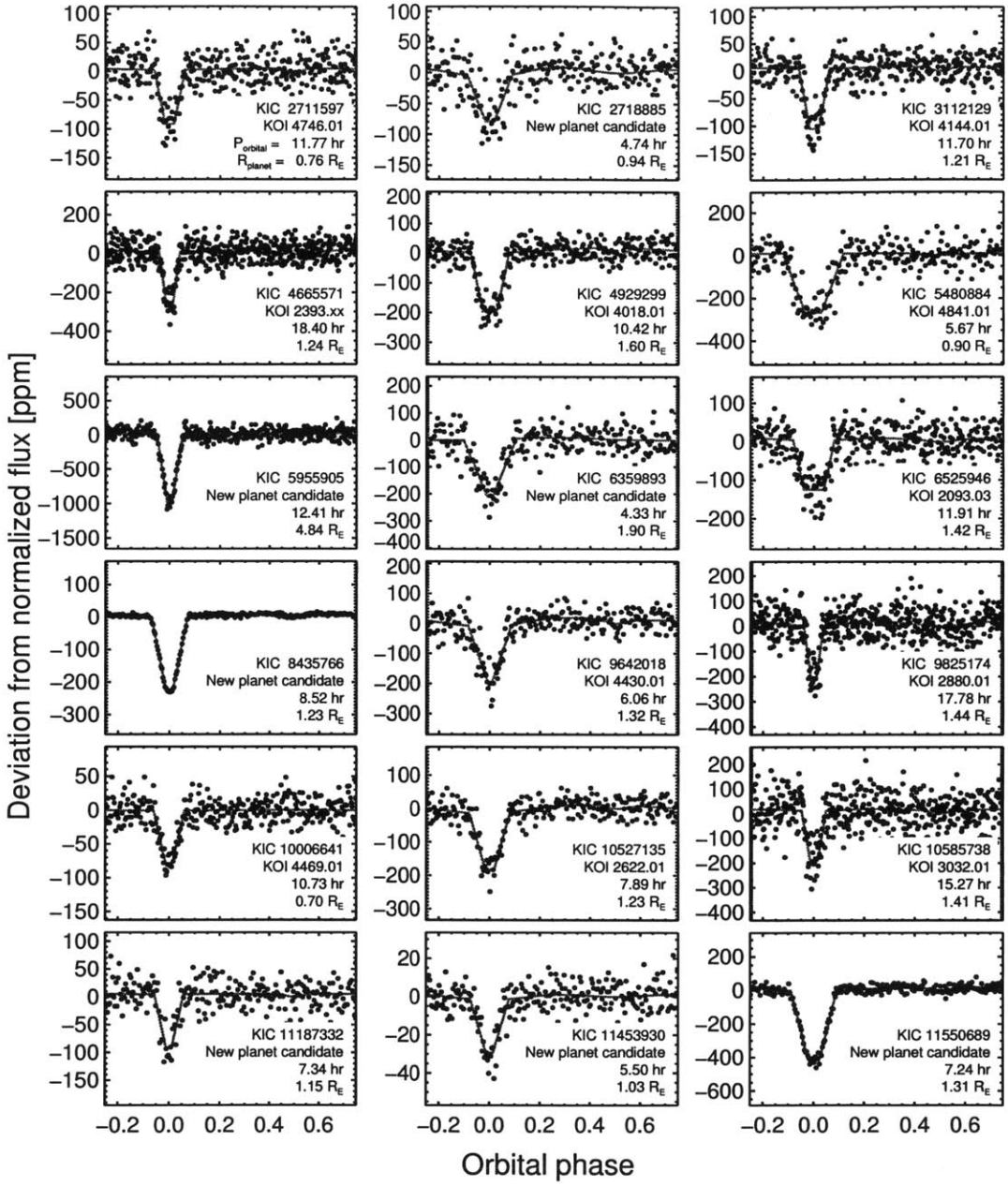

Figure 8-5: Transit light curves for new candidates.

These objects either emerged from our search for the first time, or appear on the KOI list as false positives but are considered by us to be viable candidates. All fluxes are normalized to unity during secondary eclipse. The data have been folded with the transit period and then averaged into 1 to 2-minute time bins (see text). The red curve is the best-fitting transit model.

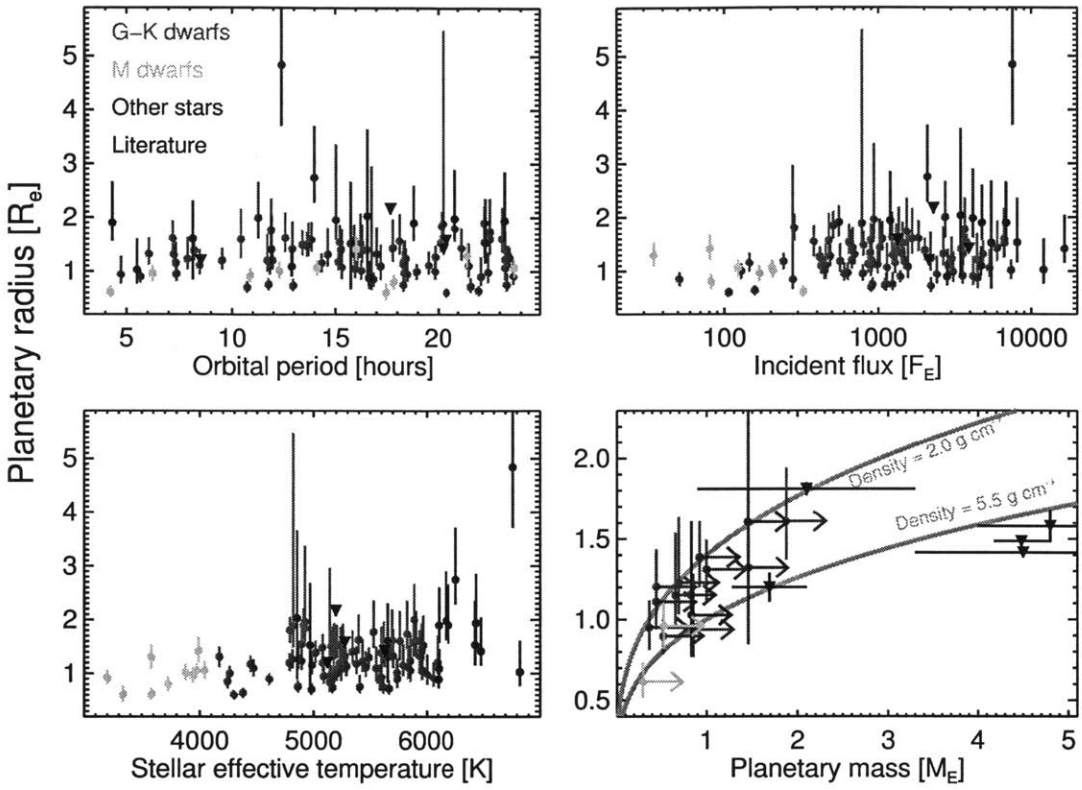

Figure 8-6: Properties of the USP candidates.

Upper left.—Planet radius vs. orbital period. Red points are for candidates with G and K dwarf host stars; notably, all the candidates around such stars have a radius smaller than 2 $R_\oplus$. Blue points are for candidates orbiting M dwarfs, F dwarfs, or evolved stars. The two candidates with $R > 2R_\oplus$ revolve around KIC 5955905 and KIC 10281221. The triangles represent 55 CnC e ([230], [49], [73]), CoRoT-7b ([110], [161]), Kepler-10b [14], Kepler-78b ([176], [94], [151]). *Upper right.*—Planet radius vs. incident bolometric flux, in units of the solar flux on Earth. *Lower left.*—Planet radius vs. stellar effective temperature, showing no clear correlation except that the two planets larger than 2 $R_\oplus$ orbit stars hotter than 6250 K. *Lower right.*—Constraints on mass and radius of the USP candidates (red and blue points) and other exoplanets drawn from the literature (black points). For the USP candidates, the mass constraint follows from the requirement that the orbit lie outside the Roche limit [169]. Candidates with $P < 10$ hr must have mean densities larger than 2 g cm^{-3}; the shortest-period candidates must have mean densities exceeding that of Earth and are likely rocky. Additional black triangles represent Kepler-36b [34], and Kepler-11b ([116], [113]), and 55 CnC e is too massive to appear in this panel.

than 2 $R_\oplus$. This finding cannot be easily attributed to a selection effect, because larger planets are easier to detect than small planets. This is in strong contrast to the planet population with periods in the range 2–100 days, for which planets with size 2-4 $R_\oplus$ ("sub-Neptunes") are just as common as planets with radius 1-2 $R_\oplus$ ([92], [68]).

The explanation that comes immediately to mind is that gaseous planets are missing from the USP candidate list because such planets would have lost most of their gaseous envelopes to photoevaporation ([222], [108], [9], [140], [216], [183], [120], [118], [149], [106]). Indeed, the levels of irradiation suffered by these planets (see Figure 8-6) are high enough to remove the entire envelope from a gaseous planet for a wide range of mass loss efficiencies and core masses [118]. If that is the case, then the USPs may be a combination of rocky planets and formerly gaseous planets that lost their atmospheres. In fact, [118] predicted that planets smaller than Neptunes with incident fluxes larger than a hundred times the Earth's incident flux would end their lives mostly as rocky planets smaller than 2 $R_\oplus$.

In the observed radius distribution, 95% of the candidates have a radius smaller than 1.9 $R_\oplus$. If we assume that the USP candidate list contains only rocky planets (because gas would have been evaporated), and that it represents a fair sampling of the full range of possible sizes of rocky planets, then this finding can be interpreted as a direct measurement of the maximum possible size of a rocky planet. The value of 1.9 $R_\oplus$ is in agreement with a limiting size of 1.75 $R_\oplus$ quoted by [119] based on the complexity of forming planets larger than this limit with no significant H/He envelopes. [223] also note that planets smaller than 1.5 $R_\oplus$ seem to have, on average, densities similar to that of Earth, which could be a sign that they are mostly rocky. It would be interesting to firm up our empirical determination of the limiting size of rocky planets after the estimates of the stellar radii have been improved using spectroscopy or other means.

There are also two USP candidates with implied planet radii larger than 2 $R_\oplus$. They both belong to the group of six USP candidates that orbit stars hotter than 6250 K. The probability of this occurring by chance is only 0.3%, and it is intriguing

that these hotter stars are distinguished from the cooler stars by the lack of a convective envelope [156]. Perhaps the weaker tidal friction associated with the lack of a convective envelope has allowed these planets to survive tidal decay, and, furthermore, their core masses could be large enough that some of their gaseous envelopes have been retained (see [149] and references therein).

For the shortest-period planets, meaningful lower limits on the mean densities can be established from the mere requirement that they orbit outside of their Roche limiting distances. We have calculated these limiting densities for all the planet candidates with orbital periods shorter than 10 hours orbiting G and K dwarfs, using the simplified expression [169]

$$\rho_{\rm p}[\text{g cm}^{-3}] \geq \left(\frac{11.3 \text{ hr}}{P_{\rm orb}}\right)^2 \tag{8.3}$$

which is based on the assumption that the planet's central density is no more than twice the mean density. From this lower limit on the density, and the best fit estimated planet radius, we were able to calculate a lower limit on the planet mass. The results are shown in Figure 8-6. Including the USP sample, it is now possible to place constraints on the mean density of about 10 additional terrestrial-sized planets. For a few of them, namely those with orbital periods shorter than 5-6 hours, the minimum mean density is large enough that the planets are likely to be rocky. The caveats here are that we have not established *individual* false positive rates for most of these planets; and without spectroscopically determined properties for the host star, the uncertainties in the planet properties are large.

8.5 Completeness and false positive rate

We will soon turn to the calculation of the "occurrence rate" of USP planets, defined as the probability that a given star will have such a planet. Before calculating the occurrence rate, there are two important issues to address. The first issue is completeness: how many transiting USP planets could have been missed in our search?

The second issue is that of false positives: how many of the 106 USP candidates are likely to be true planets as opposed to diluted eclipsing binaries or other systems that somehow mimic a planetary signal and evaded our various tests?

8.5.1 Completeness

Our search procedure was designed mainly to detect a sizable sample of new USP candidates, and in this respect it was successful, having yielded 18 new candidates. However, the procedure was complicated enough that it is not straightforward to perform quantitative tests for completeness. At least there are good signs that the completeness is high, based on a comparison between the yield of our pipeline, and the overlap with the various other searches that have been conducted with the *Kepler* data (see Figure 8-3).

We have attempted to measure the completeness of the automated portion of our search by injecting simulated transits into real *Kepler* light curves and then determining whether they are detected by our pipeline analysis. A similar inject-and-recover test for longer-period planets was recently performed by [154]. A more realistic simulation in which the signatures of background binaries and other false positive sources, as well as planet transits, are injected into pixel level data, was beyond the scope of our study.

To start, we selected a set of 105,300 *Kepler* target stars consisting of G-dwarfs and K-dwarfs with $m_{\rm Kep} < 16$. A star was then chosen at random from this set, an orbital period was chosen from a distribution with equal probabilities in equal logarithmic intervals over the range 4 hours to 24 hours, a planet radius was chosen from the same type of distribution, but over the size range 0.84 $R_\oplus$ to 4 $R_\oplus$, and a transit impact parameter was chosen at random from the interval 0 to 1. Given the period and the stellar properties, the orbital radius could be estimated from the relation $R_*/a = (3\pi/(GP^2\rho_*))^{1/3}$. The duration of each transit was then calculated using Eqn. (8.2), and the planet radius and stellar radius were used to compute the transit depth $(R_p/R_*)^2$. Simulated transit signals were then constructed using the trapezoidal model described in section 8.4.2, which takes into account the 30-minute

cadence of the observations, and injected into the mean-normalized PDC-MAP light curve for the selected star.

This procedure, starting with the random selection of a star, was repeated, on average, twice for each of the 105,000 stars in the list, and all of the resulting flux time series were processed with the part of the automated pipeline corresponding to the first four boxes in Figure 8-1 as used in our actual planet search. In brief, a 3-day moving-mean filter was applied to the light curve, and the FT was calculated. The planet was considered further if the correct frequency or an integral multiple of the correct frequency was detected in the Fourier spectrum. Given a detection, a filtered folded light curve was constructed, using the detected period, and the planet was rejected if the SNR of the transit dip was lower than 7 or if a sinusoid yielded a better fit than a transit profile. The final step was to remove those objects for which the transit signals have an SNR lower than 12 at the real orbital period (which may differ from the SNR at the detected orbital period).

We did not attempt to simulate the visual-inspection portions of the pipeline, as this would be prohibitively time-consuming (this issue is discussed further at the beginning of Section 8.6). The false positive tests also were not performed, since the transit shapes should be similar to the injected transit shapes.

The results of these numerical experiments are shown in Figure 8-7. The left portion of the figure shows the dependence of the completeness on period and planet radius. Evidently the pipeline was able to detect nearly all planets larger than 2 $R_{\oplus}$. The efficiency is also seen to generally rise at shorter periods. This may be simply explained, at least in part, by the fact that more transits occur for shorter-period planets over the duration of the observations, which usually results in a higher total SNR than that of longer-period planets of the same size and with the same type of host star.

The right side of Figure 8-7 gives information relating to the efficiency of the pipeline as a function of the "fiducial SNR" of the transit signals. We calculated the fiducial SNR of the folded transit light curve based on the average over the available quarters of the CDPP noise levels that were reported in the headers of the FITS files

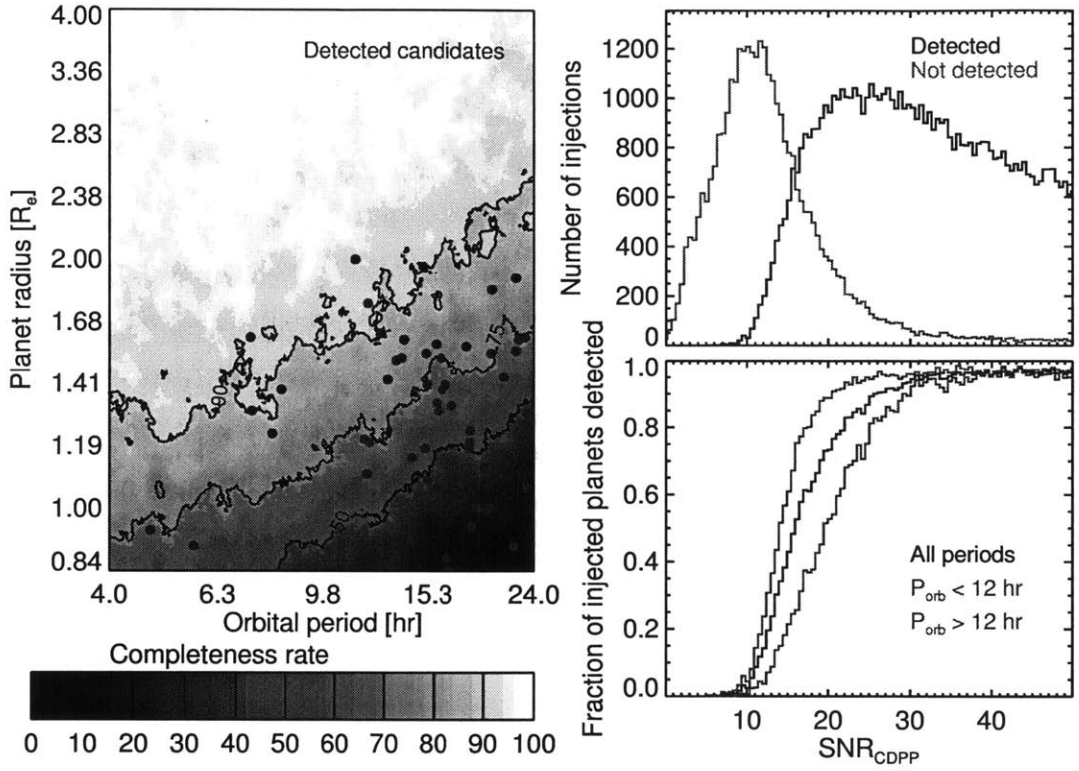

Figure 8-7: Completeness of the automated FT pipeline, for detecting USP planets orbiting G and K dwarfs with $m_{\rm Kep} < 16$.

Left.—The percentage of the artificially injected planet signals that were recovered by our automated pipeline. Three contours are plotted as thick black lines, representing completenesses of 90, 75 or 50%. Blue dots represent the actual 69 USP planets detected by the same pipeline transiting the selected sample of *Kepler* stars. *Upper Right.*—Histogram showing the distribution of the $\rm SNR_{CDPP}$ (see text) of the detected and non-detected planet candidates. *Lower Right.*—The distributions shown in the upper right panel were used to obtain the fractions of planets (in black) detected at different values of $\rm SNR_{CDPP}$. The detection efficiency is near 100% for $\rm SNR_{CDPP}$ ¿ 30, and drops almost to zero for $\rm SNR_{CDPP} \approx 10$. The efficiency seems to decrease with the orbital period as expected, as shown by the differences between the efficiencies for planets with orbital periods shorter than 12 hours (in brown) and between 12 and 24 hours (in green).

(see section 8.2.1; [92]) according to

$$SNR_{\mathrm{CDPP}} \equiv \frac{\delta_{\mathrm{tran}}}{\sigma_{\mathrm{CDPP,6\ hr}}} \sqrt{\frac{T[\mathrm{hr}](84.4\,q\,[\mathrm{days}])}{(6\,\mathrm{hr})\ P_{\mathrm{orb}}[\mathrm{days}]}} \tag{8.4}$$

where q is the number of quarters of data, the factor 84.4 represents the average number of effective days of observations per quarter and the factor of 6 hr is introduced because the CDPP is reported for a 6 hr timescale. This definition of fiducial SNR is convenient because the level of noise in the light curve depends on the filter used, but the CDPP noise is easily accessible through the *Kepler* FITS files. As seen in the upper right panel of Figure 8-7, our original $SNR > 12$ cut (see section 8.3.2) does not perfectly translate into $SNR_{\mathrm{CDPP}} > 12$. There is a small fraction (a few hundred) of simulated planets that were detected with $SNR_{\mathrm{CDPP}} < 12$, and there were also some planets with $SNR_{\mathrm{CDPP}} > 12$ that were missed by the pipeline. The efficiency increases from nearly zero at $SNR_{\mathrm{CDPP}} = 10$ (due to our $SNR > 12$ cut) to for example 90% at $SNR_{\mathrm{CDPP}} = 25$ (also in Figure 8-7).

This "ramp" in detection efficiency is reminiscent of the work of [68], who proposed that the detection efficiency of the *Kepler* transit search pipeline rises as a nearly linear function of SNR_{CDPP} from essentially zero at $SNR_{\mathrm{CDPP}} = 7$ to approximately 100% at $SNR_{\mathrm{CDPP}} = 16$. As one might have expected, our FT-based pipeline seems to be somewhat less efficient at detecting low-SNR planets than the *Kepler* pipeline. The likely reason is that the significance of the FT-based detection is spread over numerous harmonics, and since we used only two harmonics to detect signals, some of the lowest-SNR planets are not detectable. Evidence for this can be seen in the lower right panel of Figure 8-7, where the detection efficiency has been calculated for orbital periods shorter and longer than 12 hours. The pipeline detects many more low-SNR planets with short orbital periods, because their signals are spread over fewer harmonics. This may be the reason why most of our newly detected planet candidates have short orbital periods, while the candidates missed by our search and discovered by the *Kepler* pipeline tend to have longer orbital periods.

8.5.2 Low false positive rate and high multiplicity

We now investigate the issue of false positives. One approach would be to pursue the validation or confirmation of all 106 objects, most definitively by direct mass measurement (as was done for Kepler-78; [94], [151]) or, somewhat less definitively, by the lack of ELVs and by statistical arguments (as was done for KOI-1843.03; [169]). We have found that a simpler argument is available for the USP candidates, based on the empirically high probability that USP planets are found in compact, coplanar, multi-planet systems.

It has already been shown that the false positive rate for a transit candidate that is found in association with other transit candidates of different periods around the same *Kepler* target is much lower than the false positive rate of a transit candidate that is found in isolation ([115], [114]). The reason is that background binary stars (an important source of false positives) are expected to be spread randomly over the *Kepler* field of view, whereas the planet candidates are found to be clustered around a relatively smaller sample of stars. This same line of argument can be extended to the USP candidates. To be specific, in what follows we will restrict our attention to candidates detected with our pipeline and with G and K-type hosts. For convenience we will also define a "short-period planet" (SP planet) as a planet with a period in the range 1-50 days, as opposed to USP planets with $P < 1$ day.

There are 10 stars hosting USP candidates in our sample of G and K stars that also host at least one transiting SP candidate. The orbital periods and planet sizes for these 10 systems are displayed in Figure 8-8. These planet candidates are likely to be genuine planets, based on the statistical arguments by [115]. In order for this argument to work, false positives with orbital periods shorter than one day should be found less frequently orbiting multiplanet systems [114]. In particular, if we focus only on the active KOI list [3], we evaluate the fraction of false positives detected for G and K-type hosts with $P < 1$ day as being 6 times lower for stars that have at least one active SP planet candidate than for those that do not. Since all of our 10 USP candidates accompanied by transiting SP candidates have also passed conservative

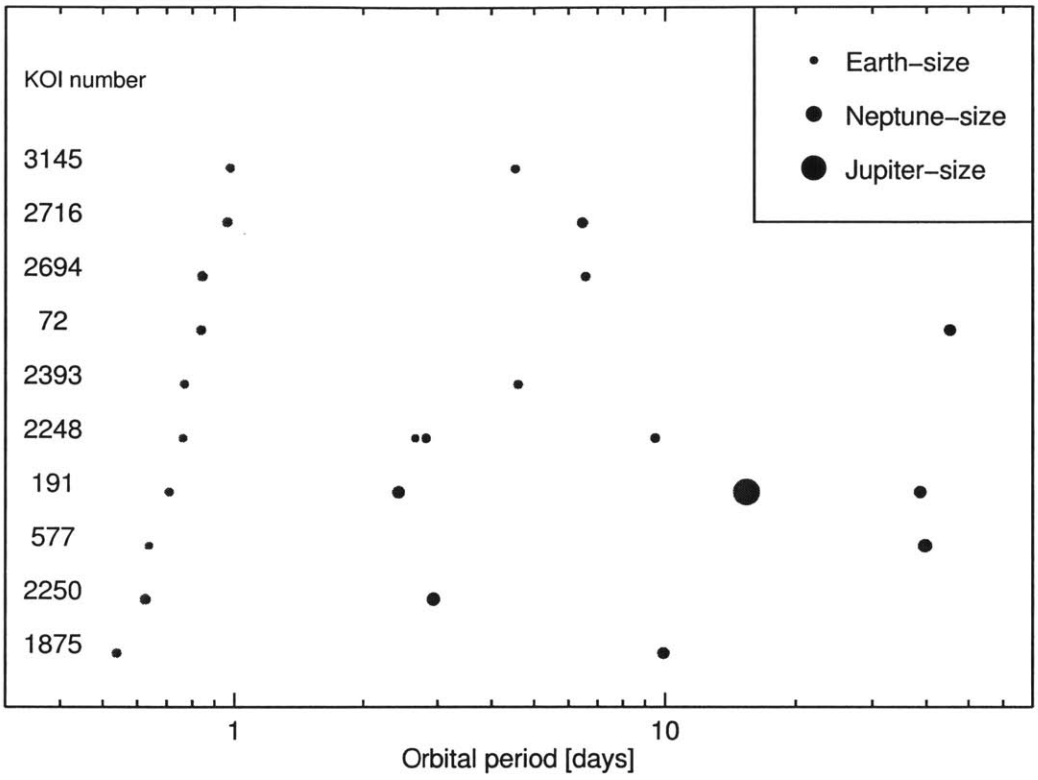

Figure 8-8: Multitransiting systems with USP planets.

Depicted are the periods and planet sizes for the subset of 10 USP candidates detected with our pipeline with G and K-type host stars and at least one other transit candidate with P = 1-50 days. The radius of the dot is proportional to the square root of the planet radius. The presence of multiple candidates causes these 10 USP candidates to have a very low false positive probability [115].

false positive tests, we feel justified in assuming that they have a high probability of being genuine planets, which we will take to be $\simeq$ 100%. Next we show that the existence of these 10 systems *implies* the existence of a larger number of transiting USP planets which have *non-transiting* SP planets. This is because the geometric probability of transits decreases with orbital distance, and is lower for the SP planet than for the USP planet.

The transit probability is given by $R_*/a \propto P^{-2/3}$ for stars of the same size. We can derive an effective transit probability for a *range* of orbital periods by integrating $P^{-2/3}$ against the period distribution of planets, $f(P)$. For the latter we utilize

Eqn. (8) of [92]:

$$f(P) \propto P^{\beta-1}\left(1-e^{-(P/P_0)^{\gamma}}\right) \tag{8.5}$$

where, for their case which includes all planet sizes, $P_0 \simeq 4.8$ days, $\beta \simeq 0.52$ and $\gamma \simeq 2.4$ [92]. We then compute the effective transit probability, $\mathcal{P}$

$$\mathcal{P}(P_1 \rightarrow P_2) \propto \left(\int_{P_1}^{P_2} f(P)\, P^{-2/3}\, dP \Big/ \int_{P_1}^{P_2} f(P) dP\right) \tag{8.6}$$

When we carry this integral out numerically for the ranges: $P = 1/6 \rightarrow 1$ day and $P = 1 \rightarrow 50$ days, we find:

$$\frac{\mathcal{P}(1/6 \rightarrow 1)}{\mathcal{P}(1 \rightarrow 50)} \simeq 6.9 \tag{8.7}$$

indicating that the effective transit probability is ~ 7 times higher in the USP range than in the SP range. If the distribution of SP planets is unaffected by the presence of a USP planet, this then implies that if we find $10 \pm \sqrt{10}$ USP planets with transiting SP planets, there should be a total of 69 ± 22 USP planets with SP planet companions.[2] We have found 69 USP candidates orbiting G and K dwarfs, which is fully consistent with the idea that essentially all USP planets are in systems with other SP planets, whether they are seen transiting or not. This also suggests that the number of false positives among the 69 USP planet candidates is likely to be quite low.

We do acknowledge that part of the above argument is somewhat circular since we have extrapolated the expression for $f(P)$ from [92], which was only derived for planets with $P > 1$ day and all sizes, into the USP range and for small planets. We do, however, find numerically that the result is rather insensitive to the choice of γ at least over the range $2 < \gamma < 5$, γ being the parameter which largely dictates the slope in the short-period range. Moreover, it turns out that the [92] extraplolated slope for $f(P)$ is essentially the same for their smallest planets as compared with

[2]Here, in computing the uncertainties, we have simply assumed that the number of detections is subject to the usual counting statistics.

all planets. Thus, at a minimum, this very plausible period distribution function provides an interesting self-consistency check.

In summary, it is very clear that the 10 USP candidates with transiting SP companions imply the existence of a much larger number of USP candidates with non-transiting SP planets – and we indeed find them.

Interestingly, [185] predicted that a large family of terrestrial planets would be found with *Kepler* with periods shorter than 1 day, and that they would be accompanied by other planets in their systems. This was based on the fact that the dynamical interactions between planets can bring a close-in planet even closer to its star, where tidal dissipation can further shrink the orbit. However, it is unclear if planets with orbital periods as long as 50 days could have had any dynamical influence on the USP, particularly since these planets are also quite small (see Figure 8-8). What is clear, though, is that the USPs are very different from hot Jupiters, which have been found to have a very low probability of having additional companions with periods <50 days [202].

8.6 Occurrence rate

8.6.1 Method of calculation

We have argued that the list of 106 USP candidates has a low false positive rate, and that we have a good understanding of the completeness of our pipeline for a wide range of orbital periods and planet radii. We can now use the estimate of the completeness to estimate the occurrence rate [154]. Out of the 106 USP planet candidates, 97 were detected by our automatic pipeline (see Figure 8-1; the 97 candidates belong to the box with $\sim 3,500$ candidates), although 7 of them were dropped in the subsequent visual inspection of the light curves, giving a final list of 90 USP candidates. This low fraction of dropped planets (7 out of 97) gives us confidence that our visual inspection procedure is fairly robust. In order to compare our results with the simulation, we should minimize the effects caused by this visual inspection step on the final

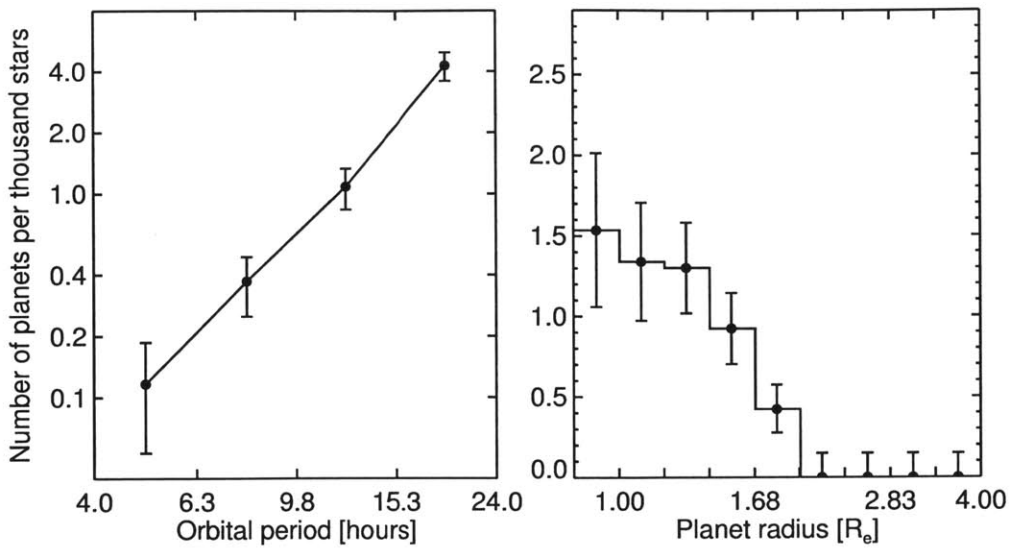

Figure 8-9: Occurrence rate for ultra-short-period planets.

Occurrence rates were computed on a two-dimensional grid of planet radius and orbital period. The occurrence rate takes into account the implied number of non-transiting planets, as well as the number of stars that were effectively searched for such a planet. Integrated over all radii and periods <1 day, the total occurrence rate is 5.5 ± 0.5 planets per thousand stars. The occurrence rate increases with orbital period, and decreases with planet radius for $R_p < 2\ R_\oplus$.

sample of planets, since this step was not taken into account in the injection/recovery simulations. We decided to use the 97 USP planet candidates in our group of 106 that were identified by our automatic pipeline prior to the visual inspection step, and acknowledge that a few additional planetary candidates could have been misclassified in this step.

We again concentrate on the 105,300 G and K dwarfs with $m_{\rm Kep} < 16$, the same stars used in our simulation of multiplanet systems. There are a total of 69 USP planet candidates detected by our pipeline orbiting the G and K dwarfs with orbital periods ranging from 4 to 24 hours and radii ranging from 0.84 to 4 $R_\oplus$ (see Figure 8-7). For each planet, we selected the 400 injected planets closest in orbital period and planet radius, where the distance to the $i^{\rm th}$ detected planet with coordinates $[R_i, P_i]$

is calculated with the following expression:

$$d^2([R,P],[R_i,P_i]) = \left(\frac{(P-P_i)}{P_i}\right)^2 + \left(\frac{(R-R_i)}{R_i}\right)^2 . \quad (8.8)$$

This formula ensures that the positions of the 400 simulated planets are selected from a circle in log-log space. We calculated the *local* completeness rate C_i as the fraction of planets detected among those 400 simulated planets. The contribution of each planet to the final occurrence rate is $f_i \equiv (a/R_*)/(C_i N_*)$, where N_* is the total number of stars searched for planets and the factor a/R_* is the inverse transit probability. Given a range of orbital periods and planet radii, we sum all the contributions from all $n_{\rm pl}$ planets detected in that range to estimate the final occurrence rate f. Following the recipe given by [92], we then define the effective number of stars searched as $n_{*,\rm eff} \equiv n_{\rm pl}/f$ and compute the uncertainties in f from the 15.9 and 84.1 percent levels in the cumulative binomial distribution that results from drawing $n_{\rm pl}$ planets from $n_{*,\rm eff}$ stars.

8.6.2 Dependence on planet radius and period

Figure 8-9 shows the resulting occurrence rates for 4 logarithmic intervals in the orbital period (marginalized over radius) and for 9 logarithmic intervals in the planet radius (marginalized over period). The occurrence rate increases with period, and is consistent with a power law, as had already been seen for longer orbital periods ([92], [68], [154]). As a function of radius, the occurrence rate changes by less than a factor of ~ 2 over the interval 0.84–1.68 $R_\oplus$, and drops sharply for larger radii. At ultra-short orbital periods, Earth-size planets are more common around these stars than sub-Neptunes or any other type of larger planets. Integrating over all periods and sizes, we find that there are 5.5 ± 0.5 planets per thousand stars (G and K dwarfs), with orbital periods in the range 4–24 hours and radii larger than 0.84 $R_\oplus$.

As mentioned in Sect. 8.4.3, the lack of planets larger than 2 $R_\oplus$ may be interpreted as a consequence of the extremely strong illumination in the tight USP orbits (see, e.g., [149] and references therein). We can compare our results to occurrence rates

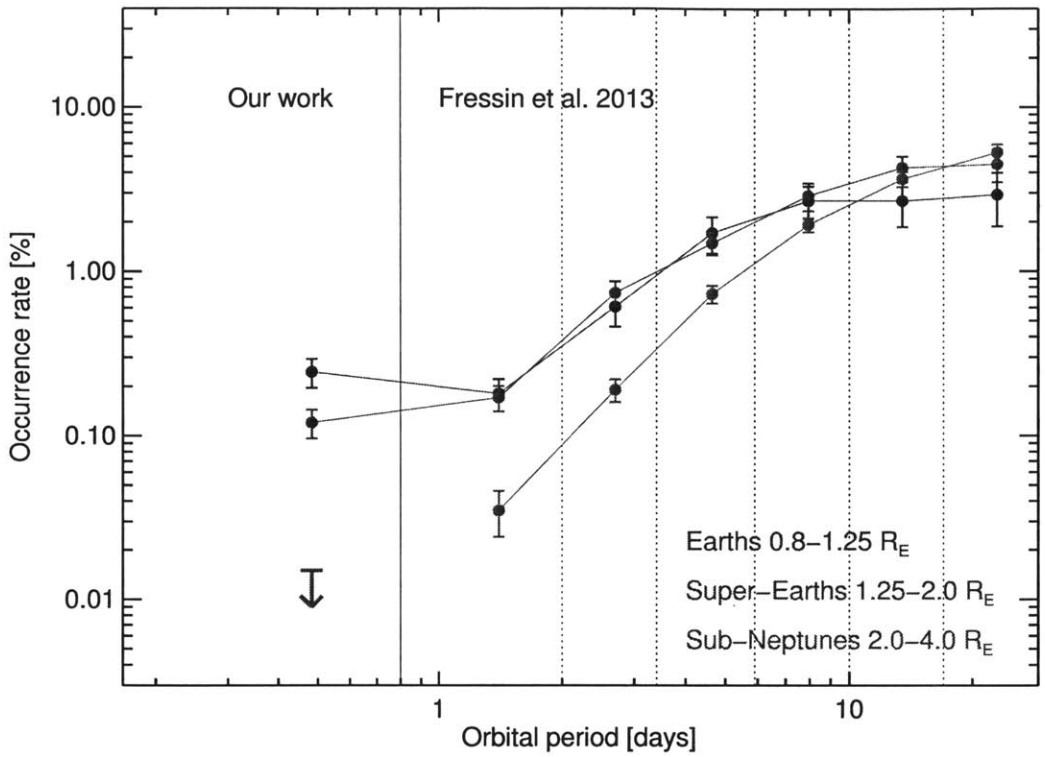

Figure 8-10: Occurrence rates for Earths, Super-Earths and Sub-Neptunes as a function of orbital period.

The data points for $P > 0.8$ days are from [68], and the shortest-period data point is from this study.

calculated at longer orbital periods, to try to detect trends that might support or refute this interpretation. We use the occurrence rates measured by [68] for planets as small as Earth and for periods of 0.8–85 days. To allow a direct comparison, we divided our 50 planet candidates with orbital periods shorter than 0.8 days into three groups according to size: Earths, super-Earths and sub-Neptunes (see Figure 8-10), and calculated the occurrence rate for each group. The results are shown in Figure 8-10.

A lack of sub-Neptunes is evident in Figure 8-10 at the shortest orbital periods; in fact, sub-Neptunes are significantly less common than super-Earths for orbital periods shorter than 5 days and possibly even up to 10 days. This absence of sub-Neptunes had been predicted by different simulations of mass loss of close-in planets ([9], [216],

[118], [149]). There also seems to be a modest excess of USP Earth-size planets relative to the occurrence rate of super-Earths, which could very well be the cores of the transmuted sub-Neptunes. A more detailed statistical analysis is required to assess the significance of this excess, and it would be convenient to update the occurrence rate at longer orbital periods with new data.

It is still possible that any mechanism that caused these planets to have such tight orbits, is less efficient for sub-Neptunes than for smaller planets. Obtaining the masses of some of these planets in order to measure their densities and compositions would provide some helpful context. Obtaining precise stellar radii (via spectroscopy) and hence planet radii for a uniform sample of close-in planets, could reveal additional signatures of photoevaporation.

8.6.3 Dependence on stellar type

We have also investigated the dependence of the occurrence rate on the type of star, to the extent that this is possible with the *Kepler* data. If ultra-short period planets had an occurrence rate independent of stellar temperature, we would expect to find most planets orbiting Sun-like stars (with $T_{\rm eff} \approx 5800$K), since these stars are the most common type of star in the *Kepler* target catalog, and they dominate the number of USP-searchable stars. However, the host stars of the detected USP candidates tend to be cooler, with temperatures closer to $T_{\rm eff} \approx 5000$ K (such as Kepler-78b). This might be a clue that planets with orbital periods shorter than one day are more common around cooler stars. In order to test this, we first calculate the occurrence rate for the hotter stars in our sample (G dwarfs, 5100–6100 K). Using all such stars with $m_{kep} < 16$, we have 48 USP candidates around 89,000 stars. Thus the occurrence rate for such planets is 5.1 ± 0.7 planets for every thousand stars. The same calculation for the cooler stars (K dwarfs, 4100–5100 K) yields 8.3 ± 1.8 planets per thousand stars, based on 21 USP candidates orbiting 16,200 stars. The difference between the occurrence rates for these two spectral classes is only marginally significant (at the 1.7σ level).

It would be interesting if USP planets are more common around K dwarfs than

Table 8.2. Occurrence rate of USP planets for different stellar types

Stellar type	Effective temperature range	Occurrence rate
F dwarfs	6100-7100K	$0.15 \pm 0.05\%$
G dwarfs	5100-6100K	$0.51 \pm 0.07\%$
K dwarfs	4100-5100K	$0.83 \pm 0.18\%$
M dwarfs	3100-4100K	$1.10 \pm 0.40\%$

G dwarfs. A similar temperature trend in the occurrence rate of planets with 1–50 day periods was found by [92], although this finding has been challenged by [68] based on the statistics of planets with even longer orbital periods. This collection of results suggests that the dependence of occurrence rate on the type of star is most pronounced for the shortest period planets. Indeed, since planet formation depends on the temperature of the materials in the protoplanetary disk, and since the protoplanetary disks around cooler stars are cooler at a given orbital distance, one could imagine scenarios in which cooler stars have a higher abundance of short-period planets. In this case it will be worth extending our study to slightly longer orbital periods to find the transition point at which K and G dwarf stars have the same number of planets, and also to extend this study to include stars of spectral types F and M.

Even though our sample of USP planets transiting F and M dwarfs is somewhat limited, we can use it to put very useful bounds on the occurrence rate of such planets. For that we repeated the completeness calculation using F and M hosts, and repeated all the steps of the computation. For F dwarfs (6100–7100 K), we find 9 planet candidates within a sample of 48,000 stars, giving an occurance rate of 1.5 ± 0.5 planets per thousand stars. For M dwarfs (3100–4100 K), we find 6 planet candidates out of a sample of 3537 stars, yielding a rate of 11 ± 4 planets per thousand stars. This represents further evidence that cooler stars are more likely to host USP planets. If we now combine the USP planet occurrence rates for all four spectral classes of host star (M, K, G, and F) the decreasing trend in occurrence rate with increasing

$T_{\rm eff}$ becomes quite significant. These results are summarized on Table 8.2.

8.7 Summary and Conclusions

In this work we have performed a systematic search of the entire *Kepler* database for ultra-short period (USP) planet candidates, defined as those having orbital periods < 1 day. We utilized a standard Fourier transform algorithm to search for periodic signals in the data, and found it to be quite efficient at finding short-period periodicities. An automated pipeline selected several thousand objects for further investigation including the analysis of transit-profile shapes in the folded light curves. The folded light curves for these candidates were also inspected by eye to yield a first-cut set of 375 interesting candidates. These objects were combined with 127 USP planet candidates from the KOI list, as well as other objects found in the literature, resulting in a set of 471 distinct candidates worthy of detailed study.

These 471 initially selected candidates were then subjected to a number of standard tests, including examination of shifts in the light centroid during transits/eclipses, symmetry between odd and even transits/eclipses, shape of transits, etc. The final result is a set of 106 USP planet candidates that have passed a set of very restrictive tests. Eight of these objects are completely new, while another 10 were KOIs that had been rejected, largely because their orbital period had been incorrectly identified by the *Kepler* pipeline.

Our final set of 106 USP candidates, and their properties, are summarized in Table 1. Among this list, 5 of the 7 USP candidates with orbital periods $\lesssim 6$ hours are attributable to this study. In the process we also eliminated some 26 USP candidates from the KOI list and others that were found in the literature. These are listed, along with reasons for rejection, and 8 more USP candidates not considered in this study due to low SNR, in Table 2.

The USP planets are inferred to occur around one out of every 200 stars, on average. This makes them nearly as abundant as hot Jupiters. We also infer that the USPs nearly always have companion planets with $P < 50$ days unlike hot Jupiters,

which rarely have such companions. The occurrence rate of USP planets rises with period from 0.2 to 1 day, and there is evidence that the occurrence rate is higher for cooler stars than for hotter stars. The population of USP planets offers a number of opportunities for follow-up ground-based observations, as has already been illustrated by the examples of Kepler-10b [14] and Kepler-78b [176].

A key finding was the relative scarcity of USP planets with radius $> 2\ R_{\oplus}$. It is worth noting that the well-known USP planet 55 Cnc e has a radius very near the top end of the range of planet sizes in our catalog; its radius has been estimated as $2.0\ R_{\oplus}$ [230] or $2.2\ R_{\oplus}$ [73]. The results of our survey would seem to imply that the discovery of an USP planet as large as 55 Cnc e was unlikely. However, it is difficult to assess the significance of this "fluke" given that the mass and radius of 55 Cnc e were determined after a process of discovery with important and complicated selection effects.

The relative scarcity of planets with $> 2\ R_{\oplus}$ could be naturally interpreted as a consequence of the strong illumination in the tight orbits. It is possible that a large fraction of the Earth-sized planets in our sample were formerly sub-Neptunes (see [149] and references therein). There might be other observational signatures of this phenomenon, such as enhanced densities or other compositional properties, that are worth exploring. It is also worth continuing the exploration of planets with slightly longer orbital periods to determine at what distance sub-Neptunes start to become common (see Figure 8-10), and to study those systems in detail to understand the speed and efficiency of the mass-loss mechanism.

It is unclear how the USP planets attained such tight orbits, although there is little doubt that they formed further away from their host stars. The relation between the USPs and the first discovered family of close-in planets—the hot Jupiters—is also not clear. For hot Jupiters, the formation problem is more difficult, in a sense, because they are supposed to have migrated from beyond the snow line, whereas current planet formation theories can accommodate the formation of smaller planets closer to the star. A full comparison between the properties of both families of planets could reveal more differences that might help us understand how the close-in small planets

evolve into their current stage. In particular, it would be interesting to test whether the host stars of USP planets are preferentially metal-rich, as is well known to be the case for hot Jupiters [182]. Studies of small planets at somewhat longer periods have not found such a metallicity effect in systems with G and K host stars ([186], [30]). It would also be interesting to measure the obliquities of the host stars to see if their rotation axes are frequently misaligned with the planetary orbits, as is the case with hot Jupiters (see, e.g., [226], [214], [5], or whether they have low obliquities similar to many of the multi-transit host stars that have been measured ([174], [84], [6], [218]). Such measurements might be challenging for small planets, but could be achievable with techniques that do not depend critically on transit observations, such as asteroseismology [37]. Given a large sample of obserations, the $v \sin i$ technique can also be used to constrain the statistical properties of the distribution of obliquities for a given family of planets ([185], [86], [87]).

A large fraction of our planet candidates should induce radial velocity changes in their host stars at levels of a few meters per second. Measuring the masses of these planets, or constraining them, may be achievable with high-precision radial velocity instruments on large telescopes, at least for the brightest host stars. This would increase our knowledge of the compositions of Earth-size planets.

We thank Simon Albrecht, Dave Charbonneau, Brice Demory, Andrew Howard, Brian Jackson, Michael Liu, Eric Lopez, Kevin Schlaufman, Peter Sullivan, Amaury Triaud and Vincent Van Eylen for helpful discussions about short-period planets. We are also grateful to the entire Kepler team for making this study possible. R.S.O. and J.N.W. acknowledge NASA support through the Kepler Participating Scientist Program. I.E. acknowledges financial support from the ENS of Cachan. This research has made use of the NASA Exoplanet Archive, which is operated by the California Institute of Technology, under contract with the National Aeronautics and Space Administration under the Exoplanet Exploration Program. The data presented in this article were obtained from the Mikulski Archive for Space Telescopes (MAST). STScI is operated by the Association of Universities for Research in Astronomy, Inc., under NASA contract NAS5-26555. Support for MAST for non-HST data is provided by

the NASA Office of Space Science via grant NNX09AF08G and by other grants and contracts. We made use of J-band images that were obtained with the United Kingdom Infrared Telescope (UKIRT) which is operated by the Joint Astronomy Centre on behalf of the Science and Technology Facilities Council of the U.K.

Table 8.3: Characteristics of the 106 USP planet candidates discoreved in the Kepler data.

KIC #	KOI #	$m_{\rm Kep}$	$T_{eff}[K]$	$Logg$	R_* $[R_\odot]$	$P_{\rm orb}$ [days]	t_0 [BJD-2454900]	Depth [ppm]	Duration [hr]	$a/R_\star$	R_p $[R_\oplus]$
2711597	4746.01	14.5	4861^{+150}_{-129}	$4.57^{+0.05}_{-0.05}$	$0.72^{+0.08}_{-0.07}$	0.49020979	64.289540	92^{+6}_{-6}	$0.910^{+0.055}_{-0.055}$	$3.63^{+0.48}_{-0.96}$	$0.76^{+0.12}_{-0.11}$
2718885	0.00	14.7	5597^{+160}_{-142}	$4.55^{+0.03}_{-0.28}$	$0.84^{+0.35}_{-0.07}$	0.19733350	64.716193	96^{+14}_{-14}	$0.372^{+0.058}_{-0.029}$	$3.43^{+0.66}_{-0.94}$	$0.94^{+0.34}_{-0.17}$
3112129	4144.01	14.4	6096^{+144}_{-201}	$4.46^{+0.05}_{-0.31}$	$1.02^{+0.48}_{-0.09}$	0.48765719	64.677406	107^{+6}_{-6}	$0.899^{+0.045}_{-0.048}$	$3.67^{+0.45}_{-0.97}$	$1.21^{+0.50}_{-0.21}$
4665571	2393.00	14.9	4894^{+149}_{-128}	$4.60^{+0.04}_{-0.06}$	$0.70^{+0.09}_{-0.06}$	0.76669043	64.430840	259^{+13}_{-12}	$0.983^{+0.046}_{-0.046}$	$5.28^{+0.64}_{-1.40}$	$1.24^{+0.19}_{-0.17}$
4929299	4018.01	14.8	5761^{+191}_{-164}	$4.33^{+0.17}_{-0.23}$	$1.05^{+0.38}_{-0.19}$	0.43436157	285.738945	192^{+8}_{-8}	$1.076^{+0.045}_{-0.044}$	$2.74^{+0.32}_{-0.73}$	$1.60^{+0.56}_{-0.35}$
5480884	4841.01	16.0	4607^{+123}_{-132}	$4.73^{+0.06}_{-0.03}$	$0.52^{+0.03}_{-0.04}$	0.23624272	102.883560	261^{+15}_{-16}	$0.844^{+0.049}_{-0.046}$	$1.89^{+0.24}_{-0.50}$	$0.90^{+0.11}_{-0.11}$
5955905	0.00	15.0	6762^{+183}_{-283}	$4.26^{+0.11}_{-0.32}$	$1.38^{+0.79}_{-0.25}$	0.51705775	1207.057671	978^{+24}_{-24}	$0.753^{+0.019}_{-0.018}$	$4.67^{+0.51}_{-1.25}$	$4.84^{+2.54}_{-1.13}$
6359893	0.00	15.9	6197^{+183}_{-226}	$4.45^{+0.05}_{-0.30}$	$1.03^{+0.47}_{-0.10}$	0.18043173	285.389235	258^{+23}_{-23}	$0.385^{+0.043}_{-0.032}$	$3.09^{+0.53}_{-0.81}$	$1.90^{+0.76}_{-0.34}$
6525946	2093.03	15.4	6487^{+187}_{-257}	$4.40^{+0.06}_{-0.31}$	$1.12^{+0.56}_{-0.12}$	0.49607106	285.534133	124^{+7}_{-7}	$1.424^{+0.059}_{-0.059}$	$2.36^{+0.27}_{-0.63}$	$1.42^{+0.63}_{-0.26}$
8435766	0.00	11.6	5085^{+106}_{-93}	$4.60^{+0.02}_{-0.06}$	$0.74^{+0.06}_{-0.03}$	0.35500753	53.604848	229^{+1}_{-1}	$0.719^{+0.004}_{-0.004}$	$3.37^{+0.37}_{-0.90}$	$1.23^{+0.14}_{-0.14}$
9642018	4430.01	15.5	5275^{+169}_{-142}	$4.59^{+0.03}_{-0.16}$	$0.79^{+0.19}_{-0.06}$	0.25255594	64.516303	223^{+23}_{-20}	$0.438^{+0.074}_{-0.051}$	$3.74^{+0.81}_{-0.96}$	$1.32^{+0.30}_{-0.20}$
9825174	2880.01	15.9	5618^{+164}_{-144}	$4.49^{+0.06}_{-0.27}$	$0.87^{+0.36}_{-0.09}$	0.74092963	102.695775	210^{+15}_{-14}	$0.894^{+0.069}_{-0.065}$	$5.56^{+0.80}_{-1.46}$	$1.44^{+0.53}_{-0.25}$
10006641	4469.01	14.3	4981^{+156}_{-127}	$4.60^{+0.03}_{-0.08}$	$0.73^{+0.11}_{-0.06}$	0.44708779	64.506995	76^{+5}_{-5}	$0.773^{+0.051}_{-0.050}$	$3.89^{+0.53}_{-1.02}$	$0.70^{+0.12}_{-0.10}$
10527135	2622.01	15.3	5430^{+174}_{-145}	$4.54^{+0.03}_{-0.25}$	$0.84^{+0.32}_{-0.07}$	0.32868757	64.454984	165^{+9}_{-9}	$0.767^{+0.041}_{-0.043}$	$2.90^{+0.37}_{-0.76}$	$1.23^{+0.41}_{-0.20}$
10585738	3032.01	15.7	5343^{+176}_{-156}	$4.54^{+0.03}_{-0.23}$	$0.89^{+0.28}_{-0.06}$	0.63642490	64.688541	196^{+18}_{-17}	$0.947^{+0.079}_{-0.082}$	$4.51^{+0.70}_{-1.17}$	$1.41^{+0.39}_{-0.22}$
11187332	0.00	15.2	5790^{+160}_{-172}	$4.53^{+0.03}_{-0.28}$	$0.90^{+0.35}_{-0.07}$	0.30598391	64.826889	126^{+13}_{-14}	$0.369^{+0.045}_{-0.027}$	$5.42^{+0.94}_{-1.43}$	$1.15^{+0.39}_{-0.19}$
11453930	0.00	13.1	6823^{+165}_{-242}	$4.21^{+0.12}_{-0.34}$	$1.49^{+0.92}_{-0.29}$	0.22924638	64.512355	37^{+3}_{-4}	$0.367^{+0.046}_{-0.025}$	$4.08^{+0.71}_{-1.07}$	$1.03^{+0.58}_{-0.26}$
11550689	0.00	14.6	4168^{+124}_{-135}	$4.65^{+0.06}_{-0.03}$	$0.60^{+0.05}_{-0.07}$	0.30160087	64.744663	412^{+6}_{-6}	$0.806^{+0.014}_{-0.014}$	$2.55^{+0.27}_{-0.68}$	$1.31^{+0.18}_{-0.19}$
1717722	3145.02	15.7	4812^{+145}_{-133}	$4.61^{+0.03}_{-0.06}$	$0.71^{+0.07}_{-0.06}$	0.97730809	102.820321	266^{+21}_{-22}	$1.249^{+0.109}_{-0.095}$	$5.22^{+0.81}_{-1.36}$	$1.27^{+0.19}_{-0.18}$
3444588	1202.01	15.9	4894^{+607}_{-904}	$4.60^{+0.10}_{-0.10}$	$0.72^{+0.11}_{-0.11}$	0.92831093	64.945619	397^{+21}_{-21}	$1.104^{+0.055}_{-0.054}$	$5.70^{+0.69}_{-1.51}$	$1.55^{+0.30}_{-0.28}$
4055304	2119.01	14.1	5203^{+171}_{-134}	$4.51^{+0.05}_{-0.19}$	$0.86^{+0.24}_{-0.07}$	0.57103885	64.653190	243^{+5}_{-5}	$0.978^{+0.019}_{-0.020}$	$3.98^{+0.43}_{-1.07}$	$1.52^{+0.39}_{-0.23}$
4144576	2202.01	14.1	5285^{+169}_{-138}	$4.59^{+0.03}_{-0.16}$	$0.78^{+0.20}_{-0.06}$	0.81316598	64.826536	162^{+6}_{-5}	$1.237^{+0.045}_{-0.044}$	$4.47^{+0.50}_{-1.19}$	$1.12^{+0.26}_{-0.16}$
4852528	500.05	14.8	4040^{+64}_{-175}	$4.70^{+0.07}_{-0.07}$	$0.57^{+0.07}_{-0.07}$	0.98678600	64.196497	295^{+11}_{-11}	$1.238^{+0.041}_{-0.041}$	$5.42^{+0.60}_{-1.44}$	$1.06^{+0.18}_{-0.17}$
5040077	3065.01	14.6	5837^{+192}_{-169}	$4.50^{+0.07}_{-0.28}$	$0.84^{+0.37}_{-0.09}$	0.89638348	65.296606	133^{+15}_{-14}	$0.965^{+0.098}_{-0.094}$	$6.19^{+1.07}_{-1.60}$	$1.11^{+0.43}_{-0.21}$
5095635	2607.01	14.5	5883^{+160}_{-165}	$4.53^{+0.03}_{-0.27}$	$0.89^{+0.33}_{-0.07}$	0.75445863	64.210363	237^{+16}_{-12}	$0.561^{+0.037}_{-0.047}$	$9.11^{+1.28}_{-2.38}$	$1.57^{+0.50}_{-0.25}$
5175986	2708.01	15.9	4790^{+159}_{-132}	$4.60^{+0.03}_{-0.06}$	$0.73^{+0.07}_{-0.05}$	0.86838702	103.275858	511^{+19}_{-18}	$0.923^{+0.033}_{-0.034}$	$6.40^{+0.72}_{-1.70}$	$1.80^{+0.25}_{-0.24}$

5340878	4199.01	14.3	5166^{+148}_{-136}	$4.65^{+0.03}_{-0.10}$	$0.68^{+0.11}_{-0.05}$	0.53991700	64.548229	96^{+6}_{-6}	$1.040^{+0.057}_{-0.059}$	$3.51^{+0.45}_{-0.93}$	$0.74^{+0.12}_{-0.10}$
5513012	2668.01	14.2	5596^{+155}_{-144}	$4.59^{+0.03}_{-0.25}$	$0.78^{+0.31}_{-0.06}$	0.67933587	65.178693	246^{+6}_{-7}	$1.066^{+0.030}_{-0.028}$	$4.33^{+0.48}_{-1.16}$	$1.39^{+0.48}_{-0.22}$
5642620	2882.02	15.4	4467^{+165}_{-160}	$4.67^{+0.04}_{-0.06}$	$0.61^{+0.07}_{-0.05}$	0.49339463	285.612655	270^{+16}_{-15}	$0.870^{+0.052}_{-0.051}$	$3.82^{+0.50}_{-1.01}$	$1.10^{+0.17}_{-0.15}$
5942808	2250.02	15.6	4922^{+195}_{-151}	$4.50^{+0.07}_{-0.65}$	$0.82^{+0.69}_{-0.07}$	0.62628076	285.358414	418^{+15}_{-16}	$1.011^{+0.038}_{-0.036}$	$4.20^{+0.48}_{-1.12}$	$1.96^{+1.41}_{-0.36}$
5972334	191.03	15.0	5700^{+167}_{-154}	$4.51^{+0.05}_{-0.28}$	$0.87^{+0.37}_{-0.08}$	0.70862545	64.944413	180^{+8}_{-9}	$1.366^{+0.056}_{-0.057}$	$3.52^{+0.41}_{-0.94}$	$1.33^{+0.49}_{-0.23}$
6129524	2886.01	15.9	5260^{+213}_{-163}	$4.59^{+0.03}_{-0.17}$	$0.78^{+0.22}_{-0.06}$	0.88183821	285.152838	268^{+17}_{-16}	$1.121^{+0.071}_{-0.076}$	$5.31^{+0.72}_{-1.40}$	$1.44^{+0.37}_{-0.22}$
6183511	2542.01	15.5	3339^{+50}_{-51}	$4.96^{+0.06}_{-0.12}$	$0.29^{+0.08}_{-0.05}$	0.72733112	64.641934	368^{+23}_{-22}	$0.773^{+0.044}_{-0.047}$	$6.36^{+0.82}_{-1.67}$	$0.61^{+0.17}_{-0.13}$
6265792	2753.01	13.6	6002^{+153}_{-178}	$4.36^{+0.10}_{-0.27}$	$1.09^{+0.45}_{-0.14}$	0.93512027	65.197130	64^{+4}_{-4}	$1.383^{+0.074}_{-0.073}$	$4.57^{+0.57}_{-1.21}$	$0.98^{+0.37}_{-0.19}$
6294819	2852.01	15.9	5966^{+178}_{-211}	$4.49^{+0.04}_{-0.30}$	$0.96^{+0.41}_{-0.09}$	0.67565200	285.617217	193^{+13}_{-12}	$1.702^{+0.085}_{-0.096}$	$2.69^{+0.33}_{-0.71}$	$1.52^{+0.56}_{-0.26}$
6310636	1688.01	14.5	5738^{+183}_{-147}	$4.49^{+0.09}_{-0.29}$	$0.82^{+0.38}_{-0.09}$	0.92103467	65.028092	94^{+5}_{-5}	$2.328^{+0.076}_{-0.072}$	$2.69^{+0.30}_{-0.72}$	$0.90^{+0.37}_{-0.17}$
6362874	1128.01	13.5	5487^{+100}_{-111}	$4.56^{+0.01}_{-0.12}$	$0.83^{+0.12}_{-0.03}$	0.97486662	54.379852	193^{+2}_{-2}	$1.448^{+0.018}_{-0.018}$	$4.59^{+0.49}_{-1.23}$	$1.30^{+0.19}_{-0.16}$
6607286	1239.01	15.0	6108^{+159}_{-234}	$4.47^{+0.04}_{-0.29}$	$1.03^{+0.43}_{-0.10}$	0.78327657	285.814763	264^{+7}_{-7}	$1.489^{+0.030}_{-0.030}$	$3.58^{+0.38}_{-0.96}$	$1.90^{+0.71}_{-0.32}$
6607644	4159.01	14.5	5406^{+170}_{-144}	$4.58^{+0.02}_{-0.24}$	$0.82^{+0.28}_{-0.06}$	0.97190650	65.184987	64^{+5}_{-5}	$1.489^{+0.090}_{-0.088}$	$4.40^{+0.58}_{-1.16}$	$0.75^{+0.22}_{-0.12}$
6666233	2306.01	14.8	3878^{+76}_{-75}	$4.73^{+0.06}_{-0.09}$	$0.52^{+0.07}_{-0.05}$	0.51240853	64.726189	321^{+9}_{-9}	$0.997^{+0.025}_{-0.027}$	$3.50^{+0.38}_{-0.94}$	$1.02^{+0.17}_{-0.15}$
6697756	2798.01	14.1	4374^{+126}_{-137}	$4.64^{+0.06}_{-0.03}$	$0.61^{+0.05}_{-0.06}$	0.91614360	65.021825	93^{+5}_{-5}	$1.025^{+0.057}_{-0.054}$	$6.03^{+0.76}_{-1.59}$	$0.64^{+0.09}_{-0.09}$
6755944	4072.01	13.4	6103^{+150}_{-177}	$4.41^{+0.08}_{-0.27}$	$1.02^{+0.39}_{-0.12}$	0.69297791	53.714011	60^{+3}_{-3}	$1.014^{+0.054}_{-0.054}$	$4.63^{+0.57}_{-1.22}$	$0.89^{+0.31}_{-0.16}$
6867588	2571.01	14.4	5203^{+177}_{-135}	$4.59^{+0.03}_{-0.14}$	$0.78^{+0.17}_{-0.06}$	0.82628363	64.444070	131^{+6}_{-6}	$0.866^{+0.049}_{-0.043}$	$6.44^{+0.81}_{-1.71}$	$1.00^{+0.21}_{-0.14}$
6934291	1367.01	15.1	5076^{+161}_{-131}	$4.61^{+0.03}_{-0.10}$	$0.73^{+0.12}_{-0.05}$	0.56785704	64.223769	338^{+8}_{-8}	$0.906^{+0.023}_{-0.023}$	$4.27^{+0.46}_{-1.14}$	$1.48^{+0.26}_{-0.20}$
6964929	2756.01	14.8	5957^{+154}_{-187}	$4.51^{+0.04}_{-0.27}$	$0.94^{+0.34}_{-0.08}$	0.66502914	64.655142	99^{+5}_{-5}	$1.541^{+0.055}_{-0.052}$	$2.93^{+0.33}_{-0.78}$	$1.06^{+0.34}_{-0.17}$
6974658	2925.01	13.5	5552^{+160}_{-135}	$4.35^{+0.15}_{-0.24}$	$1.03^{+0.38}_{-0.17}$	0.71653130	64.560833	90^{+17}_{-13}	$0.475^{+0.121}_{-0.096}$	$9.60^{+3.29}_{-2.49}$	$1.10^{+0.41}_{-0.25}$
7102227	1360.03	15.6	5153^{+170}_{-143}	$4.60^{+0.03}_{-0.12}$	$0.76^{+0.14}_{-0.06}$	0.76401932	64.458108	131^{+14}_{-13}	$0.991^{+0.101}_{-0.116}$	$5.16^{+0.93}_{-1.32}$	$0.97^{+0.18}_{-0.14}$
7605093	2817.01	15.8	5238^{+202}_{-169}	$4.60^{+0.03}_{-0.13}$	$0.75^{+0.16}_{-0.06}$	0.63400313	102.935144	338^{+21}_{-21}	$0.821^{+0.047}_{-0.050}$	$5.23^{+0.66}_{-1.38}$	$1.54^{+0.32}_{-0.23}$
7749002	4325.01	15.7	5936^{+171}_{-204}	$4.50^{+0.04}_{-0.31}$	$0.96^{+0.42}_{-0.08}$	0.60992303	102.621977	143^{+11}_{-11}	$1.118^{+0.084}_{-0.075}$	$3.65^{+0.52}_{-0.95}$	$1.32^{+0.49}_{-0.22}$
7826620	4268.01	15.2	4294^{+130}_{-146}	$4.74^{+0.07}_{-0.04}$	$0.50^{+0.04}_{-0.05}$	0.84990436	64.675047	124^{+11}_{-10}	$0.984^{+0.082}_{-0.087}$	$5.80^{+0.89}_{-1.51}$	$0.61^{+0.09}_{-0.09}$
7907808	4109.01	14.5	4968^{+149}_{-126}	$3.92^{+0.63}_{-0.40}$	$1.75^{+1.32}_{-0.97}$	0.65594057	64.444338	64^{+4}_{-4}	$1.175^{+0.075}_{-0.073}$	$3.76^{+0.50}_{-0.99}$	$1.53^{+1.16}_{-0.86}$
8235924	2347.01	14.9	3972^{+65}_{-60}	$4.69^{+0.06}_{-0.06}$	$0.56^{+0.05}_{-0.05}$	0.58800041	64.471042	300^{+8}_{-8}	$0.994^{+0.026}_{-0.026}$	$4.03^{+0.44}_{-1.08}$	$1.06^{+0.15}_{-0.14}$
8278371	1150.01	13.3	5735^{+107}_{-115}	$4.34^{+0.11}_{-0.12}$	$1.10^{+0.19}_{-0.13}$	0.67737578	54.074797	71^{+2}_{-2}	$1.701^{+0.039}_{-0.042}$	$2.71^{+0.29}_{-0.73}$	$1.02^{+0.20}_{-0.17}$
8558011	577.02	14.4	5244^{+215}_{-169}	$4.45^{+0.10}_{-0.47}$	$0.89^{+0.68}_{-0.11}$	0.63816268	103.039136	111^{+8}_{-8}	$1.078^{+0.069}_{-0.063}$	$3.98^{+0.53}_{-1.05}$	$1.08^{+0.72}_{-0.22}$
8561063	961.02	15.9	3200^{+174}_{-174}	$5.09^{+0.20}_{-0.20}$	$0.17^{+0.04}_{0.03}$	0.45328732	64.603393	1885^{+28}_{-38}	$0.385^{+0.010}_{-0.007}$	$8.01^{+0.87}_{-2.14}$	$0.92^{+0.15}_{-0.12}$

8804845	2039.02	14.3	5614^{+147}_{-142}	$4.56^{+0.03}_{-0.22}$	$0.83^{+0.27}_{-0.06}$	0.76213044	64.617466	63^{+6}_{-6}	$1.015^{+0.097}_{-0.097}$	$5.01^{+0.84}_{-1.29}$	$0.75^{+0.21}_{-0.12}$
8895758	3106.01	15.4	5853^{+177}_{-210}	$4.46^{+0.05}_{-0.31}$	$1.01^{+0.47}_{-0.10}$	0.96896529	285.390115	114^{+11}_{-12}	$1.364^{+0.119}_{-0.101}$	$4.73^{+0.72}_{-1.23}$	$1.23^{+0.50}_{-0.22}$
8947520	2517.01	14.5	5854^{+179}_{-145}	$4.44^{+0.13}_{-0.30}$	$0.87^{+0.41}_{-0.12}$	0.96852469	64.512671	118^{+7}_{-7}	$1.155^{+0.060}_{-0.063}$	$5.68^{+0.71}_{-1.50}$	$1.06^{+0.46}_{-0.22}$
9092504	2716.01	15.8	5693^{+178}_{-156}	$4.57^{+0.03}_{-0.28}$	$0.80^{+0.34}_{-0.06}$	0.96286621	102.676246	310^{+13}_{-13}	$1.438^{+0.056}_{-0.055}$	$4.55^{+0.52}_{-1.21}$	$1.61^{+0.58}_{-0.26}$
9149789	2874.01	14.9	5461^{+171}_{-137}	$4.59^{+0.03}_{-0.18}$	$0.77^{+0.23}_{-0.06}$	0.35251639	64.663443	163^{+7}_{-8}	$0.864^{+0.042}_{-0.042}$	$2.76^{+0.33}_{-0.73}$	$1.11^{+0.30}_{-0.17}$
9221517	2281.01	13.8	5178^{+172}_{-136}	$4.56^{+0.03}_{-0.15}$	$0.82^{+0.19}_{-0.06}$	0.76985432	64.749343	106^{+4}_{-4}	$0.905^{+0.038}_{-0.037}$	$5.77^{+0.67}_{-1.53}$	$0.95^{+0.20}_{-0.14}$
9388479	936.02	15.1	3581^{+65}_{-50}	$4.81^{+0.08}_{-0.08}$	$0.44^{+0.06}_{-0.06}$	0.89304119	64.861219	746^{+11}_{-11}	$0.987^{+0.014}_{-0.014}$	$6.17^{+0.66}_{-1.65}$	$1.30^{+0.23}_{-0.22}$
9456281	4207.01	15.4	4239^{+123}_{-138}	$4.70^{+0.07}_{-0.04}$	$0.54^{+0.04}_{-0.06}$	0.70194345	65.003065	216^{+32}_{-25}	$0.526^{+0.099}_{-0.086}$	$8.68^{+2.31}_{-2.23}$	$0.85^{+0.13}_{-0.13}$
9472074	2735.01	15.6	5154^{+172}_{-140}	$4.59^{+0.02}_{-0.14}$	$0.80^{+0.14}_{-0.05}$	0.55884253	64.576962	284^{+17}_{-16}	$0.708^{+0.045}_{-0.047}$	$5.33^{+0.71}_{-1.40}$	$1.51^{+0.27}_{-0.20}$
9473078	2079.01	13.0	5582^{+161}_{-153}	$4.31^{+0.15}_{-0.23}$	$1.16^{+0.42}_{-0.20}$	0.69384332	54.078837	46^{+2}_{-2}	$1.355^{+0.052}_{-0.051}$	$3.47^{+0.40}_{-0.92}$	$0.87^{+0.31}_{-0.19}$
9580167	2548.01	15.0	4865^{+183}_{-160}	$4.61^{+0.03}_{-0.07}$	$0.70^{+0.09}_{-0.06}$	0.82715274	285.928326	270^{+34}_{-33}	$1.114^{+0.156}_{-0.123}$	$4.87^{+0.98}_{-1.27}$	$1.27^{+0.21}_{-0.19}$
9787239	952.05	15.8	3727^{+104}_{-64}	$4.76^{+0.08}_{-0.08}$	$0.50^{+0.06}_{-0.06}$	0.74295778	64.794040	221^{+21}_{-21}	$1.004^{+0.100}_{-0.101}$	$4.94^{+0.84}_{-1.27}$	$0.80^{+0.14}_{-0.13}$
10024051	2409.01	14.9	5256^{+168}_{-139}	$4.61^{+0.03}_{-0.12}$	$0.72^{+0.15}_{-0.05}$	0.57736948	64.270976	395^{+8}_{-8}	$0.997^{+0.019}_{-0.019}$	$3.94^{+0.42}_{-1.06}$	$1.60^{+0.33}_{-0.23}$
10028535	2493.01	15.3	5166^{+185}_{-144}	$4.58^{+0.02}_{-0.13}$	$0.79^{+0.15}_{-0.06}$	0.66308666	64.978343	321^{+12}_{-12}	$0.991^{+0.033}_{-0.034}$	$4.55^{+0.51}_{-1.21}$	$1.58^{+0.30}_{-0.22}$
10281221	3913.01	15.0	6263^{+169}_{-211}	$4.46^{+0.05}_{-0.28}$	$1.01^{+0.40}_{-0.10}$	0.58289571	64.620720	581^{+11}_{-11}	$0.712^{+0.017}_{-0.015}$	$5.57^{+0.60}_{-1.49}$	$2.75^{+0.97}_{-0.46}$
10319385	1169.01	13.2	5676^{+100}_{-117}	$4.53^{+0.02}_{-0.14}$	$0.92^{+0.15}_{-0.03}$	0.68920948	53.191352	187^{+2}_{-2}	$1.456^{+0.020}_{-0.019}$	$3.22^{+0.34}_{-0.86}$	$1.41^{+0.22}_{-0.18}$
10468885	2589.01	15.6	5177^{+178}_{-137}	$4.58^{+0.02}_{-0.15}$	$0.80^{+0.17}_{-0.05}$	0.66407444	65.075194	221^{+19}_{-19}	$0.958^{+0.078}_{-0.085}$	$4.66^{+0.72}_{-1.21}$	$1.34^{+0.27}_{-0.20}$
10604521	2797.01	15.8	6173^{+140}_{-276}	$4.43^{+0.05}_{-0.32}$	$1.11^{+0.59}_{-0.12}$	0.86812153	285.335843	245^{+13}_{-13}	$1.398^{+0.053}_{-0.051}$	$4.22^{+0.48}_{-1.13}$	$1.98^{+0.92}_{-0.36}$
10647452	4366.01	15.6	5377^{+223}_{-170}	$4.59^{+0.04}_{-0.17}$	$0.74^{+0.23}_{-0.06}$	0.76295078	285.410004	197^{+18}_{-17}	$0.865^{+0.092}_{-0.074}$	$5.83^{+1.00}_{-1.50}$	$1.18^{+0.33}_{-0.19}$
10975146	1300.01	14.3	4441^{+142}_{-137}	$4.71^{+0.05}_{-0.03}$	$0.53^{+0.04}_{-0.04}$	0.63133223	64.418552	423^{+5}_{-5}	$0.993^{+0.013}_{-0.012}$	$4.33^{+0.47}_{-1.16}$	$1.18^{+0.15}_{-0.15}$
11030475	2248.03	15.5	5290^{+173}_{-142}	$4.60^{+0.03}_{-0.15}$	$0.75^{+0.19}_{-0.06}$	0.76196246	64.259895	182^{+11}_{-10}	$1.123^{+0.059}_{-0.060}$	$4.59^{+0.57}_{-1.22}$	$1.13^{+0.26}_{-0.17}$
11197853	2813.01	13.6	5143^{+164}_{-141}	$4.64^{+0.05}_{-1.10}$	$0.62^{+1.88}_{-0.04}$	0.69846257	53.675039	120^{+10}_{-9}	$0.732^{+0.066}_{-0.066}$	$6.38^{+1.02}_{-1.65}$	$0.84^{+2.12}_{-0.18}$
11246161	2796.01	14.8	6108^{+143}_{-196}	$4.47^{+0.05}_{-0.27}$	$1.00^{+0.38}_{-0.09}$	0.53740984	64.495864	93^{+6}_{-6}	$1.037^{+0.065}_{-0.062}$	$3.49^{+0.46}_{-0.92}$	$1.09^{+0.36}_{-0.18}$
11401182	1428.01	14.6	4911^{+157}_{-128}	$4.53^{+0.06}_{-0.65}$	$0.78^{+0.11}_{-0.07}$	0.92785963	64.122301	492^{+5}_{-5}	$1.224^{+0.013}_{-0.014}$	$5.17^{+0.55}_{-1.39}$	$1.90^{+0.31}_{-0.27}$
11547505	1655.01	13.8	5902^{+155}_{-168}	$4.44^{+0.07}_{-0.27}$	$0.99^{+0.39}_{-0.11}$	0.93846561	63.909869	206^{+5}_{-5}	$1.176^{+0.024}_{-0.025}$	$5.43^{+0.58}_{-1.46}$	$1.60^{+0.57}_{-0.28}$
11600889	1442.01	12.5	5626^{+92}_{-124}	$4.40^{+0.06}_{-0.15}$	$1.07^{+0.21}_{-0.09}$	0.66931017	53.745653	122^{+2}_{-2}	$1.461^{+0.020}_{-0.022}$	$3.12^{+0.33}_{-0.84}$	$1.31^{+0.25}_{-0.19}$
11752632	2492.01	13.8	6060^{+145}_{-170}	$4.51^{+0.04}_{-0.28}$	$0.93^{+0.36}_{-0.08}$	0.98493890	64.350365	75^{+4}_{-4}	$1.828^{+0.062}_{-0.067}$	$3.67^{+0.41}_{-0.98}$	$0.91^{+0.31}_{-0.15}$
11870545	1510.01	15.9	4924^{+156}_{-129}	$4.60^{+0.03}_{-0.07}$	$0.74^{+0.08}_{-0.06}$	0.83996160	102.954242	521^{+19}_{-20}	$1.118^{+0.042}_{-0.039}$	$5.10^{+0.58}_{-1.36}$	$1.84^{+0.27}_{-0.25}$
11904151	72.01	11.0	5627^{+44}_{-44}	$4.34^{+0.03}_{-0.03}$	$1.06^{+0.02}_{-0.02}$	0.83749060	53.687909	177^{+1}_{-1}	$1.634^{+0.010}_{-0.009}$	$3.49^{+0.38}_{-0.94}$	$1.54^{+0.15}_{-0.16}$

12170648	2875.01	14.8	5180^{+168}_{-138}	$4.55^{+0.05}_{-0.13}$	$0.78^{+0.16}_{-0.07}$	0.29969767	64.717608	344^{+11}_{-11}	$0.643^{+0.028}_{-0.028}$	$3.16^{+0.37}_{-0.84}$	$1.61^{+0.33}_{-0.24}$
12265786	4595.01	15.5	4985^{+152}_{-135}	$4.68^{+0.03}_{-0.09}$	$0.63^{+0.09}_{-0.04}$	0.59701811	64.713396	268^{+41}_{-33}	$0.464^{+0.076}_{-0.074}$	$8.41^{+2.06}_{-2.17}$	$1.15^{+0.19}_{-0.17}$
12405333	3009.01	15.2	5231^{+183}_{-140}	$4.48^{+0.08}_{-0.27}$	$0.86^{+0.30}_{-0.09}$	0.76486301	64.368844	154^{+13}_{-13}	$1.017^{+0.084}_{-0.085}$	$5.05^{+0.78}_{-1.31}$	$1.20^{+0.38}_{-0.21}$
3834322	2763.01	15.4	4787^{+144}_{-128}	$4.61^{+0.03}_{-0.06}$	$0.71^{+0.07}_{-0.05}$	0.49843515	64.569826	237^{+13}_{-12}	$0.828^{+0.045}_{-0.043}$	$4.06^{+0.51}_{-1.07}$	$1.20^{+0.17}_{-0.16}$
5008501	1666.01	14.5	6444^{+174}_{-227}	$4.38^{+0.06}_{-0.30}$	$1.20^{+0.63}_{-0.15}$	0.96802576	64.756733	203^{+9}_{-9}	$0.707^{+0.034}_{-0.035}$	$9.29^{+1.12}_{-2.47}$	$1.94^{+0.91}_{-0.38}$
5080636	1843.00	14.4	3584^{+69}_{-54}	$4.80^{+0.06}_{-0.09}$	$0.45^{+0.08}_{-0.05}$	0.17689162	64.552254	155^{+8}_{-8}	$0.581^{+0.027}_{-0.030}$	$2.07^{+0.25}_{-0.55}$	$0.61^{+0.12}_{-0.10}$
5773121	4002.01	15.0	5396^{+155}_{-133}	$4.49^{+0.05}_{-0.23}$	$0.93^{+0.30}_{-0.08}$	0.52417582	64.601474	240^{+11}_{-12}	$0.709^{+0.043}_{-0.038}$	$4.98^{+0.65}_{-1.31}$	$1.63^{+0.47}_{-0.26}$
5980208	2742.01	15.0	4258^{+120}_{-146}	$4.63^{+0.06}_{-0.02}$	$0.62^{+0.04}_{-0.07}$	0.78916057	64.505441	225^{+12}_{-11}	$0.834^{+0.044}_{-0.046}$	$6.41^{+0.80}_{-1.69}$	$1.00^{+0.14}_{-0.15}$
6750902	3980.01	14.7	5888^{+159}_{-160}	$4.39^{+0.11}_{-0.25}$	$1.01^{+0.36}_{-0.14}$	0.46933249	64.742598	316^{+11}_{-10}	$0.743^{+0.029}_{-0.031}$	$4.30^{+0.49}_{-1.15}$	$2.00^{+0.67}_{-0.38}$
7051984	2879.01	12.8	5653^{+165}_{-145}	$3.85^{+0.44}_{-0.22}$	$2.18^{+0.87}_{-1.03}$	0.33906981	53.680375	47^{+1}_{-1}	$0.987^{+0.033}_{-0.032}$	$2.33^{+0.26}_{-0.62}$	$1.61^{+0.70}_{-0.76}$
7269881	2916.01	14.4	5088^{+160}_{-130}	$4.58^{+0.04}_{-0.09}$	$0.74^{+0.12}_{-0.06}$	0.30693783	64.635907	134^{+9}_{-9}	$0.464^{+0.043}_{-0.036}$	$4.39^{+0.70}_{-1.14}$	$0.95^{+0.17}_{-0.14}$
7582691	4419.01	15.2	3939^{+61}_{-51}	$4.74^{+0.06}_{-0.06}$	$0.53^{+0.05}_{-0.05}$	0.25981944	285.437765	281^{+30}_{-26}	$0.423^{+0.053}_{-0.052}$	$4.05^{+0.81}_{-1.04}$	$0.96^{+0.14}_{-0.14}$
8189801	2480.01	15.7	3990^{+84}_{-66}	$4.69^{+0.06}_{-0.11}$	$0.55^{+0.09}_{-0.05}$	0.66682749	64.706275	539^{+26}_{-25}	$0.712^{+0.038}_{-0.037}$	$6.33^{+0.80}_{-1.67}$	$1.42^{+0.25}_{-0.21}$
8416523	4441.01	14.9	5017^{+160}_{-132}	$4.59^{+0.03}_{-0.09}$	$0.75^{+0.11}_{-0.06}$	0.34184200	64.318576	279^{+6}_{-6}	$0.856^{+0.019}_{-0.019}$	$2.72^{+0.29}_{-0.73}$	$1.39^{+0.22}_{-0.19}$
9353742	3867.01	14.9	5825^{+157}_{-180}	$4.52^{+0.03}_{-0.30}$	$0.92^{+0.38}_{-0.07}$	0.93875053	64.682273	272^{+7}_{-7}	$1.240^{+0.028}_{-0.027}$	$5.15^{+0.56}_{-1.38}$	$1.73^{+0.62}_{-0.28}$
9467404	2717.01	12.4	6437^{+151}_{-205}	$4.25^{+0.14}_{-0.31}$	$1.33^{+0.77}_{-0.26}$	0.92990607	53.162180	105^{+1}_{-1}	$1.601^{+0.019}_{-0.020}$	$3.96^{+0.42}_{-1.06}$	$1.53^{+0.82}_{-0.37}$
9475552	2694.01	15.0	4818^{+142}_{-108}	$4.48^{+0.09}_{-0.89}$	$0.86^{+1.90}_{-0.08}$	0.84338039	64.122461	337^{+7}_{-7}	$1.253^{+0.026}_{-0.026}$	$4.58^{+0.49}_{-1.22}$	$1.89^{+3.60}_{-0.40}$
9873254	717.00	13.4	5665^{+105}_{-127}	$4.39^{+0.07}_{-0.17}$	$1.09^{+0.25}_{-0.09}$	0.90037004	53.519695	34^{+3}_{-3}	$1.255^{+0.100}_{-0.099}$	$4.81^{+0.71}_{-1.26}$	$0.72^{+0.16}_{-0.11}$
9885417	3246.01	12.4	4854^{+130}_{-107}	$3.94^{+0.62}_{-0.43}$	$1.75^{+1.40}_{-0.96}$	0.68996781	53.595490	113^{+2}_{-2}	$1.042^{+0.024}_{-0.023}$	$4.51^{+0.49}_{-1.21}$	$2.03^{+1.62}_{-1.14}$
9967771	1875.02	14.5	5953^{+158}_{-175}	$4.49^{+0.05}_{-0.28}$	$0.93^{+0.37}_{-0.09}$	0.53835457	64.648809	185^{+5}_{-5}	$1.344^{+0.029}_{-0.029}$	$2.73^{+0.29}_{-0.73}$	$1.43^{+0.51}_{-0.24}$
10186945	4070.01	14.5	5080^{+178}_{-137}	$4.53^{+0.04}_{-0.13}$	$0.83^{+0.16}_{-0.06}$	0.39683023	64.395900	170^{+7}_{-7}	$0.753^{+0.033}_{-0.033}$	$3.58^{+0.42}_{-0.95}$	$1.20^{+0.23}_{-0.17}$
12115188	2396.01	14.7	5529^{+158}_{-142}	$4.47^{+0.06}_{-0.26}$	$0.94^{+0.35}_{-0.09}$	0.49543428	64.477019	281^{+6}_{-6}	$1.111^{+0.023}_{-0.026}$	$3.04^{+0.33}_{-0.81}$	$1.77^{+0.59}_{-0.29}$

Stellar parameters obtained from the compilation by [97].

Transit parameters based on an analysis of the folded transit light curve.

The first 18 objects are new planet candidates. These objects either emerged from our search for the first time, or appear on the KOI list as false positives but that we consider to be viable candidates. After the double horizontal lines, the 69 KOIs that passed our false positive tests [3].

Finally, after the next double horizontal lines, 19 other candidates that were discovered by other authors ([145], [96] and [99]).

Planets discovered transiting stars with other KOI planets with no KOI number assigned are labelled with the KOI of the star followed by a dot and two zeros.

Chapter 9

Summary and Conclusions

In this thesis I have developed a new technique to measure the obliquity of planetary systems using photometry alone, and I have studied in detail the properties of the shortest-period planets found with Kepler. Both lines of research have a lot of potential over the coming years, and in this final chapter I summarize my findings and discuss the current and future projects that will likely arise from both topics.

9.1 Measuring obliquities

Over the past decade, measurements of obliquities of planet hosts using the Rossiter-McLaughlin (RM) effect have frequently appeared in the literature (see, e.g., [162], [146], [71], [214] and [5]). The majority of measurements correspond to Hot-Jupiters, because the RM signal is enhanced by the larger transit depths, and the short orbital periods make it easier to schedule observations. As it has been pointed out throughout the first half of this thesis, extending obliquity measurements towards longer orbital periods, smaller planets, and multi planet systems is crucial to understand the formation and evolution of Hot-Jupiters and planetary systems in general. But even 4 years after the first Kepler planets were announced [21], with hundreds or even thousands of planet systems outside of the Hot-Jupiter family, obliquity measurements have not been carried over to these smaller or long period planets as much as needed. It is complicated to schedule RM observations for long orbital period planets, but the

biggest issue is the faintness of most Kepler host stars, which are not amenable to precise radial velocity work. Nevertheless, the RM effect has been used to measure a low obliquity for two Kepler multi-planet systems([84], [6]). Incidentally, in this thesis I have presented the analysis of the RM effect of Kepler-63b (see Chapter 5), which represents one of the longest period planets ($P_{orb} = 9.4$ days) with an obliquity measured using the RM effect.

In this thesis I have discussed and developed a new technique to measure obliquities using photometry alone, based on the passage of the planet over starspots. In Chapters 2 and 3, I have applied the technique to two close-in gas giants, one with a low and one with high obliquity. In both cases, the RM effect was observed before the photometric analysis was performed, and the spot-crossing technique not only produces results that agree with the previous measurements, it also improves upon the precision of the final obliquity measurement. The results of Chapter 5 are even more encouraging, where the spot-crossing technique predicted a high value of the obliquity that was later confirmed via the RM effect. This shows that the technique is reliable, and it can be safely applied to other systems like Kepler-30 (see Chapter 4) or systems in our Spot-Crossing Events Catalog (SCEC, see Chapter 6), for which a second measurement via other techniques might not be available.

It would certainly be very exciting to measure the obliquity of more multi planet systems. Currently, the large majority of multi-planet systems with obliquity measurements are aligned. The spot-crossing technique was applied to Kepler-30 (see Chapter 4), and later the obliquities of Kepler-25 and Kepler-89 were obtained with the RM effect ([84], [6]). Another promising technique, asteroseismology, has been able to measure a low line-of-sight obliquity for 3 more Kepler multi-planet systems ([37], [218]), which all follow the trend predicted in Chapter 4, where, unlike the Hot-Jupiters, multi-transiting planet systems should have low obliquities.

The recent discovery of Kepler-56, a system with two transiting planets orbiting a sub giant star, seems to contradict this trend. A detailed asteroseismic analysis shows that the line-of-sight obliquity is 45°, significantly different from zero. The presence of a fourth body in the system, inferred from a linear trend observed in the

RV signal, could potentially explain the misalignment of the orbits of the two other planets. Even if that is the case, it will be much harder to explain the more recent results that show that a small but significant fraction of multi-transiting systems might be misaligned with respect to the spin axis of their host stars [87]. This result is based on a different technique that uses the line broadening of the star to estimate $v \sin i$, where i is the line-of-sight obliquity of the multi-transiting planet system, and $v = 2\pi R_*/P_{rot}$. This technique offers lower precision measurements of the obliquity, but it can be applied to many systems with a reasonable amount of telescope time [87].

At this point it does not seem that the spot-crossing technique will be able to provide as many obliquity measurements for multi-planet systems as required in the near future. In order to be applicable, the host stars need to be chromospherically active, slightly brighter than the average Kepler stars and transits of a gas giant with an orbital period shorter than a few hundred days are required. This type of system is not so common, particularly because Nature does not seem to create many multi-planet systems with a close-in gas giant. Measuring a high obliquity for even one of the multi-planet systems in the SCEC (see Chapter 6), would provide the first clear high obliquity of such a system with a main-sequence host star, and would surely spark follow-up observations in an attempt to detect any perturbing body that could have tilted the orbits. As suggested in Chapter 6, a technique capable of extracting information about the obliquity of a transiting object based on the combination of information from several consecutive transits, and without requiring individual spot-crossing events to be detected, could open a new window towards building a large sample of multi-planet systems with obliquity constraints.

It is unclear if new transit missions will be able to provide better multi-planet targets for the spot-crossing technique. With the current design of K2 and TESS, both will have a different strategy than the original Kepler mission to detect planets. They will stare at a given field for a shorter time interval (one to three months) before moving to the next field, significantly decreasing the probability of detecting multi-transiting systems. The PLATO mission, recently selected by ESA to be launched

by 2024, will have a strategy similar to Kepler, and could provide the next great opportunity for future applications of the spot-crossing technique to multi-planet systems. Before then, other techniques that benefit from the brightness of the stars observed by K2 and TESS will likely contribute to the discussion with more obliquity measurements.

The true potential of the technique lies in the application to single transiting planets and eclipsing binaries. In both cases, we frequently have deep eclipses where the spot-crossing events are easy to detect and characterize. With the large list of such objects in the SCEC, the number of measured obliquities could be increase by 10-20 for single planet systems, and 20-40 for eclipsing binary stars (almost doubling the current set of obliquity measurements [4]). It would be interesting to extend obliquity measurements to orbital periods longer than 10 days, in an attempt to draw a fiducial line (if it exists) between single planet systems with random obliquities and planets with low obliquities. The longer the orbital period, the weaker the tidal interactions, which in principle means that the distribution of obliquities for longer orbital period planets should be more similar to the primordial obliquity distribution. Comparing the obliquity distribution of eclipsing binary stars to that of single planet systems can help us distinguish between different formation scenarios for both types of systems. Tides are expected to be stronger in eclipsing binaries, so that realigning the spin axis of the host stars with respect to the orbit should be easier, complicating the interpretation of the results. Both K2 and TESS will likely uncover many short period single planet systems and eclipsing binaries for which this method could be applied, so that in time the spot-crossing technique could become the most prolific technique for measuring obliquities.

9.2 Ultra-short period planets

Planets with orbital periods shorter than 1 day represent a great opportunity for follow-up observations, and they are also intrinsically interesting due to their unusual orbits. Their short orbital periods allows us to detect many more transits in a given

interval of time, and their close orbital distances increase the radial velocity amplitude, yielding a globally better sensitivity towards low-mass and small-size planets. CoRoT-7b ([110], [161]) and Kepler-10b [14], the first two rocky planets discovered, represent the best example, with orbital periods of only about 20 hours.

The discovery of Kepler-78b (see Chapter 7), a 1.2 Earth radius planet with an orbital period of 8.5 hours, can now be added to the short list of rocky planets known so far. Both HIREs at Keck [94] and HARPS-N at TNG [151] were capable of detecting the tiny radial velocity signal induced by this 1.7 $M_{\oplus}$ planet (1.6 m/s). From this work, new observing strategies have been created to follow up USP planets. Such short orbital periods allow us to measure a full orbit in just one night, something that will simplify future observational campaigns and can help beat night-to-night sources of systematic noise like starspots.

In Chapter 8 I have also fully described a different approach to searching for USP planets, in which transits are detected via the study of the harmonic structure of the Fourier Transform of the flux time series. This technique is fast and robust, providing unprecedented flexibility when planning a large scale survey. Missions like K2 and TESS should be able to provide more USP planets on a relatively short timescale. According to the numbers obtained in Chapter 8, these planets will not represent the majority of planets discovered by these two missions, but they will likely represent some of the best candidates for follow-up observations for planet radii smaller than $2R_{\oplus}$.

We also have produced a clean well vetted list of planet candidates discovered by Kepler that can lead to future an interesting projects. In Chapter 8 I describe several important characteristics of USP planets that might give us clues about how they formed and evolved. The scarcity of USP planets larger than $2R_{\oplus}$ points toward the presence of a mechanism that can remove the envelope of these planets, and photo-evaporation is suggested as the best candidate mechanism. Most USP candidates belong to multi-planet systems, which may indicate that the presence of several planets is required for the USP planets to get so close to their host stars. This certainly differentiates USP planets from the family of Hot-Jupiters, which are always found

alone [202]. The scarcity of USP planets in multi-planet systems with period ratios shorter than 3 [201], seems to indicate the presence of tidal interactions that could have affected the inner planet substantially more than the outer planet, and hence increased the period ratio. This might also help us to interpret the higher abundance of USP planets orbiting cold stars. If indeed tidal interactions are responsible for bringing the inner planet closer to the star, these interactions would be weaker for hotter stars, reducing the effectivity of this mechanism. This particular idea, together with simulations of the dynamical evolution of these systems, are worth exploring in detail.

The clean list of well vetted planet candidates also represents a great opportunity for follow-up work. Several observing programs are running and will allow us to study the host stars in detail by obtaining their spectra, as well as the planets themselves for those candidates amenable to RV follow-up. There are not that many rocky planets that have been characterized to date, and studying a few more in detail could help us to understand important things about our own planet. In particular, USP planets are among the few planets for which very little atmosphere is expected due to photo-evaporation. This means that in extreme cases, the planet can be considered as a "naked core", cores for which we can determine masses and radii. It is also exciting to learn about the processes that shape the planet's surface at such high temperatures, by studying their secondary eclipses. As pointed out in Chapter 8, several of the USP candidates have detected secondary eclipses, and it is worth analyzing those to understand the reflecting properties of volatiles at extreme temperatures.

Bibliography

[1] E. Agol, J. Steffen, R. Sari, and W. Clarkson. On detecting terrestrial planets with timing of giant planet transits. *MNRAS*, 359:567–579, May 2005.

[2] S. Aigrain, F. Pont, and S. Zucker. A simple method to estimate radial velocity variations due to stellar activity using photometry. *MNRAS*, 419:3147–3158, Feb. 2012.

[3] R. L. Akeson, X. Chen, D. Ciardi, M. Crane, J. Good, M. Harbut, E. Jackson, S. R. Kane, A. C. Laity, S. Leifer, M. Lynn, D. L. McElroy, M. Papin, P. Plavchan, S. V. Ramírez, R. Rey, K. von Braun, M. Wittman, M. Abajian, B. Ali, C. Beichman, A. Beekley, G. B. Berriman, S. Berukoff, G. Bryden, B. Chan, S. Groom, C. Lau, A. N. Payne, M. Regelson, M. Saucedo, M. Schmitz, J. Stauffer, P. Wyatt, and A. Zhang. The NASA Exoplanet Archive: Data and Tools for Exoplanet Research. *PASP*, 125:989–999, Aug. 2013.

[4] S. Albrecht, J. N. Winn, J. A. Carter, I. A. G. Snellen, and E. J. W. de Mooij. The Banana Project. III. Spin-Orbit Alignment in the Long-period Eclipsing Binary NY Cephei. *ApJ*, 726:68, Jan. 2011.

[5] S. Albrecht, J. N. Winn, J. A. Johnson, A. W. Howard, G. W. Marcy, R. P. Butler, P. Arriagada, J. D. Crane, S. A. Shectman, I. B. Thompson, T. Hirano, G. Bakos, and J. D. Hartman. Obliquities of Hot Jupiter Host Stars: Evidence for Tidal Interactions and Primordial Misalignments. *ApJ*, 757:18, Sept. 2012.

[6] S. Albrecht, J. N. Winn, G. W. Marcy, A. W. Howard, H. Isaacson, and J. A. Johnson. Low Stellar Obliquities in Compact Multiplanet Systems. *ApJ*, 771:11, July 2013.

[7] G. Bakos, R. W. Noyes, G. Kovács, K. Z. Stanek, D. D. Sasselov, and I. Domsa. Wide-Field Millimagnitude Photometry with the HAT: A Tool for Extrasolar Planet Detection. *PASP*, 116:266–277, Mar. 2004.

[8] G. Á. Bakos, G. Torres, A. Pál, J. Hartman, G. Kovács, R. W. Noyes, D. W. Latham, D. D. Sasselov, B. Sipőcz, G. A. Esquerdo, D. A. Fischer, J. A. Johnson, G. W. Marcy, R. P. Butler, H. Isaacson, A. Howard, S. Vogt, G. Kovács, J. Fernandez, A. Moór, R. P. Stefanik, J. Lázár, I. Papp, and P. Sári. HAT-P-11b: A Super-Neptune Planet Transiting a Bright K Star in the Kepler Field. *ApJ*, 710:1724–1745, Feb. 2010.

[9] I. Baraffe, F. Selsis, G. Chabrier, T. S. Barman, F. Allard, P. H. Hauschildt, and H. Lammer. The effect of evaporation on the evolution of close-in giant planets. *A&A*, 419:L13–L16, May 2004.

[10] T. Barclay, D. Huber, J. F. Rowe, J. J. Fortney, C. V. Morley, E. V. Quintana, D. C. Fabrycky, G. Barentsen, S. Bloemen, J. L. Christiansen, B.-O. Demory, B. J. Fulton, J. M. Jenkins, F. Mullally, D. Ragozzine, S. E. Seader, A. Shporer, P. Tenenbaum, and S. E. Thompson. Photometrically Derived Masses and Radii of the Planet and Star in the TrES-2 System. *ApJ*, 761:53, Dec. 2012.

[11] P. Barge, A. Baglin, M. Auvergne, H. Rauer, A. Léger, J. Schneider, F. Pont, S. Aigrain, J.-M. Almenara, R. Alonso, M. Barbieri, P. Bordé, F. Bouchy, H. J. Deeg, D. La Reza, M. Deleuil, R. Dvorak, A. Erikson, M. Fridlund, M. Gillon, P. Gondoin, T. Guillot, A. Hatzes, G. Hebrard, L. Jorda, P. Kabath, H. Lammer, A. Llebaria, B. Loeillet, P. Magain, T. Mazeh, C. Moutou, M. Ollivier, M. Pätzold, D. Queloz, D. Rouan, A. Shporer, and G. Wuchterl. Transiting exoplanets from the CoRoT space mission. I. CoRoT-Exo-1b: a low-density short-period planet around a G0V star. *A&A*, 482:L17–L20, May 2008.

[12] S. A. Barnes. Ages for Illustrative Field Stars Using Gyrochronology: Viability, Limitations, and Errors. *ApJ*, 669:1167–1189, Nov. 2007.

[13] G. Basri, L. M. Walkowicz, N. Batalha, R. L. Gilliland, J. Jenkins, W. J. Borucki, D. Koch, D. Caldwell, A. K. Dupree, D. W. Latham, G. W. Marcy, S. Meibom, and T. Brown. Photometric Variability in Kepler Target Stars. II. An Overview of Amplitude, Periodicity, and Rotation in First Quarter Data. *AJ*, 141:20, Jan. 2011.

[14] N. M. Batalha, W. J. Borucki, S. T. Bryson, L. A. Buchhave, D. A. Caldwell, J. Christensen-Dalsgaard, D. Ciardi, E. W. Dunham, F. Fressin, T. N. Gautier, III, R. L. Gilliland, M. R. Haas, S. B. Howell, J. M. Jenkins, H. Kjeldsen, D. G. Koch, D. W. Latham, J. J. Lissauer, G. W. Marcy, J. F. Rowe, D. D. Sasselov, S. Seager, J. H. Steffen, G. Torres, G. S. Basri, T. M. Brown, D. Charbonneau, J. Christiansen, B. Clarke, W. D. Cochran, A. Dupree, D. C. Fabrycky, D. Fischer, E. B. Ford, J. Fortney, F. R. Girouard, M. J. Holman, J. Johnson, H. Isaacson, T. C. Klaus, P. Machalek, A. V. Moorehead, R. C. Morehead, D. Ragozzine, P. Tenenbaum, J. Twicken, S. Quinn, J. VanCleve, L. M. Walkowicz, W. F. Welsh, E. Devore, and A. Gould. Kepler's First Rocky Planet: Kepler-10b. *ApJ*, 729:27, Mar. 2011.

[15] N. M. Batalha, J. F. Rowe, S. T. Bryson, T. Barclay, C. J. Burke, D. A. Caldwell, J. L. Christiansen, F. Mullally, S. E. Thompson, T. M. Brown, A. K. Dupree, D. C. Fabrycky, E. B. Ford, J. J. Fortney, R. L. Gilliland, H. Isaacson, D. W. Latham, G. W. Marcy, S. N. Quinn, D. Ragozzine, A. Shporer, W. J. Borucki, D. R. Ciardi, T. N. Gautier, III, M. R. Haas, J. M. Jenkins, D. G. Koch, J. J. Lissauer, W. Rapin, G. S. Basri, A. P. Boss, L. A. Buchhave, J. A. Carter,

D. Charbonneau, J. Christensen-Dalsgaard, B. D. Clarke, W. D. Cochran, B.-O. Demory, J.-M. Desert, E. Devore, L. R. Doyle, G. A. Esquerdo, M. Everett, F. Fressin, J. C. Geary, F. R. Girouard, A. Gould, J. R. Hall, M. J. Holman, A. W. Howard, S. B. Howell, K. A. Ibrahim, K. Kinemuchi, H. Kjeldsen, T. C. Klaus, J. Li, P. W. Lucas, S. Meibom, R. L. Morris, A. Prša, E. Quintana, D. T. Sanderfer, D. Sasselov, S. E. Seader, J. C. Smith, J. H. Steffen, M. Still, M. C. Stumpe, J. C. Tarter, P. Tenenbaum, G. Torres, J. D. Twicken, K. Uddin, J. Van Cleve, L. Walkowicz, and W. F. Welsh. Planetary Candidates Observed by Kepler. III. Analysis of the First 16 Months of Data. *ApJS*, 204:24, Feb. 2013.

[16] N. M. Batalha, J. F. Rowe, R. L. Gilliland, J. J. Jenkins, D. Caldwell, W. J. Borucki, D. G. Koch, J. J. Lissauer, E. W. Dunham, T. N. Gautier, S. B. Howell, D. W. Latham, G. W. Marcy, and A. Prsa. Pre-spectroscopic False-positive Elimination of Kepler Planet Candidates. *ApJL*, 713:L103–L108, Apr. 2010.

[17] M. R. Bate, G. Lodato, and J. E. Pringle. Chaotic star formation and the alignment of stellar rotation with disc and planetary orbital axes. *MNRAS*, 401:1505–1513, Jan. 2010.

[18] S. V. Berdyugina and G. W. Henry. Butterfly Diagram and Activity Cycles in HR 1099. *ApJL*, 659:L157–L160, Apr. 2007.

[19] I. A. Bond, A. Udalski, M. Jaroszyński, N. J. Rattenbury, B. Paczyński, I. Soszyński, L. Wyrzykowski, M. K. Szymański, M. Kubiak, O. Szewczyk, K. Żebruń, G. Pietrzyński, F. Abe, D. P. Bennett, S. Eguchi, Y. Furuta, J. B. Hearnshaw, K. Kamiya, P. M. Kilmartin, Y. Kurata, K. Masuda, Y. Matsubara, Y. Muraki, S. Noda, K. Okajima, T. Sako, T. Sekiguchi, D. J. Sullivan, T. Sumi, P. J. Tristram, T. Yanagisawa, P. C. M. Yock, and OGLE Collaboration. OGLE 2003-BLG-235/MOA 2003-BLG-53: A Planetary Microlensing Event. *ApJL*, 606:L155–L158, May 2004.

[20] A. S. Bonomo and A. F. Lanza. Starspot activity and rotation of the planet-hosting star Kepler-17. *A&A*, 547:A37, Nov. 2012.

[21] W. J. Borucki, D. Koch, G. Basri, N. Batalha, T. Brown, D. Caldwell, J. Caldwell, J. Christensen-Dalsgaard, W. D. Cochran, E. DeVore, E. W. Dunham, A. K. Dupree, T. N. Gautier, J. C. Geary, R. Gilliland, A. Gould, S. B. Howell, J. M. Jenkins, Y. Kondo, D. W. Latham, G. W. Marcy, S. Meibom, H. Kjeldsen, J. J. Lissauer, D. G. Monet, D. Morrison, D. Sasselov, J. Tarter, A. Boss, D. Brownlee, T. Owen, D. Buzasi, D. Charbonneau, L. Doyle, J. Fortney, E. B. Ford, M. J. Holman, S. Seager, J. H. Steffen, W. F. Welsh, J. Rowe, H. Anderson, L. Buchhave, D. Ciardi, L. Walkowicz, W. Sherry, E. Horch, H. Isaacson, M. E. Everett, D. Fischer, G. Torres, J. A. Johnson, M. Endl, P. MacQueen, S. T. Bryson, J. Dotson, M. Haas, J. Kolodziejczak, J. Van Cleve, H. Chandrasekaran, J. D. Twicken, E. V. Quintana, B. D. Clarke, C. Allen, J. Li,

H. Wu, P. Tenenbaum, E. Verner, F. Bruhweiler, J. Barnes, and A. Prsa. Kepler Planet-Detection Mission: Introduction and First Results. *Science*, 327:977–, Feb. 2010.

[22] W. J. Borucki, D. G. Koch, G. Basri, N. Batalha, A. Boss, T. M. Brown, D. Caldwell, J. Christensen-Dalsgaard, W. D. Cochran, E. DeVore, E. W. Dunham, A. K. Dupree, T. N. Gautier, III, J. C. Geary, R. Gilliland, A. Gould, S. B. Howell, J. M. Jenkins, H. Kjeldsen, D. W. Latham, J. J. Lissauer, G. W. Marcy, D. G. Monet, D. Sasselov, J. Tarter, D. Charbonneau, L. Doyle, E. B. Ford, J. Fortney, M. J. Holman, S. Seager, J. H. Steffen, W. F. Welsh, C. Allen, S. T. Bryson, L. Buchhave, H. Chandrasekaran, J. L. Christiansen, D. Ciardi, B. D. Clarke, J. L. Dotson, M. Endl, D. Fischer, F. Fressin, M. Haas, E. Horch, A. Howard, H. Isaacson, J. Kolodziejczak, J. Li, P. MacQueen, S. Meibom, A. Prsa, E. V. Quintana, J. Rowe, W. Sherry, P. Tenenbaum, G. Torres, J. D. Twicken, J. Van Cleve, L. Walkowicz, and H. Wu. Characteristics of Kepler Planetary Candidates Based on the First Data Set. *ApJ*, 728:117, Feb. 2011.

[23] W. J. Borucki, D. G. Koch, T. M. Brown, G. Basri, N. M. Batalha, D. A. Caldwell, W. D. Cochran, E. W. Dunham, T. N. Gautier, III, J. C. Geary, R. L. Gilliland, S. B. Howell, J. M. Jenkins, D. W. Latham, J. J. Lissauer, G. W. Marcy, D. Monet, J. F. Rowe, and D. Sasselov. Kepler-4b: A Hot Neptune-like Planet of a G0 Star Near Main-sequence Turnoff. *ApJL*, 713:L126–L130, Apr. 2010.

[24] B. P. Brown, M. K. Browning, A. S. Brun, M. S. Miesch, and J. Toomre. Persistent Magnetic Wreaths in a Rapidly Rotating Sun. *ApJ*, 711:424–438, Mar. 2010.

[25] D. J. A. Brown, A. Collier Cameron, R. F. Díaz, A. P. Doyle, M. Gillon, M. Lendl, B. Smalley, A. H. M. J. Triaud, D. R. Anderson, B. Enoch, C. Hellier, P. F. L. Maxted, G. R. M. Miller, D. Pollacco, D. Queloz, I. Boisse, and G. Hébrard. Analysis of Spin-Orbit Alignment in the WASP-32, WASP-38, and HAT-P-27/WASP-40 Systems. *ApJ*, 760:139, Dec. 2012.

[26] T. M. Brown, D. W. Latham, M. E. Everett, and G. A. Esquerdo. Kepler Input Catalog: Photometric Calibration and Stellar Classification. *AJ*, 142:112, Oct. 2011.

[27] J. H. M. J. Bruls, S. K. Solanki, and M. Schuessler. Doppler imaging: the polar SPOT controversy. *A&A*, 336:231–241, Aug. 1998.

[28] S. T. Bryson, J. M. Jenkins, R. L. Gilliland, J. D. Twicken, B. Clarke, J. Rowe, D. Caldwell, N. Batalha, F. Mullally, M. R. Haas, and P. Tenenbaum. Identification of Background False Positives from Kepler Data. *PASP*, 125:889–923, Aug. 2013.

[29] L. A. Buchhave, G. Á. Bakos, J. D. Hartman, G. Torres, G. Kovács, D. W. Latham, R. W. Noyes, G. A. Esquerdo, M. Everett, A. W. Howard, G. W.

Marcy, D. A. Fischer, J. A. Johnson, J. Andersen, G. Fűrész, G. Perumpilly, D. D. Sasselov, R. P. Stefanik, B. Béky, J. Lázár, I. Papp, and P. Sári. HAT-P-16b: A 4 M $_J$ Planet Transiting a Bright Star on an Eccentric Orbit. *ApJ*, 720:1118–1125, Sept. 2010.

[30] L. A. Buchhave, D. W. Latham, A. Johansen, M. Bizzarro, G. Torres, J. F. Rowe, N. M. Batalha, W. J. Borucki, E. Brugamyer, C. Caldwell, S. T. Bryson, D. R. Ciardi, W. D. Cochran, M. Endl, G. A. Esquerdo, E. B. Ford, J. C. Geary, R. L. Gilliland, T. Hansen, H. Isaacson, J. B. Laird, P. W. Lucas, G. W. Marcy, J. A. Morse, P. Robertson, A. Shporer, R. P. Stefanik, M. Still, and S. N. Quinn. An abundance of small exoplanets around stars with a wide range of metallicities. *Natur*, 486:375–377, June 2012.

[31] R. P. Butler, G. W. Marcy, E. Williams, C. McCarthy, P. Dosanjh, and S. S. Vogt. Attaining Doppler Precision of 3 M s-1. *PASP*, 108:500, June 1996.

[32] R. P. Butler, J. T. Wright, G. W. Marcy, D. A. Fischer, S. S. Vogt, C. G. Tinney, H. R. A. Jones, B. D. Carter, J. A. Johnson, C. McCarthy, and A. J. Penny. Catalog of Nearby Exoplanets. *ApJ*, 646:505–522, July 2006.

[33] R. C. Carrington. On the Distribution of the Solar Spots in Latitudes since the Beginning of the Year 1854, with a Map. *MNRAS*, 19:1–3, Nov. 1858.

[34] J. A. Carter, E. Agol, W. J. Chaplin, S. Basu, T. R. Bedding, L. A. Buchhave, J. Christensen-Dalsgaard, K. M. Deck, Y. Elsworth, D. C. Fabrycky, E. B. Ford, J. J. Fortney, S. J. Hale, R. Handberg, S. Hekker, M. J. Holman, D. Huber, C. Karoff, S. D. Kawaler, H. Kjeldsen, J. J. Lissauer, E. D. Lopez, M. N. Lund, M. Lundkvist, T. S. Metcalfe, A. Miglio, L. A. Rogers, D. Stello, W. J. Borucki, S. Bryson, J. L. Christiansen, W. D. Cochran, J. C. Geary, R. L. Gilliland, M. R. Haas, J. Hall, A. W. Howard, J. M. Jenkins, T. Klaus, D. G. Koch, D. W. Latham, P. J. MacQueen, D. Sasselov, J. H. Steffen, J. D. Twicken, and J. N. Winn. Kepler-36: A Pair of Planets with Neighboring Orbits and Dissimilar Densities. *Science*, 337:556–, Aug. 2012.

[35] J. A. Carter, D. C. Fabrycky, D. Ragozzine, M. J. Holman, S. N. Quinn, D. W. Latham, L. A. Buchhave, J. Van Cleve, W. D. Cochran, M. T. Cote, M. Endl, E. B. Ford, M. R. Haas, J. M. Jenkins, D. G. Koch, J. Li, J. J. Lissauer, P. J. MacQueen, C. K. Middour, J. A. Orosz, J. F. Rowe, J. H. Steffen, and W. F. Welsh. KOI-126: A Triply Eclipsing Hierarchical Triple with Two Low-Mass Stars. *Science*, 331:562–, Feb. 2011.

[36] J. A. Carter, J. N. Winn, M. J. Holman, D. Fabrycky, Z. K. Berta, C. J. Burke, and P. Nutzman. The Transit Light Curve Project. XIII. Sixteen Transits of the Super-Earth GJ 1214b. *ApJ*, 730:82, Apr. 2011.

[37] W. J. Chaplin, R. Sanchis-Ojeda, T. L. Campante, R. Handberg, D. Stello, J. N. Winn, S. Basu, J. Christensen-Dalsgaard, G. R. Davies, T. S. Metcalfe, L. A.

Buchhave, D. A. Fischer, T. R. Bedding, W. D. Cochran, Y. Elsworth, R. L. Gilliland, S. Hekker, D. Huber, H. Isaacson, C. Karoff, S. D. Kawaler, H. Kjeldsen, D. W. Latham, M. N. Lund, M. Lundkvist, G. W. Marcy, A. Miglio, T. Barclay, and J. J. Lissauer. Asteroseismic Determination of Obliquities of the Exoplanet Systems Kepler-50 and Kepler-65. *ApJ*, 766:101, Apr. 2013.

[38] D. Charbonneau, T. M. Brown, D. W. Latham, and M. Mayor. Detection of Planetary Transits Across a Sun-like Star. *ApJL*, 529:L45–L48, Jan. 2000.

[39] S. Charpinet, G. Fontaine, P. Brassard, E. M. Green, V. Van Grootel, S. K. Randall, R. Silvotti, A. S. Baran, R. H. Østensen, S. D. Kawaler, and J. H. Telting. A compact system of small planets around a former red-giant star. *Natur*, 480:496–499, Dec. 2011.

[40] J. L. Christiansen, J. M. Jenkins, D. A. Caldwell, C. J. Burke, P. Tenenbaum, S. Seader, S. E. Thompson, T. S. Barclay, B. D. Clarke, J. Li, J. C. Smith, M. C. Stumpe, J. D. Twicken, and J. Van Cleve. The Derivation, Properties, and Value of Kepler"s Combined Differential Photometric Precision. *PASP*, 124:1279–1287, Dec. 2012.

[41] A. Claret. A new non-linear limb-darkening law for LTE stellar atmosphere models III. Sloan filters: Calculations for -5.0 $\leq$ log [M/H] $\leq$ +1, 2000 K $\leq$ T_{eff} $\leq$ 50 000 K at several surface gravities. *A&A*, 428:1001–1005, Dec. 2004.

[42] A. Claret and S. Bloemen. Gravity and limb-darkening coefficients for the Kepler, CoRoT, Spitzer, uvby, UBVRIJHK, and Sloan photometric systems. *A&A*, 529:A75, May 2011.

[43] W. D. Cochran, D. C. Fabrycky, G. Torres, F. Fressin, J.-M. Désert, D. Ragozzine, D. Sasselov, J. J. Fortney, J. F. Rowe, E. J. Brugamyer, S. T. Bryson, J. A. Carter, D. R. Ciardi, S. B. Howell, J. H. Steffen, W. J. Borucki, D. G. Koch, J. N. Winn, W. F. Welsh, K. Uddin, P. Tenenbaum, M. Still, S. Seager, S. N. Quinn, F. Mullally, N. Miller, G. W. Marcy, P. J. MacQueen, P. Lucas, J. J. Lissauer, D. W. Latham, H. Knutson, K. Kinemuchi, J. A. Johnson, J. M. Jenkins, H. Isaacson, A. Howard, E. Horch, M. J. Holman, C. E. Henze, M. R. Haas, R. L. Gilliland, T. N. Gautier, III, E. B. Ford, D. A. Fischer, M. Everett, M. Endl, B.-O. Demory, D. Deming, D. Charbonneau, D. Caldwell, L. Buchhave, T. M. Brown, and N. Batalha. Kepler-18b, c, and d: A System of Three Planets Confirmed by Transit Timing Variations, Light Curve Validation, Warm-Spitzer Photometry, and Radial Velocity Measurements. *ApJS*, 197:7, Nov. 2011.

[44] N. B. Cowan and E. Agol. The Statistics of Albedo and Heat Recirculation on Hot Exoplanets. *ApJ*, 729:54, Mar. 2011.

[45] S. Czesla, K. F. Huber, U. Wolter, S. Schröter, and J. H. M. M. Schmitt. How stellar activity affects the size estimates of extrasolar planets. *A&A*, 505:1277–1282, Oct. 2009.

[46] R. I. Dawson and D. C. Fabrycky. Radial Velocity Planets De-aliased: A New, Short Period for Super-Earth 55 Cnc e. *ApJ*, 722:937–953, Oct. 2010.

[47] R. I. Dawson and J. A. Johnson. The Photoeccentric Effect and Proto-hot Jupiters. I. Measuring Photometric Eccentricities of Individual Transiting Planets. *ApJ*, 756:122, Sept. 2012.

[48] D. Deming, P. V. Sada, B. Jackson, S. W. Peterson, E. Agol, H. A. Knutson, D. E. Jennings, F. Haase, and K. Bays. Kepler and Ground-based Transits of the Exo-Neptune HAT-P-11b. *ApJ*, 740:33, Oct. 2011.

[49] B.-O. Demory, M. Gillon, D. Deming, D. Valencia, S. Seager, B. Benneke, C. Lovis, P. Cubillos, J. Harrington, K. B. Stevenson, M. Mayor, F. Pepe, D. Queloz, D. Ségransan, and S. Udry. Detection of a transit of the super-Earth 55 Cancri e with warm Spitzer. *A&A*, 533:A114, Sept. 2011.

[50] B.-O. Demory, M. Gillon, S. Seager, B. Benneke, D. Deming, and B. Jackson. Detection of Thermal Emission from a Super-Earth. *ApJL*, 751:L28, June 2012.

[51] B.-O. Demory and S. Seager. Lack of Inflated Radii for Kepler Giant Planet Candidates Receiving Modest Stellar Irradiation. *ApJS*, 197:12, Nov. 2011.

[52] J.-M. Désert, D. Charbonneau, B.-O. Demory, S. Ballard, J. A. Carter, J. J. Fortney, W. D. Cochran, M. Endl, S. N. Quinn, H. T. Isaacson, F. Fressin, L. A. Buchhave, D. W. Latham, H. A. Knutson, S. T. Bryson, G. Torres, J. F. Rowe, N. M. Batalha, W. J. Borucki, T. M. Brown, D. A. Caldwell, J. L. Christiansen, D. Deming, D. C. Fabrycky, E. B. Ford, R. L. Gilliland, M. Gillon, M. R. Haas, J. M. Jenkins, K. Kinemuchi, D. Koch, J. J. Lissauer, P. Lucas, F. Mullally, P. J. MacQueen, G. W. Marcy, D. D. Sasselov, S. Seager, M. Still, P. Tenenbaum, K. Uddin, and J. N. Winn. The Hot-Jupiter Kepler-17b: Discovery, Obliquity from Stroboscopic Starspots, and Atmospheric Characterization. *ApJS*, 197:14, Nov. 2011.

[53] J. A. Dittmann, L. M. Close, E. M. Green, and M. Fenwick. A Tentative Detection of a Starspot During Consecutive Transits of an Extrasolar Planet from the Ground: No Evidence of a Double Transiting Planet System Around TrES-1. *ApJ*, 701:756–763, Aug. 2009.

[54] A. A. Djupvik and J. Andersen. The Nordic Optical Telescope. In J. M. Diego, L. J. Goicoechea, J. I. González-Serrano, and J. Gorgas, editors, *Highlights of Spanish Astrophysics V*, page 211, 2010.

[55] J. D. Dorren. A new formulation of the starspot model, and the consequences of starspot structure. *ApJ*, 320:756–767, Sept. 1987.

[56] X. Dumusque, F. Pepe, C. Lovis, D. Ségransan, J. Sahlmann, W. Benz, F. Bouchy, M. Mayor, D. Queloz, N. Santos, and S. Udry. An Earth-mass planet orbiting α Centauri B. *Natur*, 491:207–211, Nov. 2012.

[57] J. Eastman, R. Siverd, and B. S. Gaudi. Achieving Better Than 1 Minute Accuracy in the Heliocentric and Barycentric Julian Dates. *PASP*, 122:935–946, Aug. 2010.

[58] D. Fabrycky and S. Tremaine. Shrinking Binary and Planetary Orbits by Kozai Cycles with Tidal Friction. *ApJ*, 669:1298–1315, Nov. 2007.

[59] D. C. Fabrycky. Non-Keplerian Dynamics. *ArXiv e-prints*, June 2010.

[60] D. C. Fabrycky, E. B. Ford, J. H. Steffen, J. F. Rowe, J. A. Carter, A. V. Moorhead, N. M. Batalha, W. J. Borucki, S. Bryson, L. A. Buchhave, J. L. Christiansen, D. R. Ciardi, W. D. Cochran, M. Endl, M. N. Fanelli, D. Fischer, F. Fressin, J. Geary, M. R. Haas, J. R. Hall, M. J. Holman, J. M. Jenkins, D. G. Koch, D. W. Latham, J. Li, J. J. Lissauer, P. Lucas, G. W. Marcy, T. Mazeh, S. McCauliff, S. Quinn, D. Ragozzine, D. Sasselov, and A. Shporer. Transit Timing Observations from Kepler. IV. Confirmation of Four Multiple-planet Systems by Simple Physical Models. *ApJ*, 750:114, May 2012.

[61] D. C. Fabrycky and J. N. Winn. Exoplanetary Spin-Orbit Alignment: Results from the Ensemble of Rossiter-McLaughlin Observations. *ApJ*, 696:1230–1240, May 2009.

[62] S. Faigler, L. Tal-Or, T. Mazeh, D. W. Latham, and L. A. Buchhave. BEER Analysis of Kepler and CoRoT Light Curves. I. Discovery of Kepler-76b: A Hot Jupiter with Evidence for Superrotation. *ApJ*, 771:26, July 2013.

[63] S. Ferraz-Mello, M. Tadeu Dos Santos, C. Beaugé, T. A. Michtchenko, and A. Rodríguez. On the mass determination of super-Earths orbiting active stars: the CoRoT-7 system. *A&A*, 531:A161, July 2011.

[64] A. Fogtmann-Schulz, B. Hinrup, V. Van Eylen, J. Christensen-Dalsgaard, H. Kjeldsen, V. Silva Aguirre, and B. Tingley. Accurate Parameters of the Oldest Known Rocky-exoplanet Hosting System: Kepler-10 Revisited. *ApJ*, 781:67, Feb. 2014.

[65] E. B. Ford. Improving the Efficiency of Markov Chain Monte Carlo for Analyzing the Orbits of Extrasolar Planets. *ApJ*, 642:505–522, May 2006.

[66] J. J. Fortney, M. S. Marley, and J. W. Barnes. Planetary Radii across Five Orders of Magnitude in Mass and Stellar Insolation: Application to Transits. *ApJ*, 659:1661–1672, Apr. 2007.

[67] P. Foukal. What Determines the Relative Areas of Spots and Faculae on Sun-like Stars? *ApJ*, 500:958, June 1998.

[68] F. Fressin, G. Torres, D. Charbonneau, S. T. Bryson, J. Christiansen, C. D. Dressing, J. M. Jenkins, L. M. Walkowicz, and N. M. Batalha. The False Positive Rate of Kepler and the Occurrence of Planets. *ApJ*, 766:81, Apr. 2013.

[69] B. J. Fulton, A. W. Howard, J. N. Winn, S. Albrecht, G. W. Marcy, J. R. Crepp, G. A. Bakos, J. A. Johnson, J. D. Hartman, H. Isaacson, H. A. Knutson, and M. Zhao. The Stellar Obliquity and the Long-period Planet in the HAT-P-17 Exoplanetary System. *ApJ*, 772:80, Aug. 2013.

[70] D. Gandolfi, A. Collier Cameron, M. Endl, A. F. Lanza, C. Damiani, R. Alonso, W. D. Cochran, M. Deleuil, M. Fridlund, A. P. Hatzes, and E. W. Guenther. Doppler tomography of transiting exoplanets: a prograde, low-inclined orbit for the hot Jupiter CoRoT-11b. *A&A*, 543:L5, July 2012.

[71] B. S. Gaudi and J. N. Winn. Prospects for the Characterization and Confirmation of Transiting Exoplanets via the Rossiter-McLaughlin Effect. *ApJ*, 655:550–563, Jan. 2007.

[72] R. L. Gilliland, J. M. Jenkins, W. J. Borucki, S. T. Bryson, D. A. Caldwell, B. D. Clarke, J. L. Dotson, M. R. Haas, J. Hall, T. Klaus, D. Koch, S. McCauliff, E. V. Quintana, J. D. Twicken, and J. E. van Cleve. Initial Characteristics of Kepler Short Cadence Data. *ApJL*, 713:L160–L163, Apr. 2010.

[73] M. Gillon, B.-O. Demory, B. Benneke, D. Valencia, D. Deming, S. Seager, C. Lovis, M. Mayor, F. Pepe, D. Queloz, D. Ségransan, and S. Udry. Improved precision on the radius of the nearby super-Earth 55 Cnc e. *A&A*, 539:A28, Mar. 2012.

[74] M. Gillon, B. Smalley, L. Hebb, D. R. Anderson, A. H. M. J. Triaud, C. Hellier, P. F. L. Maxted, D. Queloz, and D. M. Wilson. Improved parameters for the transiting hot Jupiters WASP-4b and WASP-5b. *A&A*, 496:259–267, Mar. 2009.

[75] L. Gizon and S. K. Solanki. Determining the Inclination of the Rotation Axis of a Sun-like Star. *ApJ*, 589:1009–1019, June 2003.

[76] M. N. Gnevyshev. On the nature of solar activity. *Izvestiya Glavnoj Astronomicheskoj Observatorii v Pulkove*, 16:36, 1938.

[77] P.-G. Gu, P. H. Bodenheimer, and D. N. C. Lin. On the Roche Lobe Overflow of Giant Planets with Ultra-Short Periods due to Tidal Dissipation. In D. Deming and S. Seager, editors, *Scientific Frontiers in Research on Extrasolar Planets*, volume 294 of *Astronomical Society of the Pacific Conference Series*, pages 209–212, 2003.

[78] P.-G. Gu, D. N. C. Lin, and P. H. Bodenheimer. The Effect of Tidal Inflation Instability on the Mass and Dynamical Evolution of Extrasolar Planets with Ultrashort Periods. *ApJ*, 588:509–534, May 2003.

[79] A. P. Hatzes, M. Fridlund, G. Nachmani, T. Mazeh, D. Valencia, G. Hébrard, L. Carone, M. Pätzold, S. Udry, F. Bouchy, M. Deleuil, C. Moutou, P. Barge, P. Bordé, H. Deeg, B. Tingley, R. Dvorak, D. Gandolfi, S. Ferraz-Mello,

G. Wuchterl, E. Guenther, T. Guillot, H. Rauer, A. Erikson, J. Cabrera, S. Csizmadia, A. Léger, H. Lammer, J. Weingrill, D. Queloz, R. Alonso, D. Rouan, and J. Schneider. The Mass of CoRoT-7b. *ApJ*, 743:75, Dec. 2011.

[80] L. Hebb, A. Collier-Cameron, A. H. M. J. Triaud, T. A. Lister, B. Smalley, P. F. L. Maxted, C. Hellier, D. R. Anderson, D. Pollacco, M. Gillon, D. Queloz, R. G. West, S. Bentley, B. Enoch, C. A. Haswell, K. Horne, M. Mayor, F. Pepe, D. Segransan, I. Skillen, S. Udry, and P. J. Wheatley. WASP-19b: The Shortest Period Transiting Exoplanet Yet Discovered. *ApJ*, 708:224–231, Jan. 2010.

[81] G. Hébrard, F. Bouchy, F. Pont, B. Loeillet, M. Rabus, X. Bonfils, C. Moutou, I. Boisse, X. Delfosse, M. Desort, A. Eggenberger, D. Ehrenreich, T. Forveille, A.-M. Lagrange, C. Lovis, M. Mayor, F. Pepe, C. Perrier, D. Queloz, N. C. Santos, D. Ségransan, S. Udry, and A. Vidal-Madjar. Misaligned spin-orbit in the XO-3 planetary system? *A&A*, 488:763–770, Sept. 2008.

[82] G. W. Henry, G. W. Marcy, R. P. Butler, and S. S. Vogt. A Transiting "51 Peg-like" Planet. *ApJL*, 529:L41–L44, Jan. 2000.

[83] R. Henwood, S. C. Chapman, and D. M. Willis. Increasing Lifetime of Recurrent Sunspot Groups Within the Greenwich Photoheliographic Results. *SoPH*, 262:299–313, Apr. 2010.

[84] T. Hirano, N. Narita, B. Sato, Y. H. Takahashi, K. Masuda, Y. Takeda, W. Aoki, M. Tamura, and Y. Suto. Planet-Planet Eclipse and the Rossiter-McLaughlin Effect of a Multiple Transiting System: Joint Analysis of the Subaru Spectroscopy and the Kepler Photometry. *ApJL*, 759:L36, Nov. 2012.

[85] T. Hirano, N. Narita, A. Shporer, B. Sato, W. Aoki, and M. Tamura. A Possible Tilted Orbit of the Super-Neptune HAT-P-11b. *PASJ*, 63:531–, Mar. 2011.

[86] T. Hirano, R. Sanchis-Ojeda, Y. Takeda, N. Narita, J. N. Winn, A. Taruya, and Y. Suto. Measurements of Stellar Inclinations for Kepler Planet Candidates. *ApJ*, 756:66, Sept. 2012.

[87] T. Hirano, R. Sanchis-Ojeda, Y. Takeda, J. N. Winn, N. Narita, and Y. H. Takahashi. Measurements of Stellar Inclinations for Kepler Planet Candidates. II. Candidate Spin-Orbit Misalignments in Single- and Multiple-transiting Systems. *ApJ*, 783:9, Mar. 2014.

[88] T. Hirano, Y. Suto, J. N. Winn, A. Taruya, N. Narita, S. Albrecht, and B. Sato. Improved Modeling of the Rossiter-McLaughlin Effect for Transiting Exoplanets. *ApJ*, 742:69, Dec. 2011.

[89] M. J. Holman, D. C. Fabrycky, D. Ragozzine, E. B. Ford, J. H. Steffen, W. F. Welsh, J. J. Lissauer, D. W. Latham, G. W. Marcy, L. M. Walkowicz, N. M. Batalha, J. M. Jenkins, J. F. Rowe, W. D. Cochran, F. Fressin, G. Torres, L. A. Buchhave, D. D. Sasselov, W. J. Borucki, D. G. Koch, G. Basri, T. M. Brown,

D. A. Caldwell, D. Charbonneau, E. W. Dunham, T. N. Gautier, J. C. Geary, R. L. Gilliland, M. R. Haas, S. B. Howell, D. R. Ciardi, M. Endl, D. Fischer, G. Fürész, J. D. Hartman, H. Isaacson, J. A. Johnson, P. J. MacQueen, A. V. Moorhead, R. C. Morehead, and J. A. Orosz. Kepler-9: A System of Multiple Planets Transiting a Sun-Like Star, Confirmed by Timing Variations. *Science*, 330:51–, Oct. 2010.

[90] M. J. Holman and N. W. Murray. The Use of Transit Timing to Detect Terrestrial-Mass Extrasolar Planets. *Science*, 307:1288–1291, Feb. 2005.

[91] M. J. Holman, J. N. Winn, D. W. Latham, F. T. O'Donovan, D. Charbonneau, G. A. Bakos, G. A. Esquerdo, C. Hergenrother, M. E. Everett, and A. Pál. The Transit Light Curve Project. I. Four Consecutive Transits of the Exoplanet XO-1b. *ApJ*, 652:1715–1723, Dec. 2006.

[92] A. W. Howard, G. W. Marcy, S. T. Bryson, J. M. Jenkins, J. F. Rowe, N. M. Batalha, W. J. Borucki, D. G. Koch, E. W. Dunham, T. N. Gautier, III, J. Van Cleve, W. D. Cochran, D. W. Latham, J. J. Lissauer, G. Torres, T. M. Brown, R. L. Gilliland, L. A. Buchhave, D. A. Caldwell, J. Christensen-Dalsgaard, D. Ciardi, F. Fressin, M. R. Haas, S. B. Howell, H. Kjeldsen, S. Seager, L. Rogers, D. D. Sasselov, J. H. Steffen, G. S. Basri, D. Charbonneau, J. Christiansen, B. Clarke, A. Dupree, D. C. Fabrycky, D. A. Fischer, E. B. Ford, J. J. Fortney, J. Tarter, F. R. Girouard, M. J. Holman, J. A. Johnson, T. C. Klaus, P. Machalek, A. V. Moorhead, R. C. Morehead, D. Ragozzine, P. Tenenbaum, J. D. Twicken, S. N. Quinn, H. Isaacson, A. Shporer, P. W. Lucas, L. M. Walkowicz, W. F. Welsh, A. Boss, E. Devore, A. Gould, J. C. Smith, R. L. Morris, A. Prsa, T. D. Morton, M. Still, S. E. Thompson, F. Mullally, M. Endl, and P. J. MacQueen. Planet Occurrence within 0.25 AU of Solar-type Stars from Kepler. *ApJS*, 201:15, Aug. 2012.

[93] A. W. Howard, G. W. Marcy, J. A. Johnson, D. A. Fischer, J. T. Wright, H. Isaacson, J. A. Valenti, J. Anderson, D. N. C. Lin, and S. Ida. The Occurrence and Mass Distribution of Close-in Super-Earths, Neptunes, and Jupiters. *Science*, 330:653–, Oct. 2010.

[94] A. W. Howard, R. Sanchis-Ojeda, G. W. Marcy, J. A. Johnson, J. N. Winn, H. Isaacson, D. A. Fischer, B. J. Fulton, E. Sinukoff, and J. J. Fortney. A rocky composition for an Earth-sized exoplanet. *Natur*, 503:381–384, Nov. 2013.

[95] S. B. Howell, M. E. Everett, W. Sherry, E. Horch, and D. R. Ciardi. Speckle Camera Observations for the NASA Kepler Mission Follow-up Program. *AJ*, 142:19, July 2011.

[96] X. Huang, G. Á. Bakos, and J. D. Hartman. 150 new transiting planet candidates from Kepler Q1-Q6 data. *MNRAS*, 429:2001–2018, Mar. 2013.

[97] D. Huber, V. Silva Aguirre, J. M. Matthews, M. H. Pinsonneault, E. Gaidos, R. A. García, S. Hekker, S. Mathur, B. Mosser, G. Torres, F. A. Bastien,

S. Basu, T. R. Bedding, W. J. Chaplin, B.-O. Demory, S. W. Fleming, Z. Guo, A. W. Mann, J. F. Rowe, A. M. Serenelli, M. A. Smith, and D. Stello. Revised Stellar Properties of Kepler Targets for the Quarter 1-16 Transit Detection Run. *ApJS*, 211:2, Mar. 2014.

[98] J. Irwin and J. Bouvier. The rotational evolution of low-mass stars. In E. E. Mamajek, D. R. Soderblom, and R. F. G. Wyse, editors, *IAU Symposium*, volume 258 of *IAU Symposium*, pages 363–374, June 2009.

[99] B. Jackson, C. C. Stark, E. R. Adams, J. Chambers, and D. Deming. A Survey for Very Short-period Planets in the Kepler Data. *ApJ*, 779:165, Dec. 2013.

[100] J. M. Jenkins, D. A. Caldwell, H. Chandrasekaran, J. D. Twicken, S. T. Bryson, E. V. Quintana, B. D. Clarke, J. Li, C. Allen, P. Tenenbaum, H. Wu, T. C. Klaus, J. Van Cleve, J. A. Dotson, M. R. Haas, R. L. Gilliland, D. G. Koch, and W. J. Borucki. Initial Characteristics of Kepler Long Cadence Data for Detecting Transiting Planets. *ApJL*, 713:L120–L125, Apr. 2010.

[101] D. M. Kipping. Binning is sinning: morphological light-curve distortions due to finite integration time. *MNRAS*, 408:1758–1769, Nov. 2010.

[102] H. A. Knutson, D. Charbonneau, N. B. Cowan, J. J. Fortney, A. P. Showman, E. Agol, G. W. Henry, M. E. Everett, and L. E. Allen. Multiwavelength Constraints on the Day-Night Circulation Patterns of HD 189733b. *ApJ*, 690:822–836, Jan. 2009.

[103] D. G. Koch, W. J. Borucki, G. Basri, N. M. Batalha, T. M. Brown, D. Caldwell, J. Christensen-Dalsgaard, W. D. Cochran, E. DeVore, E. W. Dunham, T. N. Gautier, III, J. C. Geary, R. L. Gilliland, A. Gould, J. Jenkins, Y. Kondo, D. W. Latham, J. J. Lissauer, G. Marcy, D. Monet, D. Sasselov, A. Boss, D. Brownlee, J. Caldwell, A. K. Dupree, S. B. Howell, H. Kjeldsen, S. Meibom, D. Morrison, T. Owen, H. Reitsema, J. Tarter, S. T. Bryson, J. L. Dotson, P. Gazis, M. R. Haas, J. Kolodziejczak, J. F. Rowe, J. E. Van Cleve, C. Allen, H. Chandrasekaran, B. D. Clarke, J. Li, E. V. Quintana, P. Tenenbaum, J. D. Twicken, and H. Wu. Kepler Mission Design, Realized Photometric Performance, and Early Science. *ApJL*, 713:L79–L86, Apr. 2010.

[104] V. I. Kondratiev, M. A. McLaughlin, D. R. Lorimer, M. Burgay, A. Possenti, R. Turolla, S. B. Popov, and S. Zane. New Limits on Radio Emission from X-ray Dim Isolated Neutron Stars. *ApJ*, 702:692–706, Sept. 2009.

[105] G. Kovács, S. Zucker, and T. Mazeh. A box-fitting algorithm in the search for periodic transits. *A&A*, 391:369–377, Aug. 2002.

[106] H. Kurokawa and L. Kaltenegger. Atmospheric mass-loss and evolution of short-period exoplanets: the examples of CoRoT-7b and Kepler-10b. *MNRAS*, 433:3239–3245, Aug. 2013.

[107] D. Lai, F. Foucart, and D. N. C. Lin. Evolution of spin direction of accreting magnetic protostars and spin-orbit misalignment in exoplanetary systems. *MNRAS*, 412:2790–2798, Apr. 2011.

[108] H. Lammer, F. Selsis, I. Ribas, E. F. Guinan, S. J. Bauer, and W. W. Weiss. Atmospheric Loss of Exoplanets Resulting from Stellar X-Ray and Extreme-Ultraviolet Heating. *ApJL*, 598:L121–L124, Dec. 2003.

[109] A. Léger, O. Grasset, B. Fegley, F. Codron, A. F. Albarede, P. Barge, R. Barnes, P. Cance, S. Carpy, F. Catalano, C. Cavarroc, O. Demangeon, S. Ferraz-Mello, P. Gabor, J.-M. Grießmeier, J. Leibacher, G. Libourel, A.-S. Maurin, S. N. Raymond, D. Rouan, B. Samuel, L. Schaefer, J. Schneider, P. A. Schuller, F. Selsis, and C. Sotin. The extreme physical properties of the CoRoT-7b super-Earth. *Icarus*, 213:1–11, May 2011.

[110] A. Léger, D. Rouan, J. Schneider, P. Barge, M. Fridlund, B. Samuel, M. Ollivier, E. Guenther, M. Deleuil, H. J. Deeg, M. Auvergne, R. Alonso, S. Aigrain, A. Alapini, J. M. Almenara, A. Baglin, M. Barbieri, H. Bruntt, P. Bordé, F. Bouchy, J. Cabrera, C. Catala, L. Carone, S. Carpano, S. Csizmadia, R. Dvorak, A. Erikson, S. Ferraz-Mello, B. Foing, F. Fressin, D. Gandolfi, M. Gillon, P. Gondoin, O. Grasset, T. Guillot, A. Hatzes, G. Hébrard, L. Jorda, H. Lammer, A. Llebaria, B. Loeillet, M. Mayor, T. Mazeh, C. Moutou, M. Pätzold, F. Pont, D. Queloz, H. Rauer, S. Renner, R. Samadi, A. Shporer, C. Sotin, B. Tingley, G. Wuchterl, M. Adda, P. Agogu, T. Appourchaux, H. Ballans, P. Baron, T. Beaufort, R. Bellenger, R. Berlin, P. Bernardi, D. Blouin, F. Baudin, P. Bodin, L. Boisnard, L. Boit, F. Bonneau, S. Borzeix, R. Briet, J.-T. Buey, B. Butler, D. Cailleau, R. Cautain, P.-Y. Chabaud, S. Chaintreuil, F. Chiavassa, V. Costes, V. Cuna Parrho, F. de Oliveira Fialho, M. Decaudin, J.-M. Defise, S. Djalal, G. Epstein, G.-E. Exil, C. Fauré, T. Fenouillet, A. Gaboriaud, A. Gallic, P. Gamet, P. Gavalda, E. Grolleau, R. Gruneisen, L. Gueguen, V. Guis, V. Guivarc'h, P. Guterman, D. Hallouard, J. Hasiba, F. Heuripeau, G. Huntzinger, H. Hustaix, C. Imad, C. Imbert, B. Johlander, M. Jouret, P. Journoud, F. Karioty, L. Kerjean, V. Lafaille, L. Lafond, T. Lam-Trong, P. Landiech, V. Lapeyrere, T. Larqué, P. Laudet, N. Lautier, H. Lecann, L. Lefevre, B. Leruyet, P. Levacher, A. Magnan, E. Mazy, F. Mertens, J.-M. Mesnager, J.-C. Meunier, J.-P. Michel, W. Monjoin, D. Naudet, K. Nguyen-Kim, J.-L. Orcesi, H. Ottacher, R. Perez, G. Peter, P. Plasson, J.-Y. Plesseria, B. Pontet, A. Pradines, C. Quentin, J.-L. Reynaud, G. Rolland, F. Rollenhagen, R. Romagnan, N. Russ, R. Schmidt, N. Schwartz, I. Sebbag, G. Sedes, H. Smit, M. B. Steller, W. Sunter, C. Surace, M. Tello, D. Tiphène, P. Toulouse, B. Ulmer, O. Vandermarcq, E. Vergnault, A. Vuillemin, and P. Zanatta. Transiting exoplanets from the CoRoT space mission. VIII. CoRoT-7b: the first super-Earth with measured radius. *A&A*, 506:287–302, Oct. 2009.

[111] J. J. Lissauer. Planet formation. *ARAA*, 31:129–174, 1993.

[112] J. J. Lissauer, D. C. Fabrycky, E. B. Ford, W. J. Borucki, F. Fressin, G. W. Marcy, J. A. Orosz, J. F. Rowe, G. Torres, W. F. Welsh, N. M. Batalha, S. T. Bryson, L. A. Buchhave, D. A. Caldwell, J. A. Carter, D. Charbonneau, J. L. Christiansen, W. D. Cochran, J.-M. Desert, E. W. Dunham, M. N. Fanelli, J. J. Fortney, T. N. Gautier, III, J. C. Geary, R. L. Gilliland, M. R. Haas, J. R. Hall, M. J. Holman, D. G. Koch, D. W. Latham, E. Lopez, S. McCauliff, N. Miller, R. C. Morehead, E. V. Quintana, D. Ragozzine, D. Sasselov, D. R. Short, and J. H. Steffen. A closely packed system of low-mass, low-density planets transiting Kepler-11. *Natur*, 470:53–58, Feb. 2011.

[113] J. J. Lissauer, D. Jontof-Hutter, J. F. Rowe, D. C. Fabrycky, E. D. Lopez, E. Agol, G. W. Marcy, K. M. Deck, D. A. Fischer, J. J. Fortney, S. B. Howell, H. Isaacson, J. M. Jenkins, R. Kolbl, D. Sasselov, D. R. Short, and W. F. Welsh. All Six Planets Known to Orbit Kepler-11 Have Low Densities. *ApJ*, 770:131, June 2013.

[114] J. J. Lissauer, G. W. Marcy, S. T. Bryson, J. F. Rowe, D. Jontof-Hutter, E. Agol, W. J. Borucki, J. A. Carter, E. B. Ford, R. L. Gilliland, R. Kolbl, K. M. Star, J. H. Steffen, and G. Torres. Validation of Kepler's Multiple Planet Candidates. II. Refined Statistical Framework and Descriptions of Systems of Special Interest. *ApJ*, 784:44, Mar. 2014.

[115] J. J. Lissauer, G. W. Marcy, J. F. Rowe, S. T. Bryson, E. Adams, L. A. Buchhave, D. R. Ciardi, W. D. Cochran, D. C. Fabrycky, E. B. Ford, F. Fressin, J. Geary, R. L. Gilliland, M. J. Holman, S. B. Howell, J. M. Jenkins, K. Kinemuchi, D. G. Koch, R. C. Morehead, D. Ragozzine, S. E. Seader, P. G. Tanenbaum, G. Torres, and J. D. Twicken. Almost All of Kepler's Multiple-planet Candidates Are Planets. *ApJ*, 750:112, May 2012.

[116] J. J. Lissauer, D. Ragozzine, D. C. Fabrycky, J. H. Steffen, E. B. Ford, J. M. Jenkins, A. Shporer, M. J. Holman, J. F. Rowe, E. V. Quintana, N. M. Batalha, W. J. Borucki, S. T. Bryson, D. A. Caldwell, J. A. Carter, D. Ciardi, E. W. Dunham, J. J. Fortney, T. N. Gautier, III, S. B. Howell, D. G. Koch, D. W. Latham, G. W. Marcy, R. C. Morehead, and D. Sasselov. Architecture and Dynamics of Kepler's Candidate Multiple Transiting Planet Systems. *ApJS*, 197:8, Nov. 2011.

[117] J. Llama, M. Jardine, D. H. Mackay, and R. Fares. Using Kepler transit observations to measure stellar spot belt migration rates. *MNRAS*, 422:L72, May 2012.

[118] E. D. Lopez and J. J. Fortney. The Role of Core Mass in Controlling Evaporation: The Kepler Radius Distribution and the Kepler-36 Density Dichotomy. *ApJ*, 776:2, Oct. 2013.

[119] E. D. Lopez and J. J. Fortney. Understanding the Mass-Radius Relation for Sub-Neptunes: Radius as a Proxy for Composition. *ArXiv e-prints*, Nov. 2013.

[120] E. D. Lopez, J. J. Fortney, and N. Miller. How Thermal Evolution and Mass-loss Sculpt Populations of Super-Earths and Sub-Neptunes: Application to the Kepler-11 System and Beyond. *ApJ*, 761:59, Dec. 2012.

[121] C. Lovis, X. Dumusque, N. C. Santos, F. Bouchy, M. Mayor, F. Pepe, D. Queloz, D. Ségransan, and S. Udry. The HARPS search for southern extra-solar planets. XXXI. Magnetic activity cycles in solar-type stars: statistics and impact on precise radial velocities. *ArXiv e-prints*, July 2011.

[122] C. Lovis and D. Fischer. *Radial Velocity Techniques for Exoplanets*, pages 27–53. 2011.

[123] N. Madhusudhan and J. N. Winn. Empirical Constraints on Trojan Companions and Orbital Eccentricities in 25 Transiting Exoplanetary Systems. *ApJ*, 693:784–793, Mar. 2009.

[124] E. E. Mamajek and L. A. Hillenbrand. Improved Age Estimation for Solar-Type Dwarfs Using Activity-Rotation Diagnostics. *ApJ*, 687:1264–1293, Nov. 2008.

[125] K. Mandel and E. Agol. Analytic Light Curves for Planetary Transit Searches. *ApJL*, 580:L171–L175, Dec. 2002.

[126] G. W. Marcy and R. P. Butler. A Planetary Companion to 70 Virginis. *ApJL*, 464:L147, June 1996.

[127] C. B. Markwardt. Non-linear Least-squares Fitting in IDL with MPFIT. In D. A. Bohlender, D. Durand, and P. Dowler, editors, *Astronomical Data Analysis Software and Systems XVIII*, volume 411 of *Astronomical Society of the Pacific Conference Series*, page 251, Sept. 2009.

[128] C. Marois, B. Macintosh, T. Barman, B. Zuckerman, I. Song, J. Patience, D. Lafrenière, and R. Doyon. Direct Imaging of Multiple Planets Orbiting the Star HR 8799. *Science*, 322:1348–, Nov. 2008.

[129] G. Matijevič, A. Prša, J. A. Orosz, W. F. Welsh, S. Bloemen, and T. Barclay. Kepler Eclipsing Binary Stars. III. Classification of Kepler Eclipsing Binary Light Curves with Locally Linear Embedding. *AJ*, 143:123, May 2012.

[130] S. Matsumura, S. J. Peale, and F. A. Rasio. Tidal Evolution of Close-in Planets. *ApJ*, 725:1995–2016, Dec. 2010.

[131] E. W. Maunder. Note on the distribution of sun-spots in heliographic latitude, 1874-1902. *MNRAS*, 64:747–761, June 1904.

[132] M. Mayor and D. Queloz. A Jupiter-mass companion to a solar-type star. *Natur*, 378:355–359, Nov. 1995.

[133] T. Mazeh, G. Nachmani, T. Holczer, D. C. Fabrycky, E. B. Ford, R. Sanchis-Ojeda, G. Sokol, J. F. Rowe, S. Zucker, E. Agol, J. A. Carter, J. J. Lissauer, E. V. Quintana, D. Ragozzine, J. H. Steffen, and W. Welsh. Transit Timing Observations from Kepler. VIII. Catalog of Transit Timing Measurements of the First Twelve Quarters. *ApJS*, 208:16, Oct. 2013.

[134] S. Meibom, R. D. Mathieu, and K. G. Stassun. Stellar Rotation in M35: Mass-Period Relations, Spin-Down Rates, and Gyrochronology. *ApJ*, 695:679–694, Apr. 2009.

[135] S. Messina and E. F. Guinan. Magnetic activity of six young solar analogues II. Surface Differential Rotation from long-term photometry. *A&A*, 409:1017–1030, Oct. 2003.

[136] S. L. Morris and S. A. Naftilan. The Equations of Ellipsoidal Star Variability Applied to HR 8427. *ApJ*, 419:344, Dec. 1993.

[137] T. D. Morton and J. A. Johnson. Discerning Exoplanet Migration Models Using Spin-Orbit Measurements. *ApJ*, 729:138, Mar. 2011.

[138] T. D. Morton and J. A. Johnson. On the Low False Positive Probabilities of Kepler Planet Candidates. *ApJ*, 738:170, Sept. 2011.

[139] P. S. Muirhead, J. A. Johnson, K. Apps, J. A. Carter, T. D. Morton, D. C. Fabrycky, J. S. Pineda, M. Bottom, B. Rojas-Ayala, E. Schlawin, K. Hamren, K. R. Covey, J. R. Crepp, K. G. Stassun, J. Pepper, L. Hebb, E. N. Kirby, A. W. Howard, H. T. Isaacson, G. W. Marcy, D. Levitan, T. Diaz-Santos, L. Armus, and J. P. Lloyd. Characterizing the Cool KOIs. III. KOI 961: A Small Star with Large Proper Motion and Three Small Planets. *ApJ*, 747:144, Mar. 2012.

[140] R. A. Murray-Clay, E. I. Chiang, and N. Murray. Atmospheric Escape From Hot Jupiters. *ApJ*, 693:23–42, Mar. 2009.

[141] M. Nagasawa, S. Ida, and T. Bessho. Formation of Hot Planets by a Combination of Planet Scattering, Tidal Circularization, and the Kozai Mechanism. *ApJ*, 678:498–508, May 2008.

[142] D. Nesvorný, D. M. Kipping, L. A. Buchhave, G. Á. Bakos, J. Hartman, and A. R. Schmitt. The Detection and Characterization of a Nontransiting Planet by Transit Timing Variations. *Science*, 336:1133–, June 2012.

[143] R. W. Noyes, L. W. Hartmann, S. L. Baliunas, D. K. Duncan, and A. H. Vaughan. Rotation, convection, and magnetic activity in lower main-sequence stars. *ApJ*, 279:763–777, Apr. 1984.

[144] P. A. Nutzman, D. C. Fabrycky, and J. J. Fortney. Using Star Spots to Measure the Spin-orbit Alignment of Transiting Planets. *ApJL*, 740:L10, Oct. 2011.

[145] A. Ofir and S. Dreizler. An independent planet search in the Kepler dataset. I. One hundred new candidates and revised Kepler objects of interest. *A&A*, 555:A58, July 2013.

[146] Y. Ohta, A. Taruya, and Y. Suto. The Rossiter-McLaughlin Effect and Analytic Radial Velocity Curves for Transiting Extrasolar Planetary Systems. *ApJ*, 622:1118–1135, Apr. 2005.

[147] M. Oshagh, I. Boisse, G. Boué, M. Montalto, N. C. Santos, X. Bonfils, and N. Haghighipour. SOAP-T: a tool to study the light curve and radial velocity of a system with a transiting planet and a rotating spotted star. *A&A*, 549:A35, Jan. 2013.

[148] M. Oshagh, N. C. Santos, I. Boisse, G. Boué, M. Montalto, X. Dumusque, and N. Haghighipour. Effect of stellar spots on high-precision transit light-curve. *A&A*, 556:A19, Aug. 2013.

[149] J. E. Owen and Y. Wu. Kepler Planets: A Tale of Evaporation. *ApJ*, 775:105, Oct. 2013.

[150] A. Pál. Properties of analytic transit light-curve models. *MNRAS*, 390:281–288, Oct. 2008.

[151] F. Pepe, A. C. Cameron, D. W. Latham, E. Molinari, S. Udry, A. S. Bonomo, L. A. Buchhave, D. Charbonneau, R. Cosentino, C. D. Dressing, X. Dumusque, P. Figueira, A. F. M. Fiorenzano, S. Gettel, A. Harutyunyan, R. D. Haywood, K. Horne, M. Lopez-Morales, C. Lovis, L. Malavolta, M. Mayor, G. Micela, F. Motalebi, V. Nascimbeni, D. Phillips, G. Piotto, D. Pollacco, D. Queloz, K. Rice, D. Sasselov, D. Ségransan, A. Sozzetti, A. Szentgyorgyi, and C. A. Watson. An Earth-sized planet with an Earth-like density. *Natur*, 503:377–380, Nov. 2013.

[152] D. Perez-Becker and E. Chiang. Catastrophic evaporation of rocky planets. *MNRAS*, 433:2294–2309, Aug. 2013.

[153] E. A. Petigura, A. W. Howard, and G. W. Marcy. Prevalence of Earth-size planets orbiting Sun-like stars. *Proceedings of the National Academy of Science*, 110:19273–19278, Nov. 2013.

[154] E. A. Petigura, G. W. Marcy, and A. W. Howard. A Plateau in the Planet Population below Twice the Size of Earth. *ApJ*, 770:69, June 2013.

[155] K. Petrovay and L. van Driel-Gesztelyi. Making Sense of Sunspot Decay. I. Parabolic Decay Law and Gnevyshev-Waldmeier Relation. *SoPH*, 176:249–266, Dec. 1997.

[156] M. H. Pinsonneault, D. L. DePoy, and M. Coffee. The Mass of the Convective Zone in FGK Main-Sequence Stars and the Effect of Accreted Planetary

Material on Apparent Metallicity Determinations. *ApJL*, 556:L59–L62, July 2001.

[157] D. L. Pollacco, I. Skillen, A. Collier Cameron, D. J. Christian, C. Hellier, J. Irwin, T. A. Lister, R. A. Street, R. G. West, D. R. Anderson, W. I. Clarkson, H. Deeg, B. Enoch, A. Evans, A. Fitzsimmons, C. A. Haswell, S. Hodgkin, K. Horne, S. R. Kane, F. P. Keenan, P. F. L. Maxted, A. J. Norton, J. Osborne, N. R. Parley, R. S. I. Ryans, B. Smalley, P. J. Wheatley, and D. M. Wilson. The WASP Project and the SuperWASP Cameras. *PASP*, 118:1407–1418, Oct. 2006.

[158] F. Pont, S. Aigrain, and S. Zucker. Reassessing the radial-velocity evidence for planets around CoRoT-7. *MNRAS*, 411:1953–1962, Mar. 2011.

[159] F. Pont, R. L. Gilliland, C. Moutou, D. Charbonneau, F. Bouchy, T. M. Brown, M. Mayor, D. Queloz, N. Santos, and S. Udry. Hubble Space Telescope time-series photometry of the planetary transit of HD 189733: no moon, no rings, starspots. *A&A*, 476:1347–1355, Dec. 2007.

[160] F. Pont, N. Husnoo, T. Mazeh, and D. Fabrycky. Determining eccentricities of transiting planets: a divide in the mass-period plane. *MNRAS*, 414:1278–1284, June 2011.

[161] D. Queloz, F. Bouchy, C. Moutou, A. Hatzes, G. Hébrard, R. Alonso, M. Auvergne, A. Baglin, M. Barbieri, P. Barge, W. Benz, P. Bordé, H. J. Deeg, M. Deleuil, R. Dvorak, A. Erikson, S. Ferraz Mello, M. Fridlund, D. Gandolfi, M. Gillon, E. Guenther, T. Guillot, L. Jorda, M. Hartmann, H. Lammer, A. Léger, A. Llebaria, C. Lovis, P. Magain, M. Mayor, T. Mazeh, M. Ollivier, M. Pätzold, F. Pepe, H. Rauer, D. Rouan, J. Schneider, D. Segransan, S. Udry, and G. Wuchterl. The CoRoT-7 planetary system: two orbiting super-Earths. *A&A*, 506:303–319, Oct. 2009.

[162] D. Queloz, A. Eggenberger, M. Mayor, C. Perrier, J. L. Beuzit, D. Naef, J. P. Sivan, and S. Udry. Detection of a spectroscopic transit by the planet orbiting the star HD209458. *A&A*, 359:L13–L17, July 2000.

[163] S. N. Quinn, R. J. White, D. W. Latham, L. A. Buchhave, J. R. Cantrell, S. E. Dahm, G. Fűrész, A. H. Szentgyorgyi, J. C. Geary, G. Torres, A. Bieryla, P. Berlind, M. C. Calkins, G. A. Esquerdo, and R. P. Stefanik. Two "b"s in the Beehive: The Discovery of the First Hot Jupiters in an Open Cluster. *ApJL*, 756:L33, Sept. 2012.

[164] E. V. Quintana, J. F. Rowe, T. Barclay, S. B. Howell, D. R. Ciardi, B.-O. Demory, D. A. Caldwell, W. J. Borucki, J. L. Christiansen, J. M. Jenkins, T. C. Klaus, B. J. Fulton, R. L. Morris, D. T. Sanderfer, A. Shporer, J. C. Smith, M. Still, and S. E. Thompson. Confirmation of Hot Jupiter Kepler-41b via Phase Curve Analysis. *ApJ*, 767:137, Apr. 2013.

[165] M. Rabus, R. Alonso, J. A. Belmonte, H. J. Deeg, R. L. Gilliland, J. M. Almenara, T. M. Brown, D. Charbonneau, and G. Mandushev. A cool starspot or a second transiting planet in the TrES-1 system? *A&A*, 494:391–397, Jan. 2009.

[166] D. Ragozzine and M. J. Holman. The Value of Systems with Multiple Transiting Planets. *ArXiv e-prints*, June 2010.

[167] S. Rappaport, T. Barclay, J. DeVore, J. Rowe, R. Sanchis-Ojeda, and M. Still. KOI-2700b A Planet Candidate with Dusty Effluents on a 22 hr Orbit. *ApJ*, 784:40, Mar. 2014.

[168] S. Rappaport, A. Levine, E. Chiang, I. El Mellah, J. Jenkins, B. Kalomeni, E. S. Kite, M. Kotson, L. Nelson, L. Rousseau-Nepton, and K. Tran. Possible Disintegrating Short-period Super-Mercury Orbiting KIC 12557548. *ApJ*, 752:1, June 2012.

[169] S. Rappaport, R. Sanchis-Ojeda, L. A. Rogers, A. Levine, and J. N. Winn. The Roche Limit for Close-orbiting Planets: Minimum Density, Composition Constraints, and Application to the 4.2 hr Planet KOI 1843.03. *ApJL*, 773:L15, Aug. 2013.

[170] F. A. Rasio and E. B. Ford. Dynamical instabilities and the formation of extrasolar planetary systems. *Science*, 274:954–956, Nov. 1996.

[171] T. M. Rogers, D. N. C. Lin, and H. H. B. Lau. Internal Gravity Waves Modulate the Apparent Misalignment of Exoplanets around Hot Stars. *ApJL*, 758:L6, Oct. 2012.

[172] D. Rouan, H. J. Deeg, O. Demangeon, B. Samuel, C. Cavarroc, B. Fegley, and A. Léger. The Orbital Phases and Secondary Transits of Kepler-10b. A Physical Interpretation Based on the Lava-ocean Planet Model. *ApJL*, 741:L30, Nov. 2011.

[173] D. Ružđjak, R. Brajša, D. Sudar, and H. Wöhl. The Influence of the Evolution of Sunspot Groups on the Determination of the Solar Velocity Field. *SoPH*, 229:35–43, June 2005.

[174] R. Sanchis-Ojeda, D. C. Fabrycky, J. N. Winn, T. Barclay, B. D. Clarke, E. B. Ford, J. J. Fortney, J. C. Geary, M. J. Holman, A. W. Howard, J. M. Jenkins, D. Koch, J. J. Lissauer, G. W. Marcy, F. Mullally, D. Ragozzine, S. E. Seader, M. Still, and S. E. Thompson. Alignment of the stellar spin with the orbits of a three-planet system. *Natur*, 487:449–453, July 2012.

[175] R. Sanchis-Ojeda, S. Rappaport, J. N. Winn, M. C. Kotson, A. Levine, and I. El Mellah. A Study of the Shortest-period Planets Found with Kepler. *ApJ*, 787:47, May 2014.

[176] R. Sanchis-Ojeda, S. Rappaport, J. N. Winn, A. Levine, M. C. Kotson, D. W. Latham, and L. A. Buchhave. Transits and Occultations of an Earth-sized Planet in an 8.5 hr Orbit. *ApJ*, 774:54, Sept. 2013.

[177] R. Sanchis-Ojeda and J. N. Winn. Starspots, Spin-Orbit Misalignment, and Active Latitudes in the HAT-P-11 Exoplanetary System. *ApJ*, 743:61, Dec. 2011.

[178] R. Sanchis-Ojeda, J. N. Winn, and D. C. Fabrycky. Starspots and spin-orbit alignment for Kepler cool host stars. *Astronomische Nachrichten*, 334:180–183, Feb. 2013.

[179] R. Sanchis-Ojeda, J. N. Winn, M. J. Holman, J. A. Carter, D. J. Osip, and C. I. Fuentes. Starspots and Spin-orbit Alignment in the WASP-4 Exoplanetary System. *ApJ*, 733:127, June 2011.

[180] R. Sanchis-Ojeda, J. N. Winn, G. W. Marcy, A. W. Howard, H. Isaacson, J. A. Johnson, G. Torres, S. Albrecht, T. L. Campante, W. J. Chaplin, G. R. Davies, M. N. Lund, J. A. Carter, R. I. Dawson, L. A. Buchhave, M. E. Everett, D. A. Fischer, J. C. Geary, R. L. Gilliland, E. P. Horch, S. B. Howell, and D. W. Latham. Kepler-63b: A Giant Planet in a Polar Orbit around a Young Sun-like Star. *ApJ*, 775:54, Sept. 2013.

[181] A. Santerne, R. F. Díaz, C. Moutou, F. Bouchy, G. Hébrard, J.-M. Almenara, A. S. Bonomo, M. Deleuil, and N. C. Santos. SOPHIE velocimetry of Kepler transit candidates. VII. A false-positive rate of 35% for Kepler close-in giant candidates. *A&A*, 545:A76, Sept. 2012.

[182] N. C. Santos, G. Israelian, and M. Mayor. Spectroscopic [Fe/H] for 98 extra-solar planet-host stars. Exploring the probability of planet formation. *A&A*, 415:1153–1166, Mar. 2004.

[183] J. Sanz-Forcada, G. Micela, I. Ribas, A. M. T. Pollock, C. Eiroa, A. Velasco, E. Solano, and D. García-Álvarez. Estimation of the XUV radiation onto close planets and their evaporation. *A&A*, 532:A6, Aug. 2011.

[184] J. D. Scargle. Studies in astronomical time series analysis. II - Statistical aspects of spectral analysis of unevenly spaced data. *ApJ*, 263:835–853, Dec. 1982.

[185] K. C. Schlaufman. Evidence of Possible Spin-orbit Misalignment Along the Line of Sight in Transiting Exoplanet Systems. *ApJ*, 719:602–611, Aug. 2010.

[186] K. C. Schlaufman and G. Laughlin. Kepler Exoplanet Candidate Host Stars Are Preferentially Metal Rich. *ApJ*, 738:177, Sept. 2011.

[187] K. C. Schlaufman, D. N. C. Lin, and S. Ida. A Population of Very Hot Super-Earths in Multiple-planet Systems Should be Uncovered by Kepler. *ApJL*, 724:L53–L58, Nov. 2010.

[188] C. J. Schrijver and A. M. Title. On the Formation of Polar Spots in Sun-like Stars. *ApJ*, 551:1099–1106, Apr. 2001.

[189] A. V. R. Silva. Method for Spot Detection on Solar-like Stars. *ApJL*, 585:L147–L150, Mar. 2003.

[190] A. Silva-Valio. Estimating Stellar Rotation from Starspot Detection during Planetary Transits. *ApJL*, 683:L179–L182, Aug. 2008.

[191] A. Silva-Valio and A. F. Lanza. Time evolution and rotation of starspots on CoRoT-2 from the modelling of transit photometry. *A&A*, 529:A36, May 2011.

[192] A. Silva-Valio, A. F. Lanza, R. Alonso, and P. Barge. Properties of starspots on CoRoT-2. *A&A*, 510:A25, Feb. 2010.

[193] A. Skumanich. Time Scales for CA II Emission Decay, Rotational Braking, and Lithium Depletion. *ApJ*, 171:565, Feb. 1972.

[194] R. W. Slawson, A. Prša, W. F. Welsh, J. A. Orosz, M. Rucker, N. Batalha, L. R. Doyle, S. G. Engle, K. Conroy, J. Coughlin, T. A. Gregg, T. Fetherolf, D. R. Short, G. Windmiller, D. C. Fabrycky, S. B. Howell, J. M. Jenkins, K. Uddin, F. Mullally, S. E. Seader, S. E. Thompson, D. T. Sanderfer, W. Borucki, and D. Koch. Kepler Eclipsing Binary Stars. II. 2165 Eclipsing Binaries in the Second Data Release. *AJ*, 142:160, Nov. 2011.

[195] J. C. Smith, M. C. Stumpe, J. E. Van Cleve, J. M. Jenkins, T. S. Barclay, M. N. Fanelli, F. R. Girouard, J. J. Kolodziejczak, S. D. McCauliff, R. L. Morris, and J. D. Twicken. Kepler Presearch Data Conditioning II - A Bayesian Approach to Systematic Error Correction. *PASP*, 124:1000–1014, Sept. 2012.

[196] S. K. Solanki. Sunspots: An overview. *A&AR*, 11:153–286, 2003.

[197] J. Southworth. Homogeneous studies of transiting extrasolar planets - IV. Thirty systems with space-based light curves. *MNRAS*, 417:2166–2196, Nov. 2011.

[198] J. Southworth, T. C. Hinse, M. J. Burgdorf, M. Dominik, A. Hornstrup, U. G. Jørgensen, C. Liebig, D. Ricci, C. C. Thöne, T. Anguita, V. Bozza, S. C. Novati, K. Harpsøe, L. Mancini, G. Masi, M. Mathiasen, S. Rahvar, G. Scarpetta, C. Snodgrass, J. Surdej, and M. Zub. High-precision photometry by telescope defocussing - II. The transiting planetary system WASP-4. *MNRAS*, 399:287–294, Oct. 2009.

[199] A. Sozzetti, P. Giacobbe, M. G. Lattanzi, G. Micela, R. Morbidelli, and G. Tinetti. Astrometric detection of giant planets around nearby M dwarfs: the Gaia potential. *MNRAS*, 437:497–509, Jan. 2014.

[200] G. F. W. Sporer. *Beobachtungen der sonnenflecken zu Anclam.* W. Engelmann, 1874.

[201] J. H. Steffen and W. M. Farr. A Lack of Short-period Multiplanet Systems with Close-proximity Pairs and the Curious Case of Kepler-42. *ApJL*, 774:L12, Sept. 2013.

[202] J. H. Steffen, D. Ragozzine, D. C. Fabrycky, J. A. Carter, E. B. Ford, M. J. Holman, J. F. Rowe, W. F. Welsh, W. J. Borucki, A. P. Boss, D. R. Ciardi, and S. N. Quinn. Kepler constraints on planets near hot Jupiters. *Proceedings of the National Academy of Science*, 109:7982–7987, May 2012.

[203] K. G. Strassmeier. Starspots. *A&AR*, 17:251–308, Sept. 2009.

[204] K. G. Strassmeier and J. B. Rice. Doppler imaging of stellar surface structure. VI. HD 129333 = EK Draconis: a stellar analog of the active young Sun. *A&A*, 330:685–695, Feb. 1998.

[205] K. G. Strassmeier, J. B. Rice, W. H. Wehlau, S. S. Vogt, A. P. Hatzes, I. Tuominen, T. Hackman, M. Poutanen, and N. E. Piskunov. Doppler imaging of high-latitude SPOT activity on HD 26337. *A&A*, 247:130–147, July 1991.

[206] M. C. Stumpe, J. C. Smith, J. E. Van Cleve, J. D. Twicken, T. S. Barclay, M. N. Fanelli, F. R. Girouard, J. M. Jenkins, J. J. Kolodziejczak, S. D. McCauliff, and R. L. Morris. Kepler Presearch Data Conditioning I - Architecture and Algorithms for Error Correction in Kepler Light Curves. *PASP*, 124:985–999, Sept. 2012.

[207] J. J. Swift, J. A. Johnson, T. D. Morton, J. R. Crepp, B. T. Montet, D. C. Fabrycky, and P. S. Muirhead. Characterizing the Cool KOIs. IV. Kepler-32 as a Prototype for the Formation of Compact Planetary Systems throughout the Galaxy. *ApJ*, 764:105, Feb. 2013.

[208] M. Tegmark, M. A. Strauss, M. R. Blanton, K. Abazajian, S. Dodelson, H. Sandvik, X. Wang, D. H. Weinberg, I. Zehavi, N. A. Bahcall, F. Hoyle, D. Schlegel, R. Scoccimarro, M. S. Vogeley, A. Berlind, T. Budavari, A. Connolly, D. J. Eisenstein, D. Finkbeiner, J. A. Frieman, J. E. Gunn, L. Hui, B. Jain, D. Johnston, S. Kent, H. Lin, R. Nakajima, R. C. Nichol, J. P. Ostriker, A. Pope, R. Scranton, U. Seljak, R. K. Sheth, A. Stebbins, A. S. Szalay, I. Szapudi, Y. Xu, J. Annis, J. Brinkmann, S. Burles, F. J. Castander, I. Csabai, J. Loveday, M. Doi, M. Fukugita, B. Gillespie, G. Hennessy, D. W. Hogg, Ž. Ivezić, G. R. Knapp, D. Q. Lamb, B. C. Lee, R. H. Lupton, T. A. McKay, P. Kunszt, J. A. Munn, L. O'Connell, J. Peoples, J. R. Pier, M. Richmond, C. Rockosi, D. P. Schneider, C. Stoughton, D. L. Tucker, D. E. vanden Berk, B. Yanny, and D. G. York. Cosmological parameters from SDSS and WMAP. *PhRvD*, 69(10):103501, May 2004.

[209] B. Tingley, E. Palle, H. Parviainen, H. J. Deeg, M. R. Zapatero Osorio, A. Cabrera-Lavers, J. A. Belmonte, P. M. Rodriguez, F. Murgas, and I. Ribas. Detection of transit timing variations in excess of one hour in the Kepler multi-planet candidate system KOI 806 with the GTC. *A&A*, 536:L9, Dec. 2011.

[210] G. Torres, J. Andersen, and A. Giménez. Accurate masses and radii of normal stars: modern results and applications. *A&AR*, 18:67–126, Feb. 2010.

[211] G. Torres, D. A. Fischer, A. Sozzetti, L. A. Buchhave, J. N. Winn, M. J. Holman, and J. A. Carter. Improved Spectroscopic Parameters for Transiting Planet Hosts. *ApJ*, 757:161, Oct. 2012.

[212] J. Tregloan-Reed, J. Southworth, and C. Tappert. Transits and starspots in the WASP-19 planetary system. *MNRAS*, 428:3671–3679, Feb. 2013.

[213] A. H. M. J. Triaud. The time dependence of hot Jupiters' orbital inclinations. *A&A*, 534:L6, Oct. 2011.

[214] A. H. M. J. Triaud, A. Collier Cameron, D. Queloz, D. R. Anderson, M. Gillon, L. Hebb, C. Hellier, B. Loeillet, P. F. L. Maxted, M. Mayor, F. Pepe, D. Pollacco, D. Ségransan, B. Smalley, S. Udry, R. G. West, and P. J. Wheatley. Spin-orbit angle measurements for six southern transiting planets. New insights into the dynamical origins of hot Jupiters. *A&A*, 524:A25, Dec. 2010.

[215] Y. C. Unruh and A. Collier Cameron. The sensitivity of Doppler imaging to line profile models. *MNRAS*, 273:1–16, Mar. 1995.

[216] D. Valencia, M. Ikoma, T. Guillot, and N. Nettelmann. Composition and fate of short-period super-Earths. The case of CoRoT-7b. *A&A*, 516:A20, June 2010.

[217] J. A. Valenti and D. A. Fischer. Spectroscopic Properties of Cool Stars (SPOCS). I. 1040 F, G, and K Dwarfs from Keck, Lick, and AAT Planet Search Programs. *ApJS*, 159:141–166, July 2005.

[218] V. Van Eylen, M. N. Lund, V. Silva Aguirre, T. Arentoft, H. Kjeldsen, S. Albrecht, W. J. Chaplin, H. Isaacson, M. G. Pedersen, J. Jessen-Hansen, B. Tingley, J. Christensen-Dalsgaard, C. Aerts, T. L. Campante, and S. T. Bryson. What Asteroseismology can do for Exoplanets: Kepler-410Ab is a Small Neptune around a Bright Star, in an Eccentric Orbit Consistent with Low Obliquity. *ApJ*, 782:14, Feb. 2014.

[219] S. S. Vogt, S. L. Allen, B. C. Bigelow, L. Bresee, B. Brown, T. Cantrall, A. Conrad, M. Couture, C. Delaney, H. W. Epps, D. Hilyard, D. F. Hilyard, E. Horn, N. Jern, D. Kanto, M. J. Keane, R. I. Kibrick, J. W. Lewis, J. Osborne, G. H. Pardeilhan, T. Pfister, T. Ricketts, L. B. Robinson, R. J. Stover, D. Tucker, J. Ward, and M. Z. Wei. HIRES: the high-resolution echelle spectrometer on the Keck 10-m Telescope. In D. L. Crawford and E. R. Craine, editors, *Instrumentation in Astronomy VIII*, volume 2198 of *Society of Photo-Optical Instrumentation Engineers (SPIE) Conference Series*, page 362, June 1994.

[220] M. Waldmeier. *Ergebnisse und Probleme der Sonnenforschung.*, volume 82. Wiley, 1955.

[221] J. Wang, J.-W. Xie, T. Barclay, and D. A. Fischer. Influence of Stellar Multiplicity on Planet Formation. I. Evidence of Suppressed Planet Formation due to Stellar Companions within 20 AU and Validation of Four Planets from the Kepler Multiple Planet Candidates. *ApJ*, 783:4, Mar. 2014.

[222] A. J. Watson, T. M. Donahue, and J. C. G. Walker. The dynamics of a rapidly escaping atmosphere - Applications to the evolution of earth and Venus. *Icarus*, 48:150–166, Nov. 1981.

[223] L. M. Weiss and G. W. Marcy. The Mass-Radius Relation for 65 Exoplanets Smaller than 4 Earth Radii. *ApJL*, 783:L6, Mar. 2014.

[224] D. M. Wilson, M. Gillon, C. Hellier, P. F. L. Maxted, F. Pepe, D. Queloz, D. R. Anderson, A. Collier Cameron, B. Smalley, T. A. Lister, S. J. Bentley, A. Blecha, D. J. Christian, B. Enoch, C. A. Haswell, L. Hebb, K. Horne, J. Irwin, Y. C. Joshi, S. R. Kane, M. Marmier, M. Mayor, N. Parley, D. Pollacco, F. Pont, R. Ryans, D. Segransan, I. Skillen, R. A. Street, S. Udry, R. G. West, and P. J. Wheatley. WASP-4b: A 12th Magnitude Transiting Hot Jupiter in the Southern Hemisphere. *ApJL*, 675:L113–L116, Mar. 2008.

[225] J. N. Winn. Transits and Occultations. *ArXiv e-prints*, Jan. 2010.

[226] J. N. Winn, D. Fabrycky, S. Albrecht, and J. A. Johnson. Hot Stars with Hot Jupiters Have High Obliquities. *ApJL*, 718:L145–L149, Aug. 2010.

[227] J. N. Winn, M. J. Holman, J. A. Carter, G. Torres, D. J. Osip, and T. Beatty. The Transit Light Curve Project. XI. Submillimagnitude Photometry of Two Transits of the Bloated Planet WASP-4b. *AJ*, 137:3826–3833, Apr. 2009.

[228] J. N. Winn, J. A. Johnson, D. Fabrycky, A. W. Howard, G. W. Marcy, N. Narita, I. J. Crossfield, Y. Suto, E. L. Turner, G. Esquerdo, and M. J. Holman. On the Spin-Orbit Misalignment of the XO-3 Exoplanetary System. *ApJ*, 700:302–308, July 2009.

[229] J. N. Winn, J. A. Johnson, A. W. Howard, G. W. Marcy, H. Isaacson, A. Shporer, G. Á. Bakos, J. D. Hartman, and S. Albrecht. The Oblique Orbit of the Super-Neptune HAT-P-11b. *ApJL*, 723:L223–L227, Nov. 2010.

[230] J. N. Winn, J. M. Matthews, R. I. Dawson, D. Fabrycky, M. J. Holman, T. Kallinger, R. Kuschnig, D. Sasselov, D. Dragomir, D. B. Guenther, A. F. J. Moffat, J. F. Rowe, S. Rucinski, and W. W. Weiss. A Super-Earth Transiting a Naked-eye Star. *ApJL*, 737:L18, Aug. 2011.

[231] J. N. Winn, R. W. Noyes, M. J. Holman, D. Charbonneau, Y. Ohta, A. Taruya, Y. Suto, N. Narita, E. L. Turner, J. A. Johnson, G. W. Marcy, R. P. Butler, and S. S. Vogt. Measurement of Spin-Orbit Alignment in an Extrasolar Planetary System. *ApJ*, 631:1215–1226, Oct. 2005.

[232] A. Wolszczan and D. A. Frail. A planetary system around the millisecond pulsar PSR1257 + 12. *Natur*, 355:145–147, Jan. 1992.

[233] J. T. Wright, O. Fakhouri, G. W. Marcy, E. Han, Y. Feng, J. A. Johnson, A. W. Howard, D. A. Fischer, J. A. Valenti, J. Anderson, and N. Piskunov. The Exoplanet Orbit Database. *PASP*, 123:412–422, Apr. 2011.

[234] S. Yi, P. Demarque, Y.-C. Kim, Y.-W. Lee, C. H. Ree, T. Lejeune, and S. Barnes. Toward Better Age Estimates for Stellar Populations: The Y^2 Isochrones for Solar Mixture. *ApJS*, 136:417–437, Oct. 2001.